# A MUSE search for the kinematic signatures of gas inflows to the nuclei of galaxies

Tutku Kolcu

A thesis submitted in partial fulfillment of the requirements of
Liverpool John Moores University
for the degree of
Doctor of Philosophy

August 19, 2024

# Declaration

The work presented in this thesis was carried out at the Astrophysics Research Institute, Liverpool John Moores University. Unless otherwise stated, it is the original work of the author.

While registered as a candidate for the degree of Doctor of Philosophy, for which submission is now made, the author has not been registered as a candidate for any other award. This thesis has not been submitted in whole, or in part, for any other degree.

Tutku Kolcu
Astrophysics Research Institute
Liverpool John Moores University
IC2, Liverpool Science Park
146 Brownlow Hill
Liverpool
L3 5RF
UK

August 19, 2024

*"The one with the thesis"*

inspired by 'Friends'

# *Abstract*

Gas inflows contribute to the evolution of galaxies in a plethora of ways. For instance, inflows can enhance star formation, lead to the formation of stellar substructures like nuclear rings and trigger starbursts. Further, gas reaching the nucleus can feed the supermassive black holes (SMBH), power active galactic nucleus (AGN) and trigger outflows, consequently causing quenching. Understanding the mechanisms causing gas inflows to the nucleus is essential for understanding the processes that drive evolution of galaxies.

Mechanisms causing gas inflows, particularly inflow to the nucleus of galaxies, have been a prominent focus of numerous observational and theoretical studies. One of the well-established mechanisms causing gas inflows is extended shocks driven by bars. These extended shocks persist over large regions and should be observable as coherent velocity jumps in the gas kinematic maps. However, these shocks weaken in the central kpc. Despite extensive research, it remains unclear whether the dominant mechanism for gas inflows to galactic nuclei is analogous to the extended shock mechanism observed along bars, or whether it has a different origin. In my thesis research, by studying the kinematic maps of barred and unbarred galaxies, I search for the signatures of extended shocks, similar to those seen along bars, within the innermost galactic regions to determine whether extended shocks are the dominant mechanism of inflow to the galactic nuclei.

In this thesis, using data from the Multi Unit Spectroscopic Explorer (MUSE) on the Very Large Telescope, I study ionised gas kinematic maps of $\sim$21 galaxies from the Composite Bulges Survey (CBS) and the Time Inference with MUSE in Extragalactic Rings (TIMER) Survey of nearby galaxies and search for extended shocks reaching to their nuclei.

I first present my pilot study using the galaxy NGC 1097 where I developed a methodology for identifying signatures of extended shocks. The coherent appearance of extended shocks in the kinematic maps can be distorted by inaccurate extraction of the velocity measurements and dominated by the global rotational flow and local perturbations like stellar outflows. If emission lines contain excess emission, associated with emission from additional sources, I include multiple components in the emission-line fits to correct the inaccurate measurements from wrong fits. Moreover, I show that removal of the global

rotational flow by subtracting the circular velocity of a fitted flat disk can produce artefacts that obscure signatures of the extended shocks in the residual velocities if the inner part of the disk is warped or if gas is moving around the centre on non-circular trajectories. As an alternative, I propose a model-independent method which examines differences in the line-of-sight velocity distribution (LOSVD) moments of H$\alpha$ and [N II]$\lambda$6583 emission lines. This new method reveals the presence of continuous shocks in the regions inward from the nuclear ring of NGC 1097, in agreement with nuclear spiral models. However, differences between LOSVD moments of H$\alpha$ and [N II]$\lambda$6583 might be disguised if star formation or AGN activity dominates the kinematics. To strengthen the argument for the presence of extended shocks, I also study the origin of ionisation through line flux ratios, and I look into the dust morphology. I conclude from my pilot study, which is further confirmed in the analysis of the sample studied in this thesis, that relying solely on one approach is insufficient to rule out the presence of extended shocks in galaxies. It is crucial to employ multiple methodologies when searching for extended shocks in gas.

Following my pilot study, I provide a detailed kinematic analysis of each galaxy I studied in this thesis. This study led to classifying galaxies based on the presence and characteristics of extended shocks within their inner kpc. Moreover, I further explore how the presence and characteristics of extended shocks relate to the dominant nuclear activity in galaxies. I also search for correlations between characteristics of extended shock signatures and the presence of nuclear bars and nuclear rings obtained from CBS, as well as with the overall characteristics of the galaxies.

I conclude that extended shocks to the nucleus are prominent in 52% of the galaxies in my sample. This figure is a lower limit since 15% of the galaxies in the sample exhibit extended shocks along bars, but their extension into the nucleus can not be traced due to obscuration from AGN outflows. The signatures of extended shocks exhibit deprojected residual velocity amplitudes in agreement with models and former observational studies. These results imply that the extended shocks may be the dominant mechanism of inflow to the nucleus of galaxies. I find a clear absence of extended shock signatures in unbarred galaxies, which highlights the critical role of bars in driving these shocks and facilitating gas inflows to the galactic nuclei. Galaxies with nuclear bars only exhibit LINER or Seyfert type emissions within their inner 150pc, while galaxies without nuclear bars show a diverse range of emission mechanisms, including a significant contribution from

star formation. This indicates that in the presence of nuclear bars, the inflows preferentially feed the AGNs while in the absence of nuclear bars inflows can also result in star formation. I also find that the majority of galaxies with nuclear rings present extended shock signatures, whereas galaxies lacking nuclear rings generally do not exhibit these signatures. This finding highlights the crucial role of extended shocks and gas inflow in the formation of nuclear rings. Finally, I find that galaxies exhibiting extended shocks with higher amplitudes tend to have higher average H$\alpha$ velocity dispersions within their inner $\sim$2kpc, suggesting that these shocks contribute to overall gas turbulence.

# Publications

This thesis so far fostered one first-author publication for T. Kolcu. The work presented in Chapters 2, 3 and 4 of this thesis is based on this publication, Paper 1. The work presented in Chapters 5 and 6 is based on the publication in progress, Paper 2.

1. *"Composite Bulges - IV. Detecting signatures of gas inflows in the IFU data: the MUSE view of ionized gas kinematics in NGC 1097"*
   **Kolcu T.**, Maciejewski W., Gadotti D. A., Fragkoudi F., Erwin P., et. al., 2023, MNRAS, 524, 207.

2. *"A MUSE View of gas inflows in to the nuclei of nearby galaxies"*
   **Kolcu T.** Maciejewski W., Erwin P., Gadotti D. A., Fragkoudi F., et. al., **in prep**.

During this thesis research, T. Kolcu published one jointly written paper as a continuity to undergraduate work from the University of Birmingham, supervised by Dr Sean McGee and Dr Jacob Crossett. The content of this work is not relevant for the PhD project and thus excluded from the thesis document.

3. *"Quantifying the role of ram pressure stripping of galaxies within galaxy groups"*
   **Kolcu T.**, Crossett J. P., Bellhouse C., McGee S., 2022, MNRAS, 515, 5877

As a part of an independent project in collaboration with PHANGS, and primarily supervised by Dr Mattia Sormani, T.Kolcu is in preparation for a forthcoming publication. The content of this work is covered briefly in Chapter 8.

4. *"Extreme cloud collisions in nearby barred galaxies"*
   **Kolcu T.**, M.Sormani, E.Schinnerer, W.Maciejewski, F.Fragkoudi, S.Stuber, (in prep.)

T. Kolcu also contributed the the following publications:

5. *"Disc galaxies are still settling–The discovery of the smallest nuclear discs and their young stellar bars"*
   De Sá-Freitas C., Gadotti D. A., Fragkoudi F., et. al. (including **Kolcu, T.**), 2023, A&A, 678, A202

6. *"Composite Bulges III. A Study of Nuclear Star Clusters in Nearby Spiral Galaxies"*
   Ashok. A, Seth A., Erwin P., et. al (including **Kolcu, T.**), 2023, ApJ, 958, 100

T. Kolcu also contributed the the following conference proceeding:

7. *"A MUSE view on gas inflows to the nuclei of barred galaxies"*
   **Kolcu T.**, July 2023, Galactic bars: driving and decoding galaxy evolution, Granada, Spain. Zenodo. https://doi.org/10.5281/zenodo.8124480

# *Acknowledgements*

Throughout this journey, I have experienced all the ups and downs of the famous PhD project curve and have truly learned a lot from every stage. There are so many people who have supported, guided, and inspired me along the way, and I consider myself incredibly lucky for that.

Firstly, I'd like to thank my supervisors who have always been there for me. I wouldn't be where I am today without their help and support. I wish everyone could be as fortunate as I am to have such an incredible team behind them.

I'd like to start with *Witold*; none of this thesis work would have been possible without you. You have been an exceptional supervisor, giving me so many good habits. You particularly taught me the importance of being patient and careful in research. I will miss our interesting long discussions. I can't thank you enough for all the countless late evenings you've spent thinking about this thesis work and for deciphering my writinig. Although, you've probably already spotted a couple of typos in this paragraph, which I left there intentionally to make you laugh. You will always be a role model for me in how to be a good and caring supervisor. Thank you very much for your support in these past years, I am truly grateful for everything.

*Dimitri* and *Francesca*, thank you for always being there for me, even after we all left ESO. Being in your research group, I grew up as a researcher in a welcoming and nurturing working environment and learnt to support one another. *Dimitri*, you have been a great supervisor and a role model. Your generosity and kindness are irreplaceable, and it has been and continues to be, a pleasure knowing and working with you. *Francescamou*, you have inspired me in many ways. Besides being a woman in STEM, we also share our Cypriot heritage and the experience of living abroad and feeling homesick all the time. I am so lucky to have had you as my mentor during this journey, ευχαριστώ.

*Peter*, thank you for all your help and support with this project, especially for the time, effort, and patience you devoted to discussing each galaxy individually, and for reviewing my writing. *Steve*, thank you for always being honest and encouraging me to think outside the box, and of course, for all your help with my thesis writing and postdoc applications.

Moving on from supervisors, I would like to thank *Rob Grand* and *Tim Davies* for taking the time to review this thesis.

To my mentors at ARI, *Ricardo* and *Sebastian*, thank you for this past years. I have always felt your genuine kindness and care. Thank you both for your help in preparing me for applications, giving feedback on my writing and for the mock interviews. You are both great people to be around of. *Ricardo*, your passion and excitement for astronomy have always been an inspiration. You also taught me how to balance my week and truly enjoy Fridays. *Sebastian*, you are one of the most honest yet kindest people at ARI. You taught me to be more ambitious and I am grateful for that. Thank you for the nice chats and all the advice for these past years.

I would like to thank *Phil James* and *Ian McCarthy*. *Phil*, thank you for all your help and comments on my thesis writing, and your wholesome personality. *Ian*, thank you for your feedback, advice, and support in my postdoc applications; without your guidance, I would not have applied for my upcoming postdoc position.

I am deeply thankful to *Marie Martig* for her endless support and kindness whenever I needed it. I also appreciate *Ivan Baldry* and *Renske Smit* for their valuable comments and discussions on my research. I am also thankful for *Sue Percival*, whose advice I kept in my mind during this thesis writing stage: "You will always feel like there are so many things left to write about, but it all will just come to an end suddenly".

I would like to thank *Sean McGee*, one of my undergraduate supervisors from the University of Birmingham, for his invaluable support and assistance with my postdoc applications. Additionally, my gratitude extends to *Mattia Sormani* for offering me an exciting research project and the opportunity to collaborate with one of the largest research groups in astronomy.

Continuing with my family, I'd like to thank my parents for always standing proudly by my side. I wouldn't be the person I am today without them. To my dearest brother *Ege*, thank you for being there for me and for always teasing me about how stressed I am; rest assured, I'll always be there for you too. To my sister *Cansu*, thank you for your support and listening to my endless whining. Also, to my *Dedom*, for just existing and making me happy.

To my aşkım *Alonso*, you are by far the most precious gift life has given me during this period. Thank you for being you, for your endless support and encouragement, and for bringing joy to my life every day, even when times are difficult for you as well.

My time during this journey wouldn't have been as enjoyable if I hadn't shared it with my dearest friends. There are so many people I am thankful for but I have to give special mentions to some of you who put up with my whining a little bit more otherwise the list gets even longer...

To my dearest Liverpool Gang at ESO, *Stephen* and *Gemma*, the two of the nicest people I know, thank you for your company and for being there for me. Also, *Anita, Elena, Juliet, Keegan*, and *Simon*, everything in life is just more fun and enjoyable with you guys. I am so grateful for having shared this journey with you. *Camila*, for a while it was just the two of us in our group. Thanks for being such a great friend and research partner. *Luca*, thank you for all the trips and good times spent together, and for not kicking me out of your house despite my clumsiness. *Alvaro*, thank you for your shine, enthusiasm and support; particularly for sending me dog videos all the time which make my day.

Moving on to my ARI friends, I want to thank *Ali, Elena, Joao, Sara, Thayse*, and *Scarlett*, you are all wonderful people. I am so grateful for all the moments we have shared for the past years. Thank you for your support and encouragement. Special thanks to the former, current, and cameo members of office 3.18, particularly to *Adrian, Andrea, Andrew, Flo, Jemima, Kyle, Phoebe, Ryan, Sara*, and *Shobit* for being great office mates, full of spirit. Thank you for watering my plants all the time, keeping me updated with all the tea and for the fun quiz evenings. Especially to my witch coven gals; I will miss our random co-star and witchy chats. Also, thank you *Dharmesh* for your encouragement on jobs, and company in going through all these submission processes together. *Fiona*, thank you for being so wholesome and caring.

To all my other friends with whom we have crossed paths during this journey, thank you all for your company, good energy, and friendship in these past years.

# Contents

**Declaration** ii

**Abstract** iv

**Publications** vii

**Acknowledgements** ix

**List of Figures** xv

**List of Tables** xviii

**Abbreviations** xix

**1 Introduction** 1
- 1.1 Mechanisms causing gas inflows in galaxies . . . 2
  - 1.1.1 Gas inflows to the inner kpc: on the formation of nuclear rings and disks . . . 4
  - 1.1.2 Gas inflows to the nucleus: on AGN fuelling . . . 5
- 1.2 Dynamics of bars, origin of extended shocks in gas . . . 7
- 1.3 Signatures of extended shocks in kinematics . . . 11
- 1.4 Integral Field Spectroscopy . . . 16
- 1.5 Thesis outline . . . 20

**2 Data and Data Extraction** 21
- 2.1 Sample Selection . . . 21
- 2.2 Observations . . . 22
- 2.3 Extraction of the kinematic measurements from MUSE Spectra . . . 29
  - 2.3.1 Deriving stellar line-of-sight velocity distribution moments . . . 29
  - 2.3.2 Deriving ionised gas line-of-sight velocity distribution moments . . . 32
  - 2.3.3 Multiple Gaussian approach to the fitting . . . 35
  - 2.3.4 Alterations in secondary component fitting and masking procedures applied to other sample galaxies . . . 41

**3 The methodology of searching for gas inflows on the example of NGC 1097** 53
- 3.1 Searching for coherent kinematic structures in deviations from circular motion . . . 53
- 3.2 Identifying the dominating ionisation mechanisms . . . 62

3.3 Searching for coherent kinematic differences between distinct emission line groups 64
3.4 Studying the dust morphology in structure maps . . . . . 67

**4 Findings within the nuclear region of NGC 1097 69**
4.1 Elliptical flow pattern in regions inward from the nuclear ring . . . . . 69
4.2 Evidence from the MUSE data for nuclear spiral shocks . . . . . 72
4.3 Multi-phase AGN outflows in the nuclear regions . . . . . 75
4.4 Conclusions on the signatures of extended shocks to the nucleus of NGC1097 . . 76

**5 Individual analysis of the sample galaxies 77**
5.1 IC2051 . . . . . 78
5.2 NGC 289 . . . . . 81
5.3 NGC 613 . . . . . 85
5.4 NGC 1300 . . . . . 89
5.5 NGC 1433 . . . . . 93
5.6 NGC 1566 . . . . . 99
5.7 NGC 3351 . . . . . 103
5.8 NGC 3368 . . . . . 106
5.9 NGC 3489 . . . . . 109
5.10 NGC 3626 . . . . . 112
5.11 NGC 4237 . . . . . 115
5.12 NGC 4303 . . . . . 117
5.13 NGC 4321 . . . . . 124
5.14 NGC 4380 . . . . . 129
5.15 NGC 4457 . . . . . 131
5.16 NGC 4643 . . . . . 134
5.17 NGC 4941 . . . . . 137
5.18 NGC 5248 . . . . . 140
5.19 NGC 7177 . . . . . 143
5.20 NGC 7513 . . . . . 146

**6 Statistical analysis of the galaxy sample 149**
6.1 Classification of galaxies based on the signatures of extended shocks and nuclear emission types . . . . . 149
6.2 Obtaining the characteristics of the sample galaxies studied in this thesis . . . . 153
6.2.1 Determining the deprojected velocity residual amplitudes of extended shocks 153
6.2.2 Obtaining the average H$\alpha$ velocity dispersion of galaxies . . . . . 155
6.3 Statistical studies of the correlations . . . . . 157
6.3.1 The dominance of extended shocks within the inner kpc region of galaxies 157
6.3.2 The correlation between extended shocks and average H$\alpha$ velocity dispersion 159
6.3.3 The correlation between extended shocks and stellar mass of galaxies . . . 160
6.3.4 The correlation of extended shocks with the presence of nuclear bars and nuclear rings . . . . . 162
6.3.4.1 Correlations with nuclear bars . . . . . 162
6.3.4.2 Correlations with nuclear rings . . . . . 164

**7 Thesis Summary & Conclusions 166**

**8 Future Outlook 172**
8.1 Extreme cloud collisions in nearby barred galaxies . . . . . 172
8.2 Multi-wavelength insights into how the synergy between large-scale interactions and internal dynamics shapes galaxy gas kinematics . . . . . 177

Appendices . . . . . 179
A Supplementary maps for the pilot study with NGC 1097 . . . . . 180
B Supplementary collective plots for sample galaxies studied in this thesis . . . . . 181
C Supplementary Tables . . . . . 189

**Bibliography** **191**

# List of Figures


1.1 Illustration of gas flow within a bar potential, off-axis shocks . . . . . 8
1.2 Distribution of density and velocity along a slit crossing shocks . . . . . 8
1.3 Demonstration of a nuclear spiral shock . . . . . 9
1.4 Illustration of gas flow within a bar potential, on-axis shocks . . . . . 10
1.5 Perturbations in the potential and kinematic response of gas . . . . . 13
1.6 $m = 2$ harmonic term perturbation in potential and kinematics . . . . . 13
1.7 An example to kinematic signatures of extended shocks from Zurita et al. (2004) . . . . . 15
1.8 The principle behind integral field spectroscopy . . . . . 17
1.9 Comparisons between the FOV of different IFUs . . . . . 19

2.1 Galaxy sample studied in this thesis . . . . . 26
2.2 Large-scale and MUSE colour composite image of NGC 1097 . . . . . 28
2.3 The implementation of the Data Analysis Pipeline. . . . . 30
2.4 A representative spectrum of NGC 1097 . . . . . 30
2.5 Stellar LOSVD moment maps of NGC 1097 . . . . . 32
2.6 LOSVD moment maps of H$\alpha$, [N II]$\lambda$6583 and [O III]$\lambda$5007 for NGC 1097 34
2.7 Spectra of spaxels in NGC 1097, with and without excess emission . . . . 37
2.8 Comparison between kinematic measurements obtained with single Gaussian fits and fits including secondary [N II]$\lambda$6583 component, NGC 1097 . 37
2.9 The mask of spaxels for NGC 1097 . . . . . 39
2.10 Corrected LOSVD moments of NGC 1097, after combining the results from single Gaussian fits with the fits including the secondary component 40
2.11 H$\alpha$ flux of the sample galaxies . . . . . 44
2.12 [N II]$\lambda$6583 flux of the sample galaxies . . . . . 45
2.13 [O III]$\lambda$5007 flux of the sample galaxies . . . . . 46
2.14 H$\alpha$ velocity maps of the sample galaxies . . . . . 47
2.15 [N II]$\lambda$6583 velocity maps of the sample galaxies . . . . . 48
2.16 [O III]$\lambda$5007 velocity maps of the sample galaxies . . . . . 49
2.17 H$\alpha$ velocity dispersion maps of the sample galaxies . . . . . 50
2.18 [N II]$\lambda$6583 velocity dispersion maps of the sample galaxies . . . . . 51
2.19 [O III]$\lambda$5007 velocity dispersion maps of the sample galaxies . . . . . 52

3.1 The velocity of the modelled disk of NGC 1097 and the corresponding residual velocity map. . . . . 55
3.2 Artefacts in the residual velocity field when the wrongly fitted disk is removed from the observed velocity field. . . . . 56

3.3 Radial distributions of parameters fitted to the Hα velocity field of NGC 1097 with `Kinemetry` . . . 59
3.4 Residual velocity map of the inner 30″×30″ of NGC 1097 . . . 61
3.5 The BPT diagram of the inner 30″×30″ . . . 63
3.6 Comparison maps for Hα and [N II]λ6583 emission and kinematics in NGC 1097 . . . 65
3.7 Structure map of NGC 1097 . . . 68

4.1 The PA of the LON and PA of the zero velocity line fitted to Hα and stellar LOS velocity maps . . . 71
4.2 NACO J-band image of NGC 1097 from Prieto et al. (2005) . . . 73
4.3 Residual velocities of NGC 1097, after subtracting the LOS velocity of the disk model from the observed [N II]λ6583 velocity field . . . 74

5.1 The diagnostic maps of IC 2051 . . . 80
5.2 The diagnostic maps of NGC 289 . . . 84
5.3 The diagnostic maps of NGC 613 . . . 88
5.4 The diagnostic maps of NGC 1300 . . . 92
5.5a Mask of spaxels in NGC 1433 . . . 95
5.5b The diagnostic maps of NGC 1433 . . . 98
5.6 The diagnostic maps of NGC 1566 . . . 102
5.7 The diagnostic maps of NGC 3351 . . . 105
5.8 The diagnostic maps of NGC 3368 . . . 108
5.9 The diagnostic maps of NGC 3489 . . . 111
5.10 The diagnostic maps of NGC 3626 . . . 114
5.11 The diagnostic maps of NGC 4237 . . . 116
5.12a NGC 4303 spectra and mask . . . 122
5.12b The diagnostic maps of NGC 4303 . . . 123
5.13a NGC 4321 mask of spaxels . . . 126
5.13b The diagnostic maps of NGC 4321 . . . 128
5.14 The diagnostic maps of NGC 4380 . . . 130
5.15 The diagnostic maps of NGC 4457 . . . 133
5.16 The diagnostic maps of NGC 4643 . . . 136
5.17 The diagnostic maps of NGC 4941 . . . 139
5.18 The diagnostic maps of NGC 5248 . . . 142
5.19 The diagnostic maps of NGC 7177 . . . 145
5.20 The diagnostic maps of NGC 7513 . . . 148

6.1 The BPT diagram of the galaxy sample studied in this thesis . . . 151
6.2 The distribution of deprojected residual velocity amplitudes of galaxies in different kinematic categories . . . 155
6.3 The distribution of average Hα velocity dispersion of galaxies in each kinematic category . . . 156
6.4 The distribution of galaxies by kinematic categories . . . 158
6.5 The deprojected residual velocity amplitudes against the average Hα velocity dispersion of galaxies in different kinematic categories. . . . 160
6.6 The distribution stellar mass of galaxies in each kinematic category . . . 161

6.7 The deprojected residual velocity amplitudes against stellar mass of galaxies in different kinematic categories. . . . 161
6.8 The fraction of galaxies in each kinematic category grouped by the presence and absence of nuclear bars. . . . 163
6.9 The fraction of galaxies in each kinematic category grouped by the presence and absence of nuclear rings. . . . 165

8.1 The CO(1–0) diagnostic maps of the Central Molecular Zone . . . 173
8.2 Mechanism of overshooting gas in galaxies . . . 174
8.3 ALMA CO(2–1) maps and JWST composite image of NGC 1512 . . . 176
A.1 LOSVD moments for fits including higher order moments, NGC 1097 . . . 180
B.1 The structure, residual velocity, velocity difference and BPT map of galaxies in the sample . . . 182
B.2 The BPT diagrams of sample galaxies studied in this thesis . . . 186
B.3 Deprojected residual velocity maps of the galaxy sample studied in this thesis. . . . 187
B.4 H$\alpha$ velocity dispersion against AON for the inner kpc region of galaxies. . . 188

# List of Tables

1 The sample of galaxies studied in this thesis . . . . . 25
2 Characteristics of the fitted emission lines . . . . . 33

3 The individual findings for the sample galaxies studied in this thesis . . . 152

C.1 Summary of large-scale and Kinemetry inferred disk orientation parameters for the sample galaxies studied in this thesis . . . . . 189
C.2 The PSF FHWM (seeing) values recorded for MUSE observations of sample galaxies . . . . . 190

# Abbreviations

| | |
|---|---|
| **ACS** | **A**dvanced **C**amera for **S**urvey |
| **AGN** | **A**ctive **G**alactic **N**ucleus |
| **ALMA** | **A**tacama **L**arge **M**illimeter/submillimeter **A**rray |
| **AO** | **A**daptive **Optics** |
| **AON** | **A**mplitude **O**ver **N**oise |
| **CBS** | **C**omposite **B**ulges **S**urvey |
| **CGS** | The **C**arnegie-Irvine **G**alaxy **S**urvey |
| **CLoGS** | **C**omplete **Lo**cal-Volume **G**roups **S**ample |
| **CMZ** | **C**entral **M**olecular **Z**one |
| **DAP** | **D**ata **A**nalysis **P**ipeline |
| **EVF** | **E**xtended **V**elocity **F**eature |
| **GIST** | **G**alaxy **I**FU **S**pectroscopy **T**ool |
| **GMOS** | **G**emini **M**ulti-**O**bject **S**pectrograph |
| **ILR** | **I**nner **L**indblad **R**esonance |
| **IFS** | **I**ntegral **F**ield **S**pectroscopy |
| **IFU** | **I**ntegral **F**ield **U**nit |
| **JWST** | **J**ames **W**ebb **S**pace **T**elescope |
| **LON** | **L**ine **O**f **N**odes |
| **LOS** | **L**ine **O**f **S**ight |
| **LOSVD** | **L**ine **O**f **S**ight **V**elocity **D**istribution |
| **MAUVE** | **M**USE and **A**LMA **U**nveiling the **V**irgo **E**nvironment |
| **MUSE** | **M**ulti **U**nit **S**pectroscopic **O**bserver |
| **NACO** | **N**asmyth **A**daptive Optics System (NAOS) – NIR Imager and Spectrograph (**CO**NICA) |
| **NED** | **N**ASA/IPAC **E**xtragalactic **D**atabase |
| **NGC** | **N**ew **G**eneral **Catalogue** |
| **OASIS** | **O**ptically **A**daptive **S**ystem for **I**maging **S**pectroscopy |
| **PHANGS** | **P**hysics at **H**igh **A**ngluar resolution in **N**earby **G**alaxie**S** |
| **PMAS** | **P**ostdam **M**ulti-**A**perture **S**pectrophotometer |
| **PPAK** | **P**MAS Fiber **PA**c**K** |
| **pPXF** | **P**enalised **P**i**X**el **F**itting |
| **SAURON** | **S**pectroscopic **A**real **U**nit for **R**esearch on **O**ptical **N**ebulae |
| **SF** | **S**tar **F**ormation |
| **SFR** | **S**tar **F**ormation **Rate** |
| **SMBH** | **S**uper **M**assive **B**lack **H**ole |
| **SNR** | **S**ignal to **N**oise **R**atio |
| **SSP** | **S**ingle-**S**tellar **P**opulation |
| **TIMER** | **T**ime **I**nference with **MUSE** in **E**xtragalactic **R**ings |
| **TIGER** | **T**raitement **I**ntégral des **G**alaxies par l'**É** tude de leurs **R**ays |
| **VLT** | **V**ery **L**arge **T**elescope |

*To my parents; who always proudly have been by my side ...*

*– Her zaman gurur ile yanımda olan annem ve babama –*

*&*

*To my late grandma; who always supported me but was slightly disappointed that I will not become a medical doctor ...*

*– Rahmetli anneanneme; beni her zaman destekleyen ama tıp doktoru olmayacağım için biraz hayal kırıklığına uğrayan –*

# Chapter I

# Introduction

Galaxies are the building blocks of the universe, providing key insights into the formation and evolution of large-scale structures across cosmic time. Studying galaxies helps us to understand the role of dark matter and dark energy, which are core ingredients in structure formation (Navarro et al., 1997; Cole et al., 2000).

Delving into galactic studies, we can grow our understanding of the fundamental physical mechanisms shaping the evolution of galaxies across cosmic time; such as the effect of merger interactions and star formation. By studying galaxies in different environments, such as groups and clusters, we can examine the effect of gravitational interactions, galaxy mergers, the accretion of gas and ram-pressure stripping on their evolution (Lagos et al., 2018). These gravitational interactions can trigger starbursts (Boselli & Gavazzi, 2006; Kapferer et al., 2009), feed supermassive black holes (SMBHs) in the cores of galaxies (Chapon et al., 2013; Roberts et al., 2023), and cause transformations in galaxy morphologies (Barnes & Hernquist, 1996; Hopkins et al., 2009). Moreover, by studying galaxies at varying redshifts, we gain a panoramic view of star formation processes across time, offering a window into the life cycles of stars (Kennicutt, 1998; Kennicutt & Evans, 2012; Madau & Dickinson, 2014).

One of the fundamental yet not fully understood topics in astronomical research is the growth of SMBHs at the cores of galaxies. The accretion of gas onto SMBHs can power active galactic nuclei (AGNs) and lead to energetic feedback mechanisms. Simulations suggest that outflows from AGNs can transform galaxies by suppressing star formation and causing quenching (Di Matteo et al., 2005; Silk, 2013; Somerville & Davé, 2015; Donnari et al., 2021). However, from an observational perspective, whether AGNs cause quenching remains debated (Fabian, 2012; Ishibashi & Fabian, 2014; Woo et al., 2017; Goubert et al., 2024). The feeding of SMBHs can be triggered via various mechanisms occurring at extragalactic scales down to nuclear scales. In isolated field galaxies, gas redistribution and the inflow to the nucleus is primarily driven by internal processes, such as bars and spirals (Athanassoula, 1992). In contrast galaxies in dense clusters or groups, along with internal processes, extragalactic interactions, such as mergers and ram-pressure stripping, also play a significant role in triggering gas migration towards

galactic nuclei (Boselli & Gavazzi, 2006; Kapferer et al., 2009). Despite extensive research into the redistribution of gas within galaxies, the dominant mechanisms driving inflows to the nucleus remain unclear. Understanding these processes is crucial for probing the feeding and feedback mechanisms that significantly affect evolution of galaxies.

In my thesis research, I study the kinematics and dynamics of gas within the inner kpc region of nearby disk galaxies, extending down to a few tens of parsecs. My goal is to understand the processes driving gas inflows to galactic nuclei. The disk galaxies are characterised by being relatively flat and settled, and typically gas rich, therefore they present an optimal environment for studying the flow of gas and stars (Larson et al., 1980; Elmegreen et al., 2005; Athanassoula et al., 2013). Therefore, by focusing on these galaxies, I aim to understand the distribution of gas within the disk and inflows to the nucleus which shape the galactic evolution and structure.

## 1.1 Mechanisms causing gas inflows in galaxies

Disk galaxies are axisymmetric (Miller, 1978a,b; Sellwood, 1980), indicating their angular momentum is conserved which allows stars and gas to orbit the galactic centre in relatively stable and circular orbits. This axisymmetry supports a fine balance within the galactic disk, regulating a steady state of star formation and evolutionary growth. However, several phenomena can disrupt this axisymmetry and redistribute angular momentum within the disk. This redistribution can lead to migration of the gas from outer kpc regions towards the inner parsec regions, commonly called **gas inflows**, which can induce significant changes in the dynamics and evolution of the galaxy.

***Galactic mergers and interactions*** stand as one of the most significant disruptors of the axisymmetry in the disk; the tidal forces exerted during close encounters or collisions distort and reshape galactic structure, and redistribute angular momentum across the galaxy, leading to gas inflows (Mihos & Hernquist, 1996; Barnes & Hernquist, 1996; Hopkins & Hernquist, 2006; Robertson et al., 2006; Lagos et al., 2018). Moreover, ***the density waves*** which create spiral arms can exert torques to the gas and stars (Roberts et al., 1975; Kendall et al., 2008), affecting the overall distribution of angular momentum in the galaxy, and causing gas inflows (Elmegreen et al., 1999; Grosbøl et al., 2004). ***Dynamical friction*** is another pivotal mechanism that can cause gas inflows. As gas clouds or dwarf galaxies orbit within/around a galaxy, the dynamical friction against the galaxy's stellar population and interstellar medium can slow these bodies down, consequently leading to angular momentum exchange between these bodies and the galaxy's medium (Combes, 2003; D'Onghia et al., 2006; Jogee, 2006; Dutton & van den Bosch, 2012). This redistribution of gas can induce the secular evolutionary

processes that slowly shape the galaxy's structure over time, promoting the growth of central bulges and the reshaping of disk profiles (Navarro et al., 1995; Shlosman & Noguchi, 1993), and contributing to nuclear feeding (Heller & Shlosman, 1994; Park & Bogdanović, 2017). Another mechanism that can introduce a dimension of complexity to galaxy dynamics are ***magnetic loops***; large-scale structures of magnetic fields that arch above the galactic plane. These structures can influence the regulation of galactic magnetic fields (Krause et al., 1989; Beck & Wielebinski, 2013), gas dynamics (Liu et al., 2023), star formation (McKee & Ostriker, 2007) and the nuclear feeding cycle (Hu et al., 2022); their influence can also interfere with other galactic structures, such as bars (Abbate et al., 2020).

Amongst numerous mechanisms, ***galactic bars*** are particularly recognised for their role in redistributing the angular momentum and causing gas inflows which can drive significant transformative changes in the evolution of the disk galaxies.

Bars are found in 60–80% of disk galaxies within the local universe (Eskridge et al., 2000; Menéndez-Delmestre et al., 2007; Sheth et al., 2012; Erwin, 2018), and they have a profound influence on the gas dynamics and shaping morphology of their host galaxy. The presence of a bar introduces strong non-axisymmetric torques which significantly alter the uniform gravitational potential of a disk galaxy and redistribute angular momentum (Athanassoula, 1992). Because of these non-axisymmetric torques the bar introduces, the stable circular orbits within the galactic disk become more elongated or oval, which can also align with the major axis of the bar; this leads formation of $x_1$ orbits – orbits that are elongated along the bar's major axis, which I revisit in more detail in Sect. 1.2. These put gas clouds on intersecting trajectories, leading to shocks in gas. Shocks lead to angular momentum transfer between the gas and the bar. Consequently, due to the loss of angular momentum, the gas starts funnelling radially inwards, by following the non-circular orbits (Athanassoula, 1992; García-Burillo et al., 2005; Lin et al., 2013; Audibert et al., 2021).

The fine balance causing the steady evolutionary growth of disk galaxies can significantly be disrupted by gas inflows; no matter which mechanism induces the inflow. The inflow of gas can consequently increase the central concentration of gas, leading to nuclear star formation (SF) (Ellison et al., 2011; Prieto et al., 2019). It can cause starbursts (Heller & Shlosman, 1994; Mazzuca et al., 2008) and change the morphology of the central regions by creating substructures, such as gaseous and stellar disks and rings (Shlosman et al., 1989; Athanassoula, 1992; Piner et al., 1995; Martini et al., 2003b; Kim et al., 2012; Sormani et al., 2015). Further, the gas reaching the very centre can feed the SMBH in the galactic core, which can power AGNs (Davies et al., 2014; Audibert et al., 2020) and lead to highly energetic feedback, or outflows (Prieto et al., 2005; Davies et al., 2014;

Audibert et al., 2019). Outflowing gas from AGN feedback can in turn rapidly suppress SF and cause quenching (Man et al., 2019; Donnari et al., 2021).

Therefore, over time, the gas inflows can significantly change the morphological and dynamical state of the disk galaxies, contributing to the diversity observed in the galactic population. Hence, to understand the structural evolution of the galaxies, it is important to understand the role of the inflowing gas. To highlight the critical importance of studying gas inflows, below, I expand more on the insights into several transformative effects gas inflows have on their host galaxies.

### 1.1.1 Gas inflows to the inner kpc: on the formation of nuclear rings and disks

Studying the inflowing gas helps us to understand how SF is being regulated within the central regions of galaxies. For example, inflow driven by bars is recognised as the primary mechanism behind the formation of nuclear rings and disks (Schwarz, 1981; Combes & Gerin, 1985; Athanassoula, 1992; Heller & Shlosman, 1994; Knapen et al., 1995b; Mazzuca et al., 2008) which are typically found within the inner kpc region of galaxies (Heller & Shlosman, 1996; Rubin et al., 1997). From the ∼10 kpc regions to the inner kpc the transport of gas is efficient. The strong shear generally prevents the formation of stars along the bar lanes (Kim et al., 2024) – formation of bar lanes (or dust lanes) are discussed in Sect. 1.2. However, within the sub-kpc regions, the efficiency of angular momentum transfer decreases. Consequently, within inner kpc the gas accumulates due to its collisional nature, triggering starbursts and leading to the formation of nuclear rings and disks (Heller & Shlosman, 1994; Piner et al., 1995; Sheth et al., 2005; Mazzuca et al., 2008; Sormani et al., 2015). The strongest SF is usually seen at the location where bar lanes connect to the nuclear rings (Knapen et al., 1995b; Ryder et al., 2001; Sandstrom et al., 2010; Sormani et al., 2023a). The nuclear rings and disks are rotationally supported and have low velocity dispersions in the kinematics. Although we have established a strong understanding of the origin of these stellar substructures, it remains unclear what determines their sizes (Combes & Gerin, 1985; Athanassoula, 1992; Knapen, 2005; Kim & Stone, 2012; Sormani et al., 2018; Gadotti et al., 2020). Understanding the formation and evolution of nuclear rings and disks is important, as the ages of nuclear rings can be correlated with the ages of the host galaxy's bar, providing us with invaluable insights into when disk galaxies settle and form bars (de Sá-Freitas et al., 2023b).

Numerical simulations reveal that galaxy mergers can also initiate the formation of nuclear discs, yet these are significantly smaller than those formed through bar-driven

processes (Mayer et al., 2008; Chapon et al., 2013). The observations reveal that 19% of nuclear rings are found in galaxies without bars, suggesting that even in these galaxies, gas can migrate inwards and lead to nuclear ring formation, though the mechanism is weaker compared to the bar-driven scenario (Comerón et al., 2010).

### 1.1.2 Gas inflows to the nucleus: on AGN fuelling

The accumulation of gas onto the central SMBH of galaxies is a fundamental process that powers AGNs (Antonucci, 1993). This continuous feeding not only regulates the growth of SMBHs (Croton et al., 2006) but also triggers AGN outflows, which can suppress star formation and lead to quenching (Man et al., 2019; Donnari et al., 2021). Thus, understanding the inflow of gas to the nucleus is crucial for deciphering how nuclear activities are fuelled in galaxies and what drives the growth of supermassive black holes.

Over the past decades, numerous studies have explored the connection between AGN activity and host galaxy properties (Kauffmann et al., 2003; Ho, 2008; Cid Fernandes et al., 2004, 2011), highlighting various large-scale external and internal mechanisms proposed for driving gas into galactic nuclei. These mechanisms range from the accretion of gas streams during merger interactions to secular evolution driven by dynamical friction and bars, as I discussed earlier in Sect. 1.1.

On large scales, the role of merger interactions in fuelling AGN remains a topic of active debate. While some research suggests a weak connection between AGN feeding and merger interactions (Kocevski et al., 2012; Schawinski et al., 2012; Villforth et al., 2014), other studies argue that mergers can play a significant role in feeding AGNs (Martini et al., 2003b; Rosario et al., 2012).

On kpc scales, a significant focus has been placed on the correlation between the presence of bars and nuclear activity (Shlosman et al., 1989; Knapen et al., 2000; Prieto et al., 2005; van de Ven & Fathi, 2010; Davies et al., 2014; Audibert et al., 2019). It is widely accepted that bars transport the gas from outer kpc regions, ∼10 kpc, to the inner kpc; where the accumulation of gas contributes to the formation of nuclear rings and disks (see Sect. 1.1.1). However, the dominant mechanism transporting gas from the inner kpc to the very nucleus, down to parsec regions, is not well established. Whether this mechanism is analogous to bar-driven shocks remains an open question.

On scales of a couple of hundred parsecs, ***nuclear bars***, akin to the large-scale bars, are critical mechanisms in channelling gas towards the galactic nucleus by facilitating a further reduction in angular momentum (Shlosman et al., 1989; Heller et al., 2007; Namekata et al., 2009; Hopkins & Quataert, 2010; Li et al., 2023). Approximately 20%

of the disk galaxy population hosts nested bar systems (Laine et al., 2002; Erwin, 2011). As shown in simulations, compared to unbarred and single-barred galaxies, galaxies with double bars have enhanced mass inflow rates to nucleus (Li et al., 2023).

Furthermore, models show evidence that under conditions of strong inflow along a galactic bar, the gas does not necessarily settle into a nuclear ring within the inner kpc region. Instead, the straight shocks along the bar may curve towards the centre, creating a spiral pattern that leads to the formation of structures known as ***nuclear spirals*** (Regan & Mulchaey, 1999; Englmaier & Shlosman, 2000). These structures are primarily observed in barred galaxies, yet some tightly wound nuclear spirals avoid barred galaxies, and are more common in unbarred galaxies (Martini et al., 2003a,c). Nuclear spirals are commonly associated with Seyfert nuclei and are proposed to be the main driver of gas inflow to the nucleus (Regan & Mulchaey, 1999; Martini & Pogge, 1999; Pogge & Martini, 2002). Hydrodynamical models further demonstrate that these nuclear spirals act as spiral shocks in gas, continuing to propagate towards the galactic centre (Pogge & Martini, 2002; Maciejewski, 2004b), facilitating the transport of gas to the nucleus (Davies et al., 2009). Even though many studies suggest extended shocks along bars, as dominant drivers of gas inflow to the nucleus (Maciejewski et al., 2002; Maciejewski, 2004a,b; Ann & Thakur, 2005; García-Burillo et al., 2005; Thakur et al., 2009), the efficiency of such mechanisms are debated and thought to depend on certain conditions, such as the sound speed of the gas and the shape of the gravitational potential (Kim et al., 2012).

Several factors can hinder or slow gas inflows towards the centre of galaxies. While galactic bars effectively transport gas from outer regions ($\sim$10 kpc) towards the inner kpc, their forces exerted on gas weaken closer to the core, decreasing the efficiency of inflow there, where AGN mass accretion occurs (Goodman, 2003). Moreover, simulations also reveal that gas driven inwards by bars often accumulates in nuclear rings, fuelling the SF rather than progressing inwards to the nucleus (Fanali et al., 2015; Li et al., 2017; Tress et al., 2020). This suggests that nuclear rings act as barriers, preventing the propagation of shocks and the inward flow of gas to the galactic nuclei. Additionally, turbulence introduced by mechanisms like AGN feedback and stellar feedback, disrupts the regular inflow of gas, making its path to the nucleus more chaotic and less predictable.

Despite considerable research into the flow of gas within the inner kpc region of galaxies, the primary mechanism funnelling gas to the nucleus remains unclear. Therefore, this thesis aims to shed light on this open question by investigating whether extended shocks driven by galactic bars are the dominant mechanism for gas inflows to the nucleus of galaxies.

## 1.2 Bar dynamics as the origin of extended shocks in gas

Pioneering studies provide a consistent view of how gas flow patterns are connected to galaxy dynamics, particularly bar dynamics. In bars, the gas is able to settle into two main stable orbit classes: the $x_1$ orbits that align with the bar and the $x_2$ orbits that run perpendicular to it. The transition of gas from $x_1$ to $x_2$ orbits leads to the formation of two significant shocks, sometimes referred to as the principal shocks, at the leading edge of the bar (Athanassoula, 1992). Such shocks in gas that form in response to the gravitational torques of bars and ovals, stretch over large distances along straight or curved (spiralling inward) lines, the latter often assuming a spiral shape. Thus, in this thesis I call them ***extended shocks***. The extended shocks are point symmetric and are along the bar major axis.

The extended shocks along the bar facilitate angular momentum transfer from the gas to the bar. As I explained in the previous sections, this transfer causes the gas to funnel towards the inner regions of the galaxy; leading to gas inflows (Athanassoula, 1992; García-Burillo et al., 2005; Lin et al., 2013; Audibert et al., 2021).

To demonstrate the shock mechanism, I provide a schematic illustration showing $x_1$ and $x_2$ orbital families within an inhomogeneous bar model, introduced in Athanassoula (1992), in Fig. 1.1. This figure is a combination of their Fig. 2 and Fig. 11 for simplicity. When there is a shock, the gas is compressed and the dust density is increased. Thus, signatures of shocks are often seen in dust morphology as lanes with high levels of dust obscuration; the *dust lanes and filaments* seen in galaxy images. The inner parts of these lanes then curl around the centre and form nuclear rings, or nuclear spirals seen in the morphology of the galaxies. The latter can continue to extend to the nucleus in the form of ***nuclear spiral shocks*** (Maciejewski, 2004b) – the resolution of the models from Athanassoula (1992) is not sufficient to show nuclear spiral shocks, thus for these, I present a separate example in Fig. 1.3. The density enhancements along the bar are shown in panels a and d of Fig. 1.1, the latter panel shows the regions with maximum density enhancement in panel a. Panel b of the same figure shows the gas flow in their bar model. Each arrow represents a velocity vector at a given point. At the outer regions of the bar, the flow lines follow the orientation of $x_1$ orbits, while there is a sudden and clear change at the inner bar regions where the flow lines follow the orientation of the $x_2$ orbits. These regions are the locations where the extended shocks originate. The examples of $x_1$ and $x_2$ orbits are shown in panel c of Fig. 1.1. Note that the pattern of the flow and the density enhancements are strictly dependent on the initial profile and parameters chosen in models. As shown in Fig. 1.2, a strong density enhancement occurs downstream from a shock, also velocity encounters a large jump and decreases.

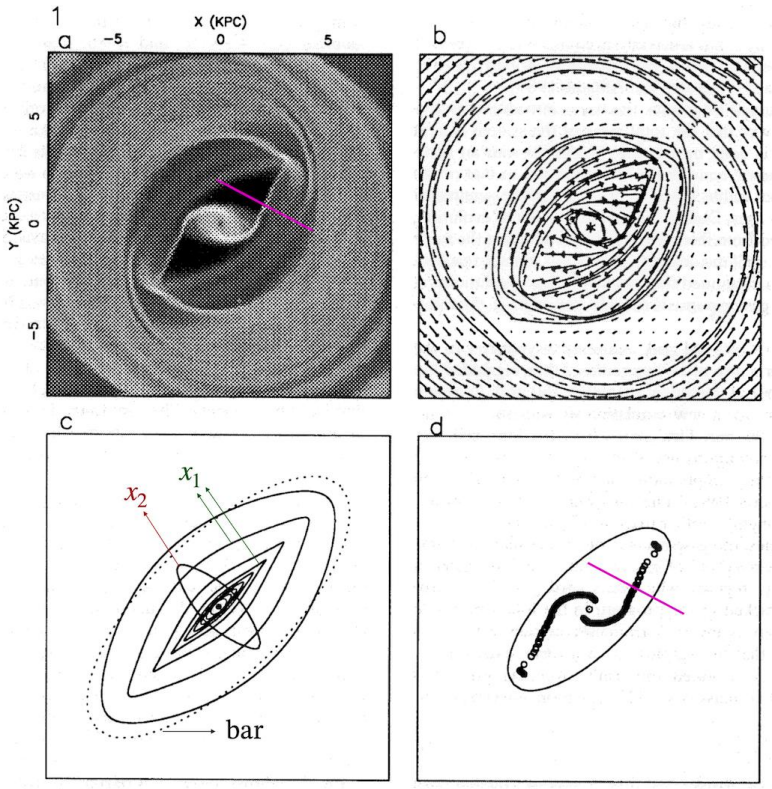


FIGURE 1.1: Schematic illustration of the gas flow within a bar potential, this figure is taken from Athanassoula, 1992 (Figures 2 and 11). In all panels, the major axis of the bar is at 45°. (a) the density response within their bar model. The solid magenta line represents the slit where density and velocity profiles are extracted, shown in Fig. 1.2. (b) for the same bar model gas flow lines and velocity vectors in a reference frame in which the bar is at rest. (c) characteristic $x_1$ and and $x_2$ orbits. The dotted line represents the bar outline. In this panel both x and y axes extend for 10 kpc, to present a better view of the innermost orbits. (d) the density maxima along the bar, the solid line represents the bar outline. The solid magenta line is the same as in panel a.

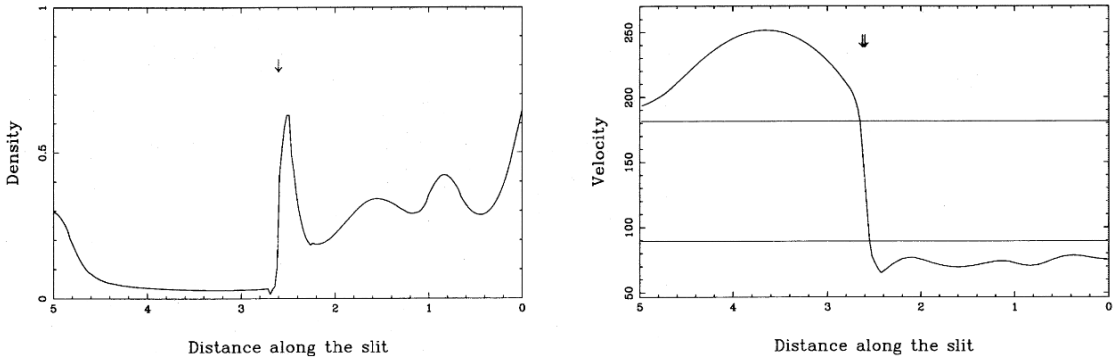


FIGURE 1.2: Distribution of density and velocity along a slit crossing the shocks. Slit is shown in panels a and d of Fig. 1.1 a magenta solid line. This figure is adopted from Athanassoula, 1992 (Figure 11). *left:* Density as a function of distance along the slit, measured from its bottom right-hand end. The arrow shows the position of the maximum gradient. *right:* velocity parallel to the slit, also measured from its bottom right-hand end. Two arrows show maximum density and velocity gradients. Horizontal lines are plotted to help measure the amplitude of the velocity jump.

To provide an example of nuclear spiral shocks, in Fig. 1.3, I present a snapshot from one of the models of Maciejewski, 2004b (model 8S20r, Figure 8). The snapshot shows a nuclear spiral shock within a gravitational potential of a strongly barred galaxy with a black hole mass of $10^8 M_\odot$, at a time 0.5 Gyr after the morphology of the flow is stabilised. The left panel shows gas density (greyscale) and the strength of the shock (contours), measured by $\mathrm{div}^2\, v$ for negative $\mathrm{div}\, v$ which is indicative of a diverging flow. The dotted circles on the figure represent radii at 40, 100, 250, 500 pc, 1 kpc and 2 kpc. The straight shocks along the bar are seen extending from the northern and southern edges of the frame towards the inner regions. Roughly at 500pc, the shocks begin to curve and extend towards the nucleus, manifesting a spiral pattern, which can be traced down to 40pc. The right panel of the figure shows the radial density profile (dotted line), $\mathrm{div}^2\, v$ (short-dashed line) and azimuthal velocity (solid line). The strength of the shock is roughly the same at 1.1, 0.3 and 0.05kpc; the first location is at the straight shock, while the other two are at the nuclear spiral shock. Thus, Fig. 1.3 demonstrates that a density enhancement occurs downstream from a shock, and it is accompanied by a strong velocity jump. This trend is most prominently seen at 0.3kpc.

Therefore, the mechanism of nuclear spirals is analogous to the bar-driven mechanism of shocks and is commonly seen as one of the predominant mechanism of inflow to the nucleus of galaxies, fuelling AGNs (Martini & Pogge, 1999; Pogge & Martini, 2002; Martini et al., 2003a,c; Maciejewski, 2004b; Prieto et al., 2005; Davies et al., 2009).

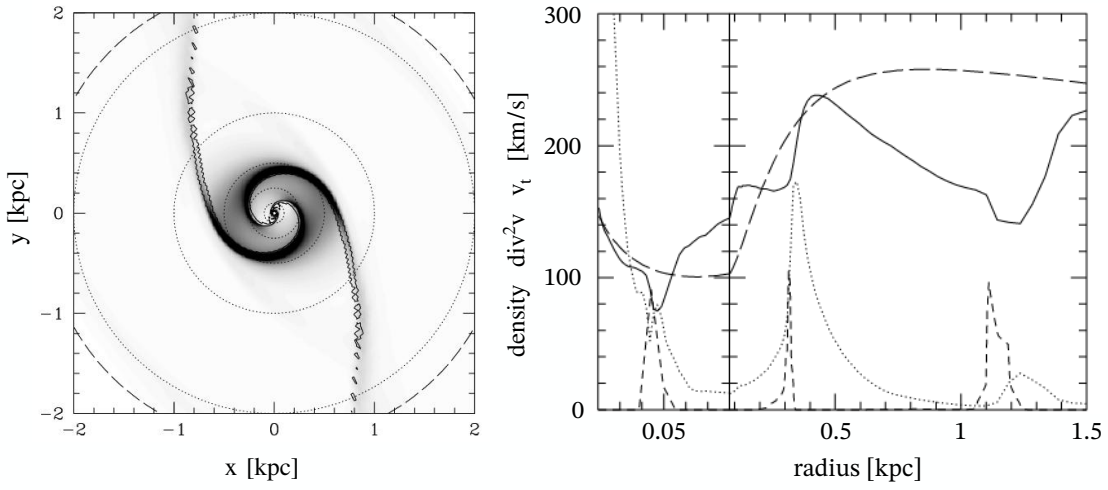


FIGURE 1.3: Nuclear spiral shock propagating to the nucleus, the figure is adopted from Maciejewski, 2004b (model 8S20r, figure 8). *left:* snapshot of gas density (greyscale) and the shock strength $\mathrm{div}^2\, v$ (contours). The dotted circles show radii at 40, 100, 250, 500pc, 1kpc and 2kpc. *right:* radial density profile (dotted line), $\mathrm{div}^2\, v$ (short-dashed line), and azimuthal velocity (solid line) with rotation curve (long-dashed line) as a reference for the snapshot at the left panel as a function of radius along the line connecting the centre with the bottom right corner of that panel. The velocity units are $\mathrm{kms}^{-1}$, and the density and $\mathrm{div}^2\, v$ units are arbitrary.

Some models shown in Athanassoula (1992) reveal that, when there is a lack of $x_2$ orbital families, the gas velocity vectors do not become close to perpendicular to the bar's major axis within the inner regions of the bar. The lanes with the density maxima are very narrow and run quite close to the major axis of the bar, almost *on-axis*. There is not a form of a spiral or ring-like structure in density enhancements either. The schematic view of this model is shown in Fig. 1.4, as introduced in Fig. 4 of Athanassoula (1992).

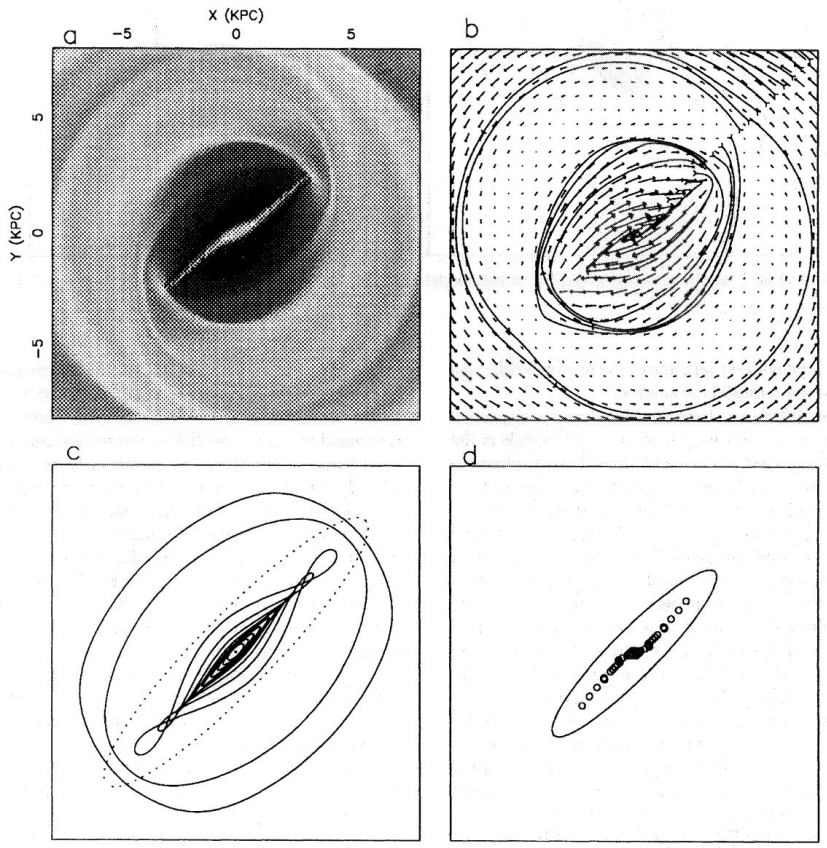


FIGURE 1.4: Illustration of the gas flow within a bar potential when there are on-axis shocks. This figure adopted from Athanassoula (1992) (Fig. 4). The panels are the same as those explained in Fig. 1.1.

In this thesis, I have conducted a comprehensive kinematic analysis of a range of galaxies, presenting signatures of different phenomena including nuclear spiral shocks and both on-axis and off-axis extended shocks, as introduced in this section. Therefore, insights gained from these theoretical examples explained in this Chapter will prove to be crucial when I later delve into the kinematic signatures of shocks observed in each of these galaxies in Chapter 5.

## 1.3 Signatures of extended shocks in gas kinematic maps

While dust lanes and filaments can form in compression of extended shocks (Prieto et al., 2005; Storchi-Bergmann et al., 2007; Davies et al., 2014), as I explained in Sect. 1.2, they can also solely form due to local perturbations in density, resultant from the stretch by differential rotation and unrelated to the extended shocks. Therefore, morphological and photometric studies are not ideal for studying shocks in gas. Since shock conditions imply a rapid change in velocity (Athanassoula, 1992; Maciejewski, 2004b), they are best studied in kinematics (Zurita et al., 2004; Fathi et al., 2005; Storchi-Bergmann et al., 2007).

The study of the velocity fields of gas within galaxies provides invaluable insights into the movement of gas, and hence are essential tools for determining the complex mechanisms at play in galactic centres, revealing how gas navigates through the galactic potential towards the nucleus. An early study from Regan et al. (1997) shows the characteristic patterns of transition of gas from $x_1$ and $x_2$ orbits superimposed on the underlying disk rotation, in the observed H$\alpha$ velocity field of galaxy NGC 1530; the zero-velocity line forms an "S" shape, associated with the flow in bars. While velocity maps on their own provide valuable insights into the presence of non-circular gas motions and where gas inflows occur in galaxies, the full extent of the extended shocks becomes more pronounced when the underlying rotation of the disk is removed. This can be done by modelling a representative disk for the galaxy, and removing its velocity from the observed data (Schoenmakers et al., 1997; Zurita et al., 2004; Fathi et al., 2005). After subtracting the underlying velocity of the disk from the observed velocity field, in the residual velocity field we can isolate the non-circular motions induced by the bar's gravitational influence, allowing for a clearer identification of extended shocks. In the residual velocity field, which highlights deviations from circular rotation, the signatures of extended shocks manifest as coherent kinematic structures that extend over large distances. These structures are indicative of regions where the gas undergoes a rapid velocity jump due to shocks, leading to its inward motion.

Following a methodology based on a higher-order harmonic expansion of a velocity field, Schoenmakers et al. (1997) studied the structures occurring when there are small deviations from the axisymmetry of a potential of a disc filled with gas. A schematic representation in the second figure of Schoenmakers et al. (1997) shows $m = 1, 2, 3$ and 4 harmonic distortions in potential and the corresponding pattern emerged in the residual velocity field along the LOS when the underlying rotation, which is assumed to be circular, is removed. They show that if the potential has a distortion of harmonic number $m$, the LOS velocity field reveals $m - 1$ and $m + 1$ distortions. I present their figure in

Fig. 1.5. The first column of the figure, from top to bottom, demonstrates $m = 1, 2, 3$ and 4 harmonic term distortions in the potential respectively. The corresponding kinematic response of gas seen in the residual velocity field observed along the LOS, after the underlying circular rotation of the disk is removed, is shown in the second. The maps in this column predominantly feature the $m - 1$ components, despite the weak presence of $m + 1$ components within the underlying field. The maps in the third column highlight the $m+1$ components, which have a weaker influence on the overall residual velocity field along the LOS, shown in the second column. Particularly, the second row of Fig. 1.5, represents perturbations from a spiral arm, leading $m = 2$ harmonic term distortion in potential (first column), which is observed as $m = 1$ terms in the residual velocity field along the LOS (second column).

A galactic bar, as a bi-symmetric structure, can be represented by the $m = 2$ harmonic term in Fourier analysis of a galaxy's gravitational potential or its observed brightness. I note that any $m = 2$ perturbations generate waves in gas which has a spiral shape, thus perturbation from a bar also has a spiral nature (Maciejewski, 2004b). Therefore, the second row of Fig. 1.5 can also represent the potential and kinematic fields when a bar is the main perturber of the field. To demonstrate these statements further, in Fig. 1.6, I present a nuclear spiral shock example adopted from Davies et al. (2009) (their Figure 7). This figure, in fact, presents the same model of Maciejewski (2004b) that produces the nuclear spiral shock I previously introduced in Sect. 1.2 (Fig. 1.3). Unlike in the former section, the disk presented in Fig. 1.6 is inclined at 60°. In the left panel of Fig. 1.6, there is an $m = 2$ harmonic term distortion from a strong bar, where a two-arm spiral shock in the brightness map emerges, exhibiting two darker and two brighter regions indicative of maximum and minimum density loci. In the right panel, the residual velocity field along the LOS is shown, exhibiting $m = 1$ distortions where a one-arm spiral pattern with one velocity maxima and one velocity minima emerges.

Such large velocity residuals extending coherently throughout the residual velocity field, are indicative of strong streaming motions; often seen as kinematic spiral arms in observations (Zurita et al., 2004; Storchi-Bergmann et al., 2007; Fathi et al., 2005, 2006, 2008; Schnorr-Müller et al., 2016, 2017). These coherent kinematic structures are the signatures of extended shocks I searched for in the observations of nearby galaxies, which I present in this thesis.

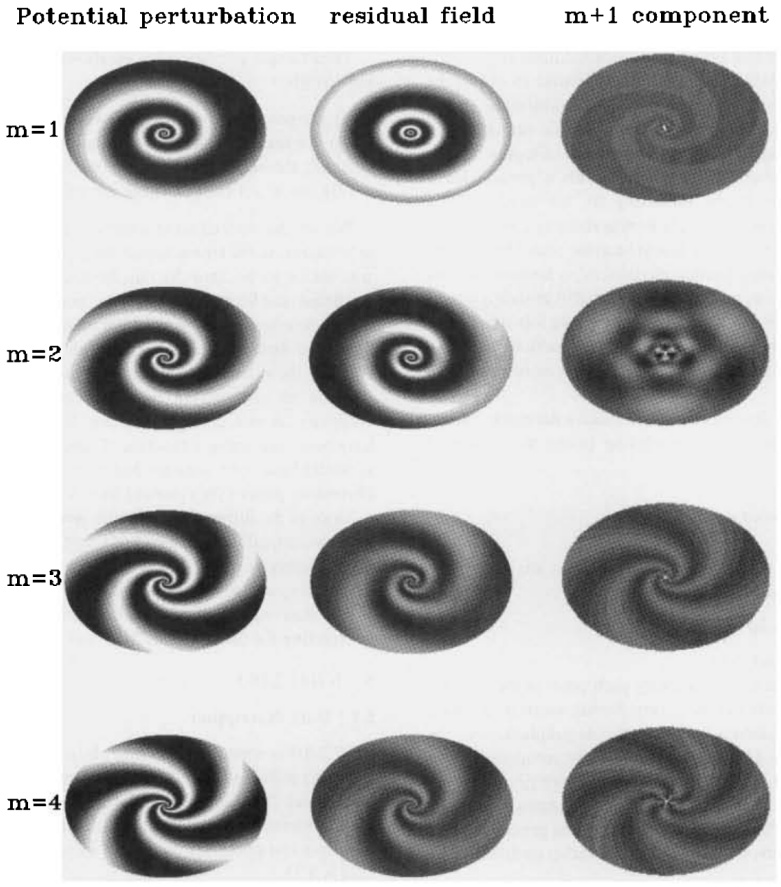


FIGURE 1.5: The figure is from Schoenmakers et al., 1997 (Figure 2). From top to bottom potential has $m = 1, 2, 3$ and 4 harmonic distortions. From left to right: perturbation in potential, the residual velocity field showing mainly the $m-1$ component, and the residual field, $m-1$ component is removed, revealing the $m+1$ component.

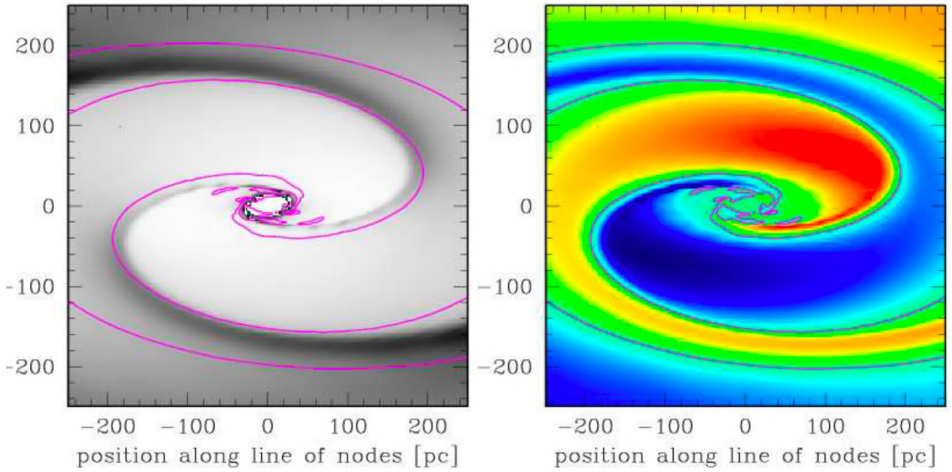


FIGURE 1.6: From Davies et al. (2009). Snapshot of the nuclear spiral shock in gas in model 8S20r from Maciejewski (2004b) at 300 Myr after the flow in the spiral stabilised. The gaseous disc is rotating clockwise. *left* Photometric spiral in gas as it would appear in the sky for the galaxy disc with inclination 60°. *right:* The corresponding kinematic response observed in the residual velocity field along the LOS. The colour scale ranges from -55 $\mathrm{kms}^{-1}$ (blue) to 55 $\mathrm{kms}^{-1}$ (red). Magenta lines mark zero LOS velocity in gas.

It is important to note that not all extended structures in the residual velocity map is associated with extended shocks in gas. Besides their coherent extension, these structures should also have large residual velocity amplitudes, indicating strong shocks and jumps in velocity. For instance, coherent structures in residual velocity field presented in Fig. 1.6, which are associated with extended shocks, exhibit the LOS residual velocities of amplitudes $30\,\mathrm{kms}^{-1}$ or higher, corresponding to deprojected velocity amplitudes of $\sim$40 $\mathrm{kms}^{-1}$ or higher. These amplitudes are indicative of a nuclear spiral shock that causes a velocity jump of approximately $70\,\mathrm{kms}^{-1}$, as shown in Fig. 1.3. Furthermore, as shown in Fig. 1.2, Athanassoula (1992) also resolves a velocity jump of $\sim$100 $\mathrm{kms}^{-1}$ when extended shocks are present, indicating deprojected velocity amplitudes larger than $\sim$50 $\mathrm{kms}^{-1}$ in extended shocks.

Studying the observations of ionised gas, Zurita et al. (2004) revealed structures of extended shocks along the bar of galaxy NGC 1530, as I show in the top row of Fig. 1.7. These structures are characterised by positive and negative residual velocities along the LOS with amplitudes up to $120\,\mathrm{kms}^{-1}$. These amplitudes would correspond to even stronger shocks and larger velocity jumps along the galaxy's bar than those determined from models. Moreover, within the innermost regions of the NGC 1530, which I presented in the bottom row of Fig. 1.7, the velocity residual map reveals two distinct structures, one with positive and one with negative velocities, both with amplitudes of $\sim$40 $\mathrm{kms}^{-1}$. These structures coincide with nuclear dust spirals visible in $J-K$ colour images of the galaxy, and are interpreted as evidence of spiralling inflow to galaxy's nucleus. Their observational findings show an excellent alignment with their kinematic model of the gas flow and velocities along the dust spirals. Similar structures associated with spiral shocks and gas inflows to the nucleus, are also seen in other galaxies, such as NGC 5236 (Fathi et al., 2008) and UG 10200 (Blasco-Herrera et al., 2013), with residual velocity amplitudes of $\sim$30–50 $\mathrm{kms}^{-1}$, and in NGC 3081 and NGC 1358 (Schnorr-Müller et al., 2016, 2017) with amplitudes of $\sim$50 $\mathrm{kms}^{-1}$.

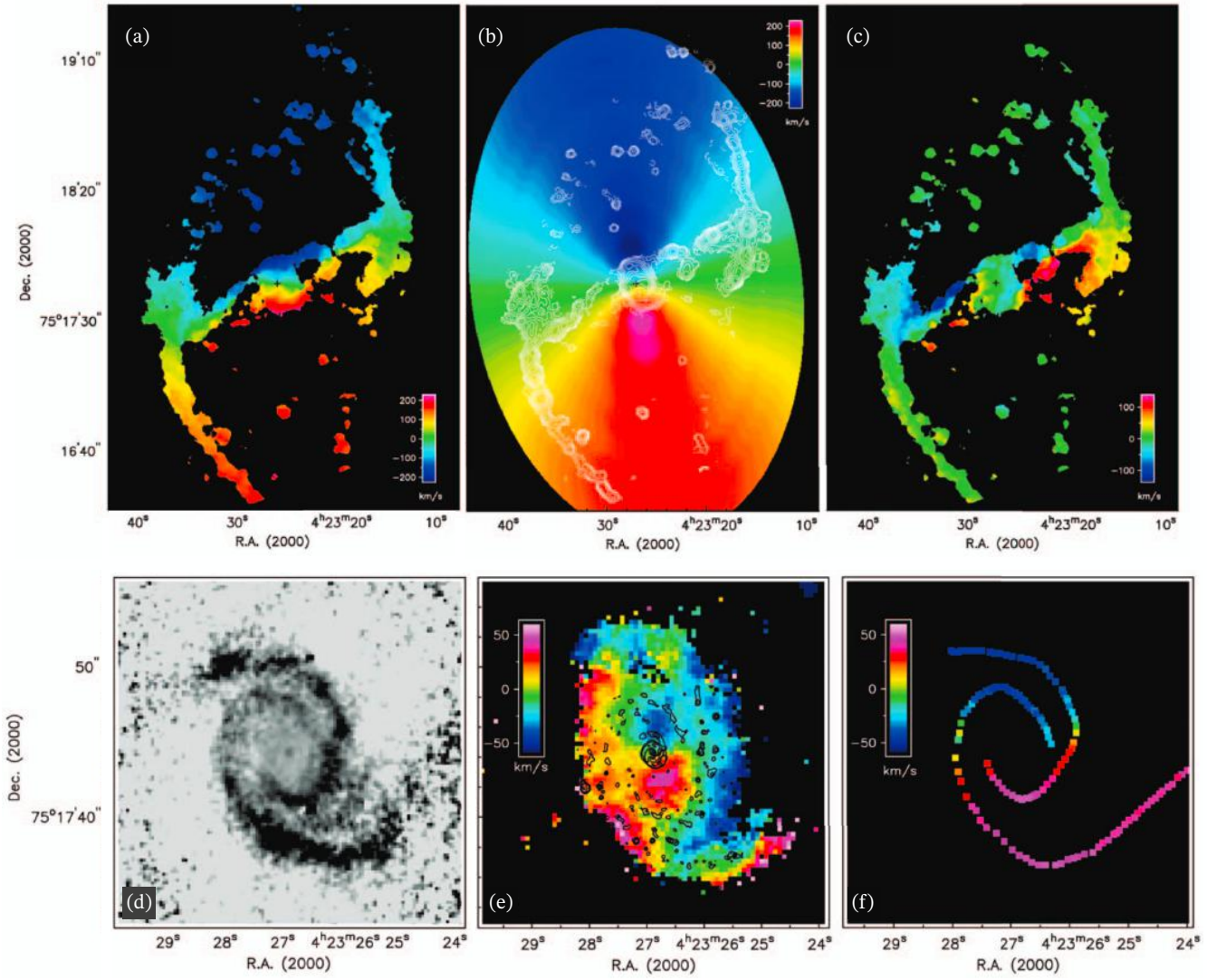


FIGURE 1.7: Diagnostic maps of NGC 1530 from Zurita et al. (2004). The top panels show the large-scale maps – H$\alpha$ velocity map (a); modelled velocity map obtained from H$\alpha$ velocity field with contours representing H$\alpha$ emission (b); residual velocity map after modelled velocity is subtracted from the observed H$\alpha$ velocity (c). A zoom-in into the large-scale map, J-K colour index image in grey scale of nuclear dust spirals (d); the residual velocity map (e); kinematic model of LOS velocity along dust spirals (f).

## 1.4 Integral Field Spectroscopy revolutionising the kinematic studies of nearby galaxies

In the field of observational astronomy, ***long-slit spectroscopy*** stands as one of the key and traditional methods for studying galaxies (Duval & Athanassoula, 1983; Bonnarel et al., 1988; Koribalski et al., 1996; Lindblad, 1999; Heald et al., 2006). This technique, employing narrow slits positioned at various angles, was critical in acquiring spectral data to study the kinematics of galaxies. However, putting together a full three-dimensional picture of a galaxy using this method was difficult and demanded substantial observing time, due to the reliance on multiple slit configurations. Consequently, such instrumental limitations significantly challenge the studies of the extended shocks and gas inflows in nearby galaxies which requires an extensive spatial coverage (Baldwin et al., 1981; Koribalski et al., 1996).

The advent of ***integral field spectroscopy (IFS)*** provides a pivotal evolution in studying nearby galaxies, by offering robust solutions to the inherent limitations and difficulties of long-slit spectroscopy. Leveraging the capabilities of *integral field units (IFUs)*, IFS dissects the field of view into an array of spatial elements, or *spaxels*, each capturing both spatial and spectral information. Figure 1.8 presents an example of the principle behind observations of IFUs. The IFS approach facilitates simultaneous data acquisition across expansive two-dimensional fields, significantly enhancing observational efficiency; also reducing the sampling errors that can occur in slit-based spectroscopy. The technology of IFUs enables us to capture extensive portions of the nearby galaxies, or in some cases, their entirety in a single capture; proving to be particularly valuable in large-scale studies (Bacon et al., 2001, 2010; de Zeeuw et al., 2002; Allington-Smith et al., 2002; Sánchez et al., 2012; Bundy et al., 2015). Therefore, IFS provides a significant step forward in our quest to understand the motion of stars and gas within nearby galaxies, and it is particularly valuable when studying extended shocks in gas that should span over large distances in galaxy disks, since we require a large field-of-view and good resolution to dissect fine details in the motion of gas.

The field of IFS practically began with pioneering instruments like ***TIGER*** (Bacon et al., 1995) and ***OASIS*** (Bacon et al., 2000), which, despite their limited FOV of around $10''\times10''$ and spatial resolutions governed by seeing conditions, laid the foundations for spatially resolved spectroscopy. Advancements with ***SAURON*** significantly expanded the capabilities we can reach in IFS. SAURON, for instance, offered a FOV of $33''\times41''$ and spatial sampling of $\sim1''$/spaxel (Bacon et al., 2001; de Zeeuw et al., 2002), covering a rest frame wavelength range of 4810 to 5400Å; providing us with invaluable insights in studying the kinematics of gas and stars in galaxies.

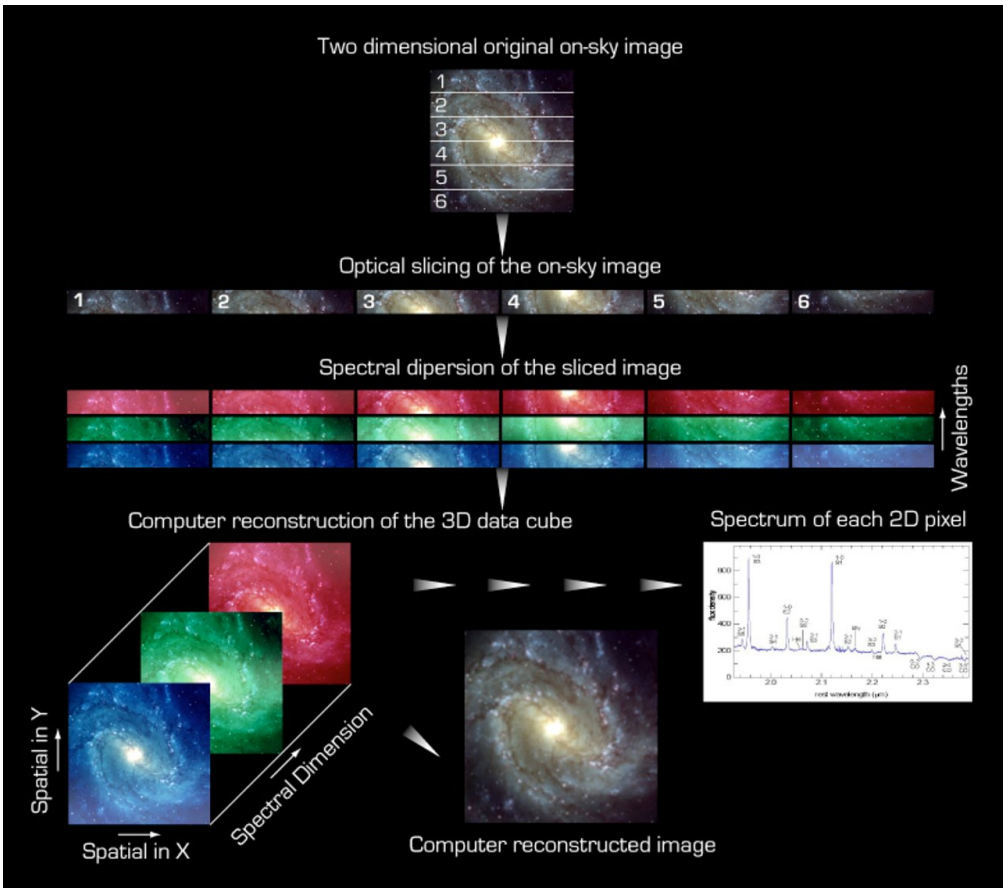


FIGURE 1.8: The principle behind IFS. Credits: European Southern Observatory, `https://www.eso.org/public/images/eso0426i/` accessed on: 01.02/24

The era of ***GMOS***, ***PMAS/PPak*** used in the ***CALIFA*** Survey and ***MaNGA*** of SDSS introduced even more flexibility and depth to galaxy evolution studies with IFS. GMOS (Allington-Smith et al., 2002) introduced configurable fiber bundles, achieving spatial resolutions up to $0\farcs2$/spaxel across a rest frame wavelength range from optical to NIR, 4000 to 11000 Å, despite its relatively small FOV of $5'' \times 7''$. Conversely, CALIFA and MaNGA optimised for more statistical and deeper studies, aiming to bridge the gap between large single-aperture surveys and resolved studies. For instance, CALIFA (Sánchez et al., 2012) with its expansive hexagonal FOV of up to $74'' \times 64''$ and spatial resolution of approximately 1kpc ($1''$/spaxel), was designed to map 600 galaxies in the local universe, across a rest frame wavelength range of 3700 to 7000 Å. Similarly, MaNGA (Bundy et al., 2015), sought to extend this depth, designed to map 10000 local galaxies. It offers a maximal FOV of $32''$ with a spatial resolution of roughly 1kpc (1–$2''$ /spaxel), covering an extended rest frame wavelength range into the near-IR, from 3600 to 10399 Å.

The study of extended shocks and gas inflows in nearby galaxies requires a comprehensive set of observational capabilities. A large FOV covering at least the inner kpc of the

galaxies, a significant portion of their central regions, is essential, allowing us to trace the radial extent of extended shocks from the outer kpc to the nucleus. At the same time, high, parsec level, spatial resolution is critical for unravelling the parsec-scale details, enabling us to resolve the coherent kinematic signatures of extended shocks. Equally important is a spectral range that allow capturing of strong emission from prominent emission lines (e.g., H$\alpha$ and [N II]$\lambda$6583), which are the key indicators of various astrophysical processes. Observations of different emission lines are critical for determining the mechanisms and physical conditions at play. Furthermore, a good sensitivity is required to achieve a high signal-to-noise ratio (SNR), which is crucial for obtaining clear, detailed observations without the need to bin the data. While binning potentially enhances the SNR, it sacrifices the resolution of the fine details, which are crucial to be preserved since we rely on the coherency of the kinematic signatures of extended shocks.

Although the earlier generations of IFUs and surveys I introduced previously in this section have been revolutionary in achieving their specific scientific objectives, tracing the signatures of extended shocks in nearby galaxies remains a challenge with the data obtained from these instruments. This difficulty primarily arises from the inherent limitations in their FOV and spatial resolution. As I explained, these constraints often restrict the ability to comprehensively cover the extent and the fine details required to be preserved while studying the kinematic signatures of extended shocks to the nucleus (Fathi et al., 2005, 2006; Storchi-Bergmann et al., 2007).

In this thesis, I primarily rely on data obtained from ***Multi Unit Spectroscopic Explorer (MUSE)***, mounted on the UT4 of the Very Large Telescope (Bacon et al., 2010). With its large, $60'' \times 60''$ FOV, and fine, $0\farcs2 \times 0\farcs2$ spatial sampling, MUSE allows capturing extensive portions of the central regions of nearby galaxies in great detail, across a wide rest frame wavelength range of 4650 to 9300Å which covers prominent emission lines. Besides these capabilities, MUSE also offers high sensitivity, providing high SNR, effectively minimising the common need for binning. Furthermore, MUSE is equipped with cutting-edge adaptive optics (AO) technology, contributing significantly to the data acquisition by correcting for atmospheric distortions, improving the seeing and allowing us to achieve fine spatial resolutions.

In Fig. 1.9, I provide a brief comparison of the FOV across various IFU instruments and surveys, using NGC 5248 as a representative example, which is one of the galaxies I studied in my thesis. It is evident that MUSE offers a larger FOV compared to many other IFUs. While GMOS and MUSE have comparable spatial resolutions of approximately $0\farcs2$/spaxel, MUSE's larger FOV grants a significant observational advantage. Although CALIFA has a larger FOV within its maximum coverage setup, the critical

advantage provided by MUSE's spatial resolution cannot be overstated. This refined resolution ensures that even a slightly smaller FOV, in comparison, does not lessen the observational capabilities of MUSE.

Therefore, MUSE stands as one of the most outstanding and powerful instruments on the ground. With the balance of its expansive field of view coupled with its exceptionally fine spatial resolution, MUSE opens up a new window to the studies of gas kinematics, particularly providing deeper insights into the mechanisms of gas inflows to the nucleus. In Chapter 2 (Sect. 2.3), I delve into the details of extracting kinematic measurements from MUSE spectra.

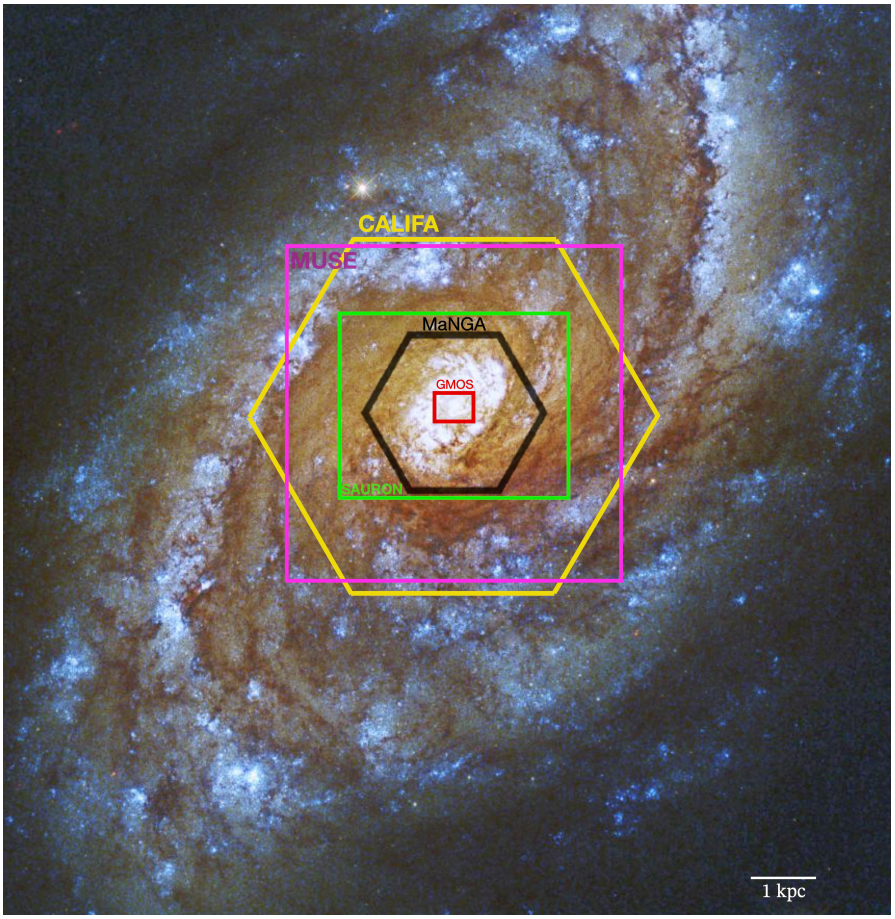


FIGURE 1.9: FOV of different IFUs on NGC 5248. The colour represents CALIFA in yellow, MUSE in magenta, SAURON in green, MaNGA in black and GMOS in red.

## 1.5 Thesis outline

In Chapter 1, I introduced several mechanisms capable of causing gas inflows to the nuclei of galaxies. I delved into the details of bar-driven extended shocks, which is recognised as one of the dominant mechanisms that facilitate gas inflow to the galactic nuclei. I explained the importance of studying extended shock and gas inflows in kinematic fields, which I study in this thesis. Shifting to an observer's perspective, I discussed the limitations of traditional techniques like long-slit spectroscopy in studying gas kinematics. In contrast, I introduced IFS as an approach that offers substantial improvements over previous traditional techniques in studying extended shocks in gas. After reviewing several groundbreaking IFUs, I introduced one of their current successors MUSE, which stands out as a revolutionary instrument, significantly advancing the resolved kinematic studies of external galaxies. Further in this thesis:

- in Chapter 2, I introduce the galaxy sample I constructed based on a detailed selection criteria. I delve into details of extracting kinematic measurements of distinct emission line groups from MUSE spectra. I provide details of the standard fitting approach and certain advancements I applied to account for inaccurate measurements from inappropriate fits caused by additional sources of emission. This Chapter is based on my published work Kolcu et al. (2023) and on my forthcoming publication in progress.
- in Chapter 3, I present my pilot study, explaining the methodology I developed to identify the signatures of extended shocks in gas on the example of galaxy NGC 1097. The methodology involves both model dependent and independent approaches. Moreover, in Chapter 4, I present my detailed findings in NGC 1097. These two chapters are also based on my published work Kolcu et al. (2023).
- in Chapter 5, I present the detailed individual kinematic analysis of each galaxy in the sample I studied in this thesis. Following this analysis, in Chapter 6, I describe the classification of galaxies based on the signatures and characteristics of extended shock signatures identified in their kinematic fields. Further, I present the relation between the shock signatures and the type of nuclear activity type dominating the innermost regions of galaxies. Also, I provide my preliminary results on the statistical analysis of the sample, explaining correlations with the characteristics of extended shocks and the presence of nuclear bars and nuclear rings, as well as with the characteristics of host galaxies.
- in Chapter 7, I provide the summary and conclusions of my thesis.
- Finally, in Chapter 8, I introduce a couple of external projects I am currently involved in, and that I will be working on in the near future.

# Chapter II

# Data and Data Extraction

In this chapter, in Sects. 2.1 and 2.2, I introduce the sample of galaxies I studied in this thesis, specifically focusing on my sample selection and MUSE observations. In Section 2.3, I present the methodologies employed to extract stellar and gas kinematic measurements by fitting the MUSE spectra. I discuss several limitations of the single Gaussian fitting technique used in the standard spectral fitting approach, and I propose a method to enhance the line fitting within the framework of the algorithm I employed in this work. This chapter is based on Section 2 of my published work Kolcu et al., 2023.

## 2.1 Sample Selection

In this thesis, I conducted my research using a selection of nearby galaxies from different observing programmes. The majority of the galaxies I studied are from the multi-wavelength imaging and spectroscopic observing campaign *Composite Bulges Survey,* ***CBS*** (PI: Peter Erwin; Erwin et al., 2024). CBS focuses on understanding the formation and growth mechanisms of bulges, and the correlation with their host galaxy properties. Moreover, from active to inactive, CBS targets a diverse range of nearby galaxies and aims to identify and characterise their different forms of nuclear stellar components within the inner 1–2 kpc; from large-scale bars down to nuclear scale discs/rings/bars and nuclear star clusters (Erwin et al., 2021a, 2024; Ashok et al., 2023).

The CBS sample is a mass- and volume-limited set of 54 disk galaxies (S0–Sbc) with optical and near-IR (NIR) imaging with *the Hubble Space Telescope (HST)*. The sample is constructed to include galaxies within a maximum distance of 20 Mpc, allowing us to resolve details as fine as ∼15 pc. All galaxies in this sample are listed in de Vaucouleurs et al. (1991), with Galactic latitude $|b|$ >20°, distances ≤20 Mpc, stellar masses ≥ $10^{10}$ $M_{\odot}$, and inclinations between 35° and 60° (Erwin et al., 2021a, 2024). Among 54 galaxies in CBS, 47 of them have been observed with MUSE, the remaining awaiting observations. While MUSE observations of 36 galaxies are obtained specifically for the CBS, observations of 11 galaxies are sourced from different programmes, including

the *Time Inference with MUSE in Extragalactic Rings Project,* ***TIMER*** (PI:Dimitri Gadotti, Gadotti et al., 2019), the *MUSE Atlas of Disks,* ***MAD*** (PI:Marcella Carollo, Erroz-Ferrer et al., 2019) and the *Physics at High Angular resolution in Nearby GalaxieS Survey,* ***PHANGS*** (PI: Eva Schinnerer, Emsellem et al., 2022).

Upon reviewing the available MUSE data for the 47 galaxies in CBS, I focused on those with strong extended line emissions, central to my study of ionised gas content in galaxies. To do this, initially I followed the emission line fitting approach to extract flux and kinematic measurements of galaxies with available MUSE data, details of which are provided in Sect. 2.3. Subsequently, I examined these extracted measurements and selected the galaxies with measurements available in more than 50% of the spaxels within a FOV of $40'' \times 40''$. This threshold was chosen to ensure the presence of sufficient emission line signal for further analysis. I selected this specific FOV as it covers the regions in which I search for kinematic signatures of extended shocks. This led to the selection of 19 galaxies from CBS for in-depth analysis.

Additionally, the TIMER Project studies nearby barred galaxies ($D < 40\,\mathrm{Mpc}$) larger than $1'$ with stellar masses above $10^{10}\,M_{\odot}$, brightness threshold of 15.5 B–mag and inclinations smaller than 60°, which exhibit prominent central components (e.g., nuclear rings/discs, inner bars) (Gadotti et al., 2019). Since the CBS dataset requires a minimum galaxy inclination of 35°, two galaxies from the TIMER sample, each with an inclination of 34°, were excluded from CBS, despite meeting all other criteria, such as distance and mass, and also surpassed the emission threshold I discussed in the previous paragraph. Therefore, I adjusted the inclination limit in my study by 1 degree to include these two TIMER galaxies, thereby expanding the size of my sample. As a result, the total sample I studied in this thesis comprises 21 galaxies. The galaxies within the sample I studied in this thesis are shown in Table 1.

In Sect. 2.2, I provide information specific to the MUSE observations of the galaxies I studied in this thesis. The detailed kinematic analysis of each galaxy is provided in their respective sections in Chapter 5.

## 2.2 Observations

Observations of all galaxies are done in MUSE Wide-Field Mode (WFM), for a nominal wavelength range of $4700 - 9350$Å, within a FOV of $60''\times60''$ and with spatial sampling of $0\farcs2$/spaxel (Bacon et al., 2010). In Table 1, I summarise the general properties of each galaxy in my sample. This table includes the Galaxy ID and their RC3 classification from de Vaucouleurs et al. (1991). Moreover, it includes logarithmic stellar mass of

each galaxy, obtained from the Spitzer Survey of Stellar Structure in Galaxies, S4G (Muñoz-Mateos et al., 2013, 2015); galaxy NGC 7177 is not in S4G, thus its stellar mass measurement is obtained from HyperLEDA B band absolute magnitude. The galaxy distance measurements from different sources specified in the table, the physical size based on these distances and the spatial resolutions (SR) are also included in the table. SR of each galaxy is calculated in physical units based on the median point spread function full width at half maximum (PSF FHWM, or seeing), measured with the VLT guide star in the V band, during the exposures with the MUSE slow guiding system, using to the formula SR = physical size (pc/″) × PSF FWHM (″). However, during the observations of 11 galaxies I studied in this thesis, those obtained for CBS and for NGC 1566 from MAD, MUSE's AO system is used. Therefore, for these galaxies, using the approach from Fusco et al. (2020), which accounts for AO monitoring, the PSF FHWMs have been reconstructed to obtain the corrected values. This method demonstrates significant improvements in seeing for most galaxies, typically between 30–50%. The PSF FHWMs recorded during observations, along with those improved by AO, are detailed in Table C.2 in Appendix C.

Observations of ten galaxies within my sample are specifically obtained for the CBS. Amongst these, observations of IC 2051, NGC 3368, NGC 4237, NGC 4321 and NGC 4380 are collected as a part of observing proposal ID:0104.B-0404(A) carried out in Period 104 from October 2019 to March 2020. Observations of NGC 3489, NGC 3626, NGC 4457, NGC 7177 and NGC 7513, are collected as a part of observing proposal ID: 109.22VU.001 during Period 109, from April to September 2022.

Observations of eighth galaxies; NGC 613, NGC 1097, NGC 1300, NGC 1433, NGC 3351, NGC 4303, NGC 4321 and NGC 5248 are provided by TIMER project as a part of observing proposal ID:097.B-0640, carried out Period 97, from April to September 2016. Further details on observations and the data reduction processes, products including stellar kinematics, ages and metallicities of the sample can be found in Gadotti et al. (2019, 2020) and Bittner et al. (2020).

Moreover, observations of NGC 289, NGC 1566 and NGC 4941 are taken for MAD project, as a part of observing proposal ID:0100.B-0116(A) for NGC 1566 during Period 100 started in November 2017, and as a part of observing proposal ID:096.B-0309(A) for NGC 289 and NGC 4941 during Period 96 started in November 2015.

In Fig. 2.1, the first and third columns show the large-scale images of 20 galaxies in the sample I studied in this work. While images of IC 2051, NGC 289, NGC 613, NGC 1300, NGC 1433, NGC 1566, NGC 4941 and NGC 7513 are taken from The Carnegie-Irvine

Galaxy Survey, CGS[1] (Ho et al., 2011), the images of the remaining galaxies in the sample are taken from SDSS[2] (*ugriz* images). Pink boxes overlaid on these large-scale images represent the MUSE pointings. The second and fourth columns of the figure show the colour composite images from within these marked MUSE pointings, constructed using MUSE data. It is revealing that the central regions of each galaxy have prominent structures.

In a pilot study, I developed a methodology of finding extended shock signatures in kinematic maps. Amongst galaxies within the sample I constructed, I selected NGC 1097 as an example target of my pilot study. NGC 1097 is an SBb galaxy with a strong bar at position angle ∼141° (Prieto et al., 2005) and it contains a prominent star-forming nuclear ring in the inner ∼8″–10″ (Bittner et al., 2020). The galaxy hosts a LINER[3] type, low-luminosity active galactic nucleus (LLAGN – $L_{bol} \lesssim 10^{42}\, erg\, s^{-1}$, Ho, 2008) with bolometric luminosity $L_{bol} = 8.6 \times 10^{41}\, erg\, s^{-1}$ (Nemmen et al., 2006). The galaxy is interacting with a companion elliptical galaxy NGC 1097A located to its northwest. Because of its complex characteristics, NGC 1097 has been a prominent focus of many studies (Quillen et al., 1995; Prieto et al., 2005; Fathi et al., 2006; Davies et al., 2009; van de Ven & Fathi, 2010; Lin et al., 2013; Bowen et al., 2016; Izumi et al., 2017; Prieto et al., 2019; Legodi et al., 2021), thus was an ideal target for my pilot study. In the left panel Fig. 2.2, I present a large-scale (360″×360″) image[4] of NGC 1097, which reveals the spiral arms on the north and the south, and the companion elliptical galaxy NGC 1097A in the northwest. In the right panel Fig. 2.2, I present the colour composite image within the inner 60″×60″, constructed from the MUSE data. In both panels, the stellar nuclear ring in the centre and the connection of dust lanes to the nuclear ring are well resolved.

The methodology I developed on the example of NGC 1097 is documented in my publication Kolcu et al. (2023), and is presented in Chapter 3 of this thesis. The data extraction from MUSE data cubes, which I explain in the further section, is also on the example of NGC 1097. After developing the methodology using galaxy NGC 1097 as an example, I applied it to the remaining galaxies within the sample I studied in this thesis, to determine whether extended shocks are the prevalent mechanism of inflow to galactic nuclei. Depending on how many galaxies in my study exhibit these kinematic signatures, I can assess whether shocks are a dominant inflow mechanism to galactic nuclei.

[1]The CGS sample images can be accessed via `https://cgs.obs.carnegiescience.edu/CGS/database_tables/sample0.html`

[2]SDSS webpage can be accessed via the link `https://skyserver.sdss.org/dr16/en/home.aspx`

[3]LINER: Low Ionisation Narrow Emission-line Regions, can be distinguished from the Seyfert type nuclei based on their [O III] luminosity and kinematics (Kewley et al., 2006)

[4]Image credits: ESO Press Release, 2004, date of observation: 09-10/12/2004, image ID: eso0438d, media source: `https://www.eso.org/public/images/eso0438d/`

[5]S4G catalogue can be accessed via the link: `https://irsa.ipac.caltech.edu/data/SPITZER/S4G/`

TABLE 1: The galaxy sample studied in this thesis.

| Galaxy ID | RC3 | $\log_{10}(M_*/M_\odot)$ | Distance (Mpc) | Physical Size (pc/″) | SR (pc) | Survey |
|---|---|---|---|---|---|---|
| (1) | (2) | (3) | (4) | (5) | (6) | (7) |
| IC 2051 | SBbc | 10.58 | 19.9[1] | 96.5 | 76.0 | CBS |
| NGC 289 | SBbc | 10.63 | 20.2[1] | 97.9 | 69.0 | MAD |
| NGC 613 | SBbc | 11.09 | 18.1[1] | 87.8 | 88.0 | TIMER |
| NGC 1097 | SBb | 11.24 | 14.8[1] | 71.7 | 58.0 | TIMER |
| NGC 1300 | SBbc | 10.58 | 19.6[1] | 95.0 | 95.0 | TIMER |
| NGC 1433 | SB(r)ab | 10.30 | 18.6[5] | 90.2 | 81.0 | TIMER |
| NGC 1566 | SABbc | 10.58 | 17.0[1] | 82.4 | 46.0 | MAD |
| NGC 3351 | SBb | 10.49 | 10.0[2] | 48.5 | 34.0 | TIMER |
| NGC 3368 | SABab | 10.72 | 10.5[2] | 50.9 | 25.0 | CBS |
| NGC 3489 | SAB0 | 10.14 | 11.7[4] | 56.7 | 30.0 | CBS |
| NGC 3626 | SAB0 | 10.59 | 19.5[3] | 94.5 | 46.0 | CBS |
| NGC 4237 | SAbc | 10.36 | 18.9[3] | 91.6 | 40.0 | CBS |
| NGC 4303 | SAB(rs)bc | 10.86 | 17.0[5] | 82.4 | 66.0 | TIMER |
| NGC 4321 | SABbc | 10.93 | 15.2[2] | 73.7 | 64.0 | CBS |
| NGC 4380 | SAb | 10.32 | 15.9[3] | 77.1 | 38.0 | CBS |
| NGC 4457 | SAB0/a | 10.58 | 16.5[6] | 80.0 | 47.0 | CBS |
| NGC 4643 | SB0/a | 11.03 | 19.1[1] | 92.6 | 84.0 | TIMER |
| NGC 4941 | SABab | 10.36 | 15.6[1] | 75.6 | 92.0 | MAD |
| NGC 5248 | SABbc | 10.67 | 17.3[1] | 83.9 | 59.0 | TIMER |
| NGC 7177 | SABb | 10.44 | 17.5[1] | 84.8 | 76.0 | CBS |
| NGC 7513 | SBb | 10.21 | 19.8[1] | 96.0 | 56.0 | CBS |

Notes – (1) Galaxy ID; (2) Galaxy classification from the RC3 catalogue of de Vaucouleurs et al. (1991); (3) Logarithmic stellar mass from S4G[5] Survey (Muñoz-Mateos et al., 2013, 2015) – mass measurement of NGC 7177 is obtained from HyperLEDA B band absolute magnitude ($B-V$) since the galaxy is not in S4G sample; (4) Galaxy distance in Mpc from sources: 1= Virgocentric-corrected redshift from HyperLEDA + $H_0$=72; 2= Cepheids, metallicity-corrected from (Freedman et al., 2001a); 3= Surface Brightness Fluctuation from (Cantiello et al., 2018); 4= Surface Brightness Fluctuation from (Tonry et al., 2001) with a correction from (Mei et al., 2005); 5= Tip of the red giant branch (TRGB) distances from (Anand et al., 2021), 6= Virgo Cluster distances; (5) Galaxy physical size in pc/″ based on galaxy distances; (6) Spatial resolution in pc; (7) Source of IFU data used in this thesis.

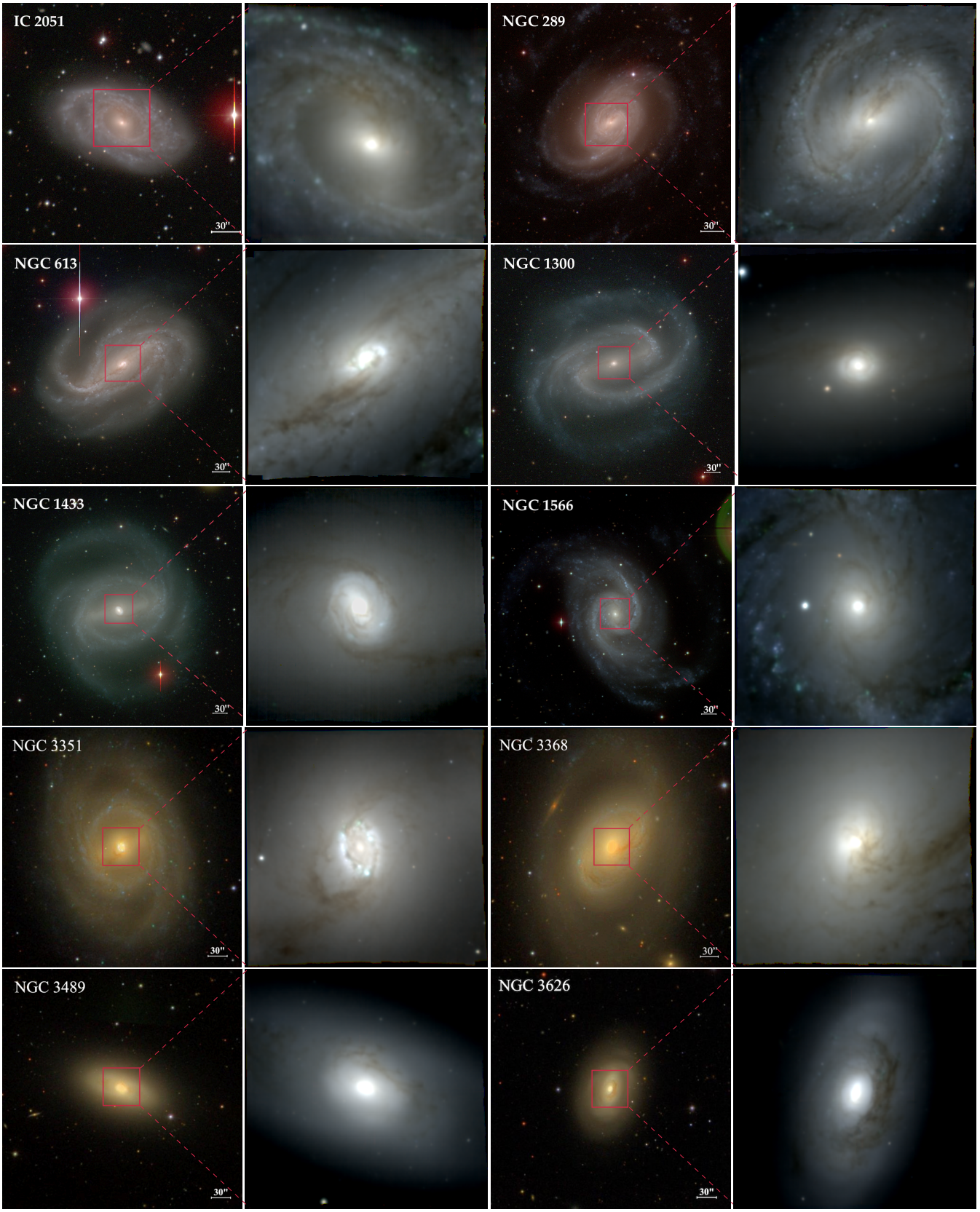


FIGURE 2.1: Galaxy sample studied in this thesis. *Columns 1 and 3:* Large-scale colour composite images. The red square represents the 60″×60″ MUSE FOV. *Columns 2 and 4:* colour composite images constructed from MUSE data, within the MUSE FOV highlighted as the red square in large-scale images.

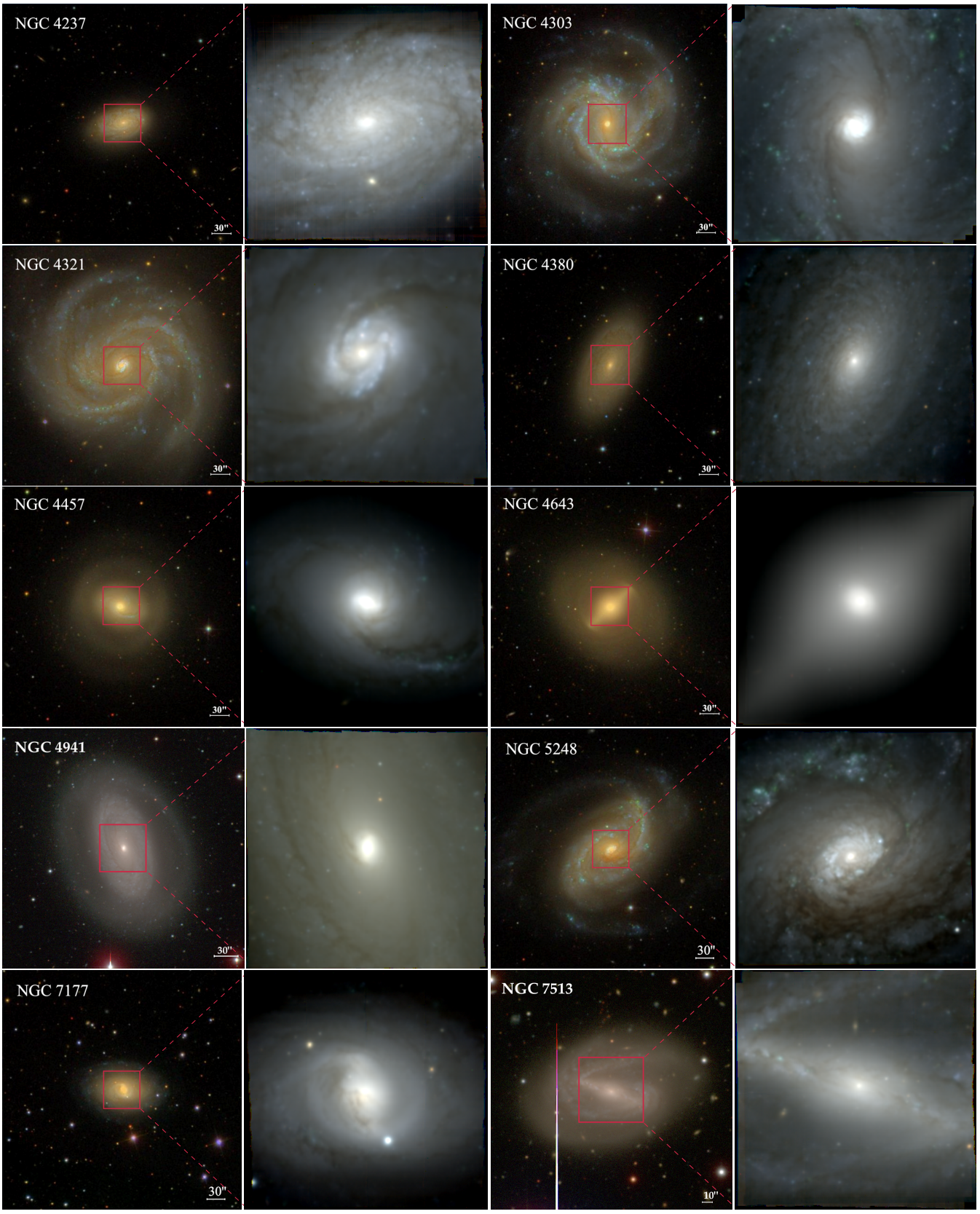


FIGURE 2.1: continued

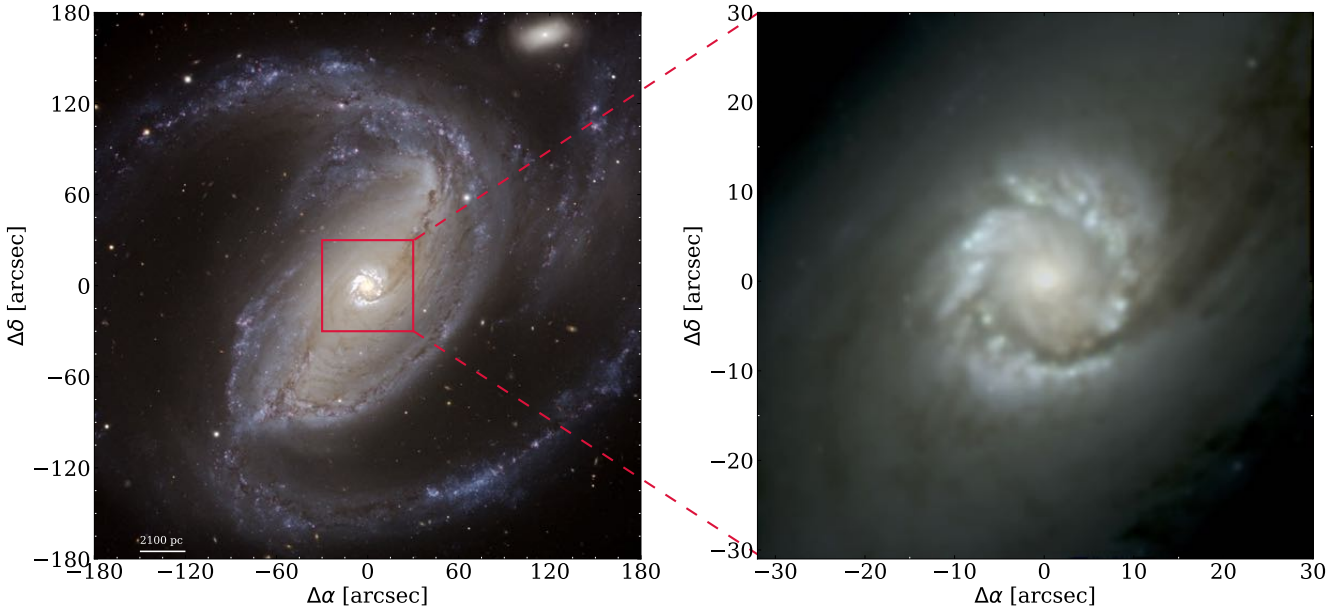


FIGURE 2.2: MUSE coverage of NGC 1097. *left:* Large-scale (360″×360″) image of NGC 1097 taken by VIMOS/VLT. The MUSE coverage of 60″×60″ is highlighted with the red box. *right:* Colour composite image within the MUSE FOV, constructed using the MUSE data cube. Images in both panels are centred on the brightest point in the centre. The North is to the top and the East is to the left.

## 2.3 Extraction of the kinematic measurements from MUSE Spectra

Extracting spatially resolved spectroscopic data from large data sets requires advanced analysis techniques. Although the concept behind the IFU reduction processes is not difficult, their routine usage can be inefficient because of employing large spectral template libraries and different scientific setups. Therefore, using an all-in-one framework software, which also provides parallelisation to speed the processing time of enormous data sets, is crucial. As a part of large surveys, various software is developed to process IFU data efficiently, such as Pipe3D (Sánchez et al., 2016b,a), MaNGA data analysis pipeline (Belfiore et al., 2019; Westfall et al., 2019) and GIST Pipeline (Bittner et al., 2019).

To derive emission line fluxes and to extract stellar and ionised gas kinematics from MUSE data, I employed the Data Analysis Pipeline[6] (`DAP`) of the PHANGS collaboration (Emsellem et al., 2022), which is an implementation based on the GIST pipeline (Bittner et al., 2019). `DAP` is an exceptionally functional software of modular structure, and it employs the commonly used penalised pixel-fitting (`pPXF`) code (Cappellari & Emsellem, 2004) to perform both stellar and emission line analysis. To optimise the processing time of `DAP`, I discarded the stellar population history module, since it was outside of the scope of this work. A schematic overview of `DAP` highlighting the main modules, the routines for data extraction and the products are presented in Fig. 2.3. A representative spectrum from a spaxel in NGC 1097, with the `pPXF` fit for both stellar and emission lines is shown in Fig. 2.4.

### 2.3.1 Deriving stellar line-of-sight velocity distribution moments

I extracted the stellar kinematics in the form of line-of-sight velocity distribution (LOSVD) moments — mean velocity (V), velocity dispersion ($\sigma$) and Gauss-Hermite higher-order moments ($h_3$ & $h_4$) (van der Marel & Franx, 1993a). Before deriving the LOSVD moments, the data are re-sampled on a logarithmic wavelength axis, then it is spatially binned with adaptive weighted implementation (Diehl & Statler, 2006) of the Voronoi tessellation (Cappellari & Copin, 2003). For the spectral fitting, I limited the rest frame wavelength range to 4800-7000Å. To fit the stellar continuum with `pPXF`, I used the EMILES single-stellar population (SSP) model library (Vazdekis et al., 2015). SSP models convolved with the LOSVD are fitted to each spectrum and the best-fitting parameters are determined by $\chi^2$ minimisation in pixel space. I used a threshold SNR of

[6] `DAP` can be accessed at: `https://gitlab.com/francbelf/ifu-pipeline`

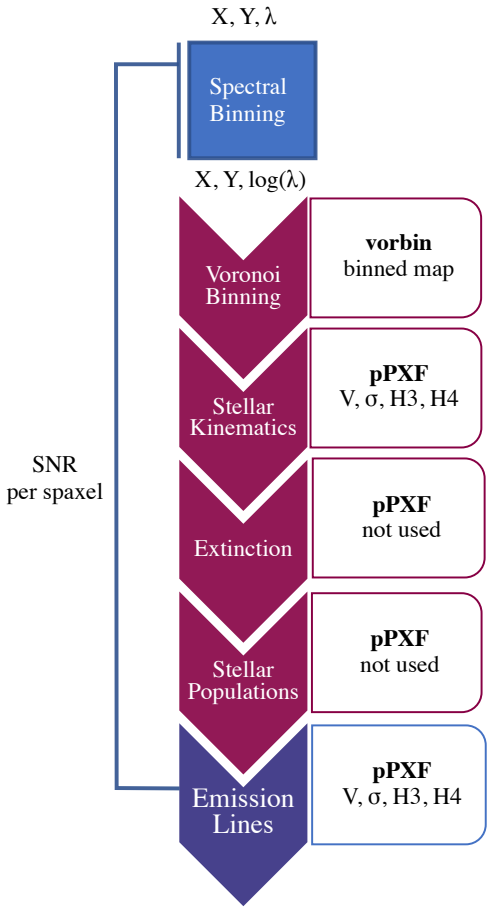


FIGURE 2.3: The implementation of the Data Analysis Pipeline. Arrows follow the order of the workflow within the pipeline. Voronoi binned data are transferred to stellar kinematics, extinction (not used), stellar population (not used) and emission line analysis modules respectively. Note that the emission line analysis can also be performed on single spaxels. In the rightmost blocks, I present the routine used in each module to perform the analysis alongside the derived products.

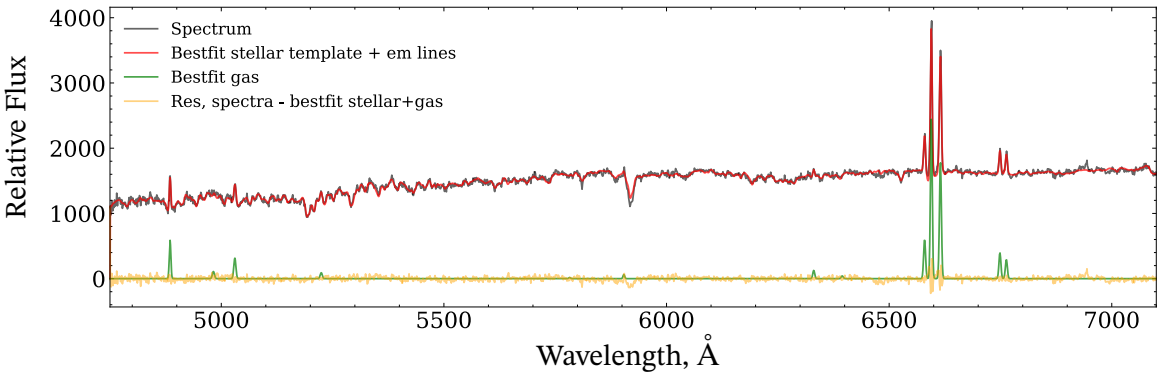


FIGURE 2.4: A representative spectrum in a spaxel in NGC 1097 and the best fitting lines from the DAP. The lines represent the MUSE spectrum (black), the combined best fit of the stellar template and emission lines (red), the best fit of emission lines (green), and the difference between the spectrum and the combined best-fit stellar template with emission lines (orange).

3 for spaxels included in Voronoi bins, to prevent contribution from low-quality spaxels whose signal is below the isophote level. I also used a target SNR of 40 for each Voronoi bin, as this value is commonly used in literature and provides a balance between the accuracy of the extracted measurements and the spatial resolution (van der Marel & Franx, 1993a).

When fitting the stellar kinematics, I used $8^{th}$ order multiplicative Legendre polynomials within the `pPXF` routine and included no additive polynomials. Multiplicative polynomials adjust the inaccuracies in the spectral calibration and make the fits independent of reddening by dust so that I do not need to provide a particular reddening curve within the routine (Cappellari, 2017). Although additive polynomials can minimise mismatches between stellar templates and absorption lines and correct impurities from the sky subtraction (Cappellari, 2017), they can also alter the equivalent width of the Balmer absorption lines and might introduce non-physical correction to the line fluxes (Emsellem et al., 2022). Therefore, I proceeded to use only multiplicative polynomials, both to avoid any non-physical flux values and for the efficiency of the routine since combining both additive and multiplicative Legendre polynomials is computationally expensive. The stellar LOSVD moments of my pilot galaxy NGC 1097, can be seen in Fig. 2.5.

The systemic velocity of each galaxy, which is required to be included in `DAP`, are taken from the NASA/IPAC Extragalactic Database (NED[7]), based on redshift measurements. For instance, the systemic velocity of NGC 1097 is set at 1271 km/s, based on its redshift value $z \approx 0.00424$ obtained from Allison et al. (2014). Subsequently, to ensure consistency across the dataset, all wavelengths in this study are corrected respectively to each galaxy's redshift.

Within the pilot study, to define the centre of NGC 1097, I first attempted to fit ellipses to the flux distribution by using the *ellipse* routine of IRAF[8] software, but I realised that the flux distribution of the galaxy is asymmetric, so the parameters of the ellipses were poorly constrained. Hence, I defined the photometric centre as the brightest spaxel in the nucleus based on the flux integrated over the entire MUSE spectral range. The kinematic centre derived for NGC 1097, shown in Chapter 3 (Sect. 3.3), differs only by $\sim$3 spaxels from the photometric centre, and the impact of this difference while fitting disk models is negligible. Therefore, to ensure consistency across the sample analysis, for all galaxies, I provide the coordinates $\Delta\alpha$, $\Delta\delta$ in relation to the photometric centre, i.e. the photometric centre is located at $[\Delta\alpha,\Delta\delta]=[0,0]$.

[7]NED can be accessed via `https://ned.ipac.caltech.edu/`
[8]IRAF: the Image Reduction and Analysis Facility software (Tody, 2000)

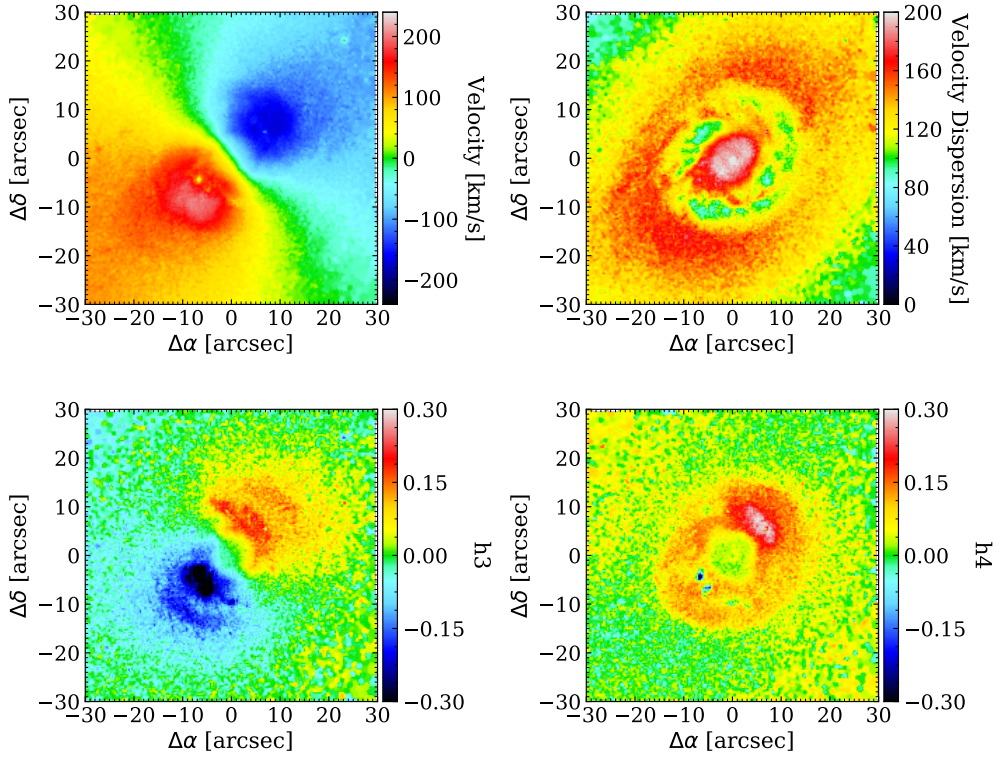


FIGURE 2.5: Stellar LOSVD moment maps of NGC 1097. Stellar velocity (top left) velocity dispersion (top right) Gauss-Hermite moments h3 (bottom left) and h4 (bottom right)

### 2.3.2 Deriving ionised gas line-of-sight velocity distribution moments

I derived the ionised gas kinematics by fitting initially single Gaussian components to the emission lines, with the stellar continuum and absorption lines fitted simultaneously. The fits were performed on individual spaxels, while the stellar velocity moments were fixed to the values determined for each Voronoi bin, specified in the prior stellar kinematics fits. Computing Gauss-Hermite higher-order moments is also possible for the emission line analysis, and for NGC 1097 I show the results from the fits including the h3 and h4 coefficients in Appendix A, Fig. A.1. However, I find fitting emission lines with single Gaussians to be a better approach when searching for multiple components (see Sect. 2.3.3), whose presence otherwise could be incorporated in the higher-order moments.

`DAP` can fit each emission line separately or fit several emission lines together by assigning each the same velocity and velocity dispersion and by imposing flux ratios. I left the fluxes free, except for the constraints from atomic physics (Osterbrock & Ferland, 2006). I gathered the emission lines into three main groups, with kinematics shared among lines in each group. Extracting kinematics for each group separately allows us to study and understand how gas regions of different physical properties move with

TABLE 2: Characteristics of the fitted emission lines. Wavelengths of the emission lines are taken from the National Institute of Standards and Technology, (NIST; `https://www.nist.gov/pml/atomic-spectra-database`).

| Line ID | Wavelength (Å) | Amplitude Ratio (fixed) |
|---|---|---|
| Group 1 - Hydrogen Balmer Lines | | |
| H$\beta$ | 4861.35 | |
| H$\alpha$ | 6562.79 | |
| Group 2 - Low Ionisation Lines | | |
| [N I]$\lambda$5198 | 5197.90 | |
| [N I]$\lambda$5200 | 5200.26 | |
| [N II]$\lambda$5754 | 5754.49 | |
| [O I]$\lambda$6300 | 6300.30 | |
| [O I]$\lambda$6364 | 6363.78 | 0.33[O I]$\lambda$6300 |
| [N II]$\lambda$6548 | 6548.05 | 0.34[N II]$\lambda$6583 |
| [N II]$\lambda$6583 | 6583.45 | |
| [S II]$\lambda$6716 | 6716.44 | |
| [S II]$\lambda$6731 | 6730.82 | |
| Group 3 - High Ionisation Lines | | |
| [O III]$\lambda$4959 | 4958.91 | 0.35[O III]$\lambda$5007 |
| [O III]$\lambda$5007 | 5006.84 | |
| He I $\lambda$5876 | 5875.61 | |
| [S III]$\lambda$6312 | 6312.06 | |

respect to each other. The grouping of the emission lines is done as follows: Group 1 consists of Balmer lines —H$\beta\lambda$4861, H$\alpha\lambda$6562 (indexed as H$\beta$ and H$\alpha$ in figures); Group 2 consists of low-ionisation lines —[N I]$\lambda\lambda$5197,5200, [N II]$\lambda$5754, [O I]$\lambda\lambda$6300,64, [N II]$\lambda\lambda$6548,83 , [S II]$\lambda\lambda$6717,31 and Group 3 consists of high-ionisation lines —He I$\lambda$5875, [O III]$\lambda\lambda$4959,5007, [S III]$\lambda$6312. I summarise the characteristics of the fitted emission lines in each group in Table 2.

In Figure 2.6 I present for NGC 1097, the kinematic maps of the each emission line group, accompanied by the flux maps of the strongest line in each group, which are H$\alpha$, [N II]$\lambda$6583 and [O III]$\lambda$5007 respectively. To avoid contribution from spaxels dominated by noise, I used a threshold SNR=10; spaxels of lower SNR are discarded from the maps. All three groups show high flux in the nuclear ring and in the nucleus. The observed velocity field of each group has a typical spider velocity pattern and is dominated by rotation, but it also shows strong distortions from circular motion caused by the presence of the bar. Such distortions in the gas kinematics have been reported in various nearby galaxy studies (Bosma, 1978; Emsellem et al., 2001; Zurita et al., 2004; Fathi, 2004; Fathi et al., 2006). The velocity dispersion is the lowest in the nuclear ring and in the outer regions and significantly increases close to the nucleus.

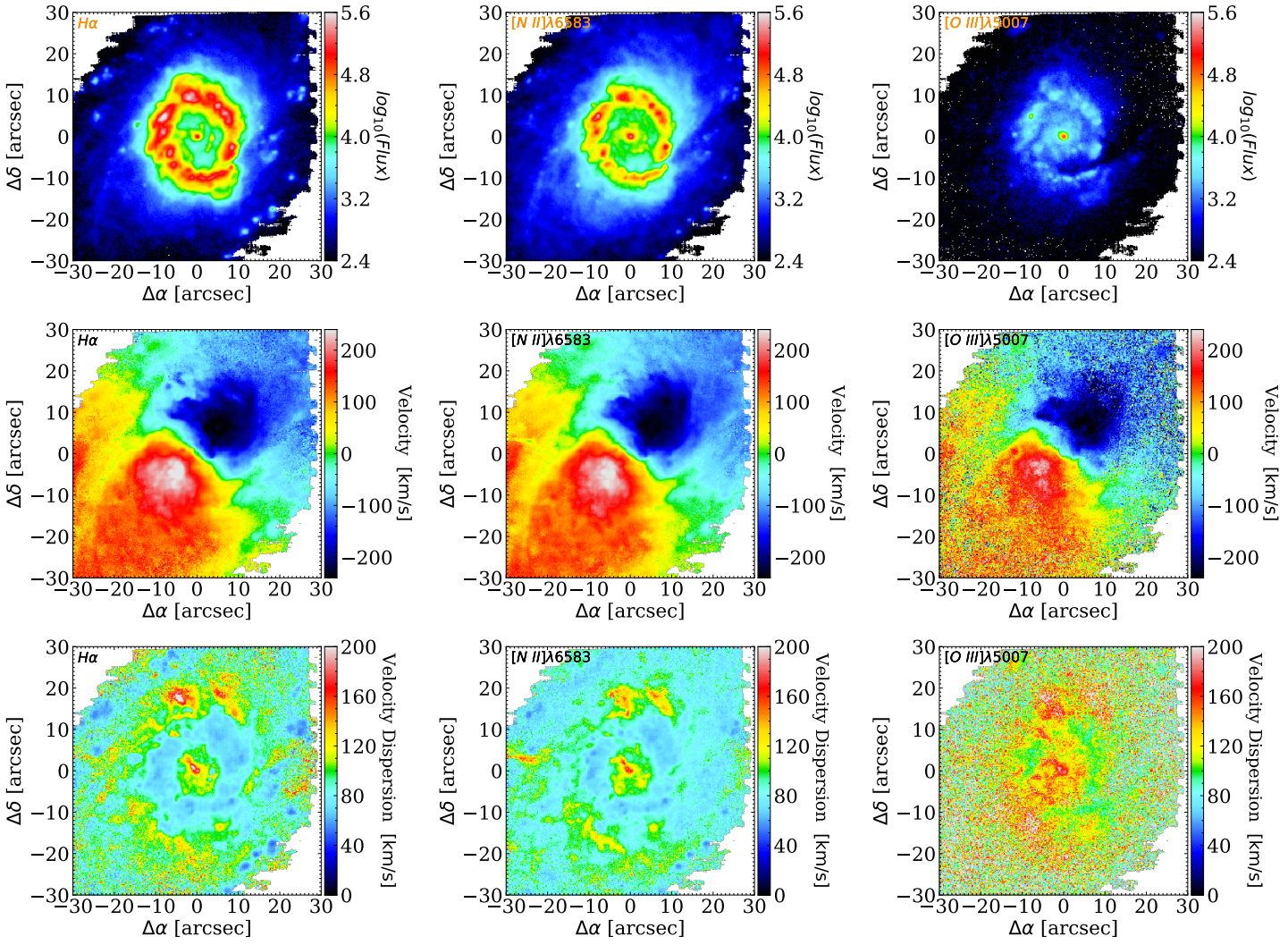


FIGURE 2.6: For NGC 1097, LOSVD moment maps of H$\alpha$ (left) [N II]$\lambda$6583 Å (middle), [O III]$\lambda$5007 Å (right). I show the flux on a logarithmic scale in units $10^{-20}$ergs$^{-1}$cm$^{-2}$spaxel$^{-1}$ (top row) velocity (middle row) and the velocity dispersion (bottom row).

### 2.3.3 Improving the quality of the fits by fitting multiple Gaussians

In the regions inner to the nuclear ring of NGC 1097, the kinematics of all emission line groups reveal a region of high velocity dispersion, extending from the centre of the galaxy $\sim 3''$ towards the northeast (see Fig. 2.6), which drove me to closely examine the spectra in those affected spaxels. In Figure 2.7, I show the H$\alpha$ and [N II]$\lambda\lambda$6548,83 region of the spectrum in one of the affected spaxels, as well as in a spaxel outside of the affected region. These spaxels are located at the positions marked by an 'x' and a '+', respectively, in the top left panel of Fig. 2.8. In the spectrum of the affected spaxel, as shown in the middle panel of Fig. 2.7, I noticed an excess emission in the blue wing of [N II]$\lambda$6583 line, a second component to the main line component, with a peak at the rest frame wavelength $\sim$6574.50Å, which hereafter I call the ***excess***.

Because of the excess, the line profile of [N II]$\lambda$6583 becomes strongly non-Gaussian, and the excess encroaches on the region between [N II]$\lambda$6583 and H$\alpha$, so the H$\alpha$ fits are also strongly affected by its presence. As I demonstrate in the top panel of Fig. 2.7, when the excess is not present, the emission lines are well-fitted, but when the excess is present, the minimisation algorithm of `pPXF` produces a broad Gaussian, especially for H$\alpha$, leading to overestimated velocity dispersion values. The presence of the excess shifts the centre of the fitted Gaussians for the main [N II]$\lambda$6583 component to slightly lower velocities, and for the H$\alpha$ component to higher velocities. I found no signs of an excess in the red wing of [N II]$\lambda$6583, or either of the wings of H$\alpha$. Although I see a weak excess in the blue wing of [N II]$\lambda$6548, its SNR is at the same level as noise, and it is insignificant compared to the excess in the blue wing of [N II]$\lambda$6583. Moreover, I found no signs of an excess in the wings of the [O III]$\lambda$5007, though its presence might be lost to the noise. However, in the spaxels of the region with high velocity dispersion, where the presence of the excess in the blue wing of [N II]$\lambda$6583 is the most pronounced, [O III]$\lambda$5007 line is well-fitted. This suggests that the high velocity dispersion of [O III]$\lambda$5007 in those regions (Fig. 2.6) is intrinsic.

To account for the excess and to improve the line fits, I introduced one additional emission component to the `DAP` configuration at a wavelength $\lambda$ $\sim$6574.50Å, which I call the ***secondary component***. Throughout the rest of this work, I work under the assumption that the secondary component is a Doppler-shifted component of [N II]$\lambda$6583. I tested how the derived kinematics depends on the initial guess of the wavelength of the secondary component by shifting it by $\pm$3.3Å (roughly equal to the dispersion broadening); I found no significant changes to the results. In the bottom panel of Fig. 2.7, I demonstrate that for the spaxel, whose spectrum and single Gaussian fits were affected by the presence of the excess, the addition of the secondary component accounts for the excess and fixes the erroneous fits. However, for the spaxels where the

excess is not strong the fits of the secondary component would be poorly constrained. Therefore, to prevent additional errors from secondary component fitting, one must carefully determine whether the spaxels are truly affected by the presence of the excess. This can be done by comparing the measurements extracted from fits with and without the secondary component.

As I explained earlier in this section, the excess emission on one side of the line not only increases the velocity dispersion of a single Gaussian fit but also alters its velocity. While high velocity dispersion can be intrinsic, a large change in the derived velocity caused by including the secondary component indicates strong asymmetry of the line profile, hence, likely the presence of multiple line components. Therefore, I search for the spaxels that are the most affected by the presence of the excess by looking for a change in derived velocities, which should be more reliable than using only the high velocity dispersion measurements.

In order to identify which spaxels in and around the region of the elevated velocity dispersion in the nucleus are affected by the presence of the excess, I fitted the secondary component in the inner $8''\times8''$. In Figure 2.8, I show the change in velocity (V) and velocity dispersion ($\sigma$) between the original values obtained from single Gaussian fits and the corrected values obtained from fits with the secondary component included. For the corrected measurements, in addition to the respective emission line ID, I use the notation *"corr"*.

The velocity dispersion in the nuclear regions remains high after including the secondary component (upper panels), with the values for [N II]$\lambda$6583 and H$\alpha$ velocity dispersion reduced by ∼20–30% and ∼30–40%, respectively, from the values obtained from single Gaussian fits which might indicate the velocity dispersion is intrinsically high. The persisting high velocity dispersion might also suggest that my approach is simplistic and that using more than two Gaussian components possibly can account for the excess better and can reduce the estimated velocity dispersion more. However, increasing the number of components introduces more free parameters, and I do not have enough constraints or resolution to fit more than two components. Moreover, I noticed that the largest reduction in velocity dispersion (middle panels) occurs in spaxels where adding the secondary component significantly changes the velocity of the main lines (lower panels).

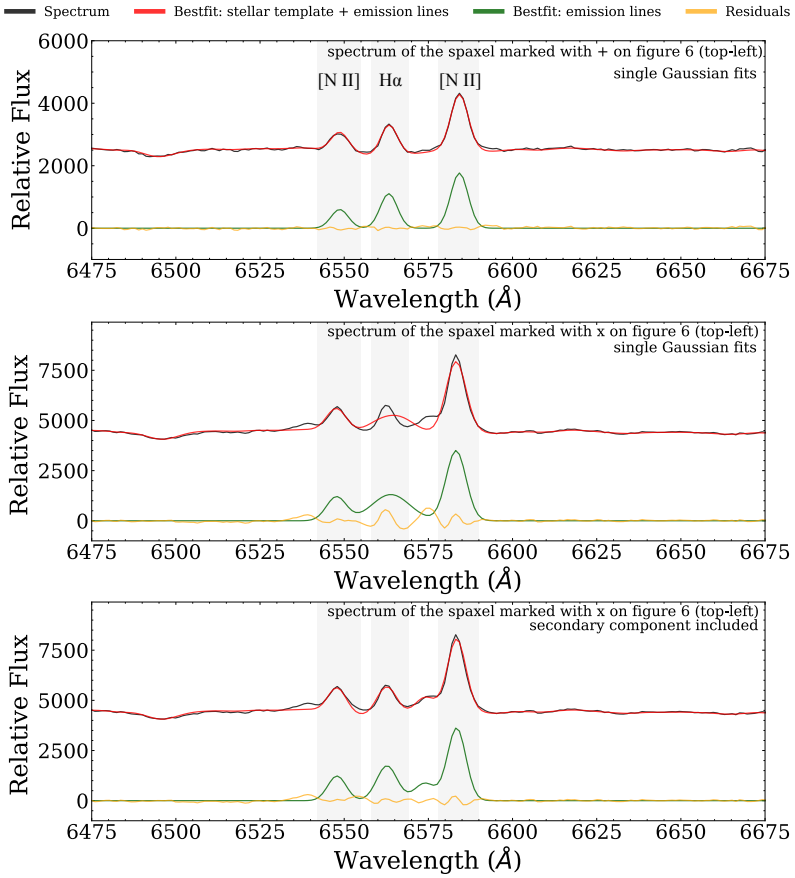


FIGURE 2.7: Representative spectra in spaxels in NGC 1097, zoomed on the region of H$\alpha$ and [N II]$\lambda$6583, and the best fits from `pPXF/DAP`. The lines represent the MUSE spectrum (black), the combined best fit of the stellar template and emission lines (red), the best fit of emission lines (green), and the difference between the spectrum and the combined best-fit stellar template with emission lines (orange). *top:* Spectrum of a spaxel without the excess, marked in the upper left panel of Fig. 2.8 with a '+'. *middle:* Spectrum of a spaxel with the excess affecting the single Gaussian fits of H$\alpha$ and [N II]$\lambda$6583, marked in the upper left panel of Fig. 2.8 with an 'x'. *bottom:* Spectrum of the spaxel shown in the middle panel, with fits that include the secondary component.

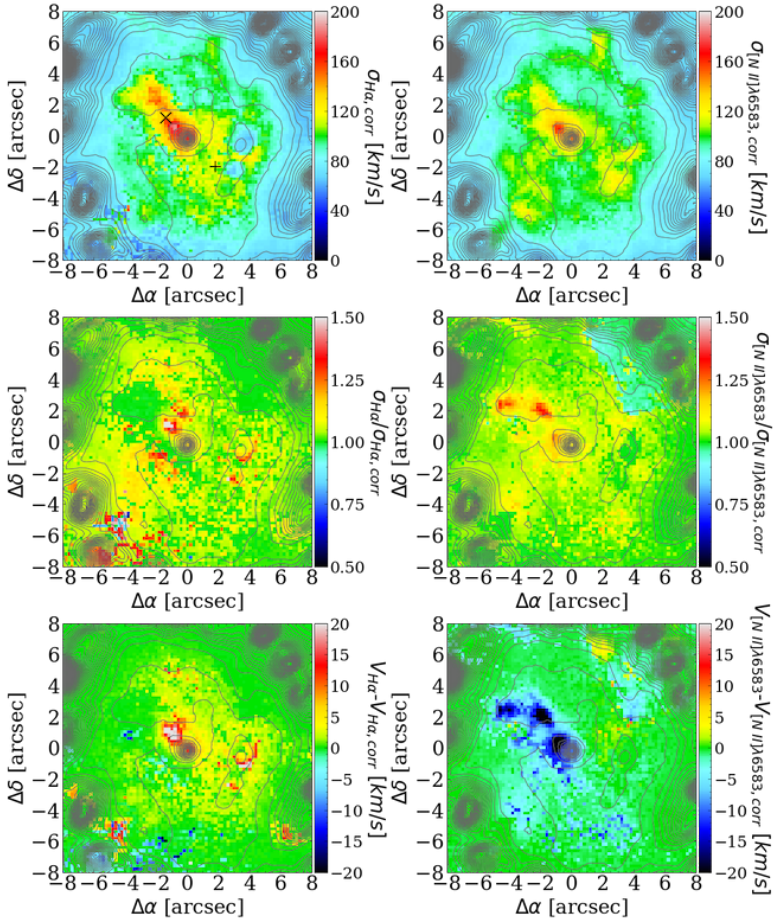


FIGURE 2.8: NGC 1097, comparison between single Gaussian fits and fits including a secondary [N II]$\lambda$6583 component. Grey contours in all panels highlight the H$\alpha$ emission. The left and right columns represent H$\alpha$ and [N II]$\lambda$6583 respectively. *top:* the corrected velocity dispersion. 'x' and '+' markers on the left panel represent the spaxels whose spectra are displayed in Fig. 2.7. *middle:* The ratio of velocity dispersion obtained from single Gaussian fits and the corrected velocity dispersion. *bottom:* The velocity differences between the corrected velocity field and the velocity field obtained with single Gaussians.

Therefore, based on the bottom panels of Fig. 2.8 I defined the following conditions to create a mask region where single Gaussian fits are not reliable, and values from the run with the secondary component will be used:

i. $V_{[\mathrm{N\ II}]\lambda6583} - V_{[\mathrm{N\ II}]\lambda6583,\mathrm{corr}} < -4\ \mathrm{kms}^{-1}$

ii. $V_{\mathrm{H}\alpha} - V_{\mathrm{H}\alpha,\mathrm{corr}} > 5\ \mathrm{kms}^{-1}$

iii. $-6'' \leq \Delta\alpha \leq 1.2''$ and $-3'' \leq \Delta\delta \leq 4''$

The application of the conditions above is shown in the left panel of Fig. 2.9. The spatial cuts are applied to discard the isolated spaxels outside the region of the elevated velocity dispersion in the nucleus where the velocity correction is low. The velocity limits are chosen to maximise the area where the secondary component can be reliably fitted. By replacing within the defined mask region, the measurements from the single Gaussian fits with those from fits with the secondary component included, I created a combined data set of corrected flux, velocity and velocity dispersion. The resultant maps are presented in Fig. 2.10. For both H$\alpha$ and [N II]$\lambda$6583, the apparent change in flux, velocity and velocity dispersion maps are not significant. However, the accurate corrected values are crucial for my further analysis in Sect. 3. Hereafter, I use measurements from the combined data set. [O III]$\lambda$5007 can still be represented by the maps in Fig. 2.6 since single Gaussian fits were not affected by the presence of the excess.

I present the flux (F) and kinematic maps of the secondary component (indexed by [N II]w) within the mask region in the right panel of Fig. 2.9, both absolute and relative to the main [N II]$\lambda$6583 component. Note that few spaxels within the mask show inconsistent values compared to the main gradient of flux and kinematic measurements. This implies that the secondary component fits in those spaxels are not reliable and those spaxels are discarded in the analysis below. The secondary component has high flux at the centre of the galaxy that extends towards the northeast side of the mask, coinciding with the high velocity dispersion of the H$\alpha$ and [N II]$\lambda$6583 components. In addition, the flux ratio of the secondary component to the main component increases away from the centre. In the velocity map of the secondary component, I see a gradient consistent with rotation, but after I subtract the disk rotation, the secondary component appears blueshifted by 300–400 $\mathrm{kms}^{-1}$ with respect to the main component, and the blueshift decreases away from the galaxy centre. The velocity dispersions of the secondary and main components are similar, though there is a slight indication that in spaxels where the contribution from the secondary component is the strongest, its velocity dispersion is smaller than that of the main component by up to 20%.

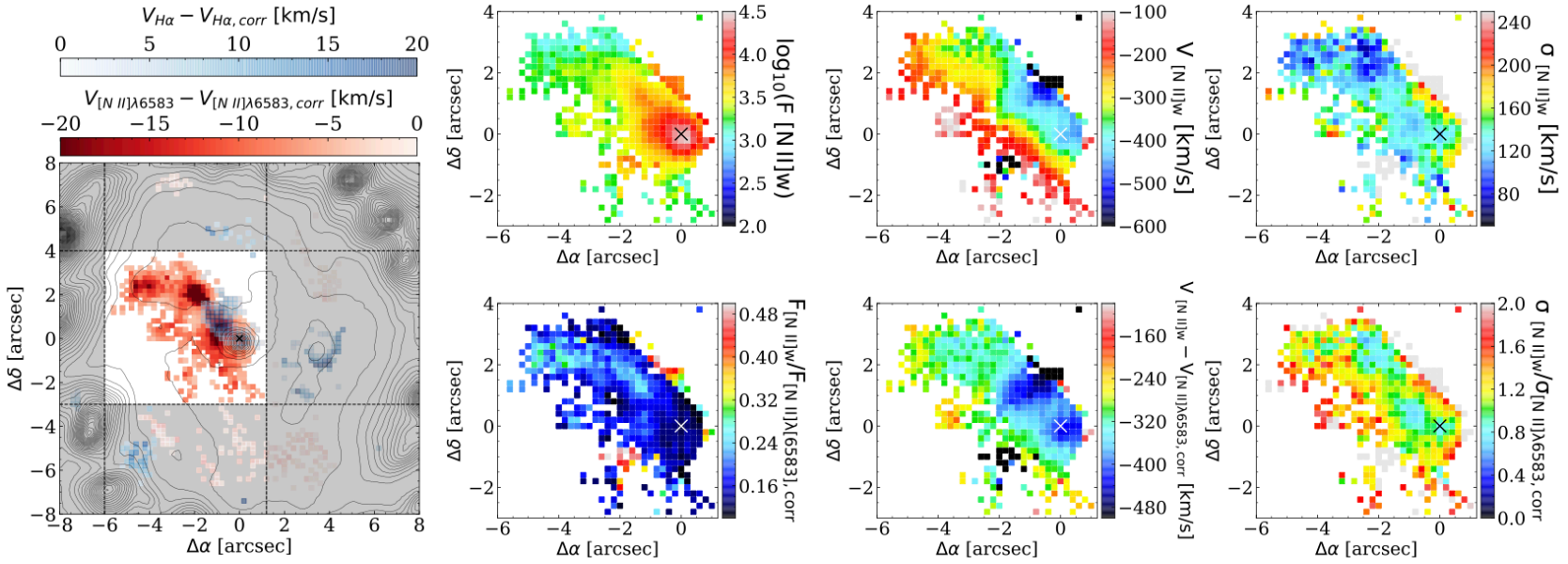


FIGURE 2.9: *left:* The mask of spaxels for which the fits including secondary component were used in further analysis of NGC 1097. Spaxels in the grey-shaded region fall outside the defined conditions and are excluded from the mask. Blue and red colours show the difference between the initial and corrected H$\alpha$ and [N II]$\lambda$6583 velocities extracted by fitting single Gaussians and after including the secondary component to [N II]$\lambda$6583 respectively. Grey contours represent the H$\alpha$ emission. The centre of the galaxy is marked with a cross. *right:* Flux and kinematics of the secondary component within the mask. Only spaxels within the mask are shown. Maps respectively show the derived flux (top left), velocity (top middle), velocity dispersion (top right), the ratio of the fluxes of the secondary component and the main [N II]$\lambda$6583 line (bottom left), the difference in velocities of the secondary component and the main [N II]$\lambda$6583 line (bottom middle), the ratio of velocity dispersion of the secondary component and the main [N II]$\lambda$6583 line (bottom right).

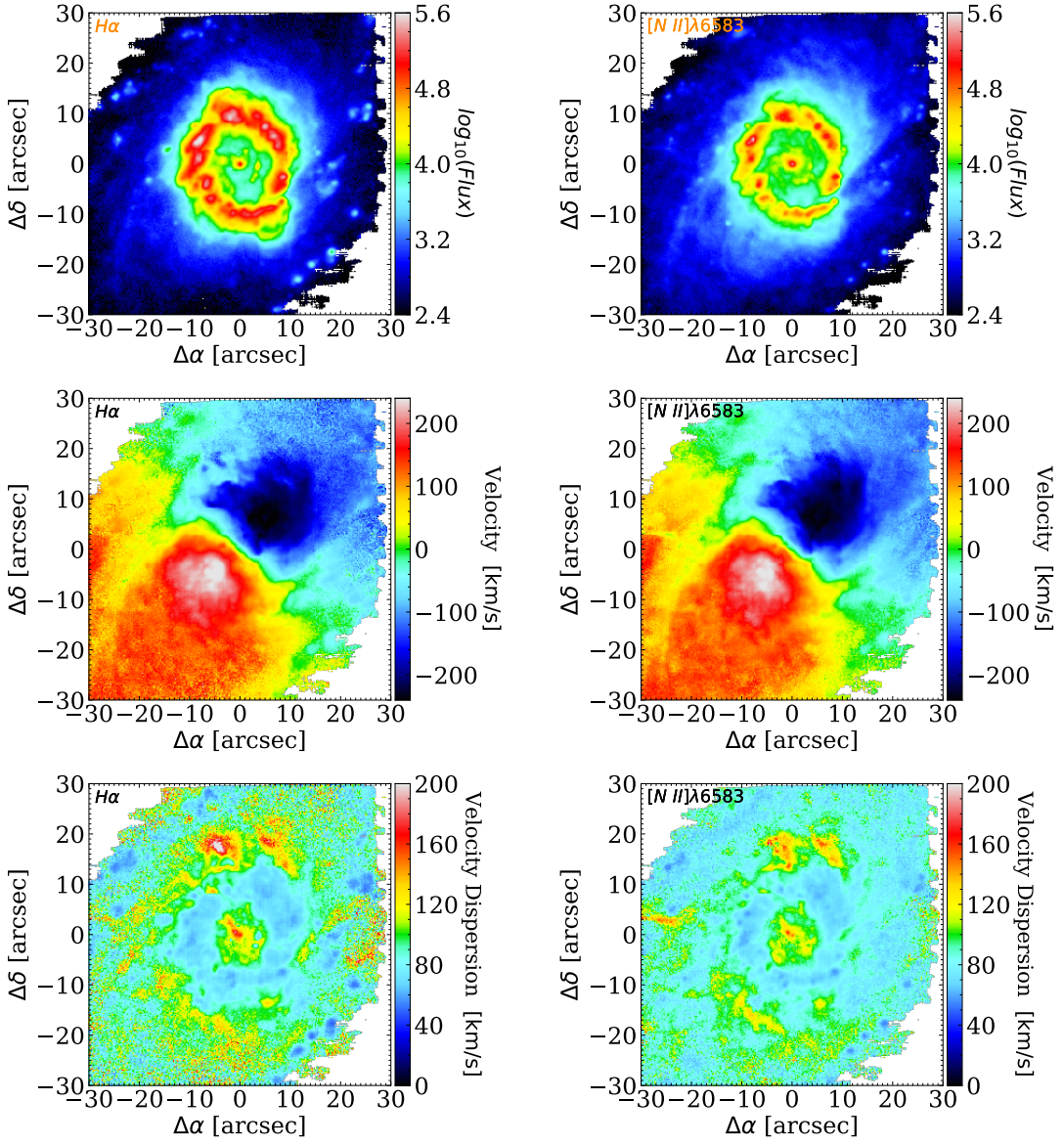


FIGURE 2.10: Corrected LOSVD moments of NGC 1097, after combining the results from single Gaussian fits with the fits including the secondary component (as explained in Sect. 2.3.3). For H$\alpha$ line (left), and for [N II]$\lambda$6583 line (right). I display the line flux on a logarithmic scale in units $10^{-20}$ergs$^{-1}$cm$^{-2}$spaxel$^{-1}$ (top row), velocity (middle row) and velocity dispersion (bottom row).

### 2.3.4 Alterations in secondary component fitting and masking procedures applied to other sample galaxies

After establishing the methodology in my pilot study with NGC 1097, my next goal was to apply it to a sample of 20 galaxies. The parameters for kinematic extraction within DAP, such as the SNR thresholds and the designated rest frame wavelength ranges, remain consistent with those used within my pilot study with NGC 1097. Initially, I used single Gaussian fitting to derive flux, velocity, and velocity dispersion maps for the sample galaxies, these are presented in Figs. 2.11 to 2.19. Given the varying SNR levels across each galaxy, to maintain consistency across the galaxy sample, I chose not to impose an additional SNR threshold for excluding noisy spaxels while presenting these maps; unlike what is done in NGC 1097 which I explained in Sect. 2.3.2.

However, as I explained in Sect. 2.3.3, my analysis of NGC 1097 revealed a significant limitation of the standard approach of fitting spectra with single Gaussians when there is excess emission from different sources along the line of sight (e.g., one from the disk and one from AGN outflows). In such cases, the line profile may become non-Gaussian, making a single Gaussian fit inappropriate. This can result in a poor fit, leading to an artificially increased velocity dispersion and altering the velocity of the main spectral line. Such inaccuracies could significantly impact my work, particularly when constructing diagnostic maps of residual velocity and velocity differences, in which I search for the kinematic signatures of extended shocks (see Chapter 3).

Therefore, while examining the kinematic maps of the galaxies, when encountering regions that show unusually high velocity dispersions for any group of emission lines, I carefully examine the spectra for signs of excess emission. Discovering such emission signature prompts me to apply the secondary component fitting approach, introduced in my pilot study Kolcu et al. (2023), also described in the previous section, Sect. 2.3.3. When two distinct emission components are dominant along the LOS, by allowing to fit for a secondary component, one can separate the emission attributed to excess sources from that of the galactic disk itself.

Besides NGC 1097, amongst the remaining 20 galaxies within my sample, three of them – NGC 1433, NGC 4303, and NGC 4321 – exhibited excess emission in their spectra that required additional attention. Some of these galaxies displayed more complex line features than those observed in NGC 1097's spectra. Therefore, I have found it necessary to tailor certain aspects of the secondary component fitting and masking to accommodate the unique characteristics of each individual galaxy, which I explain below.

During this tailored emission line fitting process, I start with the same assumption that is made in the analysis of NGC 1097. I assume that all secondary components, which are

fitted to the excess emissions in the spectra, are either blue- or red-shifted components of the main line components, depending on whether the excess emission appears on the blue or red wing of the main emission line component, respectively. I then used the following configuration within DAP to incorporate secondary component(s) to the emission line fitting: if excess emission is present in multiple emission lines from different groups, the kinematics of each fitted secondary component are determined independently; this is observed in NGC 4303 (see Sect. 5, Fig. 5.12a ). For example, a secondary component fitted to [N II]$\lambda$6583 excess emission and a secondary component fitted to [O III]$\lambda$5007 excess emission are considered independent from each other. However, when excess emission is significant across more than one emission line within the same emission line group, such as [N II] doublets, the kinematics of the fitted secondary components to account for the excess emissions are tied together, similar to the approach used for tying the kinematics of the doublets due to the constraints from atomic physics (Osterbrock & Ferland, 2006).

To identify which spaxels are most significantly affected by excess emission, I first analysed the differences between measurements from single Gaussian fits and those including secondary components. I focused on detecting large changes in the velocity and velocity dispersion measurements of the main emission line component obtained from the two fitting approaches. Upon this process for the three sample galaxies, I noticed that the influence of excess emission was only significant on the measurements of [N II]$\lambda$6583; unlike in NGC 1097's analysis, where the excess emission in [N II]$\lambda$6583 influenced measurements of both H$\alpha$ and [N II]$\lambda$6583 (see Figs. 2.7 and 2.8). Consequently, when establishing the masking criteria for these galaxies, to correct the measurements in the spaxels that are the most affected by the excess emission, I excluded the H$\alpha$ velocity shift condition previously employed for NGC 1097.

Additionally, I observed that none of the galaxies showed significant excess emission in [O III]$\lambda$5007, even in the regions with high [O III]$\lambda$5007 velocity dispersions. This suggests that [O III]$\lambda$5007 measurements from single Gaussian fits are in general reliable. For instance, slightly non-Gaussian [O III]$\lambda$5007 profiles are seen in NGC 4303's spectra, caused by a weak excess emission but including a secondary component to the fitting did not significantly influence the derived measurements. Thus, to simplify the analysis and to reduce the number of free parameters in the fit, I omitted including a secondary component for [O III]$\lambda$5007 in these cases, this decision is elaborated further in the section on NGC 4303 (see Chapter 5, Sect. 5.12).

Based on the insights gained from the observations explained above, for the three galaxies that show prominent excess emission in their spectra, for which I used the secondary

component fitting approach, I refined the masking criteria, incorporating three main conditions:

i. there should be a significant [N II]$\lambda$6583 velocity shift between single Gaussian fits and fits including the secondary component

ii. there should be a significant [N II]$\lambda$6583 velocity dispersion ratio of single Gaussian fits and fits including the secondary component

iii. the velocity dispersion of the secondary [N II]$\lambda$6583 component ([N II]w) should not reach excessively high values, to confirm that the secondary component is a representation of real emission rather than noise.

For further analysis, the flux, velocity and velocity dispersion of all emission line groups within the mask region are replaced with values for the main component in fits that include the secondary component. However, H$\alpha$ and [O III]$\lambda$5007 measurements are not significantly affected.

Detailed information on the fitting approach of the secondary component, mask conditions, and further kinematic analysis for each of the three galaxies exhibiting excess emission in their spectra is provided in their respective sections in Chapter 5 (Sects. 5.5, 5.12 and 5.13).

This refined fitting approach significantly enhances the accuracy of the kinematic measurements extracted from MUSE data cubes, thereby minimising errors associated with excess emission in the diagnostic maps I construct to search for the kinematic signatures of extended shocks. Consequently, this approach substantially improves the quality of the analysis and enhances the robustness of my findings.

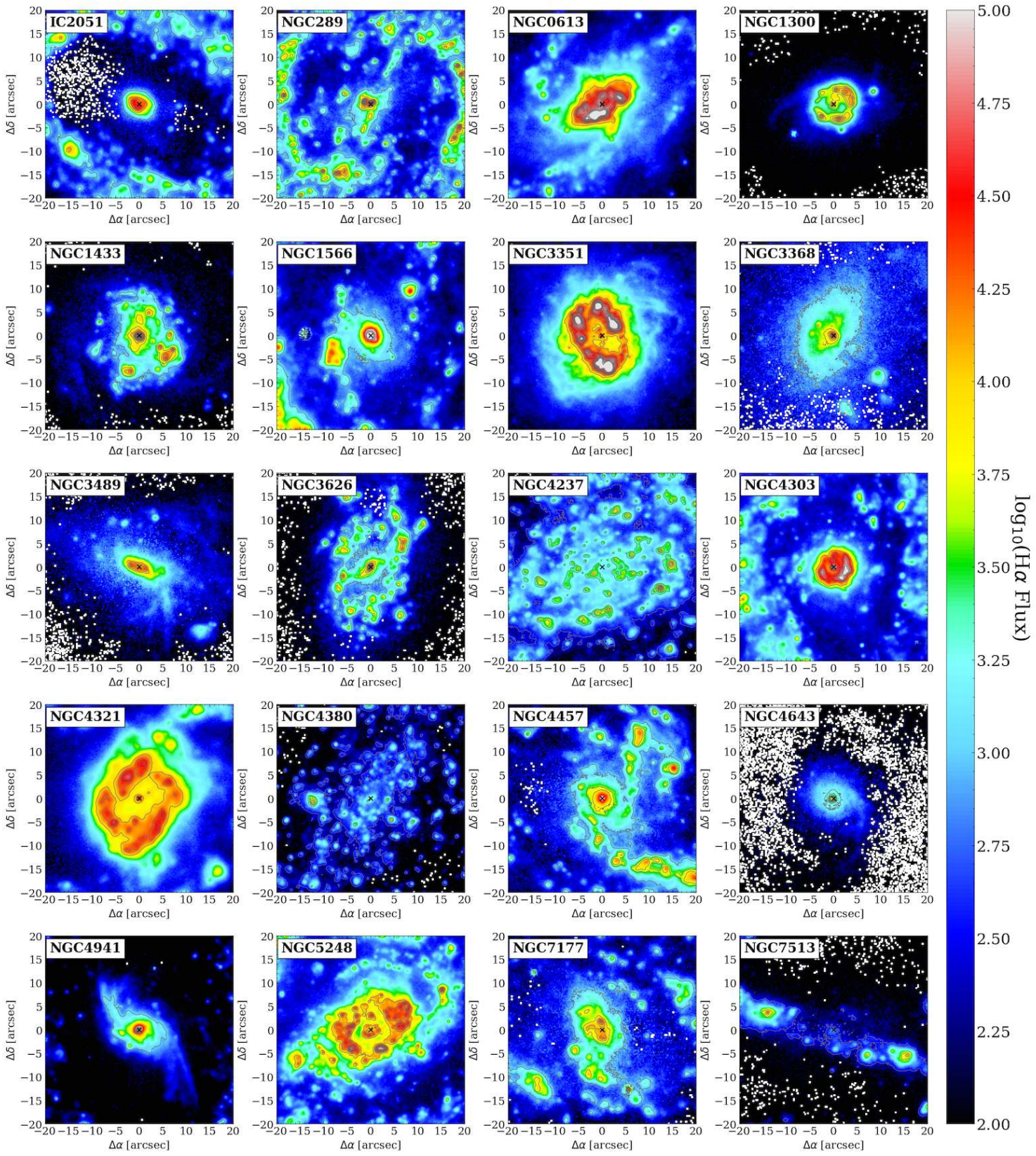


FIGURE 2.11: H$\alpha$ flux of the galaxies studied in this thesis, the units are $10^{-20} ergs^{-1} cm^{-2} spaxel^{-1}$. Grey contours represent the H$\alpha$ flux. The centre of each galaxy is marked with an "x".

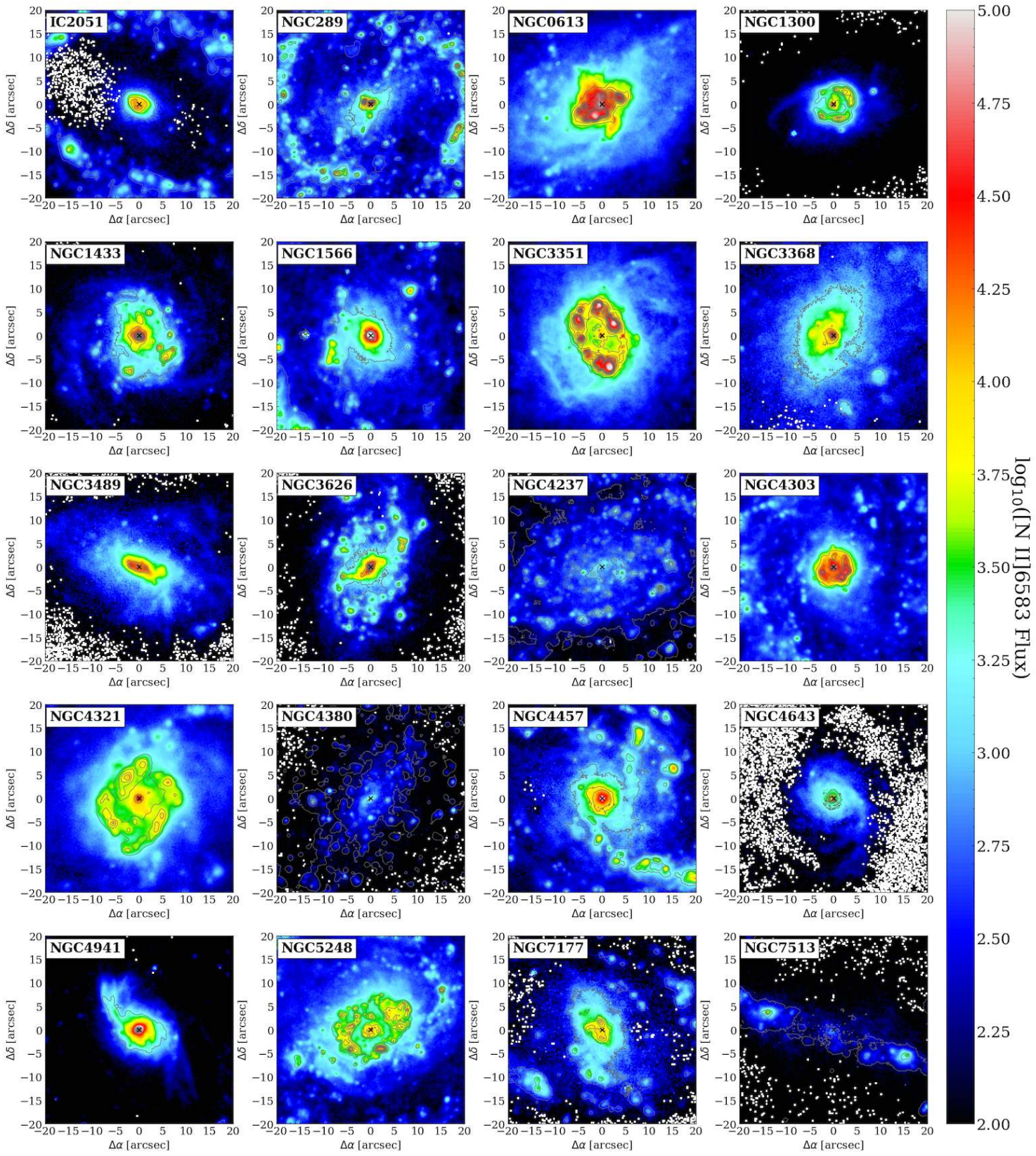


FIGURE 2.12: [N II]$\lambda$6583 flux of the galaxies studied in this thesis, the units are $10^{-20} ergs^{-1} cm^{-2} spaxel^{-1}$. Grey contours represent the H$\alpha$ flux. The centre of each galaxy is marked with an "x".

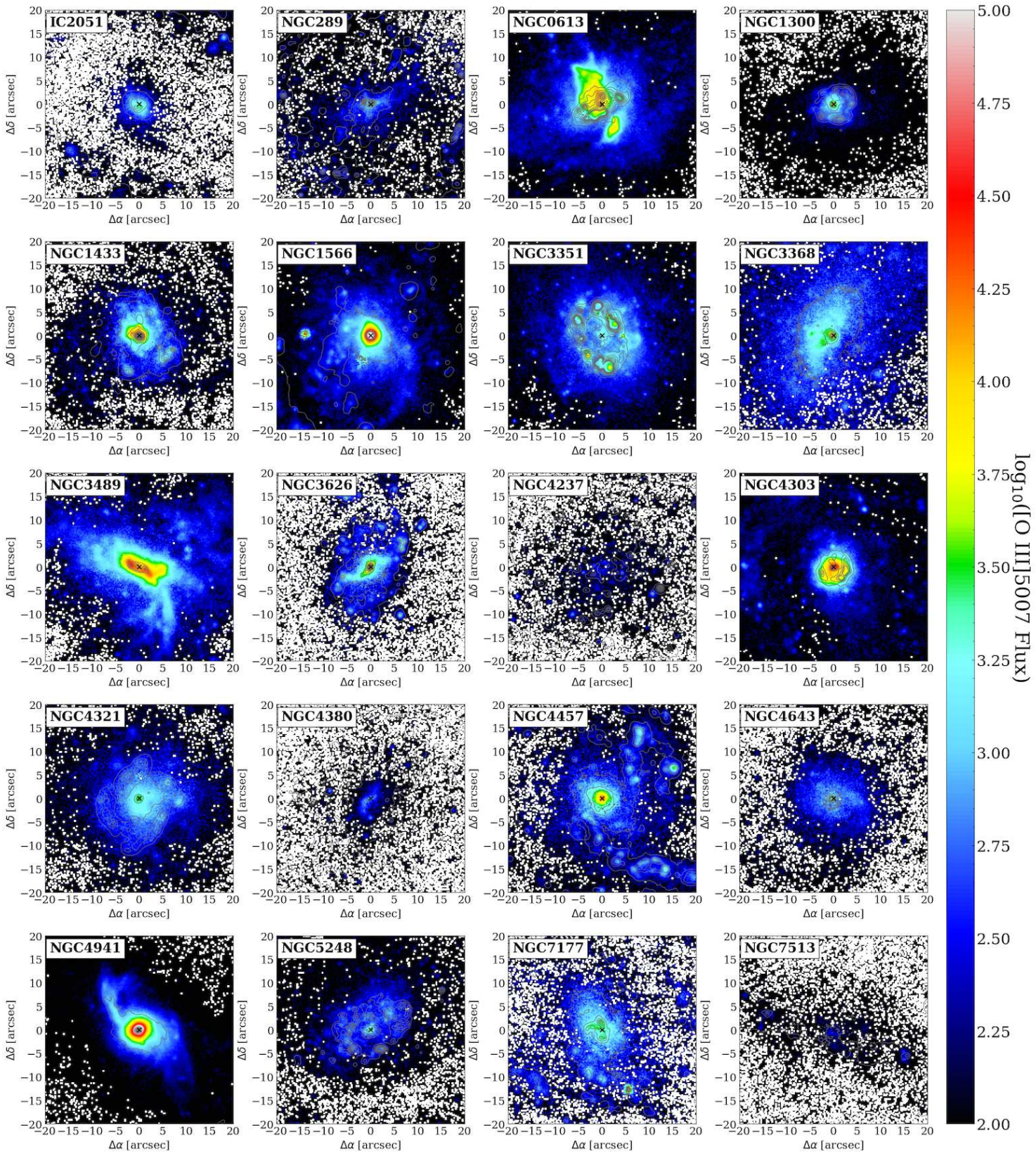


FIGURE 2.13: [O III]$\lambda$5007 flux of the galaxies studied in this thesis, in units $10^{-20} ergs^{-1} cm^{-2} spaxel^{-1}$. Grey contours represent the H$\alpha$ flux. The centre of each galaxy is marked with an "x".

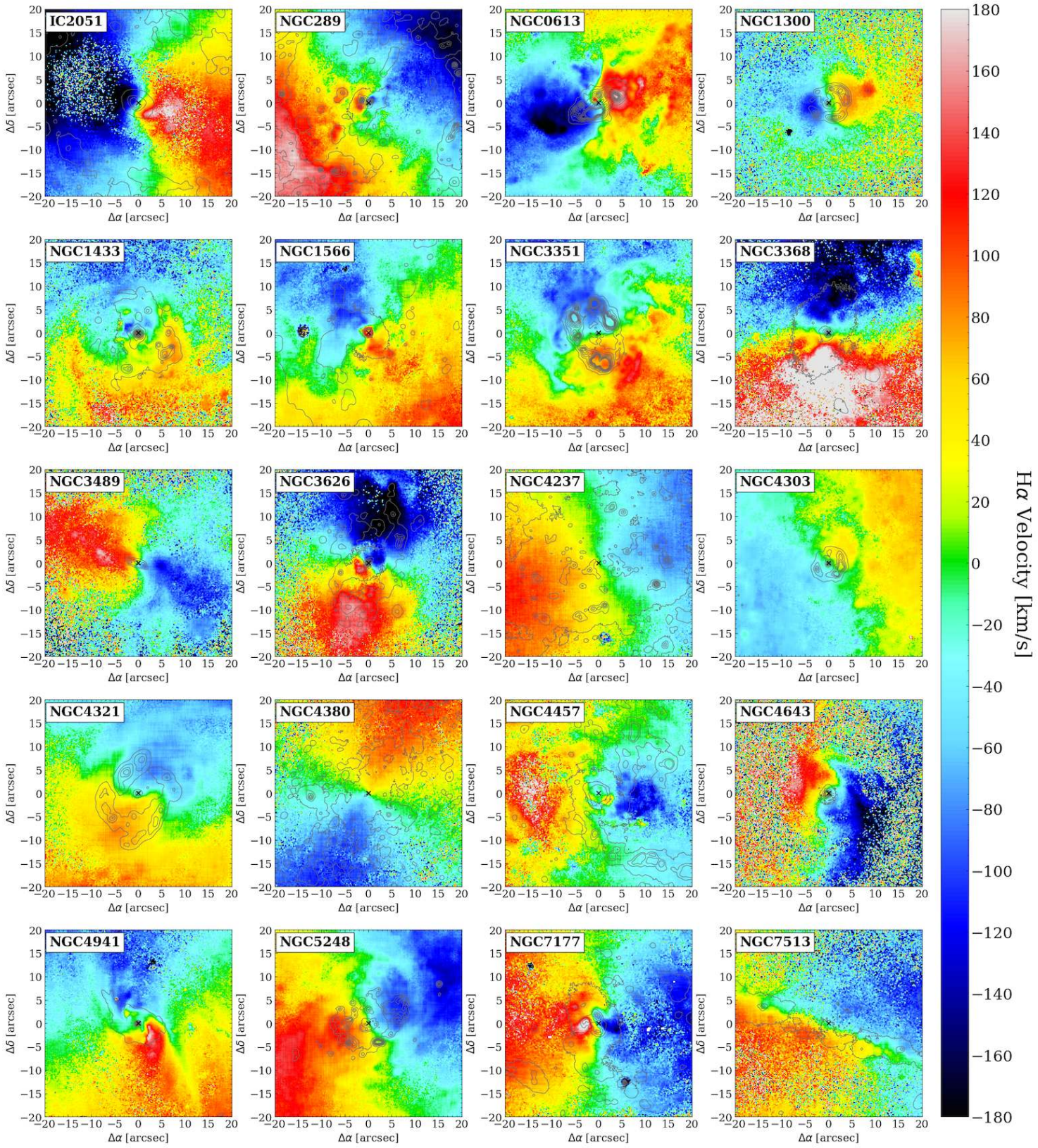


FIGURE 2.14: H$\alpha$ velocity maps of galaxies studied in this thesis. Grey contours represent the H$\alpha$ flux. The centre of each galaxy is marked with an "x".

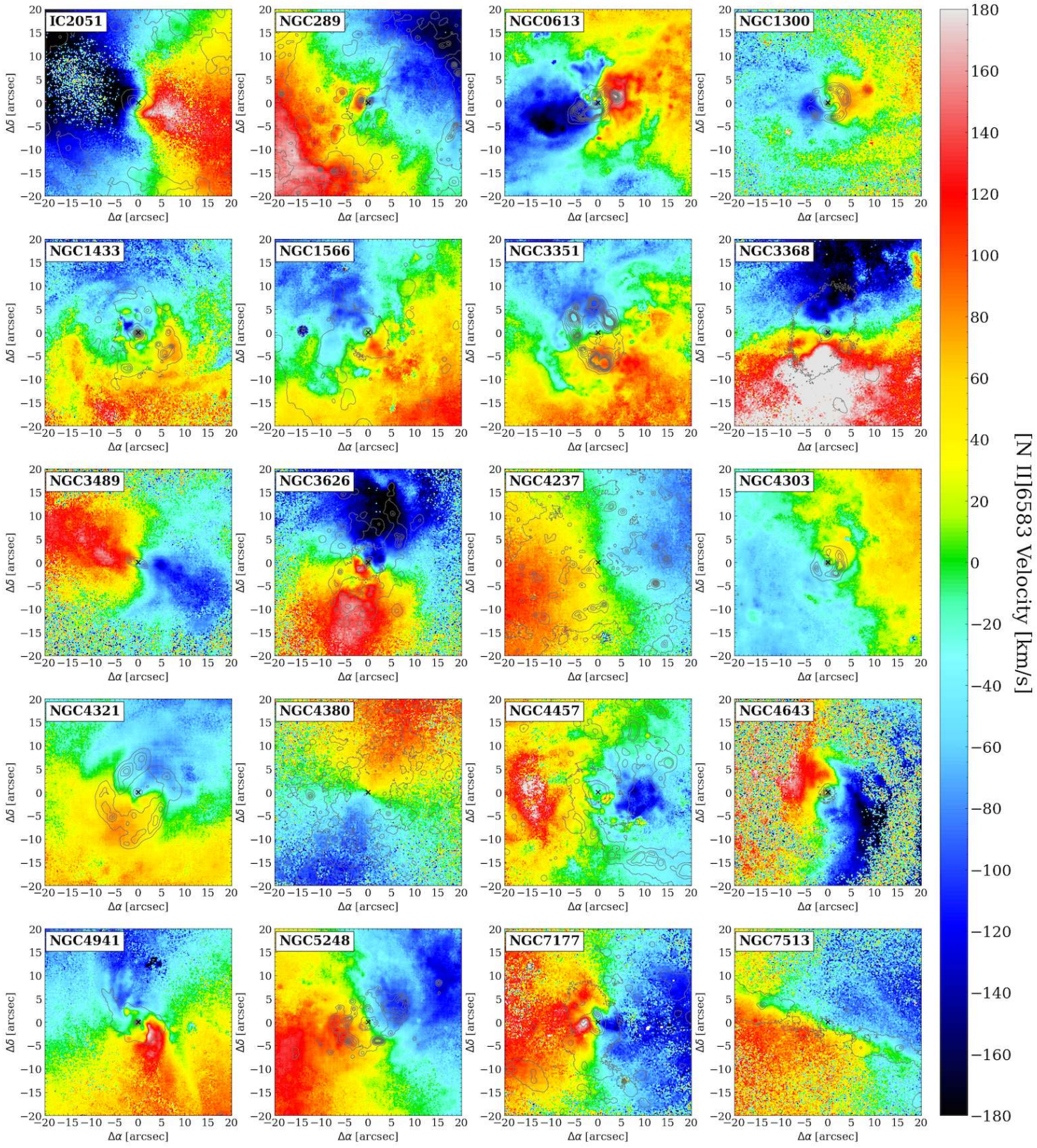


FIGURE 2.15: [N II]$\lambda$6583 velocity maps of galaxies studied in this thesis. Grey contours represent the H$\alpha$ flux. The centre of each galaxy is marked with an "x".

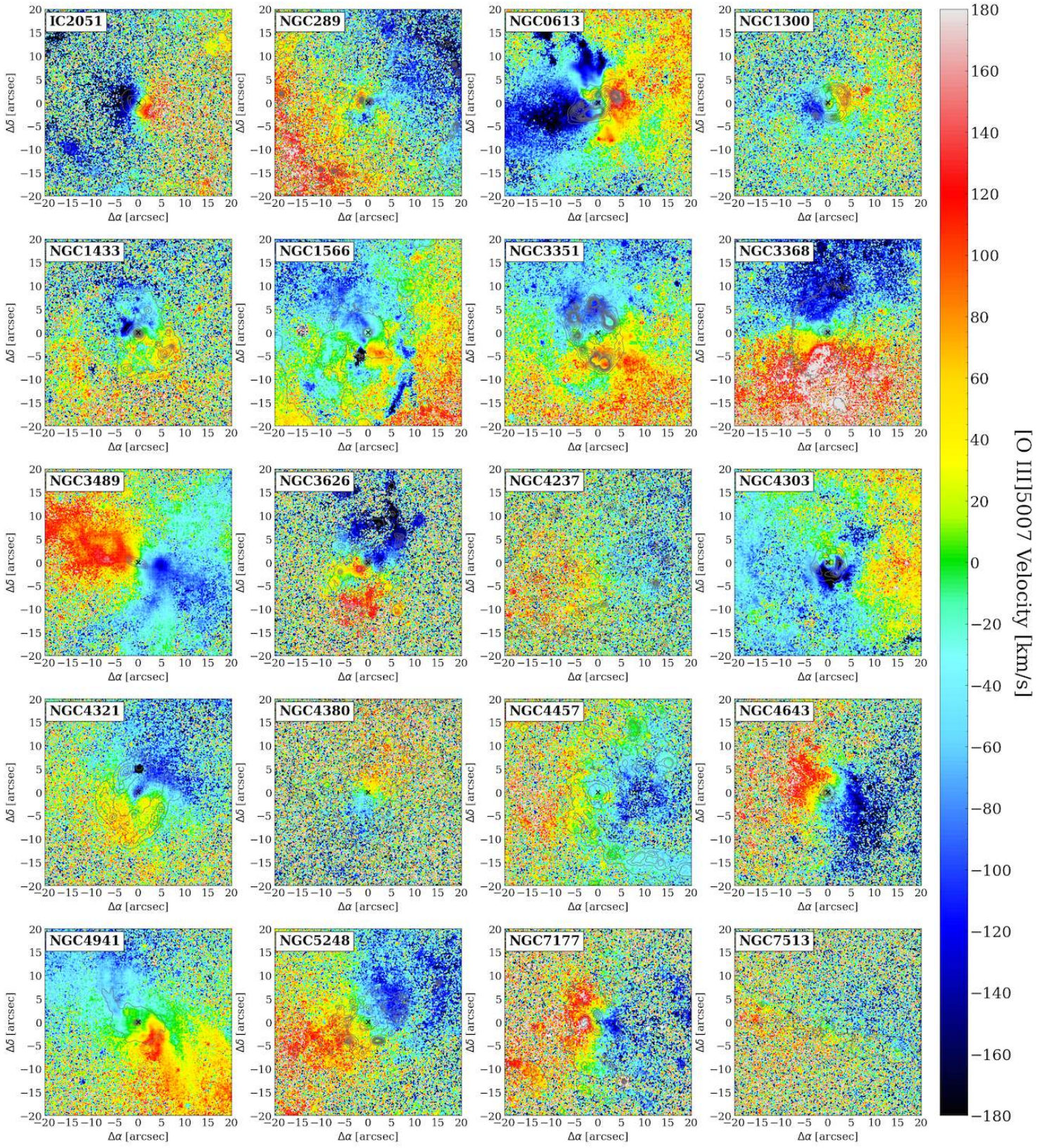


FIGURE 2.16: [O III]$\lambda$5007 velocity maps of galaxies studied in this thesis. Grey contours represent the H$\alpha$ flux. The centre of each galaxy is marked with an "x".

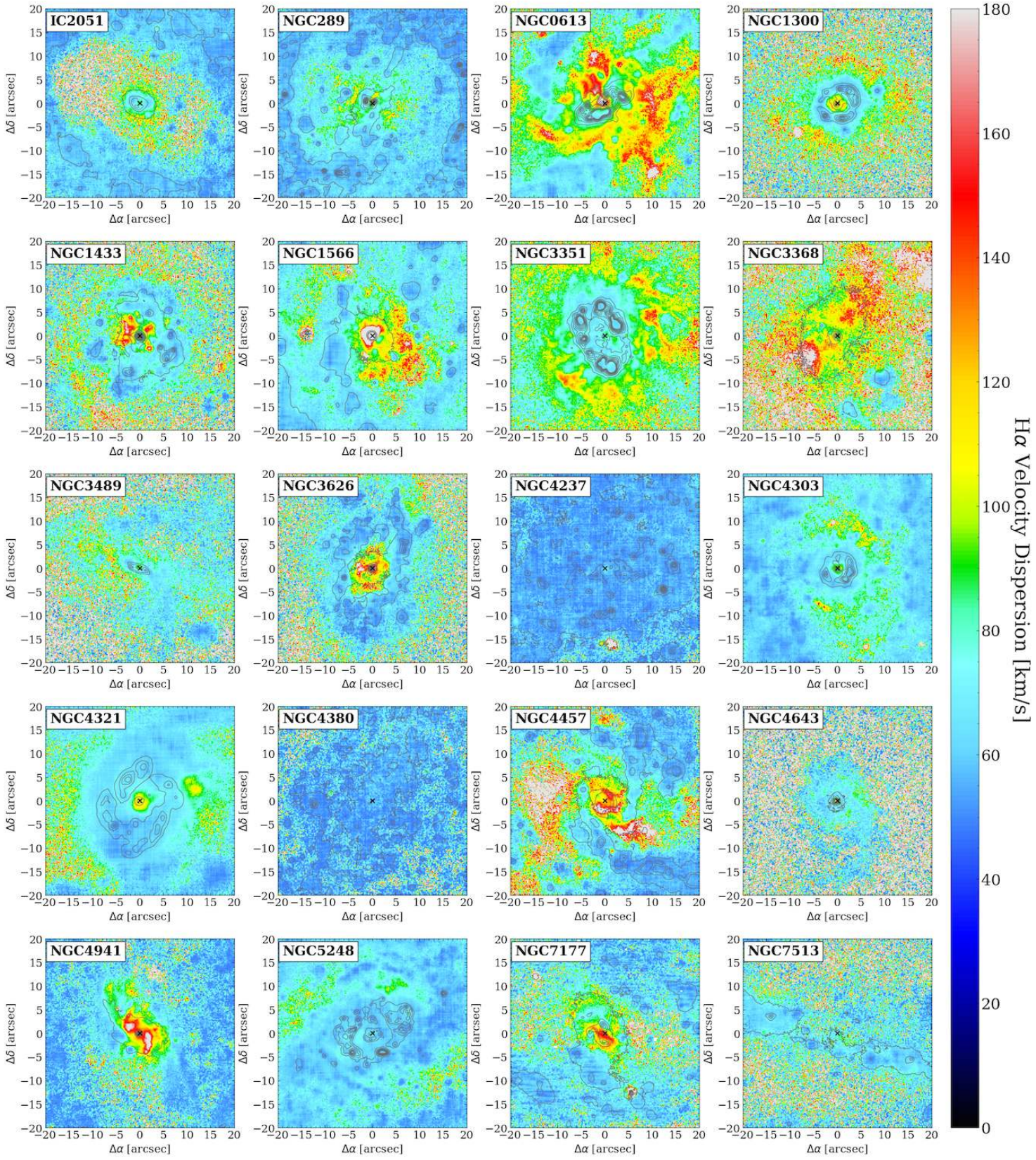


FIGURE 2.17: Hα velocity dispersion maps of galaxies studied in this thesis. Grey contours represent the Hα flux. The centre of each galaxy is marked with an "x".

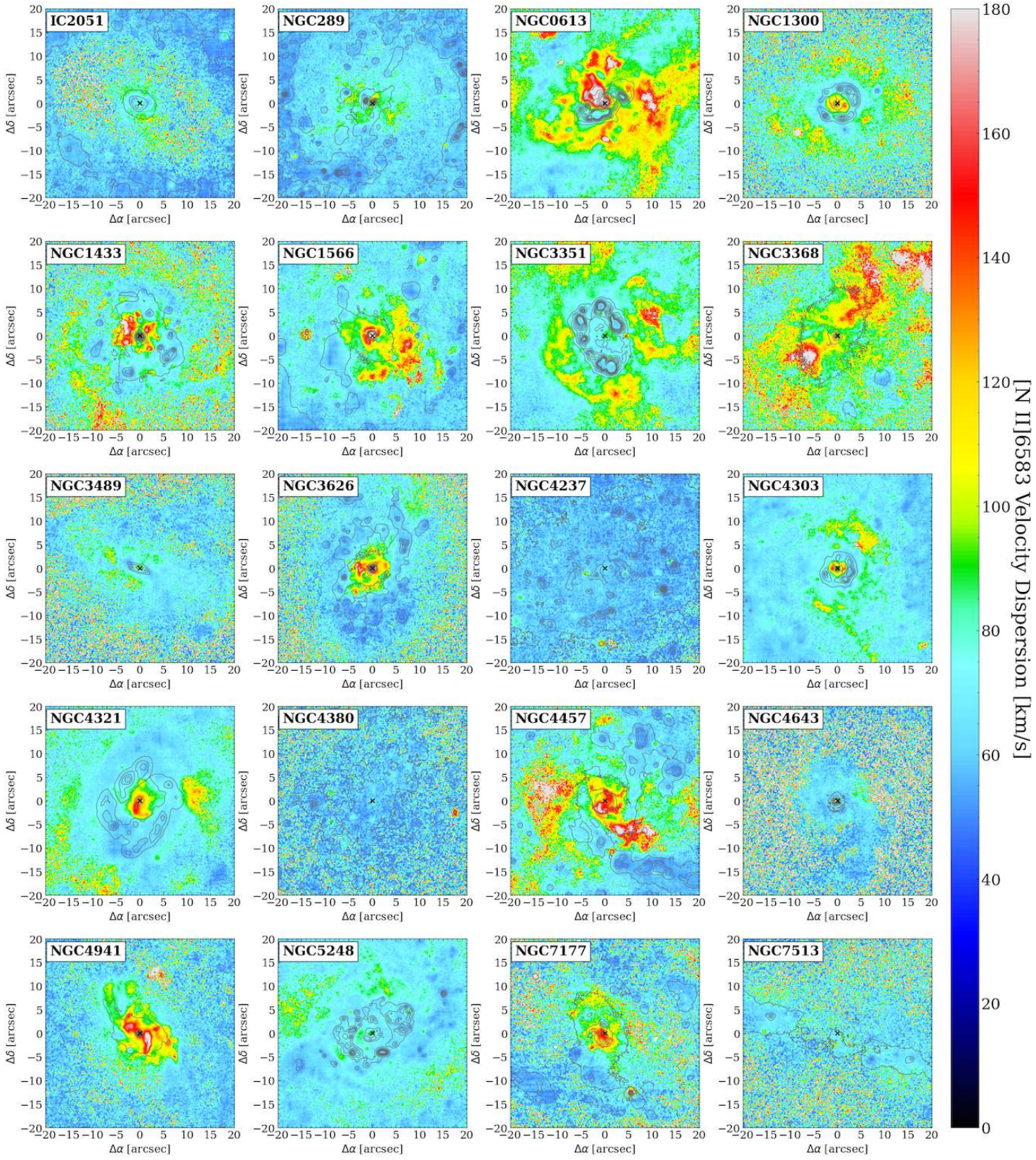


FIGURE 2.18: [N II]λ6583 velocity dispersion maps of galaxies studied in this thesis. Grey contours represent the H$\alpha$ flux. The centre of each galaxy is marked with an "x".

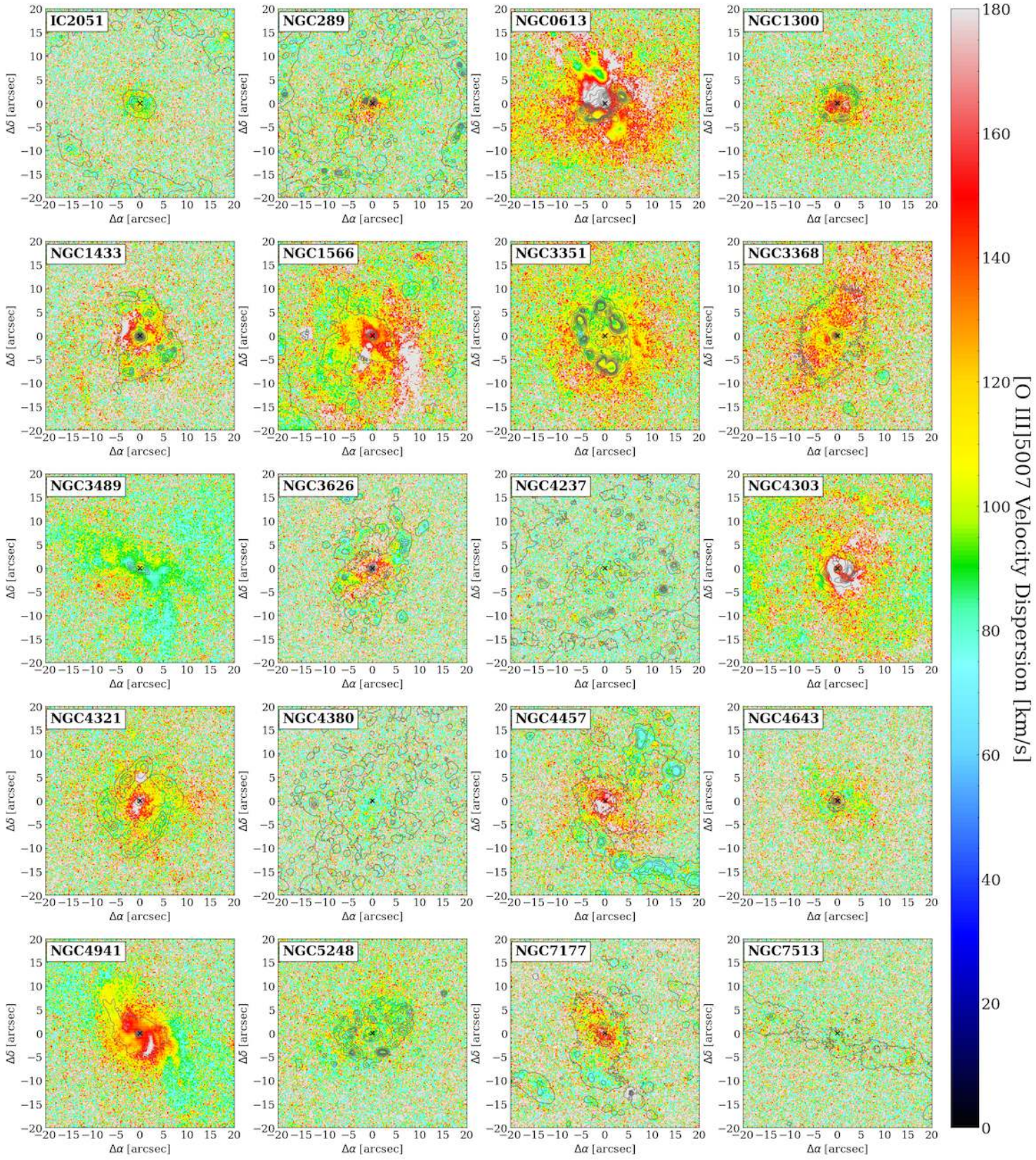


FIGURE 2.19: [O III]$\lambda$5007 velocity dispersion maps of galaxies studied in this thesis. Grey contours represent the H$\alpha$ flux. The centre of each galaxy is marked with an "x".

# Chapter III

# The methodology of searching for gas inflows on the example of NGC 1097

In this chapter, I introduce the methodology I developed using NGC 1097 in my pilot study, which I use to search for signatures of extended shocks driving gas inflows to the nucleus of galaxies. This methodology is presented in my published work Kolcu et al. (2023) and provides a new means of finding coherent kinematic structures in gas associated with extended shocks and inflows. This methodology is then applied to the remaining galaxies within the sample I studied in this thesis to assess the prevalence of extended shocks driving gas inflows to the nucleus of galaxies, as I present in Chapters 5 and 6.

## 3.1 Searching for coherent kinematic structures in deviations from circular motion

As I explained in Chapter 1 (Sect. 1.3), coherent structures in velocity maps are best traced when the rotational component of motion is removed from the data. It is most commonly done by subtracting the line-of-sight (LOS) velocity of a simple rotating disk from the observed LOS velocity. The result is displayed in a spatial map, which is called the ***residual velocity map***. Coherent structures in the residual velocity map will indicate large-scale motions of gas that depart from circular trajectories. In particular, shocks in gas result in velocity discontinuities, and extended shocks are expected to appear as coherent structures in the residual velocity map.

In Figure 3.1, I demonstrate what I define as coherent structures in a residual velocity map on the example of NGC 1097. In its upper panel, I present the LOS velocity of a representative thin flat rotating disk which I constructed using `Kinemetry` software (Krajnović et al., 2006), described in detail later in this section. The disk orientation parameters, position angle (PA) of the line of nodes (LON) of 137° and inclination ($i$) of 35°, are taken from the literature (Fathi et al., 2006). In the bottom panel of Fig. 3.1,

I present the constructed residual velocity map after subtracting the LOS velocity of the modelled disk from the observed H$\alpha$ velocity. The residual velocity map reveals two straight continuous structures, one with positive and one with negative residual velocities, which are roughly parallel to the LON and are offset from the LON to the top left and bottom right. Such large residual velocities appearing over continuous stretches in the velocity map are associated with bar-induced shocks in gas which cause velocity jumps. The shocked gas loses angular momentum and funnels from the outer regions of the galaxy towards the inner regions.

As shocks compress the gas, which is well mixed with dust, they also coincide with the loci of the dust lanes. Therefore the alignment of the kinematic structures with large residual velocities shown in Fig. 3.1 and the dust lanes shown in Figs. 2.2 and 3.7 signifies the presence of extended shocks that extend from the outer regions of the bar towards the inner regions. Although gas inflow in bar-induced shocks is efficient, in Fig. 3.1 it can be seen that the straight shocks weaken in the central regions. As a result, inflow slows down, and the density of the gas increases which can trigger SF and form stellar substructures like the nuclear rings (Shlosman et al., 1989; Athanassoula, 1992; Martini et al., 2003b; Kim et al., 2012); as I explained in Chapter 1, Sect. 1.1.1. This effect is seen in the central $\sim 8''$ of NGC 1097, where the stretches of large residual velocities are connecting to the nuclear ring (shown in Fig. 3.1).

As I emphasised in Chapter 1, although we have a good understanding of the bar-driven gas inflows to the central regions of galaxies, $\sim$1 kpc radius, we lack an understanding of the inflow to the innermost nuclear regions of galaxies, down to few tens of parsecs. In this thesis, I aim to identify the signatures of extended shocks, driving the inflow of gas from the nuclear ring towards the nucleus of the galaxy, by searching for coherent structures in the residual velocity maps. However, subtracting the LOS velocity of an incorrectly fitted disk from the observed velocity will obscure the real features (van der Kruit & Allen, 1978), as shown in the schematic diagram presented in Fig. 3.2. This figure shows the corresponding residual velocity field when the velocity field of the modelled disk is removed from the observed velocity. Different panels of the figure highlight distinct artificial patterns of harmonic term distortions when the disk is fitted with incorrect parameters. Amongst these panels, in my work, I mostly refer to the second and third diagrams of the middle panel, which show artefacts of incorrectly fitted PA of the LON and inclination.

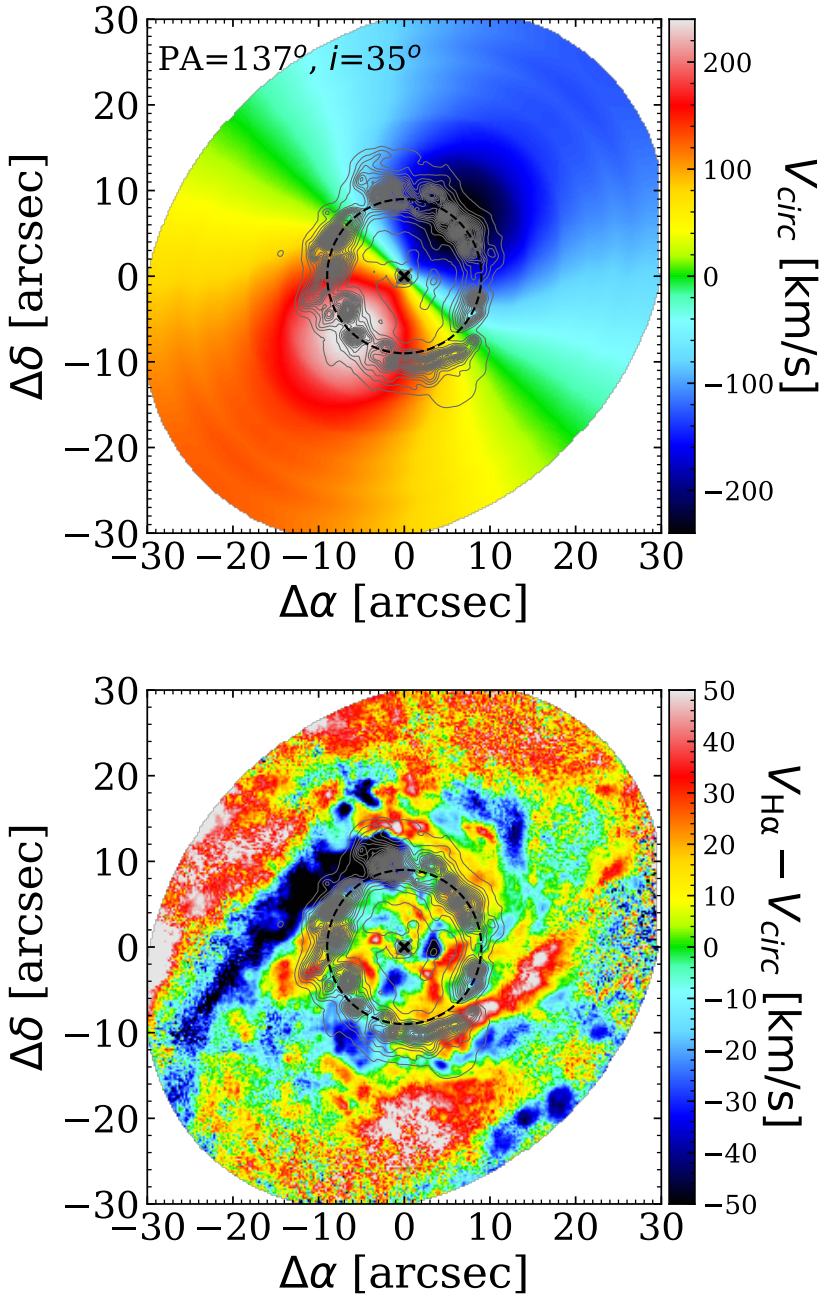


FIGURE 3.1: *top:* LOS velocity of the rotating disk with PA of the LON =137° and $i$=35° fitted to the observed H$\alpha$ velocity field of NGC 1097. *bottom:* Residual velocities after subtracting the LOS velocity of the modelled disk from the observed H$\alpha$ velocity of NGC 1097. Grey contours highlight the H$\alpha$ emission. The nuclear ring is represented by the black dashed circle. The centre of the galaxy is marked with a cross.

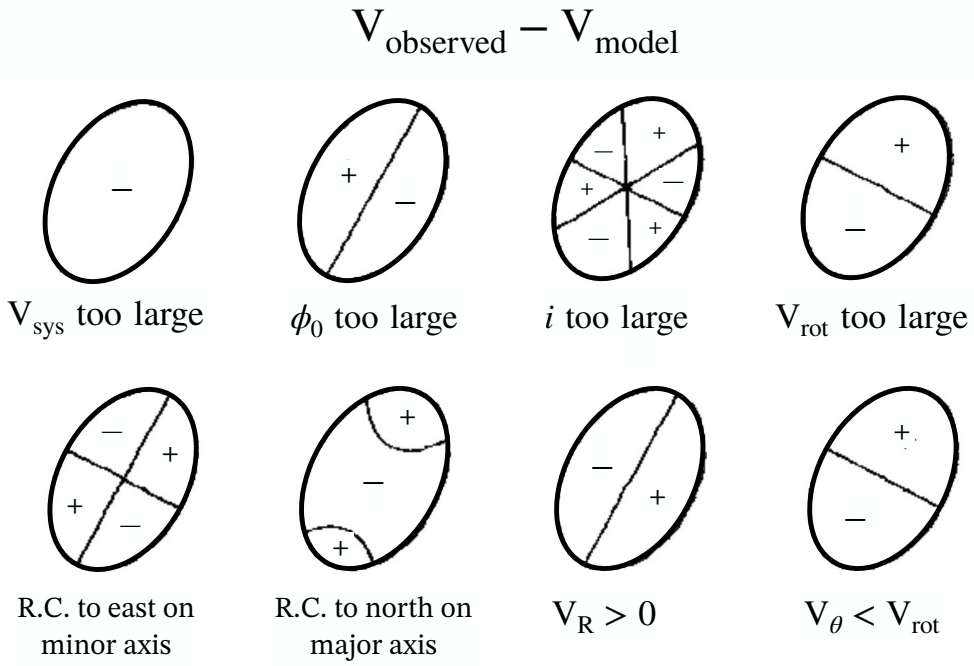


FIGURE 3.2: Artefacts in the residual velocity field when the wrongly fitted disk is removed from the observed velocity field. Figure is taken from van der Kruit & Allen, 1978 (Figure 1). I mostly refer to the second and the third panels, showing artefacts of incorrectly fitted PA of the LON and inclination.

Therefore, to ensure the signatures in the residual velocity map are real, one must construct the most accurate disk model. To do this, we must cautiously determine the galaxy centre and disk orientation parameters: PA of the LON and $i$. Below, I explain in detail the procedures of constructing a flat disk in circular motion.

For a flat thin disk in circular motion, the distribution of LOS velocities can be expressed by:

$$V(R, \psi) = V_{sys} + V_C(R)\ sin(i)\ cos(\psi) \tag{3.1}$$

where $V_{sys}$ and $V_C$ are the systemic and circular velocity respectively, $i$ and $\psi$ are the inclination of the disk and azimuthal angle measured counterclockwise from the LON in the galaxy plane, and $R$ is the radius of a circular ring in the galaxy plane. The inclination is directly related to the flattening parameter (or axial ratio) $q$ ($cos(i) = q$) of the disk projected on the sky, which is an ellipse with the major axis on the LON and ellipticity $\epsilon = 1 - q$.

To determine the orientation of the rotating disk model, I employed `Kinemetry`, which is a software specifically designed for IFU data and is a generalisation of surface photometry to higher-order moments of the LOSVD (Krajnović et al., 2006). `Kinemetry` performs harmonic expansion along best-fitting ellipses of the optimal major axis' PA, optimal ellipticity and centre using Fourier analysis. When applied to the velocity field, it produces the distribution of velocity along ellipses of semi-major axis $a$, K($a$,$\psi$), described by a finite number of harmonic terms:

$$K(a, \psi) = A_0(a) + \sum_{n=1}^{N} A_n(a) sin(n\psi) + B_n(a) cos(n\psi) \tag{3.2}$$

where $\psi$ is the eccentric anomaly, equivalent to that in Equation 3.1. To determine the best-fitting ellipse, the appropriate harmonic terms are minimised. Under the assumption of emission from a thin disk structure and fixed centre, `Kinemetry` reduces to the tilted-rings method, which breaks the disk into individual rings with different $i$, PA of the LON and rotational velocity (Rogstad et al., 1974).

Since I want to fit the rotating disk to the gas motions, I use the H$\alpha$ velocity field as the input for `Kinemetry`. To ensure the thin flat rotating disk is accurately fitted I performed three `Kinemetry` fits, starting from one with all orientation parameters allowed to vary and gradually fixing the global orientation parameters in the consecutive fits. In Figure 3.3, I summarise the estimated parameter distributions from each fit for NGC 1097. In determining the global values for the disk orientation parameters, I discard parameters estimated within the inner 2″ as the estimations within this radius are unreliable because

of the insufficient data that ellipses are being fitted to, and because of the impact of the AGN.

I first fitted the velocity field by allowing the orientation parameters of each ellipse, including the centre, to vary freely. I note that the radial increment of the fitted ellipses is set to $0\farcs2$ to represent MUSE's resolution. Since the PSF of the observations ranges from $0\farcs5$ to $1''$, it may blur finer kinematic features. This can lead to a systematic bias, causing the estimated orientation parameters to appear more uniform across different radii than they are. As shown in the top right panel of Fig. 3.3, in the regions inward from the nuclear ring, the horizontal ($\Delta\alpha$) and vertical coordinates ($\Delta\delta$) of the kinematic centre show only small variations ($\sim0\farcs7$ for $\Delta\alpha$ and $\sim0\farcs5$ for $\Delta\delta$) from the photometric centre. This indicates that in the regions inner to the nuclear ring, the estimated kinematic centre agrees with the photometric centre within $\sim$3 spaxels. Also, as shown in the middle right panel of Fig. 3.3, the $A_0$ values for ellipses fitted interior to the nuclear ring depart from the systemic velocity of the galaxy by less than $25\,\mathrm{kms}^{-1}$. Therefore, I reduced the number of free parameters within `Kinemetry` by fixing the centre of the galaxy to the coordinates of the photometric centre, and the $A_0$ to the velocity at the photometric centre ($-3.55\,\mathrm{kms}^{-1}$), and performed a second fit. In this second fit, I intended to estimate a representative PA of the LON and $i$ which can accurately describe the ellipses in nuclear regions, and I aimed to build my final circular disk model by fixing the PA of the LON and $i$ to these estimated representative values. However, as shown in the left panels of Fig. 3.3, regardless of keeping the centre free or fixed, in the regions inward from the nuclear ring, the distributions of the PA of the LON and $i$ strongly fluctuate within a radial region marked in yellow, which I refer to as ***the Dip***.

Within the Dip, the PA of the LON from the second fit varies between 125°–140°, and $q$ varies between 0.65–0.90, which translates to an $i$ range of $\sim$25°– 48°. While the impact of bar-induced noncircular motions can justify the fluctuation of these parameter values outside the nuclear ring, inward from the nuclear ring one would expect motion close to circular and therefore well fitted by single values for the PA of the LON and $i$. However, this expectation might be simplistic, as NGC 1097 is proposed to be hosting a nuclear bar (Shaw et al., 1993; Buta & Crocker, 1993) which would impact the gas flow in the regions inward from the nuclear ring.

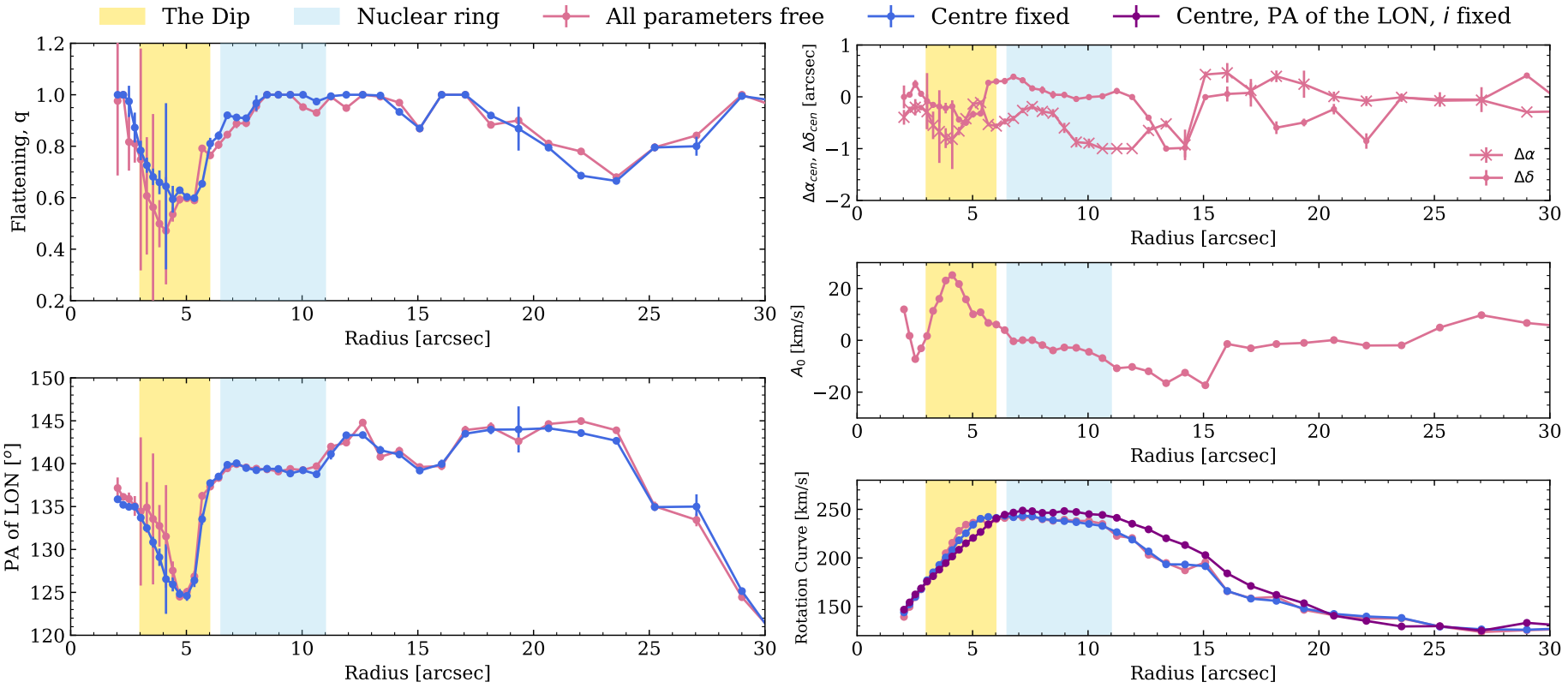


FIGURE 3.3: Radial distributions of parameters fitted to the H$\alpha$ velocity field of NGC 1097 with `Kinemetry`. The blue-shaded region represents the nuclear ring and the yellow-shaded region marks the radial range where PA of the LON and $i$ vary significantly (the Dip). Results from the run with all parameters in the `Kinemetry` fit allowed to vary freely are shown in pink, results for the centre and $A_0$ fixed are shown in blue, and results for the PA of the LON, $i$, centre and $A_0$ fixed are shown in purple. The left panels display the flattening, $q$ (top) and the PA of the LON (bottom). The right panels show the coordinates of the kinematic centre (top), the $A_0$ coefficient (middle) and the rotation curve (bottom).

As I indicated above, in the third `Kinemetry` fit I want to fix the PA of the LON and $i$ to fit a flat disk, but it is challenging to deduce reliable parameter values from such fluctuating distributions. Moreover, in Figure 3.1, which presents residual velocities for a thin disk fit with parameters taken from the literature (PA of the LON =137° and $i$=35°, Fathi et al., 2006), in the region inner to the nuclear ring I notice a periodic azimuthal variation resembling an $m = 3$ mode. My initial explanation for it was that $i$ used in the disk model was higher than the true value, which would give artefacts in the residuals in the form of $m = 3$ harmonic terms as shown in Fig. 3.2 (see also Franx et al., 1994 and Schoenmakers et al., 1997). Artefacts can be removed by choosing an $i$ value in the disk model that is closer to the actual $i$ of the galaxy, but variations in `Kinemetry` parameters are preventing us from settling on a reliable $i$.

Therefore, to find the $i$ value for which the residuals of the `Kinemetry` fits are free from the $m = 3$ azimuthal variations, I investigated the effect of changing the $i$ and PA of the LON on residual velocities by running `Kinemetry` first with a fixed PA of the LON at 137° and different $q$ (0.7, 0.9), and then with a fixed $q$ at 0.82 ($i \approx$35°) and different PA of the LON (125°, 140°). I constructed the corresponding residual velocity maps and examined the residuals, as I show in Fig. 3.4, to deduce which parameter set is best for the final disk model. When the disk is modelled with the PA of the LON 125° and $i$ 35°, I see the $m = 1$ harmonic terms in the residual velocity map as an effect of wrongly fitted PA of the LON, with one side of the map having mainly positive velocities and the other side having mainly negative velocities (van der Kruit & Allen, 1978). However, these artefacts can be largely eliminated by adopting the optimal PA of the LON. I also see $m = 3$ harmonic terms in all panels. They are strongest in the bottom right panel where I notice both positive and negative residual velocity regions extending radially from the centre beyond the nuclear ring. I must emphasise that no matter what inclination is used in the disk model, $m = 3$ azimuthal variation in the residual velocity is only minimised and not eliminated. The $i$ within the range of 25°– 35° minimises its amplitude, yet I do not see a clear minimum.

The range of acceptable parameter values agrees well with the parameters in the literature: the kinematic position angle, PA=135°, derived in Storchi-Bergmann et al. (1996) and Emsellem et al. (2001); inclination, $i$=34°, derived in Storchi-Bergmann et al. (2003) for the nuclear accretion disk, and $i$=35° derived in Fathi et al. (2006) from exponential thin disk model. Therefore I conclude that the disk parameters, PA=137° and $i$=35°, taken from Fathi et al. (2006) and applied in Fig. 3.1, are optimal. Although the parameters, PA=122° and $i$=48° adopted by Lang et al. (2020) differ from my optimal parameters, I show in Fig. 3.4 that each of these parameters would give artefacts in the residual velocity.

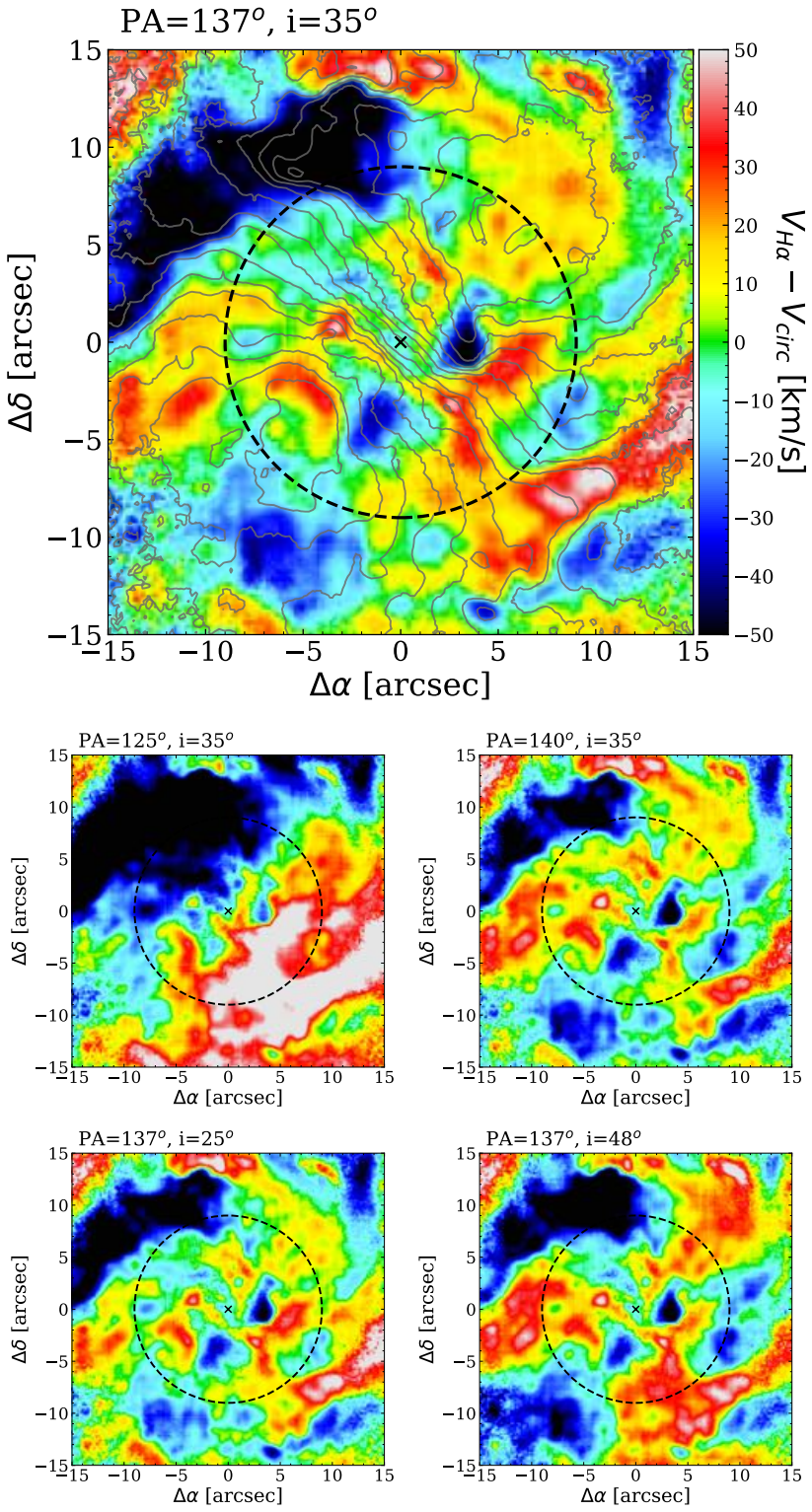


FIGURE 3.4: Residual velocity map of the inner 30″×30″ of NGC 1097. The dashed circle represents the nuclear ring. The centre of the galaxy is marked with a cross. In each panel, I subtract the LOS velocity of the disk modelled with a different combination of PA of the LON and $i$. *top:* PA=137° and $i$=35° ($q = 0.82$) as in Fig. 3.1. The grey contours represent the H$\alpha$ velocity field. *middle:* $i$ is fixed at 35° and PA of the LON is varied. *bottom:* PA of the LON is fixed at 137° and $i$ is varied.

Due to the smoother nature of the stellar velocity field compared to the gas velocity field, it is generally expected to obtain more continuous parameter distributions when fitting a disk to the stellar velocity field. However, the large velocity dispersion inward from the nuclear ring of NGC 1097 (see Fig. 2.5) reduces the LOS velocity values over an elliptical region inconsistent with a projected disk in an acceptable inclination range and therefore is likely to result in an incorrect fit, which I indeed observed when using `Kinemetry`. Therefore, parameters estimated by fitting the stellar velocity field would not be reliable inward from the nuclear ring. On the other hand, the PA of the LON and $i$ that I derive with `Kinemetry` for the stellar velocity field outside the nuclear ring is consistent with my adopted values, although the PA of the LON diverges at larger radii, likely because of the influence of the bar. Furthermore, disk orientation parameters cannot be reliably obtained from large-scale photometry due to the presence of companion and asymmetric spiral arms.

Since, even for the optimal parameters, a flat disk in circular motion does not provide a good fit to the data, because periodic azimuthal variations of residual velocities persist in those regions, I revisited the LOS velocity fields of each emission line group to check if there are any signs of these features directly in the observed velocity fields. In the top panel of Fig. 3.4, I superimpose H$\alpha$ velocity contours on the residual velocity map to show that in the regions inward from the nuclear ring, the H$\alpha$ velocity field shows wiggles at loci coinciding with two most prominent negative residual velocity regions that I interpreted above as part of the $m = 3$ harmonic terms. This indicates that the features which I initially interpreted as artefacts of the fit arise from real features present in the data. Hence, in Sect. 3.2, I focus on examining the physical processes in the regions inner to the nuclear ring, which may give rise to some of the kinematic structures observed in the velocity map.

## 3.2 Identifying the dominating ionisation mechanisms

To determine the dominating source of ionisation from optical emission lines, such as AGN or star-forming regions, one can use the Baldwin, Phillips & Terlevich (BPT) diagram (Baldwin et al., 1981). In the left panel of Fig. 3.5, I show the BPT diagram for the inner $30'' \times 30''$ region of NGC 1097. Each point on the diagram corresponds to a spaxel in the data, with its position determined by the fluxes measured for that spaxel. I mask spaxels with poor flux measurements by applying an amplitude-over-noise (AON) ratio (Sarzi et al., 2006) threshold of 7, which excludes spaxels with AON$\leq$7 from the BPT diagram, choosing a smaller threshold would give noisy results already occurring outside the nuclear ring in Fig. 3.5. This allows us to focus on the emission that is

coming from the nuclear ring and the region inner to it. To distinguish AGN from star-forming regions, I used the Kewley et al., 2001 (hereafter Kewley+01) relation which indicates what line ratios can be produced by stellar photoionization, as points above the Kewley+01 line likely originate from the AGN activity or shocks. However, the Kewley+01 relation does not take into account the composite emission which has a contribution from SF, hot old low-mass stars and AGN. Therefore, to include the composite emission, I used the modified Kewley+01 line from Kauffmann et al., 2003 (hereafter Kauffmann+03) so that the region between Kauffmann+03 and Kewley+01 lines is the location of the composite sources, and points below the Kauffmann+03 line indicate emission purely coming from SF. I also separated the AGN region into two classes, LINER and Seyfert region, based on the relation given by Cid Fernandes et al. (2011).

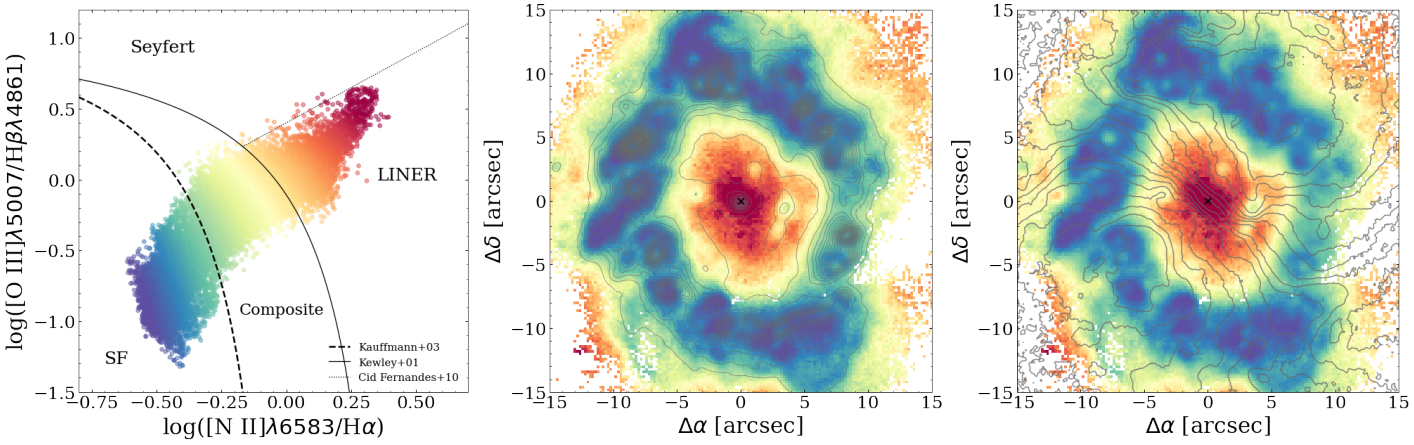


FIGURE 3.5: *left:* The BPT diagram of the inner 30″×30″ region. The SNR=10 and AON=7 thresholds are applied. Each point represents one spaxel. Dashed, solid and dotted lines represent the Kauffmann et al. (2003), Kewley et al. (2001) and Cid Fernandes et al. (2011) fits respectively which establish the dominating ionisation mechanisms. The colour coding is based on the distance from the Kewley et al. (2001) line. *middle & right:* BPT maps of the inner 30″×30″, with colour coding of the spaxels taken from the left panel. Contours represent H$\alpha$ flux (middle) and LOS H$\alpha$ velocity (right).

Each point in the BPT diagram represents a spaxel and is colour coded according to its distance from the Kewley+01 line. This colour coding is then used in the spatial map to highlight which sources of ionisation dominate in what regions (Fig. 3.5 central and right panels). I call this diagnostic map ***the BPT map***. I also included H$\alpha$ flux and velocity contours on the BPT maps to combine the BPT diagram results with kinematics and light distribution.

In the nuclear ring, the emission is strongly dominated by SF, while the regions inward from the nuclear ring predominantly show LINER emission. However, three locations in the regions inward from the nuclear ring (∼5″ east and west and ∼2″ northwest from the

centre) show composite emission due to contribution from SF and have high H$\alpha$ flux (see also Fig. 2.6). The region of composite emission to the west has the highest contribution from SF (is closest to the Kaufmann+03 line in the BPT diagram) and it appears to be part of a structure with elevated SF that extends from the nuclear ring directly north of it towards a smaller region of the composite emission to the south. The H$\alpha$ velocity field throughout the extent of this structure is strongly disturbed (Fig. 3.5, right panel), which can be caused by stellar outflows associated with elevated SF. Moreover, this structure also coincides with the strong negative velocity residual (Fig. 3.4), suggesting that the negative velocity residuals, which I initially interpreted as artefacts caused by adopting the wrong inclination of the fitted disk, arise from real features present in the data. The region of composite emission to the east shows a weaker SF component than the region to the west. This region is also associated with a disturbed H$\alpha$ velocity field, and unlike the region to the west which is extended tangentially in the north-south direction, it is curved towards the nucleus of the galaxy. Lastly, the region of the composite emission to the northwest has the weakest contribution from SF, and the H$\alpha$ velocity field in that region is only mildly disturbed. Compared to the other two regions, this region appears to be more isolated yet it still clearly shows in the velocity residuals in Fig. 3.4.

## 3.3 Searching for coherent kinematic differences between distinct emission line groups

I showed in Sect. 3.1 that velocity residuals after subtracting a flat disk in circular motion do not provide conclusive information about coherent kinematic structures inner to the nuclear ring of NGC 1097. Here, I explore what kinematic information can be extracted from the data without relying on kinematic or mass models. In Fig. 3.6, I compare the LOSVD moments of the Balmer and low ionisation lines by constructing the maps of [N II]$\lambda$6583/H$\alpha$ line flux ratio (left panel), velocity difference (middle panel) and velocity dispersion ratio (right panel).

[N II]$\lambda$6583 emission, with higher ionisation potential, may predominantly originate from post-shock gas, while H$\alpha$ emission, mostly generated by stellar photoionization, is less affected by the shock. Therefore, in the regions where shocks are present, the observed [N II]$\lambda$6583/H$\alpha$ line flux ratios should be elevated. As shown in the left panel of Fig. 3.6, in NGC 1097 [N II]$\lambda$6583/H$\alpha$ is the lowest in the nuclear ring where SF dominates the emission, and it is the highest in the nucleus where the AGN dominates. There are no other regions inward from the nuclear ring with elevated [N II]$\lambda$6583 emission. Instead, I notice regions of elevated H$\alpha$ flux associated with enhanced SF (see Sect. 3.2), which might be obscuring the possible enhancement in [N II]$\lambda$6583 in the same region if SF is

triggered by shocks. Nevertheless, if [N II]$\lambda$6583 around shocks originate mostly from the post-shock gas, extended shocks can manifest themselves by velocity differences between [N II]$\lambda$6583 and H$\alpha$ that are coherent over large distances, as explained below. The velocity of each tracer evaluated in a spaxel is the first moment of the LOSVD arising from integrating the emission along the LOS and over the spaxel area. If this includes regions of gas with different physical conditions which move with respect to each other, the integrated LOSVD recorded in a spaxel should vary between the tracers, as relative contributions to line emission from regions with different physical conditions differ between emission lines. Consequently, the value of its first moment may differ for each tracer.

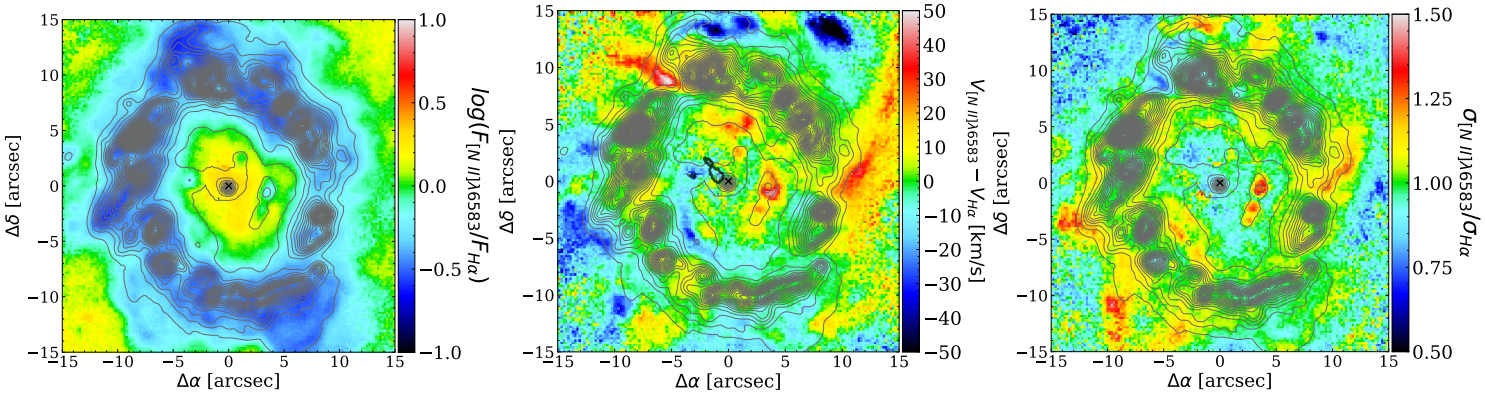


FIGURE 3.6: Comparison maps for H$\alpha$ and [N II]$\lambda$6583 emission and kinematics in NGC 1097. *left:* Line flux ratio of [N II]$\lambda$6583 and H$\alpha$. *middle:* The velocity difference map, which is constructed by subtracting the LOS velocity of H$\alpha$ from the LOS velocity of [N II]$\lambda$6583. The black contour marks the region where the velocity difference between [N II]$\lambda$6583 and H$\alpha$ was more than 30 kms$^{-1}$ for single Gaussian fits. *right:* Velocity dispersion ratio of [N II]$\lambda$6583 and H$\alpha$. In all panels, grey contours highlight the H$\alpha$ emission.

A good example of two neighbouring gas regions that differ in physical conditions and move with respect to one another are regions upstream and downstream from a shock in gas. Commonly temperature and pressure are higher in the post-shock gas than in gas upstream from the shock, and jump conditions in the shock impose a velocity difference between these two regions. Hence, for a spaxel which records emission from pre-shock and post-shock regions, the derived [N II]$\lambda$6583 and H$\alpha$ velocities will differ, as the former will be more representative of the post-shock region. Then, if extended shocks are present, they will appear as continuous structures in ***the velocity difference map***, in which the velocity difference takes consistently positive (or negative) values. In the velocity difference map shown in the middle panel of Fig. 3.6, I notice a coherent blue feature of negative velocity difference spiralling out from the nucleus towards the southeast side of the nuclear ring of NGC 1097, hereafter called the *blue spiral arm*. If it is a signature of shock in gas, it may be a spiral shock (Maciejewski, 2004b) extending inwards from the large-scale straight shocks in the bar of NGC 1097 (Fathi et al., 2006).

The largest velocity difference in the blue spiral occurs at the location where the blue spiral curves towards the nucleus and is cospatial with the H$\alpha$ enhancement to the east and with enhanced SF (see Fig. 3.5). This may indicate that the enhanced SF is associated with the inner part of the spiral shock.

Furthermore, shock conditions give rise to random motions, which increase the velocity dispersion of [N II]$\lambda$6583 in the post-shock regions. This can possibly be seen in the southeast region of the blue spiral arm, where the velocity dispersion of [N II]$\lambda$6583 is higher than H$\alpha$, their ratio is $\sim$1.25, but in the region where the blue spiral curves towards the nucleus, the velocity dispersion of [N II]$\lambda$6583 is only slightly higher, their ratio is $\sim$1. In the region $\sim5''$ west from the nucleus I notice the largest velocity dispersion ratio, which is cospatial with the largest velocity differences to the west, and the decreased [N II]$\lambda$6583/H$\alpha$ line flux ratios in the same region, as well as the enhanced SF (Sect. 3.2), but this feature is less spatially coherent than the blue spiral arm.

Although the observed velocity differences between emission lines could result from obscuration, H$\alpha$ and [N II]$\lambda$6583 emission wavelengths differ only by 20Å, so differential extinction is negligible. While incorrect line fitting can also cause the difference in the derived velocities between tracers, I minimise that possibility by addressing the non-Gaussianity of the emission lines by including the secondary component of [N II]$\lambda$6583 line in spaxels where the excess emission was present, as I explain in Sect. 2.3.3. In fact, fitting emission lines with single Gaussian components resulted in the largest velocity difference between H$\alpha$ and [N II]$\lambda$6583 in spaxels where the excess in the spectra was present. In the middle panel of Figure 3.6, I mark with a black contour the region where the velocity difference ranged from $-30$ to $-50$ kms$^{-1}$ for single Gaussian fits. Including the secondary component reduced this difference to $\sim$10 kms$^{-1}$. The spectra throughout the blue spiral arm, which is outside the contour region, are well-fitted with single Gaussians, which indicates that the velocity difference between emission lines in those regions is not caused by the incorrect fitting.

## 3.4 Studying the dust morphology in structure maps

As I previously explained in Sect 1.2, the shocks compress the gas that is mixed with dust, consequently, the extended shocks coincide with the location of the dust lanes. Thus, the alignment of the coherent kinematic structures with large residual velocities and the dust lanes signifies the presence of extended shocks that stretch from the outer regions of the bar towards the inner regions. This alignment is evident in the residual velocity map and the composite image of NGC 1097, as shown in Figs. 3.1 and 2.2 respectively.

Therefore, while studying the kinematic signatures of the extended shocks, it is important to consider the morphology of the dust to reinforce our arguments on the presence of extended shocks. However, it is important to note that, dust morphology alone is not sufficient to build a definitive argument for the presence of extended shocks. This is because the coherent morphology of dust structures can also arise from the differential rotation, unrelated to extended gas shocks.

To study the morphology of dust structures, I constructed ***the structure maps***, created using a series of image processing techniques applied to MUSE images. Initially, I created red MUSE images by isolating emissions from redder wavelengths (∼7800–9350Å). I then applied a Gaussian blur technique to the red images. This step is crucial as it reduces noise and smoothens the details in the images, enhancing the signal-to-noise ratio for subsequent analysis. For each galaxy, I altered the width of the Gaussian to emphasise dust structures within the innermost regions. While this application made inner dust structures clearer, it also weakened the visibility of dust lanes along the bars of galaxies, which ideally require a wider Gaussian for a better fit. Subsequently, I applied the unsharp masking technique, which involves subtracting the blurred version of the image from the original, to accentuate the edges and fine details of the dust structures.

In Fig. 3.7, I present the structure map of NGC 1097. As shown in the figure, the nuclear ring is revealed within the inner ∼10″. Inwards from the ring, there are several faint dust spirals extending mostly from the south and the north towards the nucleus. External to the ring, a prominent dust lane along the bar is seen extending from the northwest towards the centre, connecting to the nuclear ring at the west. There is a counterpart dust lane to the southeast but is considerably weaker than the dust lane to the northwest.

Although this unsharp masking approach and Fig. 3.7 were not included in my pilot study Kolcu et al. (2023), I followed the same concept of examining the dust structures inwards from the nuclear ring using a NIR J-band image from Prieto et al. (2005), which I detail in Sect. 4.2. While for NGC 1097 I relied on NACO observations and the study

of dust structures from Prieto et al. (2005), such observations were not available for other galaxies I studied. Therefore, to study dust structures in the remaining galaxies I used MUSE observations. The structure map of each galaxy I studied is presented in their respective sections in Chapter 6 (first row, third column) also in Appendix B (first column of Fig. B.1). These maps are presented alongside other diagnostic maps. This arrangement allows the reader to identify common structures from different approaches and facilitates following of the discussion.

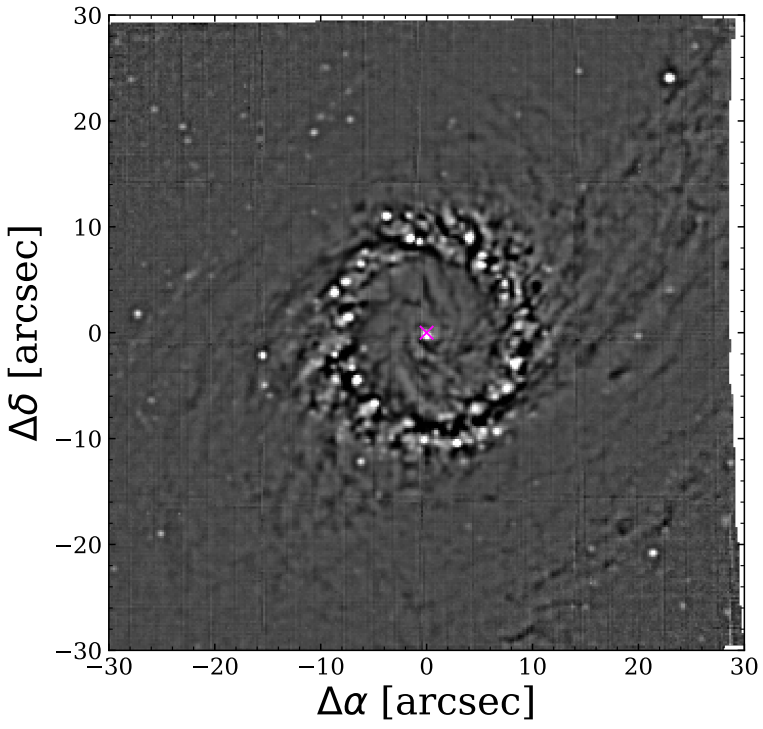


FIGURE 3.7: Structure map of NGC 1097. The centre of the galaxy is marked with an "X".

# Chapter IV

# Findings within the nuclear region of NGC 1097

In this chapter, I provide a detailed discussion of my findings for NGC 1097 after applying the methodology that I developed in Chapter 3 in the pilot study using this galaxy. This chapter is based on my published work Kolcu et al. (2023).

## 4.1 Elliptical flow pattern in regions inward from the nuclear ring

I based my studies of residual velocities (Sect. 3.1) on the assumption that inward from the nuclear ring the flow of unperturbed gas is circular. However, in Chapter 3 (Sect. 3.1), I showed that in this region `Kinemetry` cannot accurately constrain the parameters of the unperturbed circular motion in a thin flat disk. The possible reason for this is that the unperturbed flow is either not flat or not circular there. In order to obtain meaningful residuals, one needs to first correctly identify the underlying flow.

If the flow is intrinsically circular, the PA of the LON and PA of the zero velocity line are perpendicular, but this is not the case if the global flow is intrinsically not circular (e.g. elliptical; see the appendix of Mazzalay et al., 2014). Here, I test whether in the regions inward from the nuclear ring the underlying flow is intrinsically noncircular, by determining the angle between the LON and the zero velocity line, where the distribution of the PA of the LON is inferred from `Kinemetry`.

In order to derive the distribution of the PA of the zero velocity line, for each column of spaxels in the velocity field (corresponding to constant Right Ascension), I identified the spaxel with the velocity closest to the systemic velocity of the galaxy. I then connected these spaxels to produce the fit of the zero velocity line. Further, I determined the PA of each spaxel on the zero velocity line which gives us the distribution of the PA of the zero velocity line with radius. I applied these steps on both stellar and H$\alpha$ velocity fields. I expect that the angle between the LON and the zero velocity line will be less affected

by non-circular motion for stars than for gas because high velocity dispersion in stars hides the underlying non-circularity.

In the left panels of Fig. 4.1, I show the H$\alpha$ and stellar LOS velocity maps and the corresponding zero velocity line fitted on each map. In the right panel, I present the individual distributions of the PA of the LON and the PA of the zero velocity line for both velocity fields. In the figure, I show the PA of the zero velocity line values after subtracting 90°, which should be equal to the PA of the LON for circular motion. The distributions of the PA of the LON and PA of the zero velocity line for stars roughly align with each other over the whole radial range, differing slightly inside the Dip (introduced in Sect. 3.1) by at most ∼5°. The values of the PA of the LON and PA of the zero velocity line for H$\alpha$ velocity field roughly converge in the nuclear ring, but within the Dip, the two differ by ∼15°–20°. This implies that in the regions inward from the nuclear ring, the underlying orbits of the gas flow are intrinsically noncircular, which prevents `Kinemetry` from accurately constraining the disk orientation.

Thus, assuming an intrinsically circular flow of gas may compromise the search for coherent kinematic structures in the velocity residuals, and an oval or elliptical flow can be a better representation of the gas flow. Such assumption of an oval flow is allowed by the `DiskFit` software (Spekkens & Sellwood, 2007), which is specifically developed for bar-like and oval distortions and allows fitting non-axisymmetric flow patterns to two-dimensional velocity fields. Although exploring this approach is plausible, it is outside the scope of this work.

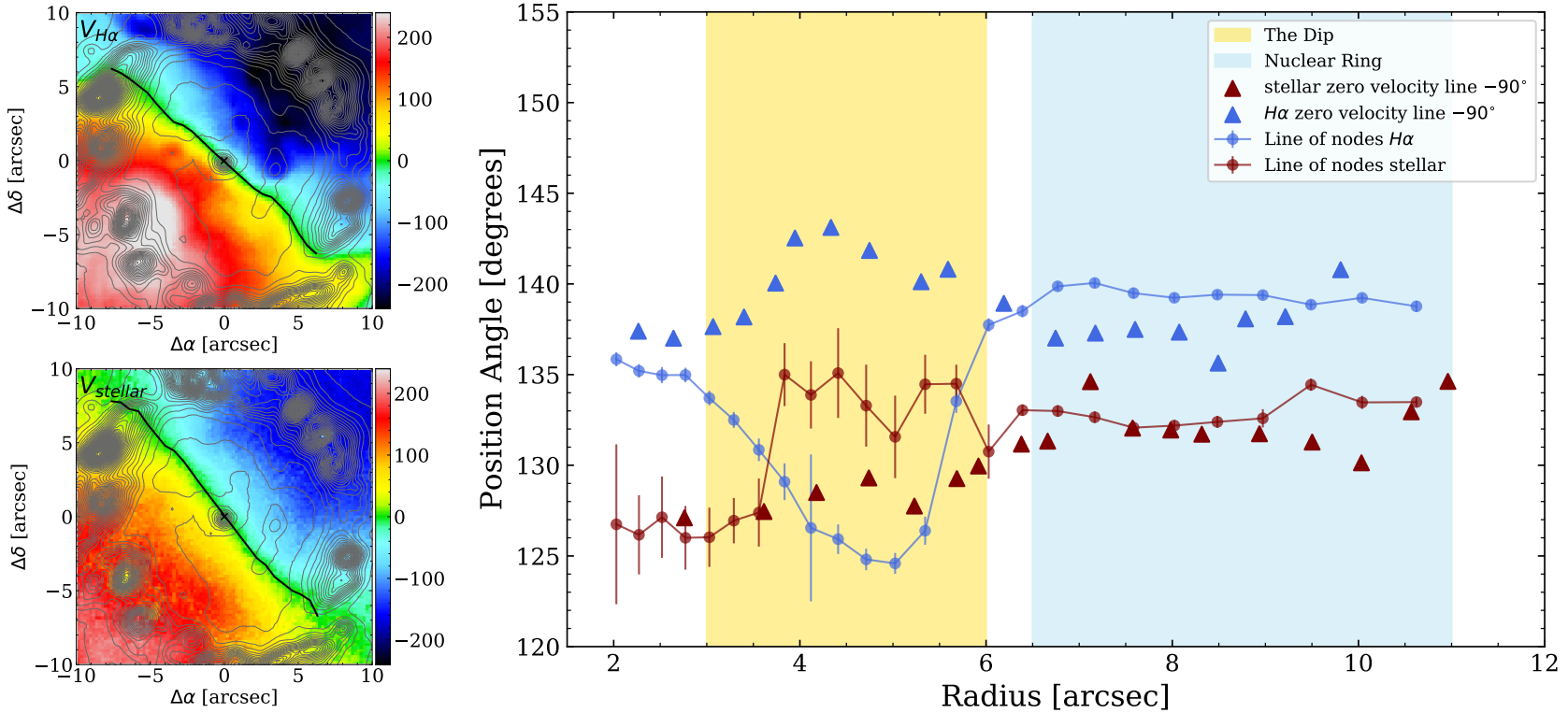


FIGURE 4.1: *left:* Hα (top) and stellar (bottom) LOS velocity maps. The black line represents the corresponding zero velocity line fit. Grey contours represent the Hα emission. The centre of the galaxy is marked with a cross. *right:* Distributions of the PA of the LON obtained from `Kinemetry` and PA of the zero velocity line. For the stars, the distribution of the PA of the LON is plotted in small red circles and the PA of the zero velocity line in red triangles. For gas, the PA of the LON is plotted in small blue circles and the PA of the zero velocity line in blue triangles. The blue-shaded region represents the nuclear ring, and the yellow-shaded region represents the Dip defined in Sect. 3.1.

## 4.2 Evidence from the MUSE data for nuclear spiral shocks

Studying the near-infrared images from the adaptive optics assisted NACO camera/spectrograph of the VLT, Prieto et al. (2005) found dust extinction in the form of a complex three-arm filamentary structure in the regions inner to the nuclear ring. The spiral arms of this structure are reaching to the centre from the north, south and west. Moreover, in good agreement with Prieto et al. (2005), a similar three-arm network is observed in the images from the Advanced Camera for Surveys (ACS) of the HST (Fathi et al., 2006). Hereafter I call this structure the *nuclear dust filaments*. In Figure 4.2, I show the NACO image of Prieto et al. (2005). Inside the oval area, the image displays the residuals after subtracting the light profile of a simple ellipse model. In the figure, I include a dashed line to represent the proposed nuclear bar of the galaxy (Shaw et al., 1993; Buta & Crocker, 1993), with a major axis PA of 28° (Quillen et al., 1995). I notice that the northern and southern arms of the nuclear dust filaments are roughly parallel to this nuclear bar, which is consistent with the expected geometry of dust lanes in a bar when the dust lanes are associated with gas inflow in shocks. The arm to the west of the nucleus is not readily associated with the nuclear bar.

In Figure 4.2, in blue contours, I outline the blue spiral arm extending from the inner southeast part of the nuclear ring towards the nucleus which is revealed in the velocity difference map (Fig. 3.6, middle panel). The region of the blue spiral where it curves towards the nucleus is cospatial with the region of the composite emission directly to the east of the nucleus, which is associated with enhanced SF, and with the disturbed H$\alpha$ velocity field (Fig. 3.5). If the velocity difference is caused by the shock, as I argued in Sect. 3.3, then the blue spiral arm can be a nuclear spiral shock in which gas inflow to the nucleus occurs. For bisymmetric mass distribution, such shock should have a symmetric red component on the other side of the nucleus (Canzian, 1993; Schoenmakers et al., 1997) in the velocity difference map. In Fig. 3.6, middle panel, I notice a red structure at $\sim$5″ west of the nucleus extending from the nuclear ring towards the south, outlined in pink in Fig. 4.2. This structure is not curved towards the nucleus and does not have as defined spiral continuity as the blue spiral arm, but it has the highest velocity differences, it is cospatial with the region of the composite emission to the west, which has the highest contribution from SF, and it coincides with the strongest distortions of the H$\alpha$ velocity field. Hereafter, I call this structure the *red spiral arm*. I hypothesise that in the red spiral arm the gas density is higher compared to the region to the east, which leads to higher SF there, whose consequences, particularly outflows, dominate the shock signature there, while the SF is less dominant in the blue spiral.

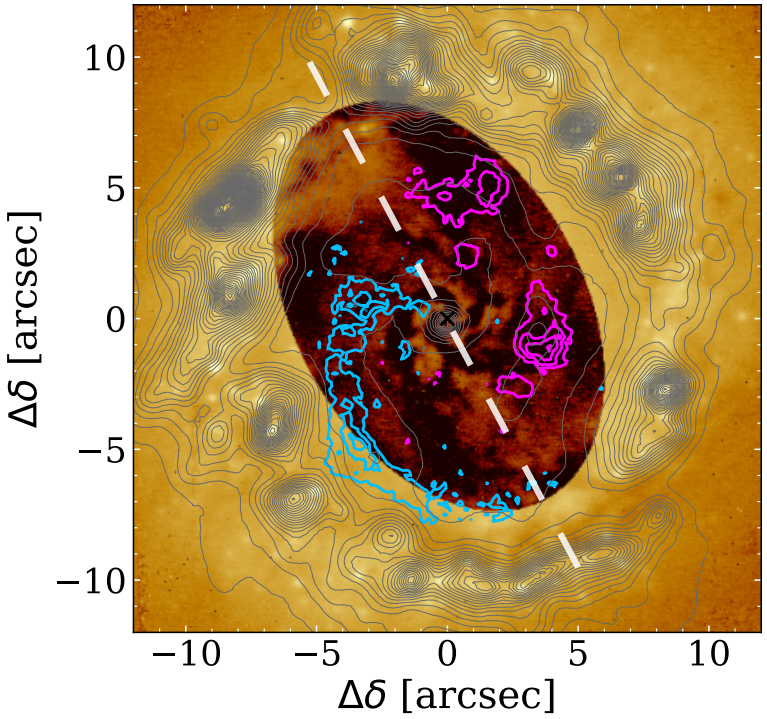


FIGURE 4.2: NACO J-band image from Prieto et al. (2005) with the light profile of a simple ellipse model subtracted inside the oval. The white dashed line represents the proposed nuclear bar with PA=28° and length ≈ 20″ (Quillen et al., 1995). Blue and pink contours represent the blue and red spiral arms in the velocity difference map (Fig. 3.6). Grey contours represent the Hα emission.

The blue and red spiral arms are shifted ∼2–3″ downstream from the northern and southern arms of the nuclear dust filaments. Hence, the combination of the structures observed in kinematics and morphology might be the imprint of the gas flowing to the nucleus under forcing from the nuclear bar. However, it is unclear whether the kinematic arms are directly associated with the dust filaments.

Hydrodynamical and kinematic modelling (Davies et al., 2009; Fathi et al., 2013) support a net molecular gas inflow to the nucleus, channelled via the arms of the nuclear dust filaments of Prieto et al. (2005). Using data from the Gemini Multi-Object Spectrograph (GMOS) on Gemini South Telescope, Fathi et al. (2006) studied the [N II]λ6583 kinematics within the inner 15″×7″ region of NGC 1097, and revealed a three-arm spiral network in residual velocities centred on the galaxy nucleus with velocity amplitudes reaching ∼20% of the rotational velocity, consistent with the nuclear spiral models of Maciejewski (2004b). Moreover, Davies et al. (2009) studied the $H_2$ kinematics within the inner 4″×4″ region and could resolve a two-arm kinematic spiral structure in their residual velocities. Benefiting from the large FoV of MUSE, I can trace these observed kinematic structures in my residual velocity map beyond their spatial coverage. I do not find any correlation between the structures found in the residual velocities by Davies et al. (2009) and my results, but the FoV of SINFONI is much smaller than the region

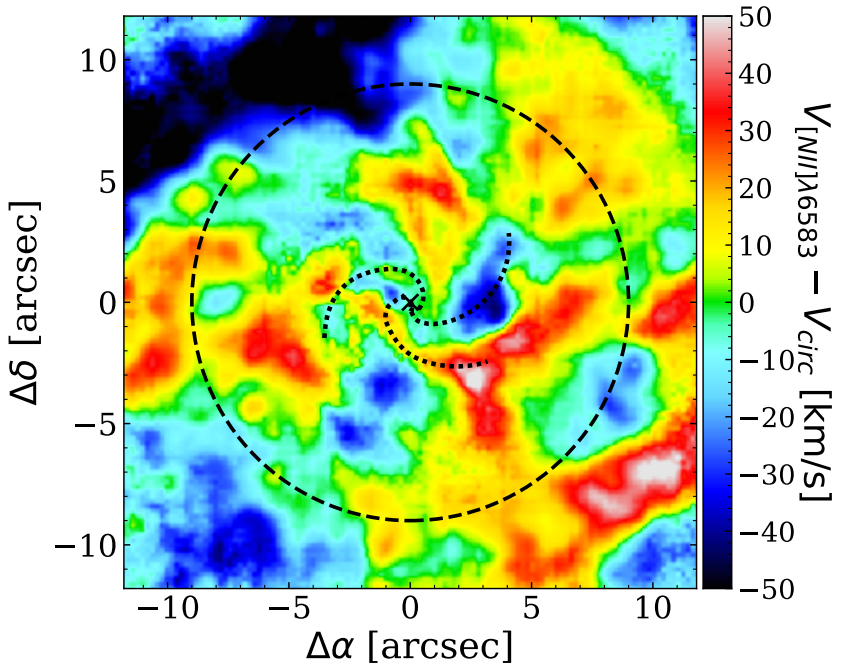


FIGURE 4.3: Residual velocities after subtracting the LOS velocity of the disk model from the observed [N II]$\lambda$6583 velocity field. The black dotted lines represent the kinematic spiral network of Fathi et al. (2006). The black dashed circle represents the nuclear ring. The centre of the galaxy is marked with a cross.

to which I fitted the disk – Note that the SINFONI data have higher spatial resolution than the MUSE data, which might possibly make it harder to find a match as well.

Since Fathi et al. (2006) used [N II]$\lambda$6583 data in their analysis, to compare my findings, I fitted my disk model with fixed PA of the LON=137° and $i$=35° (see Sect. 3.1) to [N II]$\lambda$6583 velocity field. The resulting residual velocity map is presented in Fig. 4.3, which also includes the proposed three-arm kinematic spiral of Fathi et al. (2006). I do not find a coherent spiral network extending from the galaxy nucleus towards the outer radii. Arguably, the proposed arm of the kinematic spiral to the south appears connected with a coherent structure in my residual velocity map, which might be extending from the nuclear ring towards the nuclear regions, but instead of curving towards the nucleus, it continues to the northeast. As already seen in Fathi et al. (2006) this arm runs along the arm of the nuclear dust filaments to the west. Hence, although in the region inward from the nuclear ring a three-arm spiral network is present in morphology (Prieto et al., 2005; Fathi et al., 2006), I do not find evidence of a spiral network in the residual velocities of the ionised gas. As I explained in Sects. 3.1, 3.2 and 4.1, the data inward from the nuclear ring do not allow an accurate fit of a flat disk in circular motion, therefore residual velocities have to be interpreted with caution. On the other hand, in this work, I find indications of nuclear spiral shocks in velocity difference maps.

## 4.3 Multi-phase AGN outflows in the nuclear regions

As confirmed by a number of studies, the gas funnelling into the nucleus of NGC 1097 feeds its LINER core (Davies et al., 2009; van de Ven & Fathi, 2010; Fathi et al., 2013; Izumi et al., 2013; Martín et al., 2015; Izumi et al., 2017; Prieto et al., 2019). Some of those studies also attempt to compute the mass inflow rate ($\dot{M}$) from the nuclear ring of the galaxy into its central black hole. For example, van de Ven & Fathi (2010) estimated the ionised $\dot{M}$ at $\sim$70 pc from the galaxy nucleus as $\sim$0.011 $M_{\odot}yr^{-1}$, Fathi et al. (2013) estimated a net $\dot{M}$ as $\sim$0.2 $M_{\odot}yr^{-1}$ at $\sim$40 pc and $\sim$0.6 $M_{\odot}yr^{-1}$ at $\sim$100 pc from the galaxy nucleus by using combined molecular and ionised gas observations, and Davies et al. (2009) estimated a net $\dot{M}$ of 0.06 $M_{\odot}yr^{-1}$ to the central few tens of parsecs regions. Magnetic fields in the region inner to the nuclear ring that can affect gas inflow rates have been observed (Lopez-Rodriguez et al., 2021; Hu et al., 2022).

It is known that the inflow of gas into the central black hole can feed the AGN and trigger powerful outflows (García-Burillo et al., 2005; Davies et al., 2014). Even though this phenomenon is more commonly seen in Seyfert nuclei (García-Burillo et al., 2014; Alonso-Herrero et al., 2019; Audibert et al., 2020), outflows can still be powered in less luminous cores (Nemmen et al., 2006; Santoro et al., 2020), as supported by recent multi-wavelength studies of nearby LINER galaxies (Márquez et al., 2017; Hermosa Muñoz et al., 2022a). In this section, I discuss the imprint of ionised gas outflows in the nucleus of NGC 1097, which may be triggered due to the inflow of gas into the central black hole.

As I heavily discussed in Chapter 2 (Sect. 2.3.3), I noticed a high velocity dispersion region extending from the centre of the galaxy towards $\sim$3″ northeast (see Fig. 2.6). One reason for the high velocity dispersion values is the excess to the blue wing of [N II]$\lambda$6583 line, which is affecting the line profiles and the Gaussian fits (see Fig. 2.7). However, even after modelling the excess as a separate secondary emission component, the velocity dispersion of the main component remained high (see Fig. 2.8). Contribution from the secondary component to the total [N II]$\lambda$6583 flux appears to increase with radius and its velocity is high and blueshifted compared to the main [N II]$\lambda$6583 line (Fig. 2.9).

X-ray/Chandra observations adopted by Prieto et al. (2019), highlight the X-ray-rich nucleus of the galaxy along with the energetic extension blasting from the nucleus towards the northeast, northwest and southwest. The northeast X-ray extent coincides with the high velocity dispersion region. A similar correlation between ionised H$\alpha$ emission and soft X-ray observations has been reported by previous studies on nearby LINER galaxies (Márquez et al., 2017; Hermosa Muñoz et al., 2022a). Moreover, the high velocity

dispersion of various molecular gas tracers is also observed in the regions inward from the nuclear ring (Izumi et al., 2017; Leroy et al., 2021b).

I hypothesise that the strong disturbances in the kinematics of the multiple gas phases and ionised gas disturbances coinciding with the loci of X-ray emission imply the presence of AGN outflows, triggered by the gas inflows into the black hole. In particular, emission from the secondary component could be coming from the jet-like outflow, whose interaction with the disk increases the velocity dispersion in the latter.

## 4.4 Conclusions on the signatures of extended shocks to the nucleus of NGC1097

The map of velocity difference between [N II]$\lambda$6583 and H$\alpha$ constructed for the central kiloparsec of NGC 1097 reveals a coherent structure in the form of a spiral, extending from the inner southeast part of the nuclear ring to the north and curving towards the nucleus (the "blue spiral arm"), whose southeastern region shows higher velocity dispersion of [N II]$\lambda$6583 compared to H$\alpha$. I associate the coherent velocity difference in this structure with shock conditions and argue for the blue spiral arm being a large-scale shock in the gas. In the velocity difference map, the blue spiral arm appears to have a symmetric companion on the other side of the nucleus (the "red spiral arm"). Although less coherent than the blue spiral arm, it coincides with the region of high SF and strongly disturbed H$\alpha$ velocity field, which indicates that if the red spiral arm is also a shock in gas, it is strongly affected by SF activity.

The bisymmetric geometry of the blue and red spiral arms is consistent with predictions from nuclear spiral models. The kinematic arms that I found in NGC 1097 run along the southern and northern spiral arms of the nuclear dust filaments, located $\sim$3$''$ downstream from them. Together, they appear aligned well with the nuclear bar, which suggests that the nuclear bar can play a role in gas inflow in the centre of NGC 1097.

# Chapter V

# Individual analysis of the sample galaxies

In this chapter, I present my findings from analysing each galaxy individually within the sample studied in this thesis. For each galaxy, I included a series of large-scale composite images and kinematic maps for the three emission line groups used in my analysis. Additionally, I provide the outputs of my methodology, which include structure maps, residual velocity maps, velocity difference maps, BPT maps, and BPT diagrams.

The orientation parameters used in the disk model of each galaxy, obtained from `Kinemetry` and from large-scale studies, are presented in Table C.1 in Appendix C.

## 5.1 IC2051

In Fig. 5.1, I present a collection of diagnostic maps for IC 2051. As shown in the large-scale and composite image within the MUSE FOV, presented in the first row (first and second panels) of Fig. 5.1, IC 2051 has a luminous core, a bar situated within the $\sim$11″ radius, a star-forming inner ring at approximately 12″ radius which encompasses the bar, and an outer ring encircling the inner one. The HST observations (ESA/Hubble & NASA & Erwin, 2019) of the galaxy reveal a small dusty nuclear ring within the $\sim$2″ radius. The MUSE FOV covers the entire bar of the galaxy and a portion of the inner ring surrounding it. Starting from the inner edge of the inner ring, $\sim$11″ north from the centre, a dust lane stretches towards the south along the bar. After reaching $\sim$3″ west of the centre, the dust lane curves towards the centre connecting to the nuclear ring; a counterpart of this dust lane is seen to the north of the centre. These distinctive dust lane features are more prominent in the structure map, presented in the first row (third panel) of Fig.5.1, and resemble two curving dust lanes often seen in bars.

As shown in the second, third and fourth rows (first panels) of Fig. 5.1, the strongest emission in all three line groups is concentrated within the radius of $\sim$3″. Particularly, the H$\alpha$ emission forms a crescent of radius $\sim$1–2″ southeast of the centre. Outside the $\sim$3″ radius, around the bar, the emission is strongly depleted. The inner ring has relatively high H$\alpha$ and [N II]$\lambda$6583 emission, featuring clumps of enhancements dispersed throughout due to local star formation; the [O III]$\lambda$5007 emission within the inner ring is relatively weak.

As shown in the second, third and fourth rows (second panels) of Fig. 5.1, the velocity field of all emission line groups shows signs of non-circular motions throughout the entire MUSE FOV. The zero velocity line forms an "S" shape, characteristic of the flow in bars. As shown in the third panel of the second and third rows of Fig. 5.1, for H$\alpha$ and [N II]$\lambda$6583, there is a peak of velocity dispersion at the centre with values reaching roughly 100 kms$^{-1}$. Past $\sim$1″ from the centre, the velocity dispersion drops and reaches the lowest values, approximately 50 kms$^{-1}$, in two lobes at $\sim$2″ east and west of the centre. These two lobes extend beyond the crescent seen in H$\alpha$ and [N II]$\lambda$6583 emission. Outside the two lobes, the velocity dispersion increases yet I can not reliably determine the velocity dispersion values beyond this region due to poor signal. The random motions of the gas within the inner ring are mild, with velocity dispersion values for H$\alpha$ and [N II]$\lambda$6583 staying around 50–60 kms$^{-1}$.

In the BPT map, presented in the third row (fourth panel) of Fig. 5.1, within the $\sim$3″ radius the galaxy exhibits composite emission with contribution from SF; SF being the strongest within the $\sim$2″ radius, particularly within the crescent in H$\alpha$ emission. This

BPT pattern together with the dust and low velocity dispersion is consistent with the small nuclear ring of the galaxy. The inner ring encompassing the bar has prominent star formation activity throughout.

The poor signal within the bar region makes IC 2051 a challenging target when fitting a circularly rotating disk to its velocity field. Results from `Kinemetry`, when run with free parameters and a fixed centre, show a roughly stable radial distribution of $i$ converging on $\sim$41°, but the distribution of PA of the LON is fluctuant. In an attempt to obtain more consistent parameter distributions, I binned the velocity map by aggregating the data into 2×2, 3×3, and 4×4 spaxel blocks. While this technique decreases the resolution of the velocity map, it increases the signal within each bin. However, even after applying binning, the results did not change. Therefore, I ran `Kinemetry` with different $i$ and PA of the LON values, trying to minimise the artefacts arising from their incorrect values in the residual velocity maps. A model fitted with a fixed centre, fixed $i$ at 41° and the PA of the LON at 60° effectively showed the minimum artefacts within the $\sim$3″ radius. Therefore, I fixed the parameters to these values for further analysis. However, these values differed from the values obtained in CBS obtained from large-scale fits to outer isophotes (see Table C.1). The resultant residual velocity map is presented in the first row (fourth panel) of Fig. 5.1. Since I aim to trace the inflow to the innermost regions, I focused on minimising the artefacts within the $\sim$3″ radius. Beyond this region, the artefacts of incorrectly fitted PA of the LON dominate the residual velocity map, observed as $m$=1 harmonic terms.

The best fit of the rotating disk exposes two features within the $\sim$4–5″ radius, with an amplitude of $\sim$30–40 $\mathrm{km s^{-1}}$ in the residual velocity map, one with positive and one with negative velocity residuals. The feature exhibiting negative velocity residuals overlaps with the dust lane on the west, coinciding with its curve and extension towards the centre. In the velocity difference map, presented in the second row (fourth panel) of Fig. 5.1, there is a coherent structure with positive values, with amplitude of $\sim$10–15 $\mathrm{km s^{-1}}$, extending from $\sim$4″ southwest of the centre towards $\sim$4″ east. One could argue that there is a counterpart of this feature in the northeast, exhibiting negative velocities around similar velocity amplitudes. The largest amplitudes of these two structures are co-spatial with the largest amplitudes of the features seen in the residual velocity map. Therefore, I attribute these features to coherent extended shocks in the gas. While a part of the gas shock seen in the residual velocity map coincides with the dust lanes, the structures seen in the velocity difference map are $\sim$1″ downstream from the dust lanes.

Based on the kinematic categories defined in Sect. 6.1, IC 2051 falls under the “coherent shocks” category.

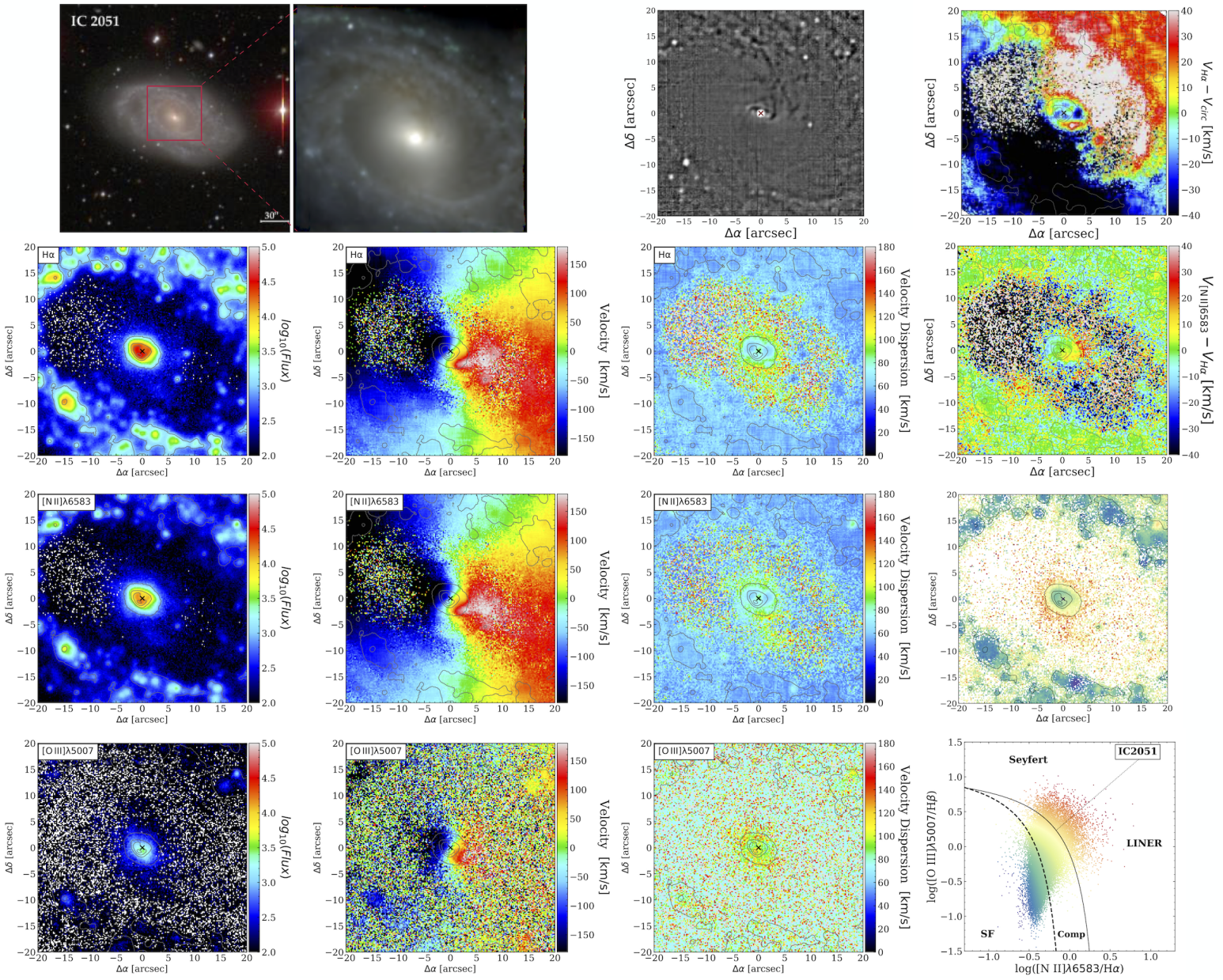


FIGURE 5.1: The diagnostic maps of IC 2051. *first row:* the large scale image with MUSE FOV marked with a pink box, the composite image within MUSE FOV, structure map and residual velocity map. *second row:* H$\alpha$ flux, velocity, velocity dispersion maps, and velocity difference map. *third row:* [N II]$\lambda$6583 flux, velocity, velocity dispersion maps, and the BPT map. *fourth row:* [O III]$\lambda$5007 velocity, velocity, velocity dispersion maps and the BPT diagram. The gray contours in kinematic and the BPT map represents the H$\alpha$ emission. "x" mark represents the centre of the galaxy.

## 5.2 NGC 289

As presented in the first row (first and second panels) of Fig. 5.2, NGC 289 has a luminous core, a bar located within the ∼15″ radius and two star-forming spiral arms surrounding the bar. Both spiral arms extend from the bar region several tens of kiloparsecs towards the outer parts of the galaxy, where they both appear disturbed; this disturbance is associated with the interacting companion of the galaxy (Arp, 1981; Bendo & Joseph, 2004). The MUSE FOV covers the entire bar region, together with a portion of the spiral arms. The dust lanes along the spiral arms and the bar are notably seen in the structure map of the galaxy, presented in the first row (third panel) of Fig. 5.2.

As shown in the second and third rows (first panels) of Fig. 5.2, there are two central peaks in H$\alpha$ and [N II]$\lambda$6583 emission. One at the nucleus and the other ∼2″ east of the centre. Within the bar region, there is clumpy H$\alpha$ emission likely originating from local SF, as well as extended emission elongated with the bar, close to the bar's major axis and on its leading side, likely related to shocks in the bar, which upon close inspection can be attributed to a set of aligned emission clumps. These structures are also seen, though relatively weaker, in [N II]$\lambda$6583 emission. The spiral arms show prominent H$\alpha$ and [N II]$\lambda$6583 emission throughout their extent. Compared to H$\alpha$ and [N II]$\lambda$6583, [O III]$\lambda$5007 emission is notably weaker and is mostly confined within the ∼4″ radius of the galaxy, its elongation at the larger radii not correlated with the orientation of the bar.

As presented in the second and third rows (second panels) of Fig. 5.2, H$\alpha$ and [N II]$\lambda$6583 velocity fields show signs of non-circular motions, particularly along the zero velocity line where several distinct features are seen. Approximately 1.5–2″ towards the northwest and 2–3″ southeast from the centre, H$\alpha$ and [N II]$\lambda$6583 velocities reach a local maximum of around 120 kms$^{-1}$. These two regions are not co-spatial with the central peaks in the emission. However, throughout the region where emission is notably high, within the ∼3–4 radius, the H$\alpha$ and [N II]$\lambda$6583 velocities also show an increase, with values ∼90–100 kms$^{-1}$. Approximately 6″ northeast from the centre, a velocity peak with H$\alpha$ and [N II]$\lambda$6583 velocities, ∼80–100 kms$^{-1}$ is seen; this coincides with a clumpy structure in H$\alpha$ emission, which may indicate a young stellar cluster moving with respect to the ambient medium.

As shown in the second and third rows (third panels) of Fig. 5.2, the centre of the galaxy exhibits H$\alpha$ and [N II]$\lambda$6583 velocity dispersion with ∼100–120 kms$^{-1}$; spanning over a region from the centre ∼4″ towards the north and southeast, almost manifesting an "S" shape. From the centre ∼2″ towards the east, velocity dispersion reaches a minimum, exhibiting values around 50 kms$^{-1}$; this region coincides with a region with

high H$\alpha$ velocity. Moreover, $\sim$6″ towards the northeast from the centre, another velocity dispersion minimum is seen which coincides with the H$\alpha$ clump of velocity higher than its surroundings. Several other features with low H$\alpha$ and [N II]$\lambda$6583 velocity dispersion are seen along the bar, coinciding with the two regions with elevated H$\alpha$ flux. Throughout the extent of the spiral arms, the velocity dispersion of both H$\alpha$ and [N II]$\lambda$6583 remains around 50–60 kms$^{-1}$.

The disk orientation parameters, PA of the LON = 125° and $i$=46° obtained from `Kinemetry` agree with the values from large-scale studies (Walsh et al., 1997: PA of the LON = 130° and $i$=46°). Thus I fit the rotating disk by fixing the parameters to these values. As shown in the first row (fourth panel) of Fig. 5.2, the residual velocity map of the galaxy reveals several distinct coherent structures. Outside the bar region, velocity residuals take a spiral pattern exhibiting amplitudes of $\sim$20–30 kms$^{-1}$. Within the bar region, the velocity residuals take a straight feature with amplitudes of $\sim$50 kms$^{-1}$, one with positive and one with negative velocities. The innermost part of the structure with positive velocities, at $\sim$2″ northeast from the centre, coincides with a region of high H$\alpha$ and [N II]$\lambda$6583 velocities. The spiral and straight structure with positive velocity residuals meet at the northwest end of the bar. The straight structure with negative velocities extending along the bar passes the centre by $\sim$7″ towards the northwest end of the bar. Approximately 5″ northeast from the centre, high positive velocity residuals with amplitudes of $\sim$50 kms$^{-1}$ are seen in the H$\alpha$ clump.

As shown in the second row (fourth panel) of Fig. 5.2, the velocity difference map is generally noisy. Along the bar, two structures with velocity difference amplitudes around $\sim$15-20 kms$^{-1}$ are visible, one stretching from the centre $\sim$5 arcseconds towards the south, and the other stretching from the centre $\sim$3″ towards the northwest. Approximately 4–5″ northeast of the centre, surrounding the clumpy region exhibiting high H$\alpha$ flux, the velocity differences reach $\sim$30 kms$^{-1}$ likely indicating a spatial overlap of two regions with different physical conditions.

The BPT map, shown in the third row (fourth panel) of Fig. 5.2, reveals composite emission in the centre. Approximately 2″ east of the centre, coinciding with the off-centre H$\alpha$ clump, contribution from SF is stronger than the central clump. Along the bar, the emission is of a composite nature with contribution from SF. Within the bar region, several distinct star-forming clumps are present, including the region at $\sim$6″ northeast from the centre, where I observed high H$\alpha$ flux. Outside the star-forming clumps, the ionisation is dominated by the LINER region. Furthermore, the spiral arms predominantly show active SF throughout their entire extent.

Although rather discontinuous, coherent spiral and straight structures seen in the residual velocity map, and the alignment of these structures with the dust lanes, are compelling evidence of the existence of extended shocks in gas. Additionally, I hypothesise that a portion of the straight feature with negative velocities, which passes the centre by $\sim 7''$ towards the northwest end of the bar, is the overshot gas after being funnelled in towards the centre from the southeast end of the bar. Instead of falling further inwards, the gas continues to flow towards the northwest bar end, where it collides with the gas present there.

Based on the kinematic categories defined in Sect. 6.1, NGC 289 falls under the "broken shocks" category.

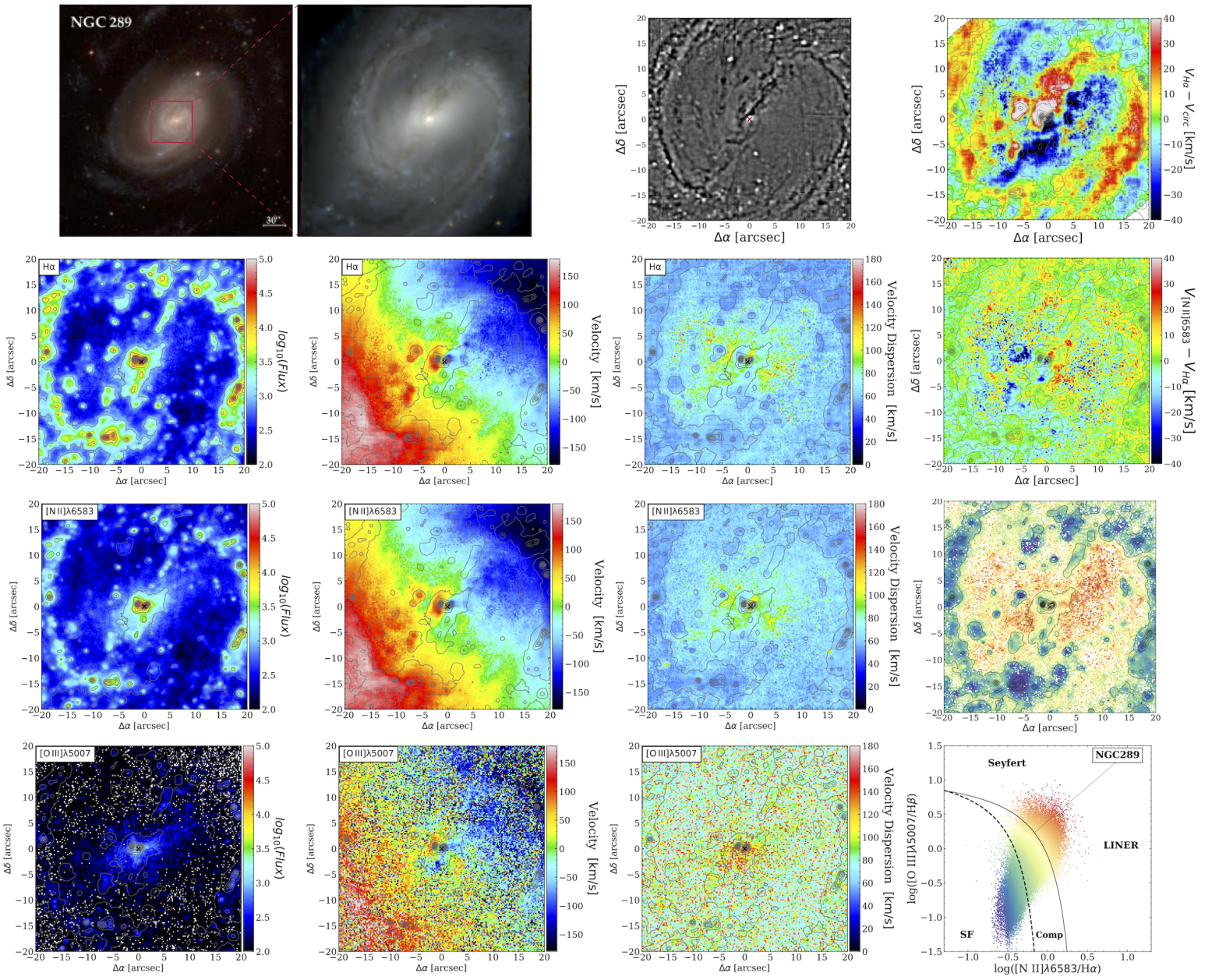


FIGURE 5.2: The diagnostic maps of NGC 289. The panels are the same as in Fig. 5.1.

## 5.3 NGC 613

As shown in the first row (first and second panels) of Fig. 5.3, NGC 613 has a luminous core, a star-forming nuclear ring of ∼6″ radius, a bar and star-forming spiral arms surrounding the bar region. The MUSE FOV encompasses the core, the nuclear ring and nearly the entire bar. Along the bar, two prominent dust lanes are seen. These dust lanes are prominent in the structure map of the galaxy, presented in the first row (third panel) of Fig. 5.3, where they curve to follow the nuclear ring over a full circle.

As presented in the second and third rows (first panels) of Fig. 5.3, the H$\alpha$ and [N II]$\lambda$6583 emission is mostly confined within the ∼5–6″ radius. The H$\alpha$ emission has several peaks in the nuclear ring and one ∼0.5″ southeast of the nucleus. The main peak of the [N II]$\lambda$6583 emission is ∼0.5″ southeast of the nucleus, the peaks in the nuclear ring correspond to the ones in H$\alpha$ emission, but they are rather weaker than the nuclear peak. As shown in the fourth row (first panel) of Fig. 5.3, [O III]$\lambda$5007 emission, rather strong and extended, is confined within a region stretching from the centre ∼8–9″ towards the northeast, indicating possibly an off-plane outflow. Some H$\alpha$ and more [N II]$\lambda$6583 emission appear to extend from the nuclear ring towards that direction as well. Moreover, there is enhanced emission across all line groups in an elongated region at ∼3–6″ southwest of the centre. While H$\alpha$ and [N II]$\lambda$6583 emission in this region appears joined with the emission from the nuclear ring, [O III]$\lambda$5007 emission appears notably separated. The separation overlaps with the region where the dust lane to the southeast connects to the nuclear ring. Clumpy H$\alpha$ emission is seen along the bar lanes, but also towards the northeast of the centre, where it appears to group into a spiral arm offset tangentially by roughly 90° from the dust lanes.

As presented in the second, third and fourth rows (second panels) of Fig. 5.3, the velocity field of all emission line groups is strongly perturbed, showing signs of non-circular motions. Outside the nuclear ring, there is a region with large negative velocities across all line groups, covering a PA between 0 and 45° and extending radially out to ∼10″ in H$\alpha$ and [N II]$\lambda$6583 and ∼15″ in [O III]$\lambda$5007, with amplitudes around ∼80–100 $\mathrm{km\,s^{-1}}$ for H$\alpha$ and [N II]$\lambda$6583, and ∼150 $\mathrm{km\,s^{-1}}$ for [O III]$\lambda$5007. This region appears separate from the main region with blueshifted velocities along the LON and is likely associated with the elevated [O III]$\lambda$5007 emission and with the outflow.

As shown in the second, third and fourth rows (third panels) of Fig. 5.3, within a region extending from the centre towards ∼5–6″ northeast, the velocity dispersion across all emission line groups reaches a peak, with values exceeding 150 $\mathrm{km\,s^{-1}}$ for H$\alpha$ and [N II]$\lambda$6583, and 200 $\mathrm{km\,s^{-1}}$ for [O III]$\lambda$5007. This region coincides with the regions of negative velocities across all line groups. The velocity dispersion values of H$\alpha$ and

[N II]$\lambda$6583 in the nuclear ring are around $\sim$70 kms$^{-1}$. Outside the nuclear ring, the velocity dispersion across all line groups is high, around $\sim$100–140 kms$^{-1}$ but in the spiral towards the northeast with clumpy H$\alpha$ emission, H$\alpha$ and [N II]$\lambda$6583 velocity dispersion values reach a minimum of $\sim$50–70 kms$^{-1}$.

The disk orientation parameters, the PA of the LON=115° and $i$=37°, obtained from `Kinemetry` agree well with the parameters estimated from large-scale fits; the PA of the LON differing by 5° from the value estimated from Bajaja et al. (1995) (see Table C.1). The residual velocity map presented in the first row (fourth panel) of Fig. 5.3, exposes several strong localised extremes within the nuclear ring, likely originating from the complex interaction between the inflow, SF and the AGN outflows. Throughout the region to the northeast of the nucleus, associated with AGN outflows, strong negative residual velocities with amplitudes exceeding 50 kms$^{-1}$ are seen. Coinciding with the dust lanes along the bar, two coherent structures with amplitudes $\sim$30–40 kms$^{-1}$ are seen, one exhibiting negative and one exhibiting positive velocity residuals. While the structure with positive velocities can be traced towards its connection to the nuclear ring, the structure with negative velocities is dominated by the strong AGN outflows likely located in front of the line of sight. To the east of the nuclear ring, there is a coherent region where the amplitudes of the residual velocity exceed 50 kms$^{-1}$. This region is not co-spatial with the SF spiral structure with clumpy H$\alpha$ emission seen in the BPT map; only their innermost parts overlap.

The velocity difference map, presented in the second row (fourth panel) of Fig. 5.3, exposes two coherent structures with amplitudes of $\sim$40–50 kms$^{-1}$. One of these structures, characterised by negative velocity differences, extends from the centre $\sim$10–11″ towards the north. The other structure, characterised by positive velocity differences, is situated $\sim$3″ east of the centre and extends $\sim$6″ towards the northeast. These two structures nearly encircle the area exhibiting coherent negative velocity residuals, which are associated with the AGN outflows. This suggests the presence of two distinct regions of gas with differing physical conditions along these structures, where there is a transition from emission dominated by the disc to that dominated by outflow. Moreover, there is a faint coherent continuous structure with amplitudes of $\sim$10–15 kms$^{-1}$ upstream from the coherent structure with positive residual velocities along the dust lane to the southeast.

The core of NGC 613 is classified as a LINER type (Audibert et al., 2019). In the BPT map, presented in the third row (fourth panel) of Fig. 5.3, LINER emission is seen at the very core as well as in the northeast region, where velocity dispersion across all line groups peaks, and in the southeast region with enhanced emission across all line groups. The latter two regions resemble a bi-symmetric structure, co-spatial with pronounced [O III]$\lambda$5007 emission. This confirms that these features are likely originating from

AGN outflows. However, the emission from a high energy mechanism occurs where the innermost part of the dust lane connects to the nuclear ring, which may indicate the inflowing gas irradiated by the AGN. Except for the northeast region, where the nuclear ring is dominated by SF. Furthermore, the clumpy H$\alpha$ emission in the northeast appears as a coherent spiral in SF, winding from the northeast of the centre and connecting to the nuclear ring at the east. This spiral was not identified clearly in the emission or characterised by the dust lanes, but it is notably revealed in the BPT map.

Various approaches of the methodology provide evidence of extended shocks along the dust lanes in the bar, connecting to the nuclear ring. However, the presence of strong AGN outflows within the nuclear ring prevents identifying the signatures of extended shocks to the innermost regions. Based on the kinematic categories defined in Sect. 6.1, NGC 613 falls under the "AGN dominated" category.

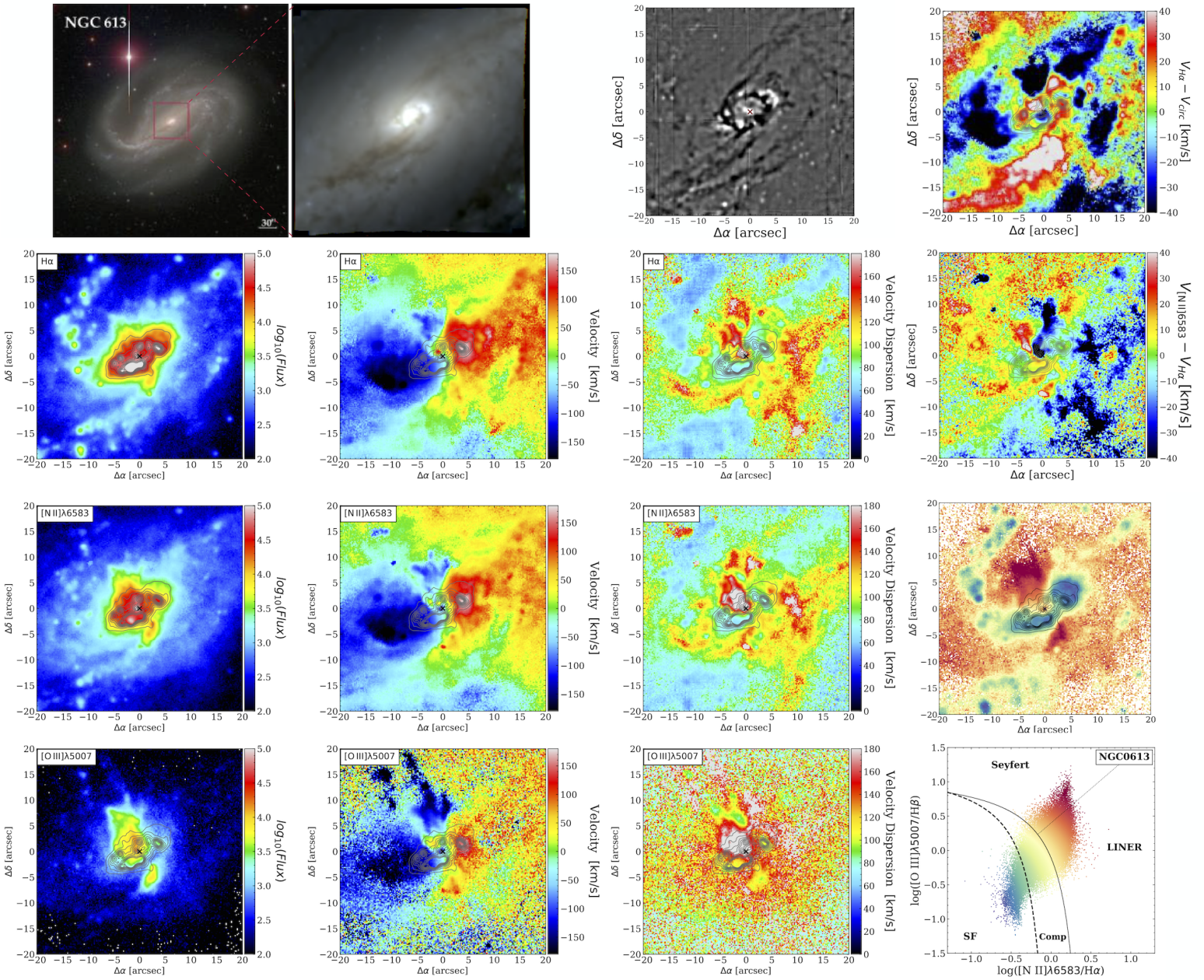


FIGURE 5.3: The diagnostic maps of NGC 613. Panels are the same as in Fig. 5.1.

## 5.4 NGC 1300

As presented in the first row (first and second panels) of Fig. 5.4, NGC 1300 has a luminous core encircled by a nuclear ring or disk and a prominent classical bar (Lindblad & Kristen, 1996; Lindblad et al., 1997). The galaxy also has two star-forming spiral arms surrounding the bar region. The MUSE FOV encompasses the core, the nuclear ring, and approximately two-thirds of the bar. Along the bar, I see two dust lanes, one stretching from the east towards the centre, connecting to the nuclear ring from the north, and the other as the weak counterpart of the former, stretching from the west towards the centre, connecting to the nuclear ring from the south. Several other faint dust lanes downstream from the main dust lane to the east are seen, yet these do not join to the nuclear ring, and instead they continue towards the northwest and join the dust lane to the west. Within the nuclear ring, I notice two dust spirals curving towards the core of the galaxy. They appear to connect with the dust lanes in the bar; at the inner end of the western lane, south of the nucleus, the spiral lane looks doubled. The structure map shown in the first row (third panel) of Fig. 5.4 enunciates these faint dust structures.

As shown in the second and third rows (first panels) of Fig. 5.4, H$\alpha$ and [N II]$\lambda$6583 emission is high in the nucleus, drops at $\sim$2–3″ from the centre, and then is high in the nuclear ring of $\sim$5″ radius. In comparison with H$\alpha$ and [N II]$\lambda$6583, the [O III]$\lambda$5007 emission, presented in the fourth row (first panel) Fig. 5.4, is relatively weak and is confined within the $\sim$3″ radius. Outside the nuclear ring, within the bar region, the emission across all line groups is weak, yet several round regions with enhanced H$\alpha$ and [N II]$\lambda$6583 emission are seen, likely originating from local SF.

The velocity field of H$\alpha$ and [N II]$\lambda$6583, shown in the second and third rows (second panels) of Fig. 5.4, present signs of non-circular motions. Outside the nuclear ring, the zero velocity line has a strong indent and inside the nuclear ring, it shows a strong wiggle due to several local velocity peaks. As shown in the second, third and fourth rows (third panels) of the same figure, the velocity dispersion of all line groups shows a peak within the inner $\sim$3″ region, with values $\sim$110–140 kms$^{-1}$. The values decrease and remain around $\sim$50–60 kms$^{-1}$ within the nuclear ring. Outside the nuclear ring, within the round region where enhanced H$\alpha$ and [N II]$\lambda$6583 emission is seen, at $\sim$9″ northwest of the centre, there is low H$\alpha$ and [N II]$\lambda$6583 velocity dispersion around $\sim$60 kms$^{-1}$. Moreover, there is a relative increase in velocity dispersion outside the nuclear ring but I can not determine the values reliably due to poor signal within the bar region.

Because of the poor signal within the bar region, the disk orientation parameters of the galaxy are not well constrained with `Kinemetry`; the estimated distributions of $i$ and PA of the LON fluctuate as a function of the radius of the fitted ellipse. Therefore,

I ran `Kinemetry` with different $i$ and PA of the LON values, to fit various rotating disks to the H$\alpha$ velocity field and, I studied the corresponding residual velocity maps to identify parameter values that minimise the artefacts. A rotating disk fitted with a fixed centre, PA of the LON at 107° and $i$ at 35° minimised the artefacts seen in residual velocity maps. Consequently, these values are selected as the final orientation parameters for the disk. When compared to the disk orientation parameters estimated from the large-scale fits in Lindblad et al. (1997) ($i$=35° and PA of the LON =87°), the settled value for $i$ aligns well with theirs, but there is a notable 20° difference in the PA of LON. However, this is anticipated and can be attributed to the large-scale fits incorporating contributions from the entire bar and the asymmetric spiral arms of the galaxy (Elmegreen et al., 1996; Martini et al., 2003b).

In the residual velocity map, presented in the first row (fourth panel) of Fig. 5.4, inwards from the nuclear ring, three clumpy regions with negative velocity residuals of amplitudes ∼20–30 kms$^{-1}$, situated ∼1″ towards the northeast, southeast and southwest from the centre are exposed. The northern region exhibits the strongest amplitudes. While these three regions resemble $m$=3 harmonic terms, raised from wrongly fitted $i$ in the disk model, they also coincide with the local velocity peaks seen in the original velocity maps, and therefore they are real and driven by the data. None of these regions overlap with the dust spirals inside the nuclear ring. External to the nuclear ring, I notice a coherent structure with negative velocities, with amplitudes around ∼30–40 kms$^{-1}$, winding from ∼15″ east of the centre towards the northwest, coinciding with one of the faint dust lanes downstream from the main dust lane. Where this coherent structure ends, ∼10″ northwest of the centre, a round region with high positive residual velocities, with amplitudes exceeding 50 kms$^{-1}$, is seen. This region coincides with enhanced H$\alpha$ and [N II]$\lambda$6583 emission and low velocity dispersion.

As presented in the second row (fourth panel) of Fig. 5.4, inwards from the nuclear ring, the velocity difference map reveals two peaks, one with positive and one with negative values, with amplitudes of ∼15–25 kms$^{-1}$. Both peaks are located at a similar distance, ∼4″ from the centre, one towards the northeast and the other towards the southwest. These two peaks also appear to have an extension of elevated velocity difference amplitudes in the clockwise direction. Considering their similar distances from the centre, and the possible extended natures, these two kinematic structures can be counterparts of one another. Outside the nuclear ring, where velocity residuals were showing an increase, the velocity differences are also coherent, exhibiting amplitudes around ∼20–30 kms$^{-1}$. This trend persists throughout the dust lane. However, once reaching the round region, where enhanced H$\alpha$ and [N II]$\lambda$6583 emission and low velocity dispersion are seen, the amplitudes are ∼0 kms$^{-1}$; around this region, the velocity differences remain consistent with those observed in the dust lane.

The core of NGC 1300 is classified as a weak low-mass AGN (Atkinson et al., 2005; Hughes et al., 2005). As shown in the BPT map, presented in the third row (fourth panel) of Fig. 5.4, the nuclear ring exhibits composite emission with contribution from SF, with the most significant SF occurring in the northwest. Inwards from the nuclear ring, ionisation is predominantly driven by high-energy mechanisms. Outside the nuclear ring, two clumps, each showing contribution from SF, are observed – one $\sim$10″ northwest of the centre and the other $\sim$6″ south of the centre. These structures coincide with round regions displaying enhanced H$\alpha$ and [N II]$\lambda$6583 emission. Considering high residual velocities co-spatial with the structure at the northwest, and elevated velocity differences surrounding it, I hypothesise that this structure can be a young star cluster moving with respect to the surrounding medium of different physical conditions.

Although NGC 1300 shows a clear coherent spiral structure in dust that can be traced down to $\sim$1″ from the nucleus, this structure does not appear to have a coherent kinematic counterpart. The kinematic structures in the residual velocity and velocity difference maps are likely the result of local shocks and are not associated with extended shocks. Based on the kinematic categories defined in Sect. 6.1, NGC 1300 falls under the "other perturbations" category.

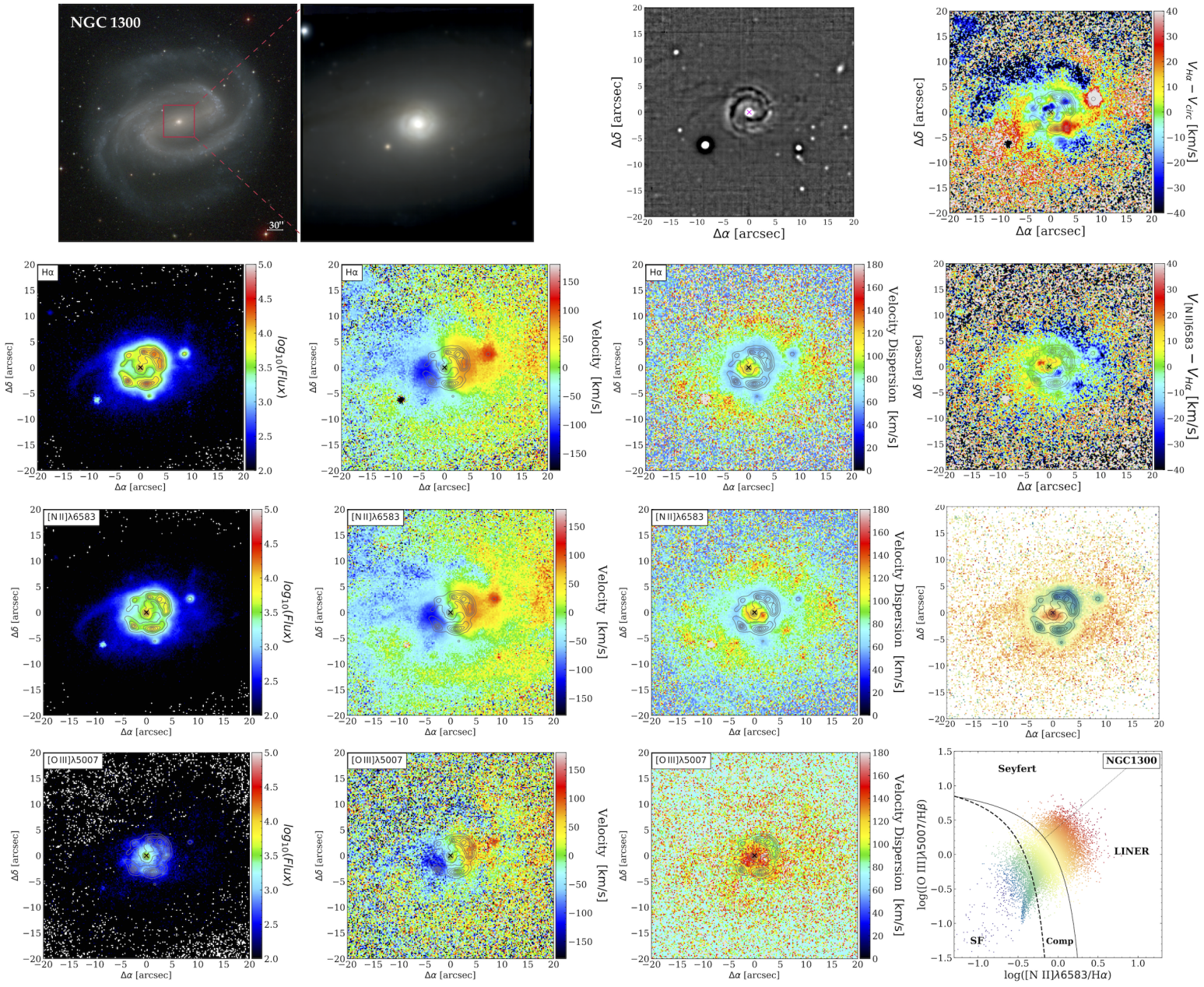


FIGURE 5.4: The diagnostic maps of NGC 1300. The panels are the same as in Fig. 5.1.

## 5.5 NGC 1433

As shown in the first row (first and second panels) of Fig. 5.5b, NGC 1433 has a luminous core, a prominent nuclear disk, a bar, an inner ring surrounding the bar region, outside of which there are two or possibly four spiral arms. The MUSE FOV covers the core, the nuclear disk and roughly half of the bar. There remains a subject of ongoing debate about whether NGC 1433 hosts a nuclear bar. While several photometric (Erwin, 2004; Buta et al., 2015) and kinematic (Bittner et al., 2019) studies present evidence in favour of a nuclear bar, contrasting kinematic studies challenge its existence de Lorenzo-Cáceres et al. (2019). Along the main bar, two prominent dust lanes are seen which curve around the nuclear disk. Moreover, a faint dust lane is seen following the same pattern as the dust lane to the southwest, yet it extends further beyond and connects to the dust lane to the northeast. Further inwards, there are several dust spiral arms within the nuclear disk, curving towards the centre. These dust features are more clearly seen in the structure map, presented in the first row (third panel) of Fig. 5.5b, where they appear as a continuation of the straight dust lanes along the main bar.

The flux, velocity and velocity dispersion maps of NGC 1433 which I refer to in this paragraph show the measurements obtained from single Gaussian fits, presented in Chapter 2. As shown in Figs. 2.11–2.13, emission across all line groups is confined within the nuclear disk. The strongest emission comes from the core, confined within ∼3–5″ radius for H$\alpha$ and [N II]$\lambda$6583 emissions, and within ∼3″ radius for [O III]$\lambda$5007. There is no nuclear ring in H$\alpha$ or [N II]$\lambda$6583 emission. Within the nuclear disk, distinct clumpy regions with enhanced H$\alpha$ and [N II]$\lambda$6583 emissions are seen. One of the most prominent of these regions is seen as a single blob at ∼9″ southeast of the centre. Another notable region with enhanced emission is characterised by three maxima and is situated ∼6–8″ southwest of the centre. In comparison to H$\alpha$ emission, the [N II]$\lambda$6583 emission from these regions is weaker. These regions also exhibit elevated [O III]$\lambda$5007 emission. As presented in Figs. 2.14–2.16, the velocity fields of all emission line groups exhibit signs of non-circular motions, with indents in the zero-velocity-line characteristic to strong streaming motion in the spiral arms. As shown in Figs. 2.17–2.19, outer parts of the nuclear disc, at ∼8″, have the smallest velocity dispersion with ∼60 kms$^{-1}$. Throughout the nuclear disk, where enhanced clumpy H$\alpha$ and [N II]$\lambda$6583 emissions are seen, the velocity dispersion of H$\alpha$ and [N II]$\lambda$6583 drops and remains around ∼60–70 kms$^{-1}$. Closer to the nucleus, there is an extended region ( 5″ across) of high velocity dispersion to the east and two small ones (∼2″ in size) to the west where high dispersion values exceed ∼150 kms$^{-1}$. Anomalous velocities are seen in these regions in the H$\alpha$ and [N II]$\lambda$6583 velocity maps. Due to poor [O III]$\lambda$5007 emission, the velocity dispersion

values within the nuclear disk are not reliably estimated, but in the regions with high H$\alpha$ and [N II]$\lambda$6583 velocity dispersion, values are also elevated for [O III]$\lambda$5007.

The high velocity dispersion in the nucleus prompted us to examine the Gaussian fits in the corresponding spaxels. As I explained in Sects. 2.3.3 and 2.3.4, if there are multiple emission sources along the LOS, which can appear as excess emission in the spectra, the standard single Gaussian fitting approach will produce a poor and broad fit in the spectra of spaxels that are affected from the excess emission. Such poor fits correspondingly can shift the recorded velocity of main lines, and can artificially increase the velocity dispersions. Correspondingly, the artificial measurements can significantly influence the residual velocity and velocity difference maps I construct to search for the signatures of extended shocks. Upon the checks of spectra, I noticed that spectra in several spaxels within the inner $\sim3''$ radius are poorly fitted due to an excess emission in the blue wing of the [N II]$\lambda$6583 line. Therefore, to address this excess emission, I followed the same procedures introduced in Kolcu et al. (2023), and allowed for fitting a secondary component to [N II]$\lambda$6583.

Further, I compare the kinematic measurements obtained from single Gaussian fits and fits including a secondary component to determine regions that are the most affected by the excess emission. In general, H$\alpha$ and [O III]$\lambda$5007 are not affected throughout the entire FOV. However, within a localised region extending from $\sim3''$ east of the centre $\sim4''$ towards the north, the introduction of the secondary component shifts the derived velocity of [N II]$\lambda$6583 significantly, by $\sim$15–20 kms$^{-1}$. The velocity dispersion of [N II]$\lambda$6583 in this region remains high. This region is presented in Fig. 5.5a, after certain mask conditions are applied which I explain below.

Therefore, by establishing the criteria explained further, I determine the region where the fits to spaxels are the most affected by the excess emission, to correct the [N II]$\lambda$6583 kinematic measurements in the regions, by using the values for the main component from the fits that include a secondary component there. The criteria are as follows:

i. $V_{[N\,II]} - V_{[N\,II],corr} \leq -10$ kms$^{-1}$

ii. $\sigma_{[N\,II]}/\sigma_{[N\,II],corr} \geq 1.2$

iii. $\sigma_{[N\,II]w} \leq 300$ kms$^{-1}$

iv. $-4'' \leq \Delta\alpha \leq -1''$ and $-1'' \leq \Delta\delta \leq 4''$

where *corr* indicates the values extracted from the fits including the secondary component. The third condition, the velocity dispersion limit of the secondary [N II]$\lambda$6583

component ([N II]w) ensures that the secondary component is real and is not fitted to noise. The spatial cuts are applied to select the region where the change in velocity and velocity dispersion ratio is consistently large. For further analysis, the flux, velocity, and velocity dispersion values for all emission line groups within the mask region are replaced with those from the corresponding main components in fits that include the secondary component. Although H$\alpha$ and [O III]$\lambda$5007 measurements are not affected, I continue to use measurements from fits with a secondary component to maintain consistency. The corrected flux, velocity and velocity dispersions maps of all line groups are presented in the second, third and fourth rows (first, second and third panels) of Fig. 5.5b.

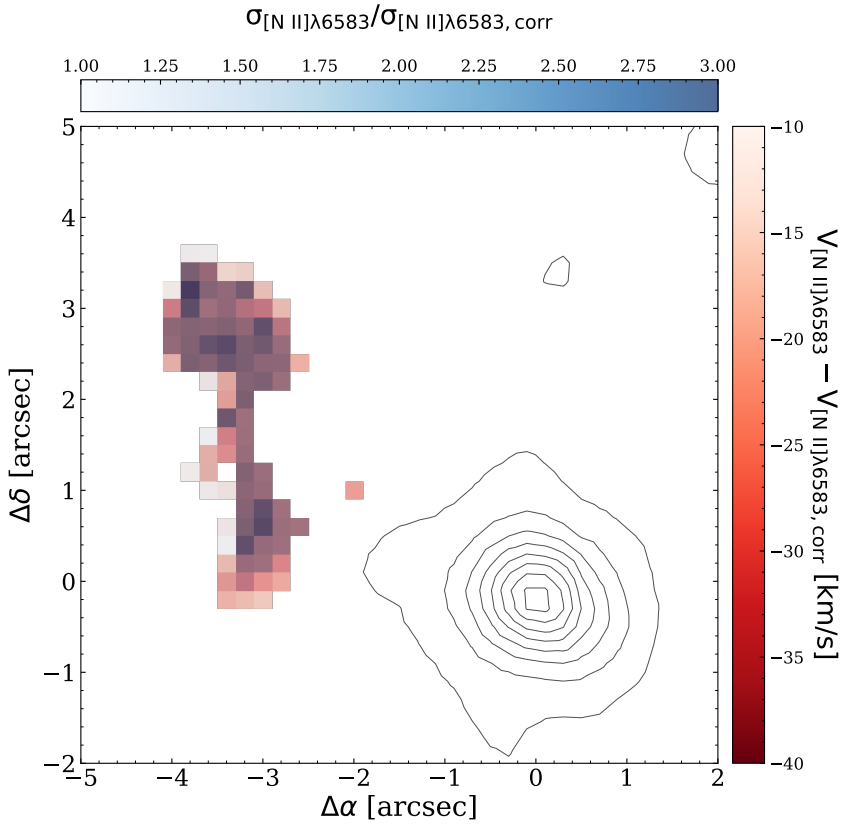


FIGURE 5.5A: The mask of spaxels for which the fits including secondary component were used in further analysis of NGC 1433. The red and blue colour maps show the velocity shift of [N II]$\lambda$6583 and the ratio of [N II]$\lambda$6583 velocity dispersion, respectively, before and after including the secondary component in the fitting.

When run with a fixed centre the distributions of the $i$ and PA of the LON obtained from `Kinemetry` show strong variation with radius. Therefore, I adopted initial values PA of the LON=19.7° and $i$=29° from the large-scale study Lang et al., 2020, and by adjusting these values with small increments, I ran `Kinemetry` with different fixed PA of the LON and $i$ values to identify the values that raise the minimum level of artefacts in the residual velocity map. Despite these adjustments, I did not observe a significant

change in the residual velocity map. Therefore, I selected the initial parameter values as the final $i$ and PA of the LON.

In the residual velocity map of the galaxy, shown in the first row (fourth panel) of Fig. 5.5b, there are several pronounced coherent structures within the nuclear disk. One of these structures exhibiting positive velocities with amplitudes of ∼30–50 $\mathrm{kms}^{-1}$, forms an arch ∼8″ west of the centre, extending for over 15″. A possible counterpart to this structure, exhibiting negative velocities, extends from ∼10″ south of the centre towards the northeast. Both structures align well with the outer curvature of the nuclear disk, and the dust lanes. Another coherent structure with negative velocity residuals is seen, with amplitudes around 40–50 $\mathrm{kms}^{-1}$, forming an arch ∼4″ west of the centre extending almost 10″. The largest amplitude of this structure coincides with one of the peaks of H$\alpha$ and [N II]$\lambda$6583 velocity and velocity dispersion. Throughout the extent of this structure, the [N II]$\lambda$6583 velocity dispersion is ∼30–40% larger than that of H$\alpha$. Between ∼2″ and ∼5″ to the northeast of the nucleus there are clumpy regions of high negative and positive velocity residuals – they are likely related to the AGN outflows, explained further below. In addition, throughout the nuclear ring, several other regions exhibit high residual velocity amplitudes. However, these regions rather have an amorphous structure and are likely originating from local SF. Outwards from the nuclear ring, extending from the southeast of the centre towards the northeast for ∼20″, a coherent structure forms an arch, exhibiting velocity residual amplitudes around ∼30 $\mathrm{kms}^{-1}$. This structure coincides with the faint dust lane seen in the same region, likely indicative of overshot gas.

In the velocity difference map, presented in the second row (fourth panel) of Fig. 5.5b, regions of high positive and negative values are seen to the south and southeast of the nucleus, where the velocity dispersion is high. In addition, several clumpy regions with enhanced velocity differences, up to ∼20 $\mathrm{kms}^{-1}$ are seen throughout the nuclear disk, that do not particularly coincide with the structures seen in the residual velocity map.

The classification of the galaxy's core remains the subject of a debate (Veron-Cetty & Veron, 1986; Sosa-Brito et al., 2001). Nevertheless, the contribution from the AGN to the ionisation is evident in the BPT map, presented in the third row (fourth panel) of Fig. 5.5b. Up to ∼4″ radius, in two regions exhibiting a distinct horizontal biconical shape, characteristic to AGN outflows, the ionisation is primarily influenced by a high-energy mechanism. Particularly along east-west direction, in the regions where the velocity dispersion is high. A part of this region coincides with where I corrected for excess emission in the fitting, indicating the excess emission seen in this region is likely originating from AGN outflows. Furthermore, throughout the nuclear disk, there is composite emission with a contribution from SF. The regions with the strongest SF, to

the southeast and southwest, are co-spatial with the most prominent H$\alpha$ and [N II]$\lambda$6583 enhancements seen in emission. These coincide with the two coherent structures with high positive and negative residual velocity amplitudes, situated at the curvature of the nuclear disk. These alignments are indicative of SF being triggered by enhanced gas density at the leading side of the bar and provide evidence of large-scale extended shocks propagating within those regions.

Within the nuclear disk of NGC 1433, the residual velocity map exhibits elongated structures with large velocity amplitudes, coinciding with dust spirals. These structures together resemble a nuclear spiral shock, but they lack the continuity expected from such a shock. Nevertheless, the alignment of the dust structures with structures seen in residual velocity, together with enhanced velocity differences and the elevated SF activity occurring in these structures can all be associated with extended shocks in gas. I hypothesise that strong SF activity within the nuclear disk and potentially the AGN activity, interrupt the propagation of the shock, leaving portions of it visible in the residual velocity map. Based on the kinematic categories defined in Sect. 6.1, NGC 1433 falls under the "broken shocks" category, due to the discontinuous extents of the shock signatures.

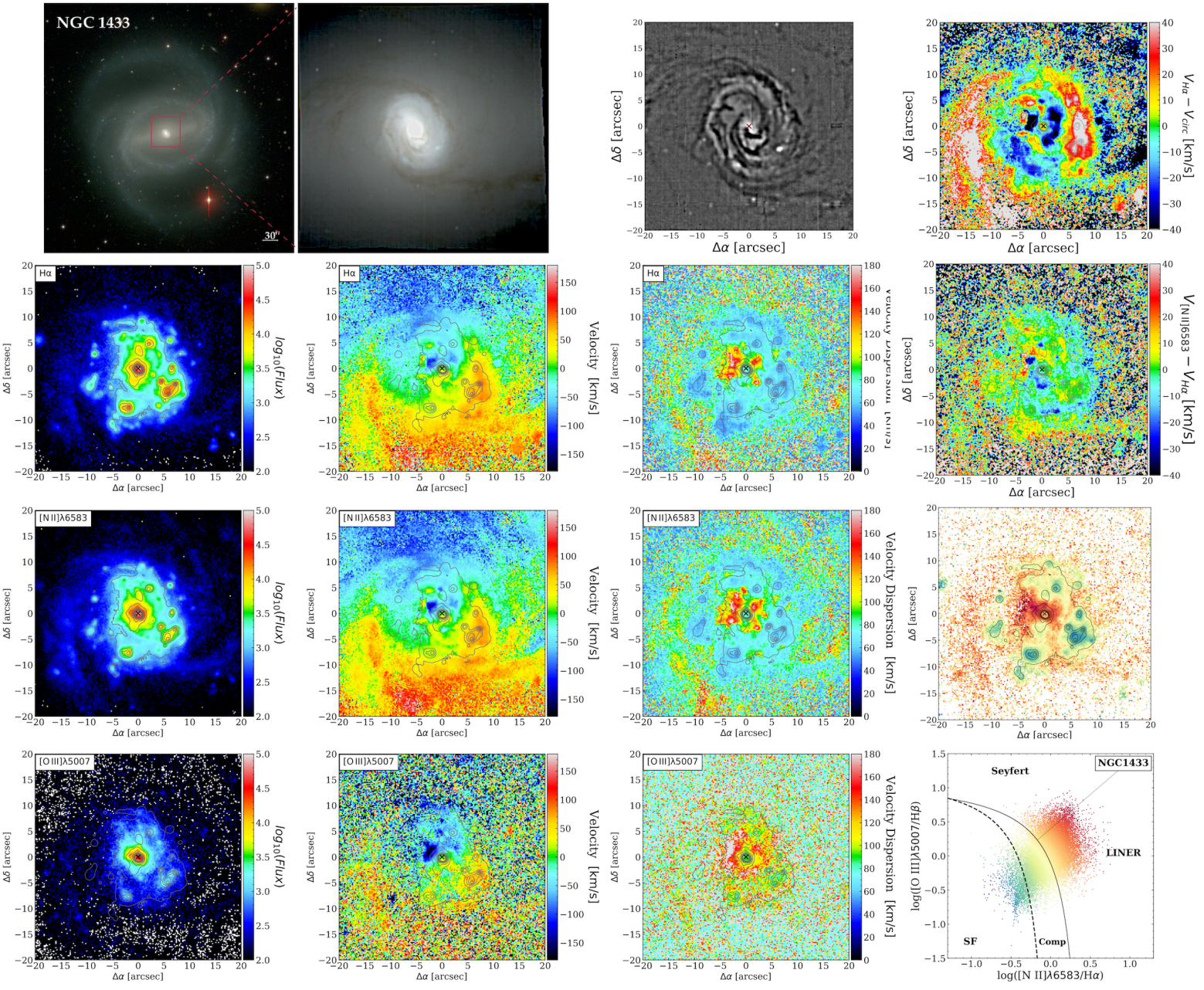


FIGURE 5.5B: The diagnostic maps of NGC 1433. Panels are the same as in Fig. 5.1.

## 5.6 NGC 1566

As shown in the first row (first and second panels) of Fig. 5.6, NGC 1566 has a bright core, which is classified as Seyfert 1.2 type based on its optical broad line ratio, yet also exhibiting optical narrow line ratio typical of Seyfert 2 cores (Alloin et al., 1985; Kriss et al., 1991; Smajić et al., 2015). The galaxy also has a weak bar (de Vaucouleurs et al., 1991; Sheth et al., 2010), and two or possibly four star-forming spiral arms encircling the bar region. The MUSE FOV encompasses the core and the entire bar. In the bar region, originating in the north and south, there are dust lanes winding in clockwise direction. These dust features are more prominent in the structure map, presented in the first row (fourth panel) of Fig. 5.6. Particularly, within the inner 15″, I notice the multiplicity of spiral arms in clockwise direction.

As presented in the second, third and fourth rows (first panels) of Fig. 5.6, the emission across all line groups is concentrated within ∼3″ radius. In the bar region, two strong lanes of emission are seen with clumpy H$\alpha$ and [N II]$\lambda$6583 emission; some of these regions align as a straight line, likely indicating enhanced SF within the bar lanes. The H$\alpha$ emission in these regions is stronger than [N II]$\lambda$6583 emission. I do not discern a nuclear ring in emission. [O III]$\lambda$5007 emission beyond the inner ∼3″ region significantly weakens. However ∼8″ from the centre towards south–southeast enhanced [O III]$\lambda$5007 emission is seen; since there is no counterpart to this structure seen in any other emission, it is likely originating from AGN outflows.

The velocity across all emission line groups, as shown in the second, third and fourth rows (second panels) of Fig. 5.6, reveals significant non-circular motions of no clear pattern. In the [O III]$\lambda$5007 velocity map, ∼4–8″ from the centre, at PA of the LON ∼160°, a region of high negative velocities (up to ∼300–400 kms$^{-1}$) occurs at the location of enhanced [O III]$\lambda$5007 emission, confirming its origin being AGN outflows. There is also a blueshifted quasi-linear structure ∼10″ to the southwest of the nucleus, co-spatial with a filament seen in [O III]$\lambda$5007, but not in H$\alpha$ or [N II]$\lambda$6583, inconsistent with the spiral pattern, possibly related to the AGN outflows.

Within the ∼2″ radius, an ambiguous round structure with high velocity across all line groups is seen. Upon closer examination of the spectra, within ∼1″ radius of this region, I noticed strong broad emission primarily in the H$\alpha$ and [N II] wavelength ranges, which can be attributed to the AGN. The emission from AGN was so strong that it even caused saturation in the innermost couple of spaxels. As a result, the Gaussians are not well fitted to the H$\alpha$ and [N II] lines, indicating that the kinematic measurements derived from them are unreliable within the inner 1″. Broad emission is also seen in [O III]$\lambda$5007, but the Gaussian fits to [O III]$\lambda$5007 are still reliably fitted. Although the

broad emission is associated with the characteristic of the AGN, there can also be a potential contribution from a small nuclear ring in that region, which has a size smaller than 100 pc, standing as one of the smallest nuclear rings ever found de Sá-Freitas et al. (2023b). Nevertheless, the erroneous Gaussian fits due to broad emission in the spectra indicate that the measurements within the $\sim 1''$ radius are not reliable. The complexity of the broad emission extends beyond the standard approach of including a secondary component in the fitting process and requires careful attention to be addressed. Given that addressing this issue is beyond the scope of this work, I excluded the measurements within the $1''$ radius in my further analysis. In Fig. 5.6, the excluded spaxels appear as an empty white region with no measurements.

As shown in the second, third and fourth rows (third panels) of Fig. 5.6, within the $\sim 3$–$4''$ radius, beyond the excluded region, the velocity dispersion across all line groups is high, exceeding 150 $\mathrm{km s^{-1}}$. In the bar region, particularly to the southwest, the velocity dispersions remain high, with values $\sim$100–130 $\mathrm{km s^{-1}}$ which can be related to AGN features explained above. Along the dust lanes in the bar region, the velocity dispersion of H$\alpha$ and [N II]$\lambda$6583 decreases and remains around $\sim$50–70 $\mathrm{km s^{-1}}$. Where strong blueshifted velocities are seen, to the southwest of the centre, the velocity dispersion of [O III]$\lambda$5007 is high, with values $\sim$170–200 $\mathrm{km s^{-1}}$.

The disk orientation parameters estimated with `Kinemetry`, $i = 40°$ and position angle (PA) of the Line of Nodes (LON) = 37°, are consistent with the parameters estimated from large-scale fits from Lang et al. (2020), differing by approximately ±5° (see Table C.1). Therefore, I settle on these parameters in the final disk model. The residual velocity map, presented in the first row (fourth column) of Fig. 5.6, reveals coherent continuous structures with velocities around $\sim$30 $\mathrm{km s^{-1}}$. The structure with negative velocities is seen extending from the south of the centre towards the northeast. While a part of this structure curves towards the centre in the northeast, another part continues extending further north by another $\sim 5$–$6''$. These structures likely reflect the inflow along the two dust lanes seen extending from the south towards the north. A counterpart, exhibiting positive residual velocities, extends from the north of the centre towards the west, coinciding with the dust lane to the north.

In the velocity difference map, presented in the second row (fourth columns) of Fig. 5.6, two extended regions are seen with amplitudes of $\sim$15–25 $\mathrm{km s^{-1}}$; one to the southeast–north with positive and the other to the northwest–west with negative velocity differences. These two structures appear upstream from the two lanes seen in emission, and the coherent positive and negative residuals, by $\sim 1''$.

In the BPT map, shown in the third row (fourth panel) of Fig. 5.6, the majority of the emission is of LINER/Seyfert type. The star-forming regions are rather in clumps

grouped along several strings that largely correspond to the two lanes seen in emission. The region with the strongest SF coincides with the strongest H$\alpha$ enhancement seen in emission, and with a portion of the coherent structure with negative residual velocities. Moreover, in the region where the coherent structure with negative residual velocities continues further north, several aligned round regions with enhanced SF are seen.

Even though the presence of AGN outflows and the possible contribution from the small nuclear ring to the emission prevents us from resolving the propagation of shocks into the very core, there is compelling evidence of extended shocks within the inner kpc, along the bar lanes and curving towards the nucleus, reaching the innermost regions, down to the inner $\sim 2''$ region. Therefore, based on the kinematic categories defined in Sect. 6.1, NGC 1566 falls under the "coherent shocks" category.

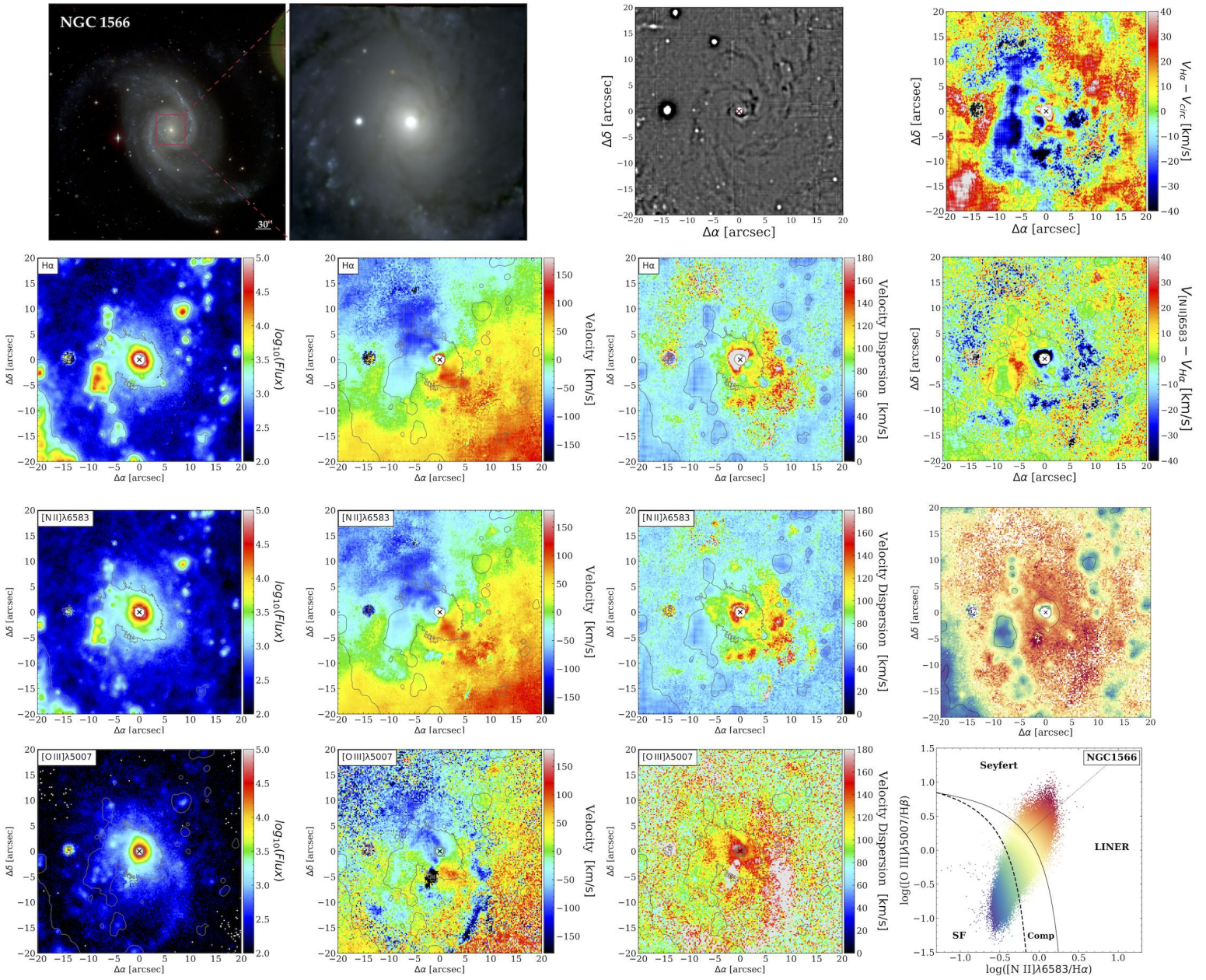


FIGURE 5.6: The diagnostic maps of NGC 1566. Panels are the same as in Fig. 5.1.

## 5.7 NGC 3351

NGC 3351 is a well studied galaxy (Mazzalay et al., 2014; Smirnova & Wiebe, 2019; Gadotti et al., 2019; Leaman et al., 2019; Calzetti et al., 2021), and is one of the members of the Leo Group. As shown in the first row (first and second panels) of Fig. 5.7, NGC 3351 has a luminous core, a star-forming nuclear ring within the ∼10″ radius, a prominent bar, an inner ring surrounding the bar region and two or more spiral arms surrounding the inner ring. The MUSE FOV encompasses the core, the nuclear ring and almost the entire bar of the galaxy. Along the bar, two faint dust lanes are seen; one of these extends from the northwest towards the centre and the other extends from the southeast towards the centre. These two dust lanes continue to curve within the nuclear ring over a full circle. Furthermore, within the bar region, an additional and more prominent dust lane is seen, manifesting an "L" shape. More specifically, this dust lane appears just outside the nuclear ring, where it is initially almost parallel to the southeastern lane and at ∼10″ towards south from the centre becoming orthogonal to it. To the east and the west of the nuclear ring, several faint dust lanes are also seen. All dust structures are more prominently seen in the structure map of the galaxy, presented in the first row (third panel) of Fig. 5.7.

As presented in the second, third and fourth rows (first panels) of Fig. 5.7, the emission across all line groups is the strongest in the nuclear ring. Inwards from the nuclear ring the emission decreases, though it remains relatively high. In comparison to H$\alpha$ and [N II]$\lambda$6583, the [O III]$\lambda$5007 emission is notably weak. As shown in the second, third and fourth rows (second panels) of Fig. 5.7, the velocity field of H$\alpha$ and [N II]$\lambda$6583 show strong distortions from circular motion. Outside the nuclear ring, the zero velocity line has a strong indent at ∼8-10″ northwest and southeast from the centre. The indent is less pronounced in the OIII velocity field, but there it extends further, all the way to the nuclear ring. As shown in the second and third rows (third panels) of Fig. 5.7, the velocity dispersion of H$\alpha$ and [N II]$\lambda$6583 is the lowest in the nuclear ring, reaching around ∼50–60 kms$^{-1}$ inside the nuclear ring the velocity dispersion values increase up to 90 kms$^{-1}$ in the region ∼3″ southwest of the nucleus. Outside the nuclear ring, the velocity dispersion values increase up to well above 120 kms$^{-1}$. The velocity dispersion values for [O III]$\lambda$5007 can not be reliably estimated due to poor signal, although even the noisy values suggest the same trends as in H$\alpha$ and [N II]$\lambda$6583.

After fitting the rotating disk with `Kinemetry`, $i$ and PA of the LON converged to 46° and 23° respectively. While the $i$ aligns well with measurements from a large-scale study of Erwin et al. (2008) ($i$=46°, PA of the LON=10°), the PA of the LON slightly deviates from them. As presented in the first row (fourth panel) of Fig. 5.7 the residual velocity

map exposes two coherent structures with amplitudes of $\sim$50 kms$^{-1}$, one exhibiting negative and one exhibiting positive velocities. The feature with positive velocities can be traced from the right edge of the panel at $\Delta\delta\sim8''$ towards the northern tip of the nuclear ring, coinciding with one of the main faint dust lanes along the bar. The feature with negative velocities coincides with the L-shaped dust lane. Along the dust lanes within the nuclear ring, there are two more coherent structures, one with positive and one with negative velocities with amplitudes up to $\sim$50 kms$^{-1}$.

Furthermore, several other relatively extended structures with high residual velocity amplitudes are exposed to the east and west of the nuclear ring; one exhibiting negative and two exhibiting positive velocities. The structure with negative velocities has velocity amplitudes $\sim$40 kms$^{-1}$, and extends $\sim6''$ northeast from the centre directly towards the south, coinciding with the faint dust lane observed to the east of the nuclear ring. The two other features with positive velocities, have velocity amplitudes above $\sim$50 kms$^{-1}$, each having roughly $\sim5''$ extent that curves towards the west of the nuclear ring. This appearance of the residual velocity map challenges the textbook understanding of shocks in bars, as in NGC 3351 outside the nuclear ring their kinematic signatures extend along the bar only over a short distance, and then take a right-angle turn, past which they coincide with dust lanes *perpendicular* to the bar.

The velocity difference map, presented in the second row (fourth panel) of Fig. 5.7, exposes two coherent structures with amplitudes of $\sim$30-40 kms$^{-1}$, one at the west of the nuclear ring exhibiting negative velocity, and the other at the east of the nuclear ring exhibiting positive velocity. These two structures are among the structures with highest velocity difference amplitudes I observed in other galaxies I studied in this thesis; not related to AGN. They are consistent with the textbook picture of shocks in bars, they occur downstream from the dust lanes associated with those shocks, but their morphology shows little or no consistency with that of the velocity residuals. Inwards from the nuclear ring, near locations of the peak residual velocities, the velocity differences also show an increase, reaching amplitudes of $\sim$15–20 kms$^{-1}$.

The BPT map presented in the third row (fourth column) of Fig. 5.7, shows that the emission from the nuclear ring is strongly dominated by SF. Outside the nuclear ring, there is composite emission with a contribution from SF. Particularly, to the west of the nuclear ring, there is composite emission with a contribution from LINER emission. Inwards from the nuclear ring, towards the southwest of the nucleus, there is composite emission.

NGC 3351 exhibits clear signatures of extended shocks. These structures have elevated residual velocity amplitudes, and they are cospatial with coherent morphology of dust structures, especially inside the nuclear ring. Along with elevated velocity differences,

there is dominating composite emission inwards from the nuclear ring. Therefore, even though these structures appear rather discontinuous, and are not continuously extending from outer regions towards the nucleus, I still associate them with extended shocks, dominating the inner kpc of the galaxy. Therefore, based on the kinematic categories defined in Sect. 6.1, NGC 3351 falls under the "broken shocks" category.

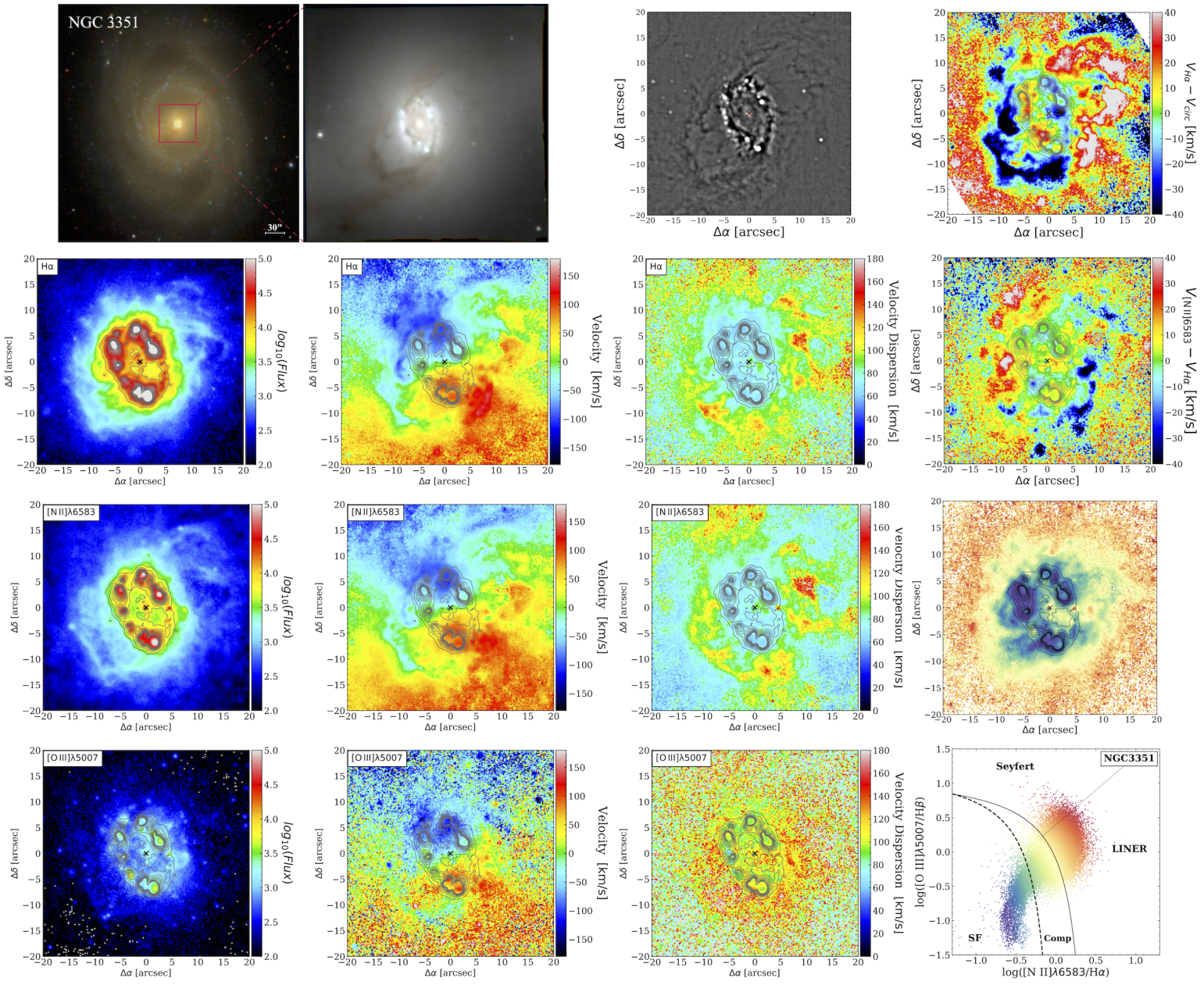


FIGURE 5.7: The diagnostic maps of NGC 3351. Panels are the same as in Fig. 5.1.

## 5.8 NGC 3368

NGC 3368 belongs to the Leo Group together with the galaxy NGC 3351. As presented in the first row (first and second panel) of Fig. 5.8, the galaxy hosts a luminous dusty core and two bars – an outer bar with a length of 75″ and an inner bar with a length of 5″ (Erwin, 2004; Erwin et al., 2015); in between the two bars, there is a nuclear disk (Möllenhoff & Heidt, 2001; Erwin, 2004; Erwin et al., 2015). The outer bar is surrounded by spiral arms. The MUSE FOV covers the core with roughly two-thirds of the outer bar. The dust structures around the core of the galaxy are more clearly seen in the structure map, presented in the first row (third panel) of Fig. 5.8.

As presented in the second, third and fourth rows (first panels) of Fig. 5.8, the strongest emission across all line groups is concentrated within the ∼3″ radius, mostly to the west of the centre. As presented in the second, third and fourth rows (second panels) of Fig. 5.8, the velocity field of all emission line groups does not exhibit strong perturbations; the zero velocity line remains relatively straight. Two structures, showing local velocity maxima, at PA 100° and –80°, extend radially by ∼8″. Another linear structure, showing velocity maxima, also at a PA −80°, is located slightly outside the frame, roughly at ∼20″ from the centre. This structure has positive velocities, counter-rotating with respect to the surroundings.

As presented in the second and third rows (third panels) of Fig. 5.8, the overall velocity dispersion of H$\alpha$ and [N II]$\lambda$6583 is high, with values around ∼100–150 kms$^{-1}$. The regions with the highest dispersion, where values exceed 150 kms$^{-1}$, form a biconical structure extending from the centre towards the northwest and southeast. This structure is more prominently seen in the [N II]$\lambda$6583 velocity dispersion map. Another region with velocity dispersions exceeding 150 kms$^{-1}$ appears towards the edge of the frame, where the gas is counter-rotating, as seen in the velocity map. The velocity dispersion values of [O III]$\lambda$5007, presented in the fourth row (third panel) of Fig. 5.8, are overall noisy due to poor signal within the FOV, yet the values still suggest an increase along the biconical structure seen in H$\alpha$ and [N II]$\lambda$6583 fields.

The disk orientation parameters estimated with Kinemetry, $i$=46° and PA of the line of nodes (LON)=172°, agree with estimations from large-scale studies (e.g., Erwin et al., 2008: $i$=50° and PA of the LON=172°). Upon analysing the residual velocity map, presented in the first row (fourth panel) of Fig. 5.8, within the ∼5″ radius towards the northeast, there are extended structures that show similar winding with dust spiral arms which may be related to the kinematics. Moreover, two structures, one with positive and one with negative velocities extend along the biconical structure seen in velocity

dispersion, the highest amplitudes of velocity residuals roughly coincide with the highest velocity dispersion. The velocity difference map, presented in the second row (fourth panel) of Fig. 5.8, is noisy and does not exhibit coherent structures. However, where the highest velocity dispersion values are seen along the biconical structure, the velocity differences also show an increase. The region to the southeast exhibits negative velocity differences and the region to the northwest exhibits positive velocity differences, both with amplitudes around $\sim$20–30 $\mathrm{kms}^{-1}$. The biconical morphology of the observed structure with extreme velocity dispersions, along with structures seen in velocity residual and velocity difference maps confirm that this structure outflows from the AGN. The counter-rotating portion of the gas is a consequence of the outflowing gas, moving in different conditions with respect to its surroundings.

Furthermore, the BPT map presented in the third row (fourth panel) of Fig. 5.8, reveals that the ionisation throughout the entire FOV is predominantly coming from the LINER emission with weak contribution from composite emission.

Although the galaxy is dominated by an AGN, which could potentially prevent identifying extended shocks near the nucleus, I have resolved structures within the innermost regions that are not obscured by AGN outflows. Generally, there is no compelling evidence of extended shocks within the inner kpc of NGC 3368. Thus, I classify this galaxy as showing no signs of extended shocks. Based on the kinematic categories defined in Sect. 6.1, NGC 3368 falls under the "other perturbations" category.

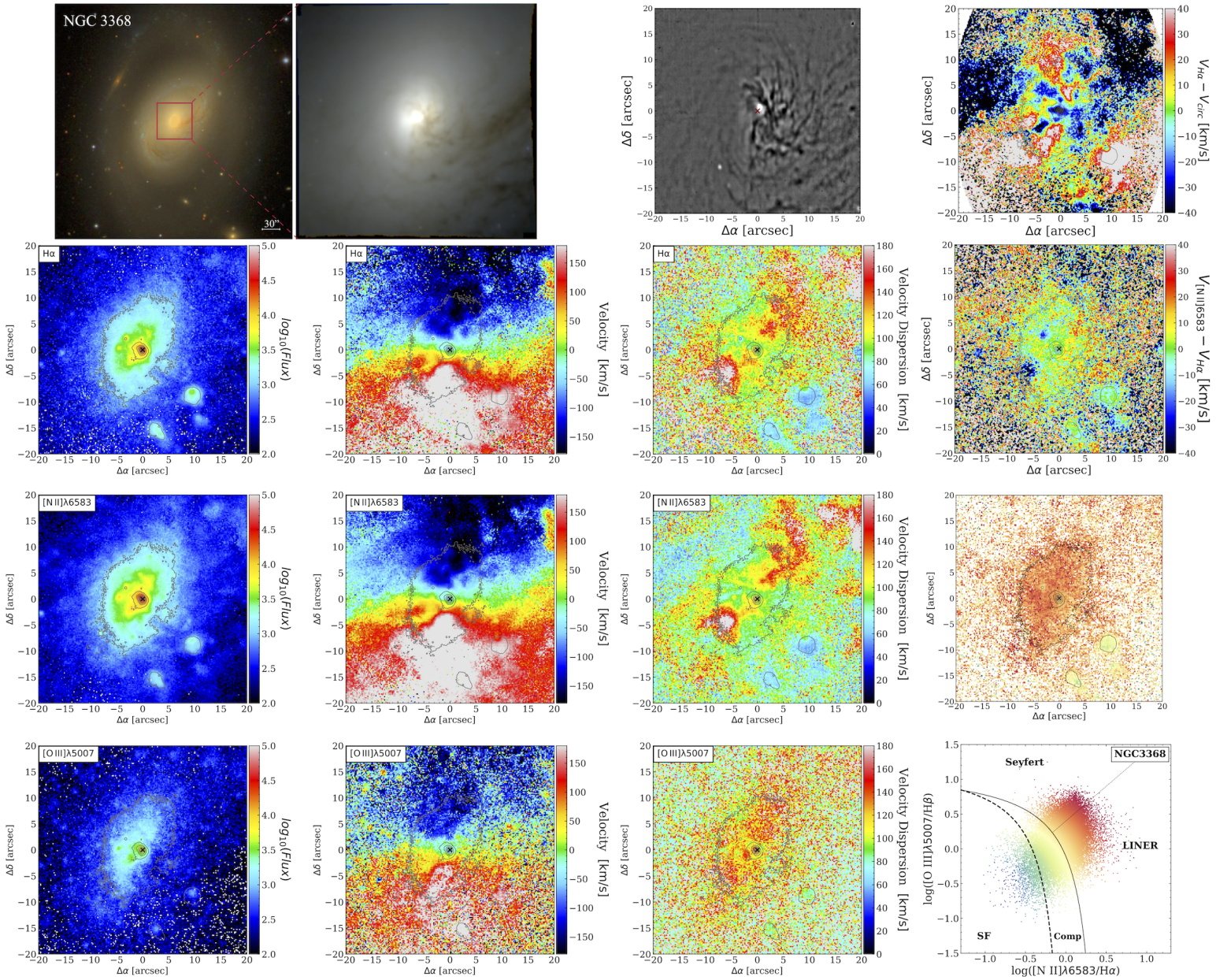


FIGURE 5.8: The diagnostic maps of NGC 3368. Panels are the same as in Fig. 5.1.

## 5.9 NGC 3489

As presented in the first row (first and second panel) of Fig. 5.9, NGC 3489 hosts a bright core, and a bar with $\sim 20''$ in size (Erwin & Sparke, 2003), embedded in a dusty disk of size. The spectral classification of the galaxy's core falls within the Seyfert region (Ho et al., 1997; Sarzi et al., 2006). The MUSE FOV covers the core, the bar and the disk. The structure map presented in the first row (third panel) of Fig. 5.9, enunciates a prominent dust spiral, originating from the west of the frame and circling the bar region in the counter-clockwise direction. Moreover, to the northeast and southwest, two very faint straight dust lanes are seen along the bar; these two lanes appear to connect a dusty ring of semi-major axis $\sim 3$–$4''$.

As presented in the second, third and fourth rows (first panels) of Fig. 5.9, the strongest emission across all line groups is mostly confined within the inner $\sim 5''$. Within the radius of approximately $\sim 2$–$3''$, the strongest emission exhibits several off-centred and elongated peaks, indicative of a small nuclear ring. A similar ring structure of size $\sim 3''$ is reported in former works (Erwin & Sparke, 2003; Nowak et al., 2010). Within the same region, [O III]$\lambda$5007 emission is exceptionally strong, exhibiting quasi-radial extensions to the southwest, that may be related to shocks in the bar.

The velocity fields across all line groups, shown in second, third and fourth rows (second panels) of Fig. 5.9, reveal a wiggly zero velocity line, where it forms an "S" shape within the $\sim 4''$ radius, associated with the characteristic flow in bars. There is also a peculiar "blue arm", with negative velocities extending to the southeast, strongest in [O III]$\lambda$5007. As demonstrated in the second, third and fourth rows (third panels) of Fig. 5.9, the velocity dispersion of all line groups is high in the nucleus, with values around $\sim 100$–$120\,\mathrm{km s^{-1}}$. Within the nuclear ring, the velocity dispersion decreases; values remain consistent towards the southwest end of the frame. To the northeast and southwest of the centre, I discern two local velocity dispersion minima with values $\sim 50$–$60\,\mathrm{km s^{-1}}$; these structures coincide with the off-centred peaks in emission. Throughout the dust spiral surrounding the bar region, the velocity dispersion values of H$\alpha$ and [N II]$\lambda$6583 remain around $\sim 50$–$60\,\mathrm{km s^{-1}}$, values for [O III]$\lambda$5007 cannot be estimated reliably due to poor signal in those regions, yet the dispersion is generally low.

After fitting the rotating disk to the H$\alpha$ velocity field, the $i$ and the PA of the LON converged to $60^\circ$ and $80^\circ$ respectively. While $i$ agrees well with the measurements estimated from large-scale fits, the PA of LON differs by $10^\circ$ (e.g., Erwin et al., 2008: PA of the LON=$71^\circ$, $i$=$58^\circ$). However, when employing the large-scale PA of the LON in the disk model, artefacts of $m$=1 harmonic terms appear in the residual velocity field. These artefacts were not observed when using values deduced by `Kinemetry` in

the model. Consequently, I chose to use the `Kinemetry` inferred parameters in the final disk model.

The residual velocity map of the galaxy, presented in the first row (fourth panel) of Fig. 5.9, exposes two structures located $\sim 2''$ towards the north and south of the centre; one with negative and one with positive velocities, both exhibiting amplitudes $\sim 40\,\mathrm{kms}^{-1}$. Both structures have an additional $\sim 2''$ extension towards northeast and southwest with weakened velocity amplitudes ($\sim$10–20 $\mathrm{kms}^{-1}$); these extensions coincide with the faint dust lanes along the bar and they are consistent with the conception of shocks in gas. Moreover, strong residuals of radial extend, with values around $\sim$40–50 $\mathrm{kms}^{-1}$ or more, are also seen where there is quasi-radial emission.

The velocity difference map, presented in the second row (fourth panel) of Fig. 5.9, appears rather noisy, yet it does reveal very faint negative and positive velocities, with values around $\sim$5–10 $\mathrm{kms}^{-1}$, within the $\sim 2''$ radius, coinciding with the regions with high residual velocity amplitudes. The aligning coherent structures of elevated velocity residuals and velocity differences, together with the aligning dust morphology, can be associated with extended shocks in gas, extending from the outer regions towards the core.

The BPT map shown in the third row (fourth panel) of Fig. 5.9 reveals strong AGN dominance in the radiation from a Seyfert core. In the nuclear ring, there is a slightly reduced AGN contribution, coinciding with the region with low velocity dispersion, suggestive of the nuclear ring being fed by the inflowing gas. In literature, the galaxy is discussed to have a rejuvenated nucleus with a young central stellar population based on luminosity-weighted ages (Annibali et al., 2007), and this is further associated with the potential gas inflow within the central region towards the AGN (Annibali et al., 2010; Marino et al., 2011). Therefore, the interpretation of the coherent structures being extended shocks propagating towards the nucleus appears to align with these findings.

Generally, the overall emission in NGC 3489 seems to be of an AGN nature, but the gas flow is not affected by the AGN. The galaxy exhibits signatures of extended shocks, and based on the kinematic categories defined in Sect. 6.1, it falls under the “coherent shocks” category.

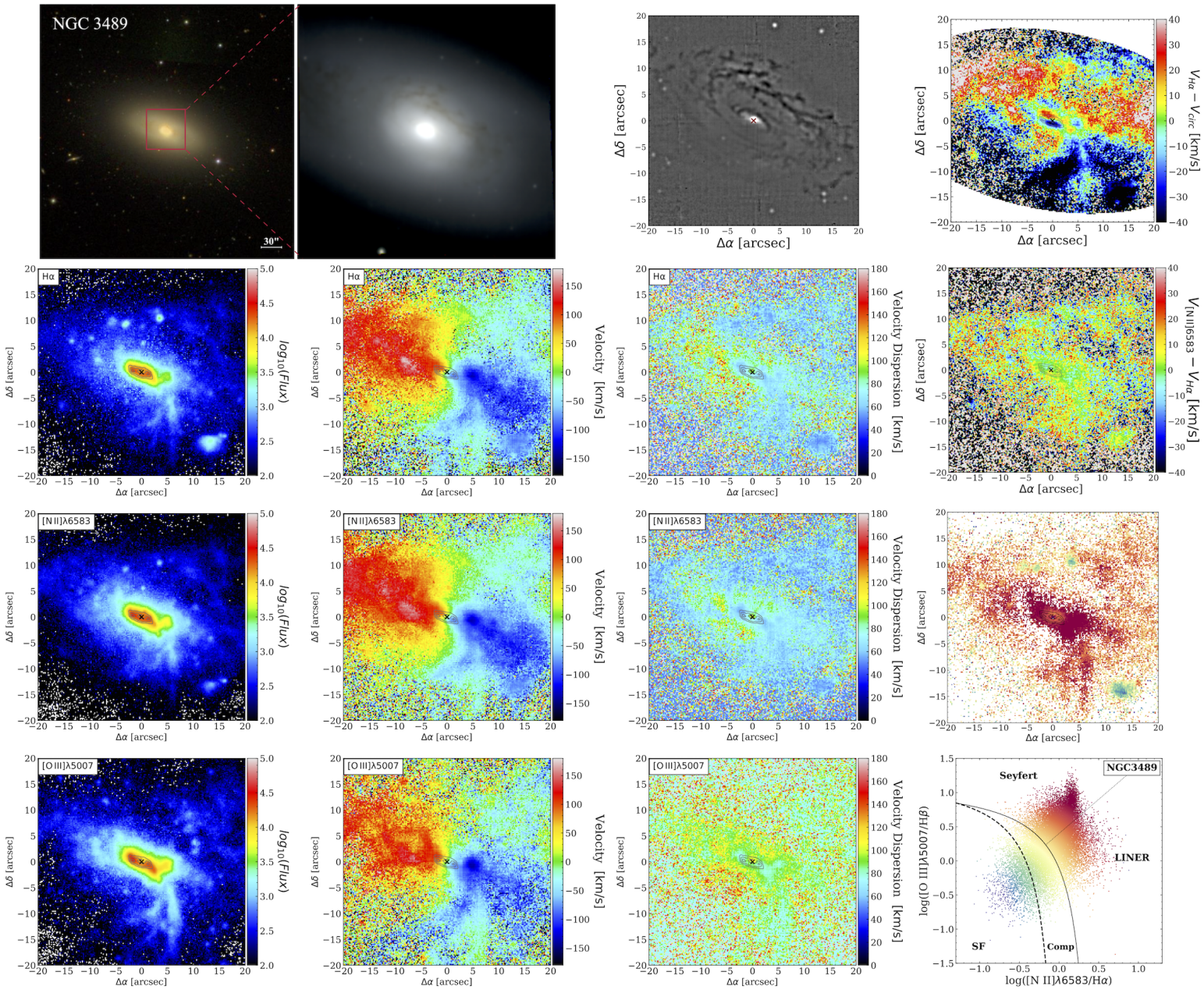


FIGURE 5.9: The diagnostic maps of NGC 3489. Panels are the same as in Fig. 5.1.

## 5.10 NGC 3626

NGC 3626 is one of the most complex sample galaxies I studied in this thesis. It is a member of the Leo II group. It is classified as an unbarred galaxy de Vaucouleurs et al. (1991), although several photometric studies show evidence of a double barred morphology (Möllenhoff & Heidt, 2001; Gutiérrez et al., 2011); the inner bar is within ∼2–2.5″ radius and outer bar is within ∼20″ radius. Examining the stellar velocity dispersion and higher order moments of NGC 3626, I identify the velocity dispersion signatures, $\sigma$-hollows, characteristic to double-barred galaxies (see de Lorenzo-Cáceres et al., 2008), agreeing well with the proposed orientation and size of the inner bar. Therefore, for further analysis, I settle on using double barred morphology for NGC 3626. The gas in the galaxy is counter-rotating with respect to the stars (Ciri et al., 1995; García-Burillo et al., 1998), which I confirm after comparing the stellar and gas velocity maps.

In the first row (first and second panel) of Fig. 5.10, it can be seen that NGC 3626 hosts a luminous core and a nuclear bar embedded in a dusty disk; the outer bar is not well defined in the composite image. The MUSE FOV covers more than half of the entire galaxy. As notably seen in the structure map, presented in the first row (fourth panel) of Fig. 5.10, there are prominent dust lanes surrounding the outer bar region.

As shown in the second, third and fourth rows (first panels) of Fig. 5.10, across all line groups, the emission within the ∼4″ radius is relatively strong and extended towards the northwest and southeast direction, manifesting an "S" shape. There is also strong and clumpy emission forming a boxy ring structure of ∼15″ radius, coinciding with some of the dust lanes. Extending from the ends of the inner bar towards northwest and southeast, two lanes of emission connect to the boxy ring structure. These two emission lanes resemble the characteristic emission along the bar for gas co-rotating with (or trailing) the stars, but since the gas is counter-rotating in that region, the emission lanes are leading instead of trailing the stars. This indicates that the gas in NGC 3626 likely has two different origins.

As shown in the second, third and fourth rows (second panels) of Fig. 5.10, the velocity field across all emission line groups shows peculiar structures. Overall the velocity map follows the typical spider pattern, yet inwards from the boxy ring, there is a notable change in the PA of the zero velocity line. Within the ∼5″ radius, the PA of the LON is around 130°, while beyond this region, the PA of the LON is almost perpendicular to the zero velocity line, measuring ∼160°. This shift in the PAs suggests that the gas is moving in two different planes, indicating likely two different origins. At ∼3″ towards the northwest and southeast from the centre, two local velocity peaks are seen.

As shown in the second and third rows (third panels) of Fig. 5.10, throughout the boxy ring, the velocity dispersion of H$\alpha$ and [N II]$\lambda$6583 remains around 50 kms$^{-1}$. Inwards from the boxy ring, the velocity dispersions are generally high, with the highest values being in the core. Almost perpendicular to the inner bar, a region extending from the centre towards $\sim$4″ east and west, shows consistently high velocity dispersions, with values around $\sim$130 kms$^{-1}$; in certain spaxels values even exceed $\sim$150 kms$^{-1}$. Additionally, situated $\sim$1-2″ beyond the endpoints of the inner bar, the velocity dispersions are also high, with values around 130 kms$^{-1}$. This observation further confirms the presence of two kinematically distinct regions inwards from the boxy ring, supporting the argument for gas having two different origins there. The velocity dispersion of [O III]$\lambda$5007 is not reliably estimated due to poor signal, but the values generally show a similar trend to H$\alpha$ and [N II]$\lambda$6583 velocity dispersion values.

While the distributions of PA of the LON and $i$ obtained from Kinemetry strongly vary inwards from the boxy ring, the distributions estimated outwards from the boxy ring converge around $i$=53° and the PA of the LON=163°, which agree well with the values estimated from large-scale photometric fits in CBS (see Table C.1). This indicates that outwards from the boxy ring, the gas is moving within the galaxy plane, while inward from the boxy ring inwards, the gas is moving out of the galaxy plane and can not be described by a planar motion. Consequently, the residual velocity map, presented in the first row (fourth panel) of Fig. 5.10, reveals distinct artefacts of wrongly fitted PA of the LON, $m$=1 harmonic terms, inwards from the boxy ring. Despite attempting various parameter adjustments for fitting the rotating disk better inwards from the boxy ring, these artefacts persisted and were not minimised. Although several extended structures are present throughout the boxy ring, they do not exhibit a turning behaviour towards the inner regions.

The velocity difference map presented in the second row (fourth panel) of Fig. 5.10, is noisy and does not show prominent extended structures. However, only within $\sim$1–2″ radius, I notice a blue and a red structure with residual velocity amplitudes $\sim$20 kms$^{-1}$, possibly counterparts of one another, though these structures are rather amorphous. Moreover, from the centre $\sim$4″ towards the north and south, there are also two regions with elevated velocity differences, one region exhibiting negative and the other region exhibiting positive velocities, with amplitudes $\sim$15–20 kms$^{-1}$.

As shown in the BPT map, presented in the third row (fourth panel) of Fig. 5.10, inwards from the boxy ring, the ionisation is dominated by the AGN, where there is mostly LINER emission. Throughout the boxy ring, there is composite emission with weak contribution from star formation.

The complex nature of kinematically distinct gas regions within NGC 3626, prevents us from accurately modelling the disk inwards from the boxy nuclear ring; thus the residual velocity map of the galaxy was dominated by the artefacts. Although I identify emission along the inner bar and a possible flow along the inner bar from the velocity difference map, these structures are rather weak to be interpreted as extended gas shocks. Therefore the galaxy is classified as not showing signatures of extended shocks. Particularly, based on the kinematic categories defined in Sect. 6.1, NGC 3626 falls under the "other perturbations" category.

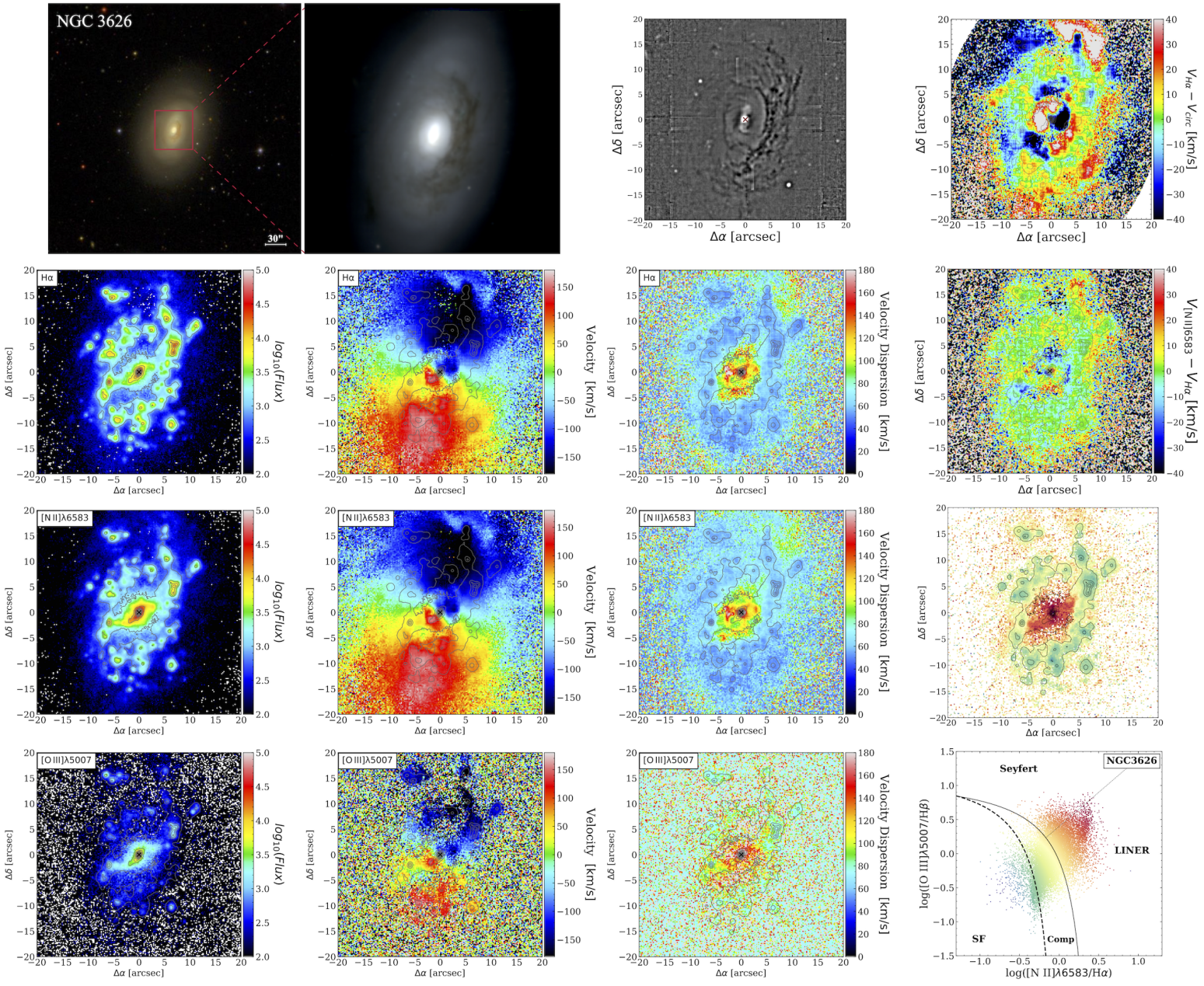


FIGURE 5.10: The diagnostic maps of NGC 3626. Panels are the same as in Fig. 5.1.

## 5.11 NGC 4237

NGC 4237 is a member of the Virgo Galaxy Cluster (Tully, 1988). As shown in the first row (first and second panel) of Fig. 5.11, the galaxy is unbarred and has prominent star formation and dusty spiral arms encircling its bright core. The MUSE FOV covers almost the entire galaxy. The dust structures in spiral arms are enunciated in the structure map, presented in the first row (third column) of Fig. 5.11.

As shown in the second, third and fourth rows (first panels) of Fig. 5.11, there is clumpy emission across all line groups forming a broken spiral structure. The H$\alpha$ emission, likely originating from SF, is significantly stronger compared to [N II]$\lambda$6583 and [O III]$\lambda$5007. The velocity fields of H$\alpha$ and [N II]$\lambda$6583 presented in the second and third rows (second panels) of Fig. 5.11, are relatively unperturbed, exhibiting motion close to circular. The H$\alpha$ and [N II]$\lambda$6583 velocity dispersions presented in the second and third rows (third panels) of Fig. 5.11, remain around $\sim$50 kms$^{-1}$ across the whole FOV.

The PA of the LON=107° and $i$=53° obtained from `Kinemetry` agree well with the same parameters estimated in large-scale studies, (Chemin et al., 2006), as shown in Table C.1. Residual velocity map, presented in the first row (fourth panel) of Fig. 5.11, exposes weak quasi-spiral structures, with amplitudes of $\sim$5–10 kms$^{-1}$, but due to their low amplitudes, I do not interpret them as extended shocks; I will elaborate on the velocity amplitudes of shocks more in Chapter 6. Across the entire FOV, the velocity difference map, presented in the second row (fourth panel) of Fig. 5.11, is noisy. In this map, I observe a weak $m$=0 signature of amplitude $\sim$5–10 kms$^{-1}$ mirroring the velocity distribution, which for a presumably single-component gaseous medium may indicate a slight offset between the derived H$\alpha$ and [N II]$\lambda$6583 velocity fields that is proportional to the velocity magnitude. This further confirms the absence of extended shocks in the field.

The BPT map, presented in the third row (fourth panel) of Fig. 5.11, exhibits predominant SF in multiple spiral arms, together with some composite emission. Several round regions show the emission of the LINER type, coinciding with the regions with enhanced [N II]$\lambda$6583 velocity dispersion, which may indicate local shocks.

NGC 4237 has relatively unperturbed kinematic fields and does not exhibit signatures of extended shocks. Therefore, based on the kinematic categories defined in Sect. 6.1, this galaxy falls under the “unperturbed” category.

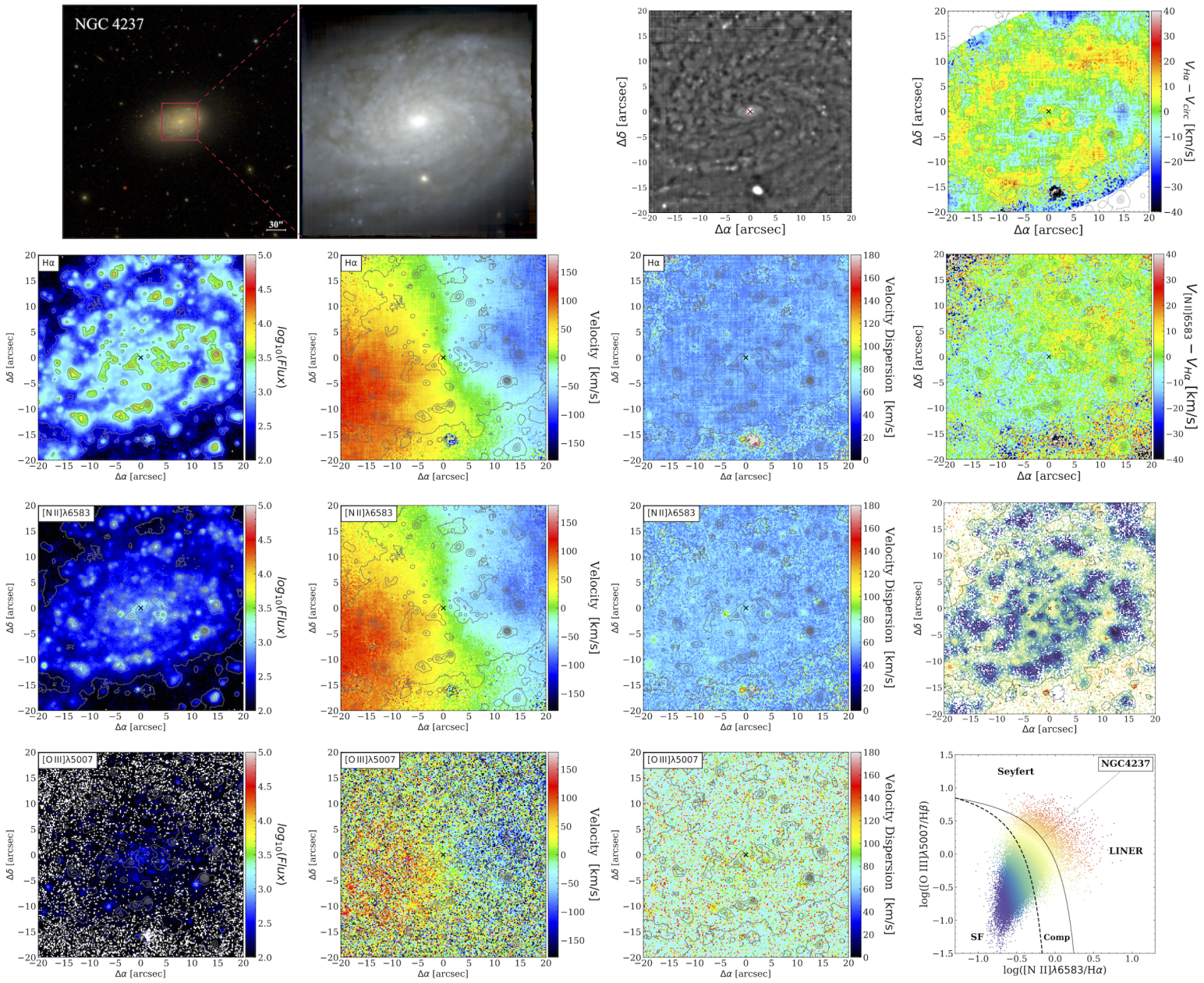


FIGURE 5.11: The diagnostic maps of NGC 4237. Panels are the same as in Fig. 5.1.

## 5.12 NGC 4303

NGC 4303 has a luminous core surrounded by a star-forming nuclear ring of ∼3″ radius (Colina & Wada, 2000). This galaxy also has a nested bar system; an inner nuclear bar of ∼2″ radius and an outer bar of ∼20″ radius (Laine et al., 2002; Schinnerer et al., 2002), the outer bar is encircled by spiral arms. As shown in the first row (first and second panel) of Fig. 5.12b , the MUSE FOV, covers the core, the nuclear ring and two bars. As enunciated in the structure map, presented in the first row (third column) of Fig. 5.12b , two prominent dust lanes along the outer bar are connecting to the nuclear ring; inwards from the nuclear ring, the dust lanes along the nuclear bar are also visible.

The flux, velocity and velocity dispersion maps of NGC 4303 referred to in this paragraph show the measurements obtained from single Gaussian fits, presented in Chapter 2. As shown in Figs. 2.11–2.13, the strongest emission across all line groups is confined within the nuclear ring and the core. Outside the nuclear ring, there is clumpy H$\alpha$ and [N II]$\lambda$6583 emission; H$\alpha$ being stronger. The velocity field of all emission line groups, shown in Figs. 2.14–2.16 reveals perturbations superimposed on the circular rotation, clearly manifested in the rugged zero velocity line. Also, ∼5–10″ west to northwest of the nucleus, where the velocities are anticipated to be redshifted, several regions with blueshifted velocities are seen, most notably in [N II]$\lambda$6583 and [O III]$\lambda$5007. In the [O III]$\lambda$5007 velocity map, there is also a region with strong blueshifted velocities, extending from the centre ∼7″ towards the south, suggesting a contribution from outflows. As shown in Figs. 2.17 and 2.18, inwards from the nuclear ring, the velocity dispersion values are up to ∼100 kms$^{-1}$ in H$\alpha$ and up to ∼150 kms$^{-1}$ in [N II]$\lambda$6583 in two peaks ∼2″ offset from the centre. In the nuclear ring and to the east of it, there is low H$\alpha$ and [N II]$\lambda$6583 velocity dispersion, with values around ∼ 60 kms$^{-1}$. Outside the nuclear ring, both H$\alpha$ and [N II]$\lambda$6583 velocity dispersion values are generally around 60–80 kms$^{-1}$, but to the northwest and southeast of the centre, the values are high, around 100–130 kms$^{-1}$. Particularly, in a small region ∼7″ to the northwest of the centre, the [N II]$\lambda$6583 velocity dispersions reach their highest values, exceeding 200 kms$^{-1}$. The [O III]$\lambda$5007 velocity dispersions, shown in Fig. 2.19, exhibit values over 200 kms$^{-1}$ in a ring of ∼1–4″ around the centre, and ∼6″ extension to the south. The region extending to the south coincides with the strong blueshifted [O III]$\lambda$5007 velocities.

The high velocity dispersion of [O III]$\lambda$5007 prompted us to search for an excess emission in the spectra, and the Gaussian fits. If there is an excess emission in the spectra, fitting the excess and the main emission line with single Gaussians is not sufficient. The fitted Gaussian will be broad and will artificially increase the velocity dispersion and alter the velocity of the main emission line, as I explained in Chapter 2 (Sects. 2.3.3 and 2.3.4).

Upon a closer examination of the spectra where velocity dispersion of [O III]$\lambda$5007 is high, I noticed a weak asymmetry in the [O III]$\lambda$5007 line profile. To ensure this asymmetry does not artificially influence the measurements, following the same concept introduced in Kolcu et al. (2023), I allowed for fitting a secondary component to [O III]$\lambda$5007. If the emission is dominated by two components along the LOS, coming from both the excess emission sources and the disk, fitting two components will allow separating them. After allowing to fit a secondary component to [O III]$\lambda$5007, in the region where highly blueshifted [O III]$\lambda$5007 velocities and high [O III]$\lambda$5007 velocity dispersions are seen, I did not notice a significant [O III]$\lambda$5007 velocity shift. The velocity dispersion of [O III]$\lambda$5007 in the same region was reduced by 30–40%; despite this reduction, the values remained high, confirming that the disturbance of the [O III]$\lambda$5007 is real. The extreme kinematics of [O III]$\lambda$5007 likely indicate a contribution from AGN outflows. Since kinematics are not significantly affected by the excess emission, to reduce the number of free parameters of the fit I only use single Gaussians to fit [O III]$\lambda$5007.

Not only in [O III]$\lambda$5007 but high velocity dispersions are also seen in [N II]$\lambda$6583. Thus, to ensure these values are real, following the same concept and procedure in Kolcu et al. (2023), I allowed for fitting a secondary component to the [N II]$\lambda$6583 within the entire FOV. I note that an excess emission to the blue wing of [N II]$\lambda$6583 can affect the Gaussian fits to both H$\alpha$ and [N II]$\lambda$6583, causing artificially high velocity and velocity dispersions for both, as seen in my pilot study with NGC 1097 (see Sect. 2.3.3). This issue can consequently affect the residual velocity map of NGC 4303, which I construct by fitting a disk model to the H$\alpha$ velocity field. Comparisons between measurements obtained from single Gaussian fits and fits including the secondary component, did not show a significant velocity shift or velocity dispersion change for H$\alpha$, indicating that the residual velocity map is not affected by an excess emission. However, the introduction of the secondary component led to a [N II]$\lambda$6583 velocity shift of $\sim$5–10 kms$^{-1}$ and a [N II]$\lambda$6583 velocity dispersion reduction of $\sim$40% in the regions to the east and west of the centre, where velocity dispersion of [N II]$\lambda$6583 was originally high, but also to south of the centre, which coincide with highly blueshifted [O III]$\lambda$5007 velocities and high [O III]$\lambda$5007 velocity dispersions. This spatial coincidence likely indicates that [N II]$\lambda$6583 is also affected by the AGN outflows. Such differences in [N II]$\lambda$6583 measurements are large enough to recognise the contribution from the AGN outflows but have a negligible effect on the velocity difference maps, which incorporate [N II]$\lambda$6583 velocity field together with H$\alpha$. Therefore, to the east, west and south of the centre, I do not apply masking and the measurements are kept with those obtained from the single Gaussian fits.

However, the most prominent [N II]$\lambda$6583 velocity shifts, $\sim$40–60 kms$^{-1}$, occur outside the nuclear ring, $\sim$7″ northwest of the centre, where the highest [N II]$\lambda$6583 velocity

dispersions are originally seen; see Fig. 5.12a . Including the secondary component to the fitting reduced the velocity dispersions there by ∼60–70%. This region is outlined by a pink box in the second panel of Fig. 5.12a , also presented in the third panel of the same figure after certain mask conditions are applied, which is explained below in more detail. Additionally, this region has anomalously blueshifted [N II]λ6583 velocities, while Hα velocities are at similar values to the surrounding.

Because of such large changes in [N II]λ6583 velocity and velocity dispersion after introducing the secondary component to the fitting, I had a closer look at the spectra of spaxels in that region. The Hα and [N II]λ6583 wavelength region of spectra exhibited features much more complex than those seen in NGC 1097. To demonstrate this, in the first panel of Fig. 5.12a , I present two spectra: (a) from a spaxel where the fits are unaffected by the excess emission, (b) from a spaxel where the fits to [N II] components are significantly affected from the excess emission, (c) from the same spaxel in (b), after the excess emission is fitted with the secondary component. In all three sub-panels, there are two emission line components associated with components of [N II] doublet and of Hα; unlike what is seen in the spectra of NGC 1097, NGC1433 and NGC4321 where the excess emission only appears as an asymmetry to the main emission line. In spaxel marked with an "x" in the second panel (left) of the figure, fitting single Gaussians to each emission line recovers well the parameters of the main component. However, in spaxel marked with an "+" in the second panel (left) of the figure, the fit to the Hα line incorporates the main component only, and the fit to [N II]λ6583 line incorporates both the main and secondary components which artificially increases the [N II]λ6583 velocity dispersion and blueshifts the [N II]λ6583 velocities for that spaxels. Since Hα is fitted well, the measurements are not affected by the second component of [N II]λ6583. Moreover, since [N II]λ6548 and [N II]λ6583 fits are kinematically bound, the wrongly fitted single Gaussian to [N II]λ6583 also affects Gaussian fits to [N II]λ6548. As shown in subpanel (c), including the secondary component effectively separates the two [N II]λ6583 components, correcting the Gaussian fits. Consequently, the [N II]λ6583 velocity dispersions are reduced and the blueshifted velocities are brought back to values similar to the surrounding, as shown in the region outlined with a pink box in the second panel (right) of Fig. 5.12a .

Since such large [N II]λ6583 velocity shifts, with ∼40–60 $\mathrm{kms}^{-1}$, would affect the velocity difference maps significantly, I proceed to mask the artificial measurements in the affected region, and then use the measurements of the main line component of fits including the secondary component. The spaxels that are most affected by the excess emission are presented in the third panel of Fig. 5.12a . To correct the measurements in these spaxels, I have followed the masking concept explained in Sect. 2.3.4; ensuring there is

a significant velocity shift and velocity dispersion change for [N II]$\lambda$6583 between measurements from the two fitting approaches. Since H$\alpha$ is not affected by the secondary component, I do not include any conditions regarding H$\alpha$ measurements, unlike in the case with NGC 1097 (Kolcu et al., 2023). The conditions applied to construct the mask are as follows:

i. $V_{[N\,II]} - V_{[N\,II],corr} \leq -10$ kms$^{-1}$

ii. $\sigma_{[N\,II]}/\sigma_{[N\,II],corr} \geq 1.5$

iii. $\sigma_{[N\,II]w} \leq 300$ kms$^{-1}$

iv. $3'' \leq \Delta\alpha \leq 6''$ and $3.5'' \leq \Delta\delta \leq 6.5''$

where *corr* indicates the values extracted from the fits including the secondary component. The third condition, the velocity dispersion limit of the secondary [N II]$\lambda$6583 component ([N II]w) ensures that the secondary component is real and is not fitted to noise. The spatial cuts are applied to select the region where the change in velocity and velocity dispersion ratio is consistently large. For further analysis, the flux, velocity, and velocity dispersion values for all emission line groups within the mask region are replaced with those from the corresponding main components in fits that include the secondary component. Although H$\alpha$ and [O III]$\lambda$5007 measurements are not affected, I continue to use measurements from fits with a secondary component to maintain consistency. The resultant flux, velocity and velocity dispersion maps of all emission line groups are presented in the second, third and fourth rows (first, second and third panels) of Fig. 5.12b .

The PA of LON returned from `Kinemetry` varies from 110°, within outer regions, to 140° within regions inside the nuclear ring. Since the flow is more circular inside the nuclear ring, I explored around 140°, and converged using 135° as the PA of the LON since this value minimised the artefacts seen in the residual velocity map; 135° also agrees with values obtained from large-scale fits within a couple of degrees (Chemin et al., 2006: PA of LON=132°). $i$ inferred from `Kinemetry` converged around 42°, which differs by 18° from the inclination obtained from large-scale fits (Chemin et al., 2006: $i$=23.5°). Upon several checks, the residual velocity map resultant from subtracting a disk with $i$=23.5°, reveals weak m=3 harmonic terms, while such artefacts are less emphasised when the disk model is constructed with $i$=42°. Thus for further analysis, I settle on using the $i$ and PA of the LON inferred from `Kinemetry`. As shown in the first row (fourth panel) of Fig. 5.12b , the residual velocity map reveals a coherent structure exhibiting negative velocities, with amplitudes of $\sim$20 kms$^{-1}$ to the west of the nucleus. This structure extends from the north towards the south and connects to the nuclear

ring at the southwest, roughly coinciding with the northwestern dust lane external to the nuclear ring. After crossing the nuclear ring, the same coherent structure extends towards the nucleus from the west of the centre, roughly along the major axis of the nuclear bar. Although several extended structures exhibit enhanced positive residual velocities throughout the FOV, particularly in the nuclear ring, I do not see a clear counterpart to the structure with negative residual velocities.

As shown in the second row (fourth panel) of Fig. 5.12b , outside the nuclear ring, roughly coinciding with the coherent structures in the velocity residuals there, a coherent structure with negative velocity differences of $\sim$15–20 $\mathrm{kms}^{-1}$ is seen, extending inwards from the nuclear ring and approaching to the nucleus from the east of the centre. This structure is located $\sim$0.2–0.5″ downstream of a dust lane, which appears to be related to the nuclear bar; thus this kinematic structure can be indicative of an inflow along the nuclear bar. Moreover, two regions $\sim$1–2″ northwest and southeast from the centre, show elevated velocity differences of amplitudes $\sim$15 $\mathrm{kms}^{-1}$, one with negative and one with positive velocities, supporting the argument of potential inflow seen along the nuclear bar.

The BPT map presented in the third row (fourth panel) of Fig. 5.12b , shows predominant SF in the nuclear ring and outside of it where clumpy H$\alpha$ emission is seen. In the remaining regions, the ionisation is dominated by composite and LINER emission. Inwards from the nuclear ring, the emission is of LINER kind, agreeing with the classification from former works (e.g., Ho et al., 1997).

Both residual velocity and velocity difference maps reveal consistent signatures of extended shocks along both the outer and the nuclear bar of NGC 4303. This consistency across different methodologies indicates that signatures of extended shocks can be reliably detected using various approaches. Such findings reinforce the argument that extended shocks should be searched for using all available methods. Based on the kinematic categories defined in Sect. 6.1, NGC 4303 falls under the “coherent shocks” category.

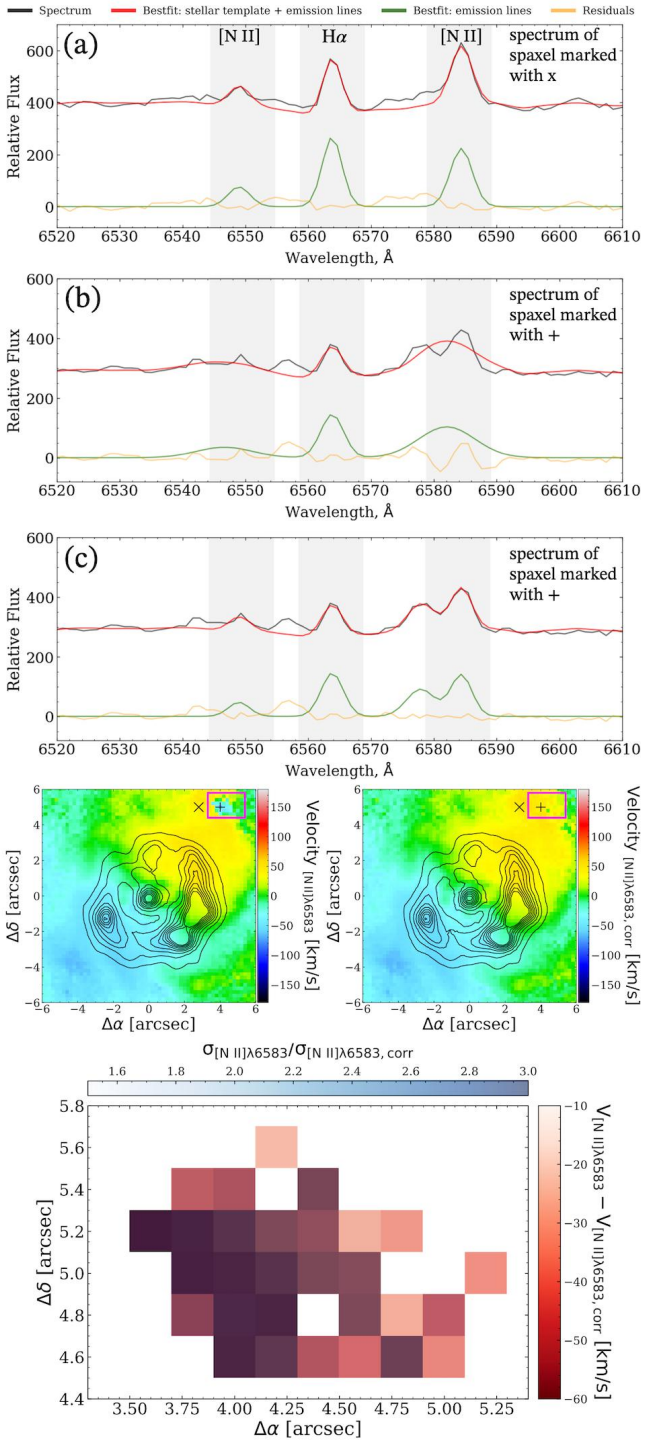


FIGURE 5.12A : *first:* Spectrum of spaxels: marked with an "x" in the second panel, excess emission does not affect the fits (a); marked with a "+" in the second panel, excess emission affects the fits (b); same spaxel as in (b), after the excess emission is fitted with a secondary component (c). The lines represent the MUSE spectrum (black), the best fit of the stellar template with emission lines (red), the best fit of the emission lines (green) and the difference between the MUSE spectrum and the combined best fit with stellar template with emission line templates (orange). *second:* velocity map of [N II]λ6583 when emission lines are fitted with single Gaussians (left), and with the secondary component included (right). The pink box represents the region where [N II]λ6583 measurements are the most affected by the excess emission. Black contours represent the Hα emission from the nuclear ring. *third:* region enclosed by the magenta box in the second panel, showing the mask of spaxels for which the fits including secondary component were used in further analysis. The red and blue colour maps show the velocity shift of [N II]λ6583 and the ratio of [N II]λ6583 velocity dispersion, respectively, before and after including the secondary component in the fitting.

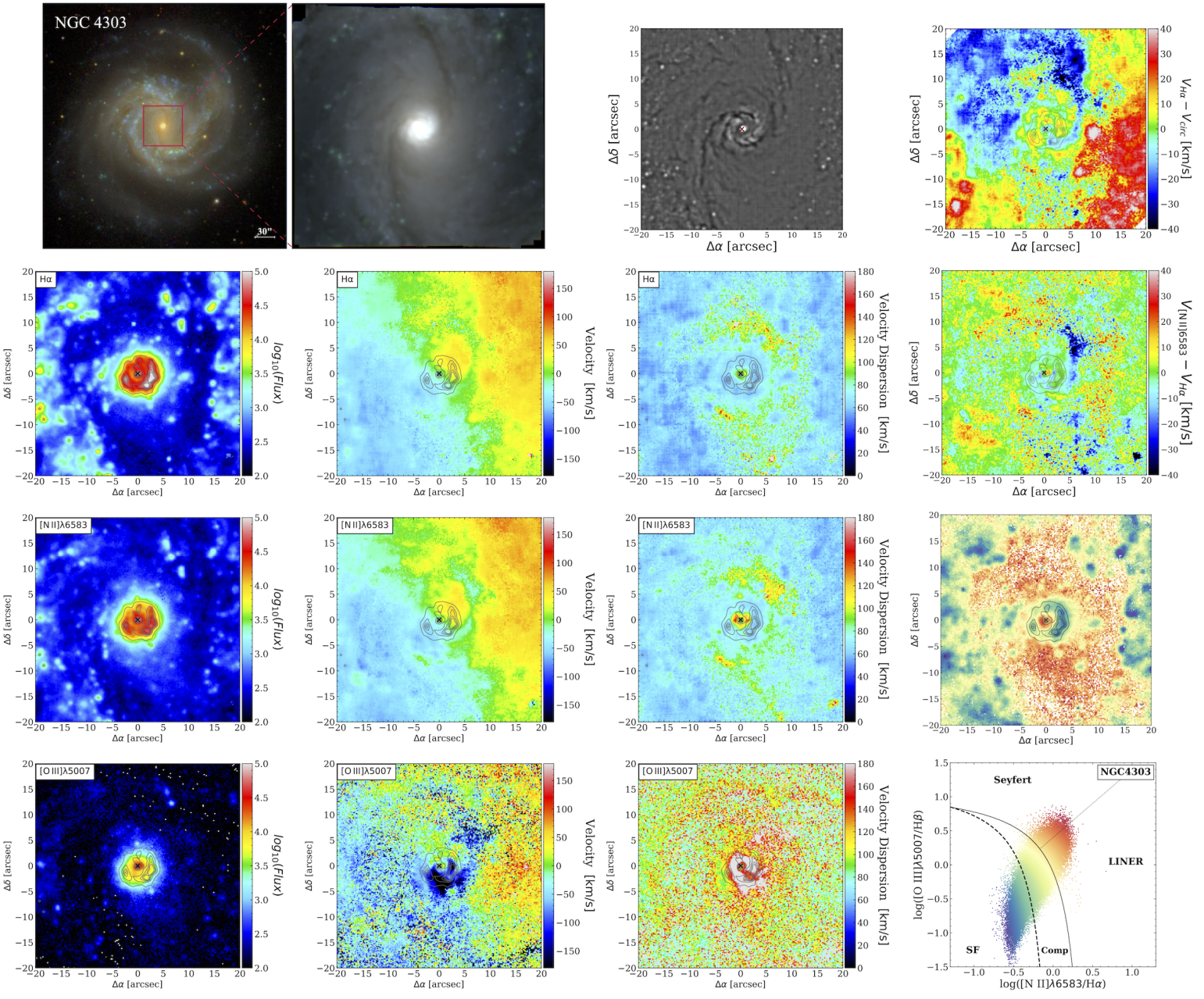


FIGURE 5.12B : The diagnostic maps of NGC 4303. Panels are the same as in Fig. 5.1.

## 5.13 NGC 4321

NGC 4321, also known as M100, is a member of the Virgo Cluster and has been extensively studied in former works (Knapen et al., 1995a,b, 2000; Ryder et al., 2001; Allard et al., 2005; García-Burillo et al., 2005; Haan et al., 2008; Pohlen et al., 2010; Hermosa Muñoz et al., 2022b; Liu et al., 2023). As shown in the large-scale and MUSE FOV images, in the first row (first and second panel) of Fig. 5.11, the galaxy has a bright core and a nuclear ring within the ∼8–10″ radius. The galaxy is double barred, hosting a nuclear bar within ∼5″ radius and an outer bar within ∼26″ radius (Knapen et al., 1995a,b; Erwin, 2004). There are several star-forming spiral arms surrounding the outer bar. Both large-scale and MUSE FOV images, and the structure map presented in the first row (third panel) of Fig. 5.13b reveal the curved dust lanes along the outer bar, joining the nuclear ring and continuing towards the nucleus.

The flux, velocity and velocity dispersion maps of NGC 4321 referred to in this paragraph show measurements obtained from single Gaussian fits, presented in Chapter 2. As presented in Figs. 2.11 and 2.12, the strongest H$\alpha$ and [N II]$\lambda$6583 emission is in the nuclear ring and the core; H$\alpha$ emission is significantly stronger than [N II]$\lambda$6583 emission. Outside the nuclear ring, clumpy H$\alpha$ and [N II]$\lambda$6583 emission is seen. [O III]$\lambda$5007 emission, shown in Fig. 2.13, is weak throughout the FOV, yet the most pronounced emission is confined within the core. Velocity maps, shown in Figs. 2.14 – 2.16, reveal perturbations from circular rotation with the zero velocity line having strong indents outside the nuclear ring at ∼5–7″ radius. There is also an indent in the zero velocity line, ∼3″ southeast of the nucleus, evident in [N II]$\lambda$6583 and [O III]$\lambda$5007, but absent in H$\alpha$. As shown in Figs. 2.17–2.19, in the nucleus the velocity dispersion of all emission line groups is high. Moreover, in a region extending from the centre ∼4″ towards the south, which partially overlaps with the indent in the zero velocity line, the [N II]$\lambda$6583 velocity dispersions are up to ∼170 kms$^{-1}$ and [O III]$\lambda$5007 velocity dispersions are up to ∼200 kms$^{-1}$; while H$\alpha$ velocity dispersions are not elevated there. Throughout the nuclear ring and the curved dust lanes, the velocity dispersion of H$\alpha$ and [N II]$\lambda$6583 is low, around ∼60–70 kms$^{-1}$. Outside the nuclear ring, to the west and southeast of the centre, several regions exhibit enhanced H$\alpha$ and [N II]$\lambda$6583 velocity dispersions with values ranging from 90 kms$^{-1}$ to 120 kms$^{-1}$.

Examining the spectra in the regions south of the nucleus, where the highest [N II]$\lambda$6583 velocity dispersions are seen, I noticed an excess to the blue wing of [N II]$\lambda$6583, similar to that seen in NGC 1097 (Kolcu et al., 2023) and NGC 1433. This indicates that the high velocity dispersion in those sapxels is artificial and caused by poorly fitted Gaussians in those spaxels. Thus, to account for the excess, I allowed for fitting a

secondary component to [N II]$\lambda$6583, following the approach introduced in Kolcu et al. (2023). The secondary component fitted to the excess will allow separating the main emission coming from the disk and an excess source.

Next, to identify the regions that are the most affected by the excess emission, I compared the kinematic measurements of main emission lines obtained from single-Gaussian fits and the fits with the secondary component. The H$\alpha$ and [O III]$\lambda$5007 measurements throughout the FOV are generally unaffected. However, extending from the centre $\sim$4″ towards the south, I identified a localised region with large [N II]$\lambda$6583 velocity shifts, up to $\sim$45 kms$^{-1}$, between the two kinematic measurements explained above; this region is shown in the top panel of Fig. 5.13a, after the masking criteria explained in further are applied.

To correct the kinematic measurements of [N II]$\lambda$6583, which are the most affected by the excess emission in spectra, I must define the region where including the secondary component alters the kinematic measurements of the [N II]$\lambda$6583 significantly. To define this region, I used the following criteria:

i. $V_{[N\,II]} - V_{[N\,II],corr} \leq -10$ kms$^{-1}$

ii. $\sigma_{[N\,II]}/\sigma_{[N\,II],corr} \geq 1.2$

iii. $\sigma_{[N\,II]w} \leq 300$ kms$^{-1}$

iv. $-2.5'' \leq \Delta\alpha \leq 2.5''$ and $-4'' \leq \Delta\delta \leq 2''$

where *corr* indicates the values extracted from the fits including the secondary component. The third condition, the velocity dispersion limit of the secondary [N II]$\lambda$6583 component ([N II]w) ensures that the secondary component is real and is not fitted to noise. The spatial cuts limit, defined in criterion iv., is applied to select the region where the change in velocity and velocity dispersion ratio is consistently large. The above criteria ensure that within the region, where the derived flux, velocity and velocity dispersion measurements are significantly affected by the presence of the excess [N II]$\lambda$6583 emission, those measurements are replaced by the ones from the fit that include the secondary component. Although, for NGC 4321 only [N II]$\lambda$6583 measurements are affected by the excess emission, I also replaced the H$\alpha$ and [O III]$\lambda$5007 measurements obtained from single Gaussian fits with those obtained from the fits with the secondary component, to maintain consistency across different line groups. After these corrections, H$\alpha$ and [N II]$\lambda$6583 velocities and velocity dispersion are in much better agreement than before the correction. The velocity dispersion of [N II]$\lambda$6583 within the masked region is reduced by roughly $\sim$30%. The resultant flux, velocity and velocity dispersion maps of

all emission line groups are presented in the second, third and fourth rows (first, second and third panels) of Fig. 5.13b; [O III]$\lambda$5007 and H$\alpha$ maps are not affected.

As shown in the bottom panels of Fig. 5.13a, the secondary component appears blueshifted by $\sim$300 kms$^{-1}$ with respect to the main component, and the blueshift decreases away from the galaxy centre. The velocity dispersion of the secondary component is larger than that of the main component by up to 20%, and this ratio increases away from the nucleus. The coherent morphology of the region where excess is dominating, and extreme kinematics of the secondary component within this region suggest the presence of AGN outflows.

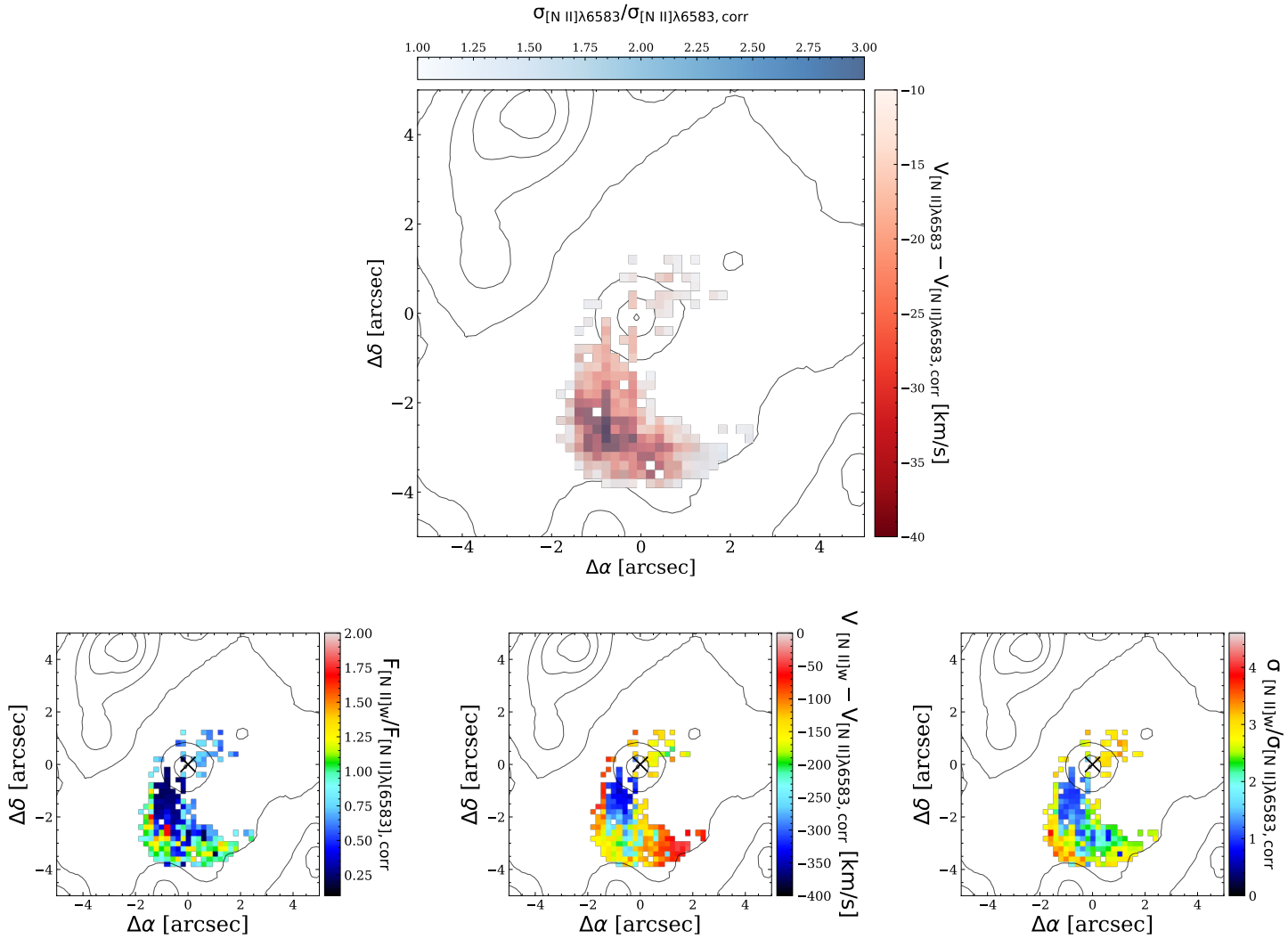


FIGURE 5.13A: *top:* mask of spaxels for which the fits including secondary component were used in further analysis of NGC 4321. The red and blue colour maps show the velocity shift of [N II]$\lambda$6583 and the ratio of [N II]$\lambda$6583 velocity dispersion, respectively, before and after including the secondary component in the fitting. *bottom:* comparison of the secondary and main component. their flux ratio (left) velocity difference (middle) and velocity dispersion ratio (right).

The disk orientation parameters inferred from `Kinemetry`, PA of the LON=155° and $i$=36°, are within only a couple of degrees from parameters estimated from large-scale fits (e.g., Haan et al., 2008: PA of the LON=152°, $i$=32°). The residual velocity map presented in the first row (fourth panel) of Fig. 5.13b, exposes two strong coherent structures, one with positive and one with negative velocities, with amplitudes of ∼25–30 $\mathrm{km s^{-1}}$. The structure with positive velocities extends from the northwest and joins the nuclear ring from the east, and the structure with negative velocities extends from the southeast and joins the nuclear ring from the southwest. After joining the nuclear ring both structures continue extending along the nuclear ring. These coherent structures are downstream from the dust lanes by ∼0.5–1″ and are consistent with being their counterparts. Outside the nuclear ring, to the northwest, a part of the coherent structure with negative velocities continues extending straight, towards the north rather than following the ring; this region coincides with the region with enhanced [N II]λ6583 and H$\alpha$ velocity dispersion, likely indicating the overshooting of the postshock gas there. Inwards from the nuclear ring, two regions with enhanced residual velocities with amplitudes of ∼20–30 $\mathrm{km s^{-1}}$ are seen; one exhibiting negative and one positive velocities. These regions can be a continuation of the structures extending along the nuclear ring and likely indicate the continuity of inflow to the innermost region.

The velocity difference map presented in the second row (fourth panel) of Fig. 5.13b exposes several distinct structures. Inwards from the nuclear ring, there are regions with positive and negative velocity differences of amplitudes ∼20–30 $\mathrm{km s^{-1}}$, but these regions are rather amorphous and show no point symmetry around the nucleus. Outside the nuclear ring, there is a coherent structure exhibiting positive velocity differences, with amplitudes of ∼10 $\mathrm{km s^{-1}}$ which roughly coincides with the coherent structure with positive velocities in the residual velocity map. Within the region associated with overshot gas, and west of it, the velocity differences are elevated, exhibiting amplitudes of ∼15 $\mathrm{km s^{-1}}$ or more; this observation supports the presence of complex dynamics there.

The BPT map presented in the third row (fourth panel) of Fig. 5.13b shows the emission of LINER type in the nucleus. The nuclear ring and the regions with clumpy H$\alpha$ and [N II]λ6583 emission are predominantly star-forming. Within the remaining regions outside the nuclear ring, there is predominant LINER emission.

NGC 4321 reveals strong coherent continuous structures in the residual velocity map, extending over large radii, which are consistent with the concept of extended shocks. Based on the kinematic categories defined in Sect. 6.1, this galaxy falls under the “coherent shocks” category.

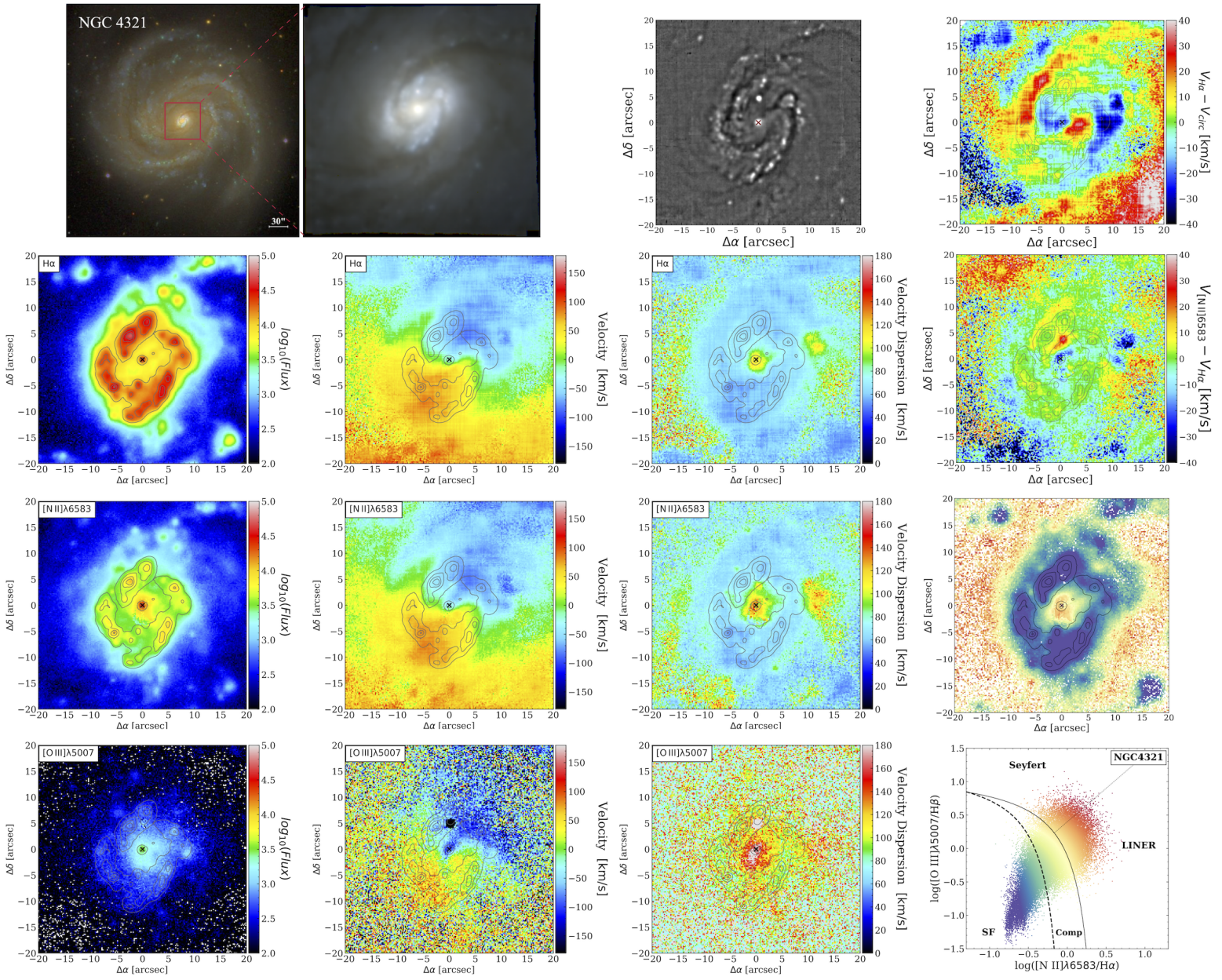


FIGURE 5.13B: The diagnostic maps of NGC 4321. Panels are the same as in Fig. 5.1.

## 5.14 NGC 4380

As presented in the first row (first and second panel) of Fig. 5.14, NGC 4380 is an unbarred galaxy with a bright core encircled by flocculent SF and dusty spiral arms. The MUSE FOV encompasses the core and a portion of the dusty spirals around it. As presented in the structure map, in the first row (fourth panel) of Fig. 5.14, the prominent spiralling dust features around the core are enunciated.

As presented in the second, third and fourth rows (first panels) of Fig. 5.14, the emission across all line groups is weak, particularly [O III]$\lambda$5007. H$\alpha$ and [N II]$\lambda$6583 emission is clumpy. The velocity fields of H$\alpha$ and [N II]$\lambda$6583, shown in the second and third rows (second panels) of Fig. 5.14, are mostly unperturbed. The zero velocity line remains straight. The velocity dispersion of H$\alpha$ and [N II]$\lambda$6583, shown in the second and third rows (third panels) of Fig. 5.14, remains low, around $\sim$50–60 kms$^{-1}$ throughout the entire FOV.

The PA of the LON=161° and $i$=59° estimated by fitting the velocity field with `Kinemetry` agrees well with the parameters obtained from large-scale photometry (Erwin et al., 2024; PA of the LON=157° and $i$=59°). The residual velocity map presented in the first row (fourth panel) of Fig. 5.14, exposes faint and noisy $m$=1 harmonic terms; after finely adjusting the PA of the LON in 1° increments, I settled on using 159° since this value raises the weakest artefacts. This demonstrates that once the velocity field is undisturbed, `Kinemetry` can estimate the disk orientation parameters consistent, within couple of degrees, with those obtained from large-scale photometric fits. Similarly, the velocity difference map presented in the second row (fourth panel) of Fig. 5.14, is overall noisy and exposes no prominent structures.

The BPT map, presented in the third row (fourth panel) of Fig. 5.14, shows prominent SF interspersed with LINER emission spots in the spiral arms, where clumpy H$\alpha$ and [N II]$\lambda$6583 emission is seen. Moreover, within $\sim$3–4″ radius, ionisation is dominated by LINER emission. While the central LINER emission can be associated with contribution from the core, the LINER emission along the spiral arms can be attributed to hot old low-mass stars or potentially to supernovae.

NGC4380 has relatively unperturbed kinematic fields and does not present signatures of extended shocks. This quiescence possibly can be attributed to the unbarred morphology of the galaxy, similar to my findings for NGC 4237. Therefore, based on the kinematic categories defined in Sect. 6.1, NGC 4380 falls under the "unperturbed" category, showing no signatures of extended shocks.

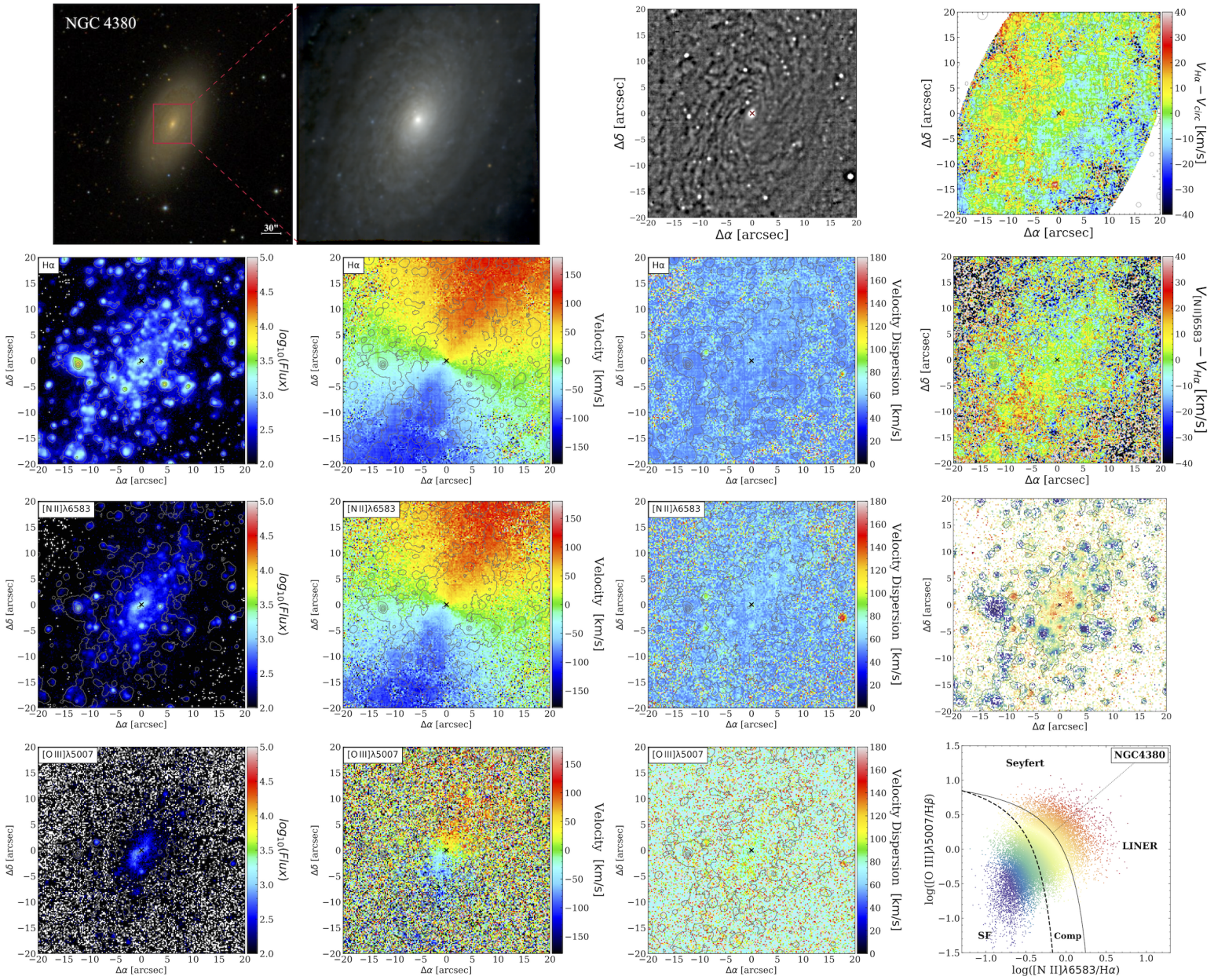


FIGURE 5.14: The diagnostic maps of NGC 4380. Panels are the same as in Fig. 5.1.

## 5.15 NGC 4457

NGC 4457 has been well-studied in many former works (Vollmer et al., 2013; Nemmen et al., 2014; Cortés et al., 2015; Querejeta et al., 2021; Stuber et al., 2021; Pan et al., 2022; Hermosa Muñoz et al., 2022b; Roberts et al., 2023). As shown in the colour composite images in the first row (first and second panel) of Fig. 5.15, the galaxy has a bright core, classified as LINER type (Terashima et al., 2000; Hermosa Muñoz et al., 2022b), and a bar of ∼2–3″ radius (Erwin et al., 2024). Moreover, based on its brightness profile, the galaxy is classified as having a lensed morphology (Querejeta et al., 2021); the lens is visible within the ∼30″ radius. The MUSE FOV covers almost the entire lens, the bar and the core. In colour composite images, two dust lanes are seen, resembling standard dust lanes along bars but instead in an oval with major axis ∼80°, measured from North to the East (Erwin et al., 2024). A string of young stars is seen downstream the dust lanes. The formation of these stars is likely triggered by the increased gas density downstream of the extended shocks, unlike in standard bar lanes where strong shear usually inhibits SF. In the structure map, shown in the first row (third panel) of Fig. 5.15, the dust lane that extends from the southwest end of the frame and connects to the disk at east-southeast is more pronounced than its counterpart. The most prominent region of the counterpart dust lane is seen extending north to south within the inner 5″ radii.

In the second, third and fourth rows (first panels) of Fig. 5.15, the emission for all line groups is concentrated within the ∼3–4″ radius. A string of H$\alpha$ and [N II]$\lambda$6583 emission is seen along the dust lane to the southwest. Several H$\alpha$ and [N II]$\lambda$6583 clumps, aligned in north to south direction at ∼5″ radius, are present downstream from the counterpart dust lane. Examining the velocity fields of H$\alpha$ and [N II]$\lambda$6583, shown in the second and third rows (second panels) of Fig. 5.15, I notice disturbances and velocities inconsistent with the rotating disk. Within ∼4″ radius, the zero-velocity line has strong indents, and positive velocities are present to the southwest of the centre where negative velocities would be expected for a rotating disk. A string of H$\alpha$ and [N II]$\lambda$6583 velocities, positive or close to zero, extends into the region where velocities are expected to be blueshifted, at $\Delta\delta \sim -7$, starting at $\Delta\alpha \sim 0''$ and stretching up to $\Delta\alpha \sim 10''$.

The velocity dispersion of H$\alpha$ and [N II]$\lambda$6583, shown in the second and third rows (third panels) of Fig. 5.15, is high in the core and around it; within ∼4″ radius values exceed 150 kms$^{-1}$. Similarly, high velocity dispersion is recorded to the east from the centre, up to a 15″ distance. Additionally, in a region extending from ∼6″ to ∼15″ of the centre, the velocity dispersion values are as high as the values seen in the core. This region roughly coincides with the abovementioned string of regions with anomalous

positive velocities. In regions with clumpy H$\alpha$ and [N II]$\lambda$6583, the velocity dispersion of H$\alpha$ and [N II]$\lambda$6583 remain around $\sim$60 kms$^{-1}$. The velocity and velocity dispersion maps of [O III]$\lambda$5007, shown in the fourth row (second and third panel) of Fig. 5.15, are rather noisy due to poor signal, yet the values suggest the same trends to the values seen in H$\alpha$ and [N II]$\lambda$6583 velocity and velocity dispersion maps.

The PA of the LON=80° and $i$=20 estimated using `Kinemetry` agree well with the parameters obtained from large-scale fits within CBS (see Table C.1). Consequently, I adopt these parameters for the final disk model of the galaxy. The residual velocity map, presented in the first row (fourth panel) of Fig. 5.15, reveals several regions within $\sim$4″ radius with velocity residuals of amplitudes $\sim$30–50 kms$^{-1}$. Four of these regions exhibit negative velocities. Three of them are towards the northeast to northwest and one towards the south. The other two regions exhibit positive velocities, one to the east and one to the west. There are no signs of wrongly fitted $i$ or the PA of the LON in the residual velocity map, indicating that the structures seen in the residual velocity map, particularly within $\sim$4″, are not due to modelled disk and are likely caused by AGN outflow cone piercing the disk and raising complex signatures in the kinematics (Fischer et al., 2013).

In the region to the southwest, where elevated velocity dispersions and anomalous velocities are seen, the velocity residuals exhibit coherent positive values with amplitudes exceeding 50 kms$^{-1}$. Moreover, high positive residual velocities are partially coinciding with the emission lane to the southwest. This structure potentially continues towards the east of the frame where values reach above 50 kms$^{-1}$; in the same region to the east, the velocity dispersion of both H$\alpha$ and [N II]$\lambda$6583 is high.

The velocity difference map in the second row (fourth panel) of Fig. 5.15, is rather noisy. Inside the north to south running dust lane, at $\sim$4–5″, velocity differences are increased with amplitudes around 15 kms$^{-1}$.

In the BPT map, shown in the third row (fourth panel) of Fig. 5.15, exhibits LINER-type emission within the $\sim$4″ radius. This supports the idea that the AGN might be contributing to disturbances of gas in the core region. In regions of strong H$\alpha$ emission, there is composite emission with a contribution from SF.

Despite indications of extended shocks across the FOV, the presence of strong local SF and signatures of nuclear activity in the innermost regions make it challenging to accurately trace potential extended shocks to the innermost regions. Therefore, I do not classify this galaxy as showing signs of coherent extended shocks. Based on the kinematic categories defined in Sect. 6.1, NGC 4457 falls under the “AGN dominated” category.

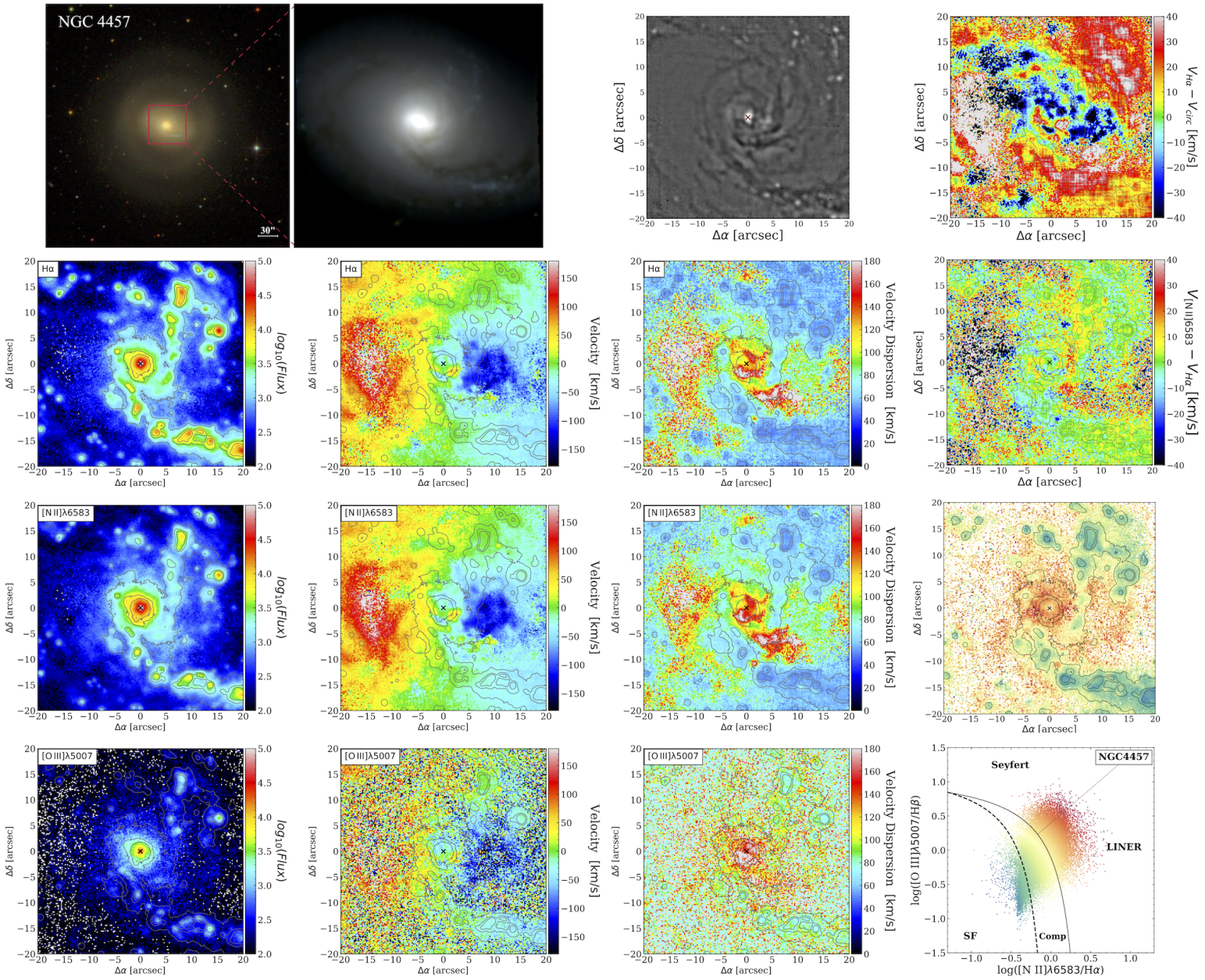


FIGURE 5.15: The diagnostic maps of NGC 4457. Panels are the same as in Fig. 5.1.

## 5.16 NGC 4643

NGC 4643 is one of the galaxies for which CBS provides a detailed morphological, photometric, and stellar kinematic study (Erwin et al., 2021a).

As shown in the first row (first and second panel) of Fig. 5.16, NGC 4643 has a bright core and a strong bar surrounded by a ring. The MUSE FOV covers the core and almost the entire bar region. The structure map of the galaxy, presented in the first row (fourth panel) of Fig. 5.16 highlights a faint nuclear ring with ∼3–4″ radius. However, this ring appearance is a side effect of Galaxy's nuclear disk having a broken-exponential radial profile, more details can be found in Erwin et al. (2021a). Therefore, I refer to this structure as nuclear disk instead of nuclear ring.

As shown in the second, third and fourth rows (first panels) of Fig. 5.16, compared to other galaxies I studied in this thesis, NGC 4643 has the weakest emission across all line groups. The strongest emission is confined within ∼4–5″ radius, there is no sign of the nuclear ring in emission. Weak emission lanes are seen extending from the western side of the nuclear disk to the south, and a weak one from the eastern side to the north. These may be the inner parts of the bar lanes curving onto the nuclear disk. As can be seen in the velocity maps shown in the second, third and fourth rows (second panels) of Fig. 5.16, the zero-velocity line has a wiggly shape, within the central ∼1″ there is an intrusion of positive velocities to the south and negative to the north. Further to the north, intrusions of negative-positive velocities repeat interchangeably forming indents in the zero-velocity line.

The velocity dispersion of H$\alpha$ and [N II]$\lambda$6583, shown in the second and third rows (third panels) of Fig. 5.16, is high in the core, with values reaching ∼100 kms$^{-1}$. Within the nuclear disk, and along the bar lanes, the values decrease and remain around 70–60 kms$^{-1}$. The velocity and velocity dispersion of [O III]$\lambda$5007 are not reliably estimated due to poor signal, the maps are rather noisy but still show a similar trend to H$\alpha$ and [N II]$\lambda$6583 fields.

The PA of the LON=58° and $i$=43° estimated by using `Kinemetry` differs by 5° from the parameters estimated from large-scale photometric fits in Erwin et al. (2008) (PA of the LON=53° and $i$=38°). This difference can be attributed to the kinematics within central regions being dominated by the strong bar, which can influence the parameter estimations in that region. Once I model the rotating disk with parameters adopted from large-scale fits, the resultant residual velocity map is dominated by the $m$=1 harmonic terms, which are the artefacts of wrongly fitted PA of the LON. The artefacts

are minimised when incorporating the parameters obtained from `Kinemetry`, yet subtracting the disk with parameters taken from large scale photometric fits does not affect the residual maps significantly. Therefore, I chose to adopt both parameters from the `Kinemetry`, while constructing the final disk model.

The residual velocity map, presented in the first row (fourth panel) of Fig. 5.16, exposes two strong coherent continuous structures. One exhibits positive velocity residuals, while the other exhibits negative velocity residuals, both with amplitudes of approximately 40–50 $\mathrm{kms}^{-1}$. The structure with negative velocities extends from the south edge of the frame, completing almost a full turn around the nuclear disk as it is winding inwards to connect the disk. The counterpart to this structure is seen in positive velocities. These two structures provide strong evidence of extended shocks in gas. Additionally, $\sim$0.5–1″ to the north and southeast of the centre, two regions with enhanced residual velocities are seen. These regions exhibit similar amplitudes to those found around the nuclear disk. One of these structures exhibits negative velocities, while the other exhibits positive velocities, suggesting a likely inflow to the core.

The velocity difference map, shown in the second row (fourth panel) of Fig. 5.16, is noisy and does not exhibit any strong structures. The BPT map presented in the third row (fourth panel) of Fig. 5.16, is dominated by LINER emission.

NGC 4643 exhibits weak emission across all line groups and has relatively less disturbed velocity and velocity dispersion fields compared to other sample galaxies I studied in this thesis. Nevertheless, I identify clear signs of extended shocks with large velocity amplitudes in the velocity residual map. Therefore, this galaxy is classified as showing extended shocks, falling under the “coherent shocks” category defined in Sect. 6.1.

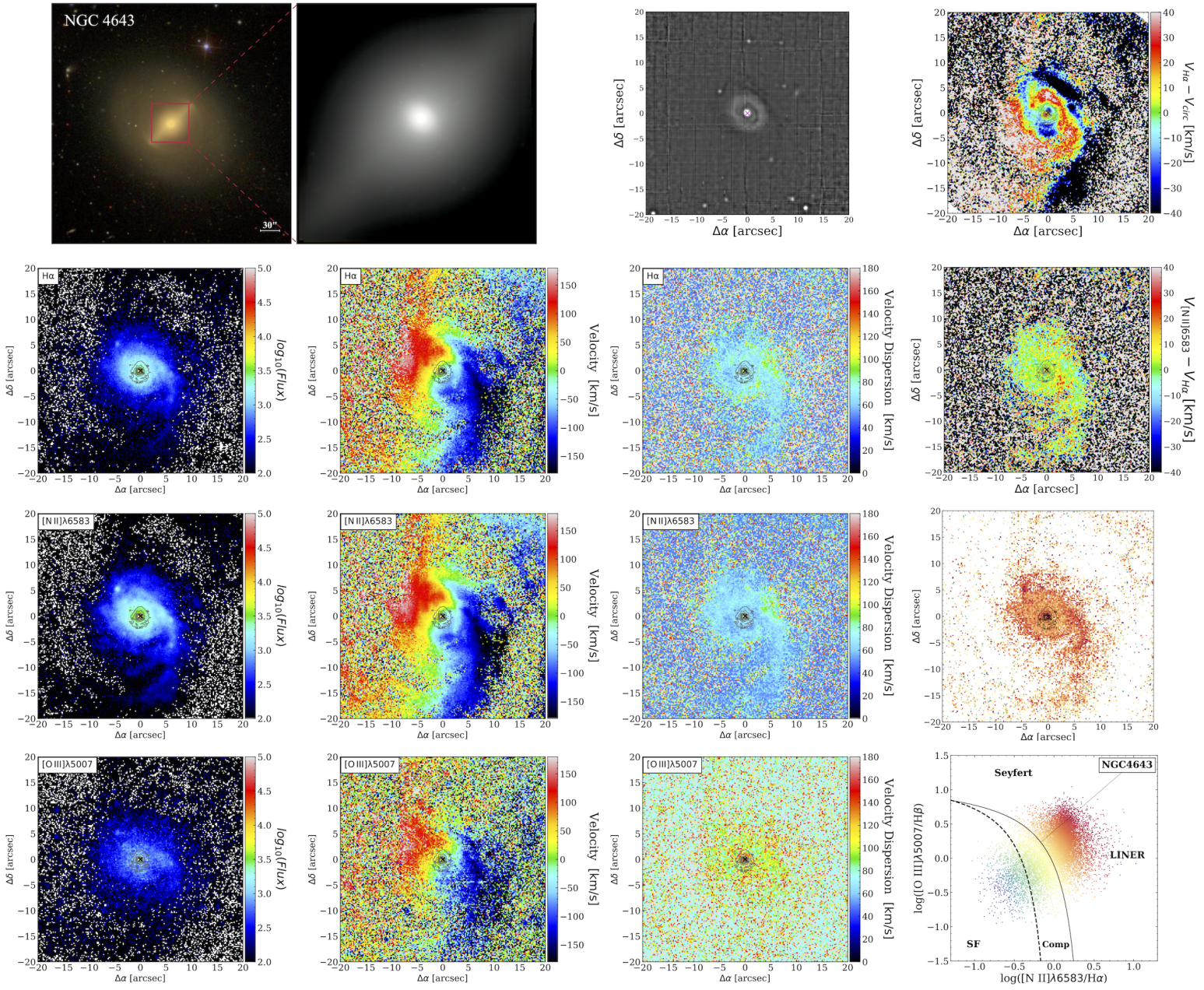


FIGURE 5.16: The diagnostic maps of NGC 4643. Panels are the same as in Fig. 5.1.

## 5.17 NGC 4941

As shown in the first row (first and second panel) of Fig. 5.17, NGC 4941 has a bright, dust-obscured (Jana et al., 2022) Seyfert 2 type (Véron-Cetty & Véron, 2006; Asmus et al., 2012) core, and a nuclear bar (Greusard et al., 2000) within ∼5–6″ radius; the bar can be more clearly seen in the structure map of the galaxy, presented in the first row (third panel) of Fig. 5.17. Additionally, the existence of a weak boxy outer bar is also proposed in this galaxy, with a radius of ∼20″, both from visual and kinematic studies (Eskridge et al., 2002; Erwin, 2004; Erwin et al., 2024; Stuber et al., 2023a), which is surrounded by a dusty star-forming ring. The existence of the outer bar remains a subject of an ongoing debate (de Vaucouleurs et al., 1991; Greusard et al., 2000). The MUSE FOV covers the core, the nuclear bar, a portion of the proposed outer bar and the ring. In the structure map, presented in the first row (third panel) of Fig. 5.17, several dust lanes are seen along the proposed outer bar; one of them, extending from the northeast, appears broken into segments and connects to the nuclear bar at the southeast, and another, as a much fainter counterpart to the former, connects to the nuclear bar at the northwest.

As shown in the second, third and fourth rows (first panels) of Fig. 5.17, the strongest emission across all line groups is confined within the ∼2″ radius for H$\alpha$ and [N II]$\lambda$6583, and ∼3–4″ radius for [O III]$\lambda$5007, but it is not extended along the nuclear bar. Beyond this region, two weak emission lanes are seen extending towards the northeast and southwest, stronger in the northeast. Both lanes appear to fork into two components ∼8-10″ from the centre. The northeast lane is stronger in [N II]$\lambda$6583, and the southwest lane in H$\alpha$. These lanes mostly align with the dust lanes along the proposed outer bar. Within the ring, there is weak and clumpy H$\alpha$ emission, likely originating from local SF.

The velocity maps displayed in the second, third and fourth rows (second panels) of Fig. 5.17, reveal pronounced signs of strong non-circular motions for all emission line groups. Approximately 3″ to the northeast of the centre there is a region with kinematics inconsistent with a rotating disk. Notably, the zero velocity line exhibits prominent indents at a radius of ∼8–10″. The velocity dispersion maps of all emission line groups, shown in the second, third and fourth rows (third panels) of Fig. 5.17, reveal very peculiar structures. In the core, and in two regions extending from the centre ∼4–5″ towards northeast and southwest, the velocity dispersion values exceed 150 kms$^{-1}$. These structures have a bi-symmetric nature, indicative of strong outflows from the AGN. Along the emission lane to the northeast, both H$\alpha$ and [N II]$\lambda$6583 velocity dispersions are notably high, reaching values around 100 kms$^{-1}$. On the other hand, in the outer regions

of the southwest lane, the velocity dispersion drops to $\sim$50 kms$^{-1}$, while in its inner region [N II]$\lambda$6583 velocity dispersions are around 130 kms$^{-1}$. While [O III]$\lambda$5007 velocity dispersions exhibit some noise, a clear trend mirrors what is seen in H$\alpha$ and [N II]$\lambda$6583 velocity dispersion. In the remaining regions, the velocity dispersion remains around $\sim$50–70 kms$^{-1}$.

While PA of the LON=25° and $i$=60° estimated from `Kinemetry`, slightly differ from parameters estimated from large-scale fits (e.g., Gutiérrez et al., 2011: PA of the LON=21°, $i$=48°), the differences can be attributed to the outer bar affecting the kinematic fits within the innermost regions. Since, I do not notice signs of artefacts from incorrectly fitted geometry in the residual velocity map, presented in the first row (fourth column) of Fig. 5.17, I use the parameters derived from `Kinemetry` fits. As seen in the residual velocity map, two strong coherent continuous structures with amplitudes of $\sim$40 kms$^{-1}$ are seen within the proposed outer bar region. One of these structures has positive velocities, and extends from the north edge of the frame to the south, east of the centre, while the other with negative values extends from the south edge of the frame to the north, west from the centre. These two structures manifest as straight lines parallel to the LON and follow the dust lanes. Therefore, I attribute these structures to straight shocks, indicative of inflow along the bar, providing compelling evidence supporting the existence of the outer bar. At $\sim$2–5″ the centre towards the northeast and southwest, there are two regions with high positive velocity residuals, with amplitudes exceeding $\sim$50 kms$^{-1}$. These structures coincide with the enhanced velocity dispersion seen across all emission line groups and further indicate its association with the AGN outflows. Although the two lane structures appear to wind towards inner regions, the structures associated with the AGN prevent us from tracing them further in.

The velocity difference map presented in the second row (fourth column) of Fig. 5.17, is noisy but there are regions of coherent velocity differences of magnitude $\sim$10–20 kms$^{-1}$, in alignment with the straight shocks observed along the bar in the residual velocity map. The region to the south exhibits positive and the one to the north exhibits negative velocity differences, providing further support for the disturbance of gas and the inflow along the bar. Moreover, in the regions associated with the AGN outflows, there are positive velocity differences with amplitudes around $\sim$15–30 kms$^{-1}$.

The BPT map, presented in the third row (fourth column) of Fig. 5.17, reveals strong Seyfert emission within the core due to irradiation from the AGN. Beyond this central region, ionisation is mostly dominated by LINER emission, except within the emission lanes, where there is also contribution from composite emission and very weak SF. Additionally, within the ring, where clumpy H$\alpha$ emission is seen, there is a contribution from SF.

The kinematic fields of NGC 4941 reveal pronounced extended shocks along the outer bar. However, due to the strong AGN outflows, I cannot trace these extended shocks to the innermost regions. Therefore, based on the kinematic categories defined in Sect. 6.1, NGC 4941 falls under the "AGN dominated" category.

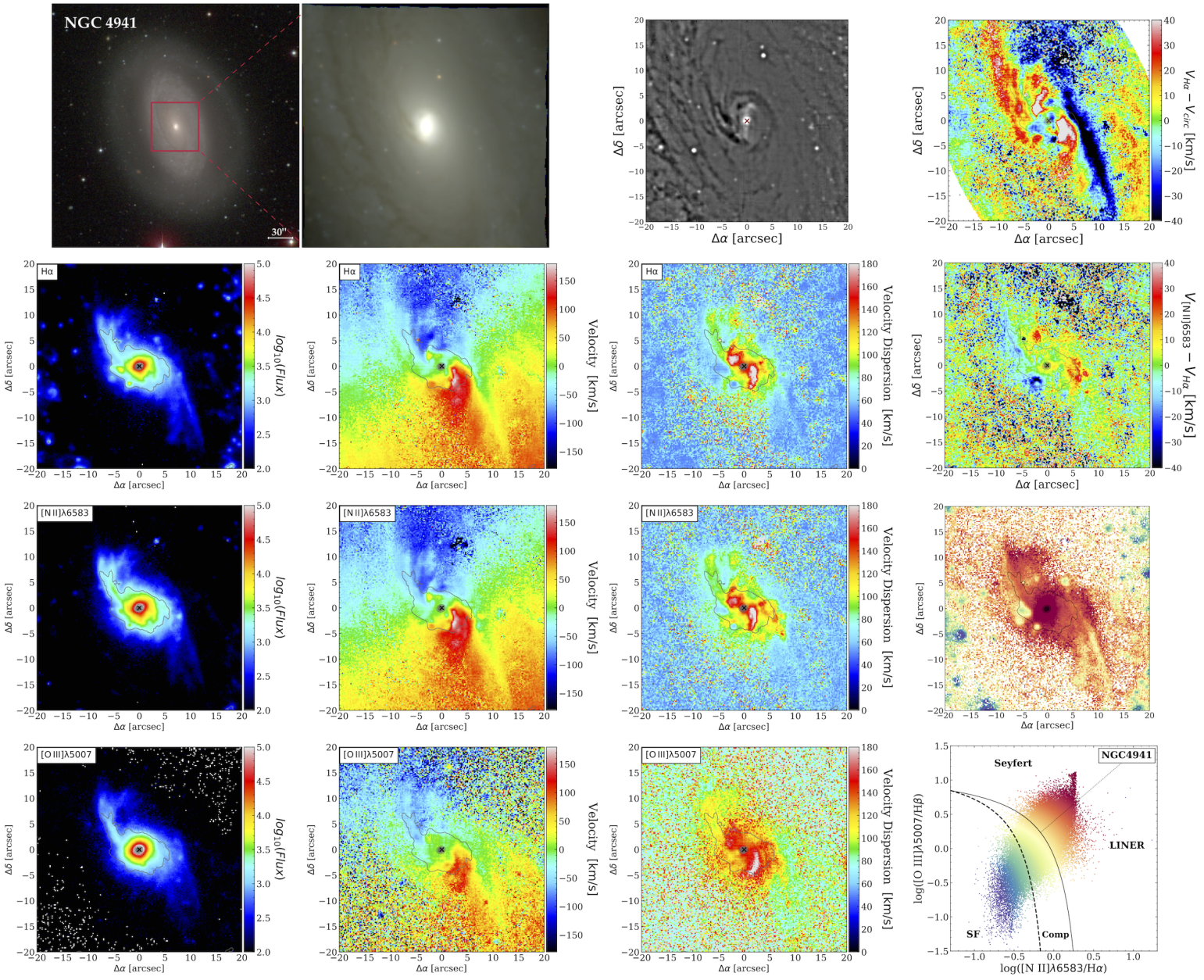


FIGURE 5.17: The diagnostic maps of NGC 4941. Panels are the same as in Fig. 5.1.

## 5.18 NGC 5248

As shown in the colour images, presented in the first row (first and second panel) of Fig. 5.18, NGC 5248 has a bright core surrounded by an inner nuclear ring with $\sim 2''$ radius and an outer nuclear ring with $\sim 7''$ radius. The galaxy has a weak bar with $\sim$20–25$''$ radius, surrounded by spiral arms. The MUSE FOV covers the core, the inner and outer nuclear rings, the bar and a portion of the spiral arms. In the first row (fourth column) of Fig. 5.18, the structure map of the galaxy reveals prominent dust structures throughout the entire FOV, many extending as spirals from the outer regions towards the outer nuclear ring and then towards innermost regions.

As shown in the second and third rows (first panels) of Fig. 5.18, the strongest H$\alpha$ and [N II]$\lambda$6583 emission is confined within the inner and outer nuclear rings and there is [N II]$\lambda$6583 emission peak in the nucleus; between the two rings the emission decreases. There is clumpy H$\alpha$ and [N II]$\lambda$6583 emission outside the rings, some aligned with the dusty spirals seen in colour images (see the first row of the same figure). The [O III]$\lambda$5007 emission across the entire FOV is weak but it has a clear peak at the nucleus. As presented in the second and third rows (second panels) of Fig. 5.18, the H$\alpha$ and [N II]$\lambda$6583 velocities are relatively unperturbed within the nuclear rings. However, outwards from the outer nuclear ring, the zero velocity line shows a strong indent at $\Delta\delta$ roughly 13$''$–14$''$ and $-5''$ indicating streaming motion along the spiral arms.

The velocity dispersion of H$\alpha$ and [N II]$\lambda$6583, shown in the second and third rows (third panels) of Fig. 5.18, is low with values $\sim$60–70 within both rings. Between the two rings, the [N II]$\lambda$6583 velocity dispersion shows local peaks with values around $\sim$90–100 kms$^{-1}$ in several regions to the east and southeast of the centre. Moreover, the velocity dispersion of H$\alpha$ and [N II]$\lambda$6583 is around $\sim$60 kms$^{-1}$ where clumpy H$\alpha$ and [N II]$\lambda$6583 emission are seen outside the rings. However, outside the rings, the velocity dispersion shows an increase in two arms upstream from the spiral dust lanes; possibly indicating some shocks there.

The disk orientation parameters, the PA of the LON=114° and $i$=44°, obtained from `Kinemetry` agree well with parameters estimated from the large-scale fits (Haan et al., 2008, 2009a), as shown in Table C.1. Thus, I employ these parameters for the final disk model. The residual velocity map presented in the first row (fourth panel) of Fig. 5.18, exposes two coherent continuous spiral structures – one with positive velocities and the other with negative velocities. Both of these structures are winding from the outer edge of the FOV in clockwise direction towards the innermost regions. These two spiral structures appear as counterparts of one another and are consistent with extended shocks in gas propagating to the innermost regions. These structures reach the outer nuclear

ring, even though further in they are more patchy; there is an indication that the red structure is crossing and entering the inner ring, down to $\sim 1''$.

The velocity differences presented in the second row (fourth panel) of Fig. 5.18, show enhancements with amplitudes of $\sim$10–20 $\mathrm{km s^{-1}}$. Especially inwards from the outer ring and extending to the innermost spaxel, the enhancements in velocity differences remain prominent, maintaining the characteristic positive and negative pattern. The strongest amplitudes are within the inner $\sim 1''$. These consistent signatures provide further support for the presence of extended shocks propagating down to the innermost regions.

The BPT map, presented in the third row (fourth panel) of Fig. 5.18, reveals LINER emission in the core and prominent SF within both the outer and inner nuclear rings. The region between the rings, where signatures of extended shocks are seen both in velocity residual and velocity difference maps, shows a contribution from composite emission, indicating the complex interaction of a high-energy mechanism there. Outside the rings, there is composite emission with a strong contribution from SF; the SF is particularly strong where clumpy H$\alpha$ emission is seen. Additionally, outside the rings, there is a contribution from LINER emission in the regions where enhanced velocity dispersions are seen.

NGC 5248 exhibits compelling signatures of extended shocks propagating from larger radii to its innermost regions, as identified through various applied methodologies. These signatures of extended shocks are particularly pronounced and align very well with the expected LOS velocity residual patterns shown in (Davies et al., 2009); which I presented in Fig. 1.6. Consequently, based on the kinematic categories defined in Sect. 6.1, NGC 5248 falls under the "coherent shocks" category.

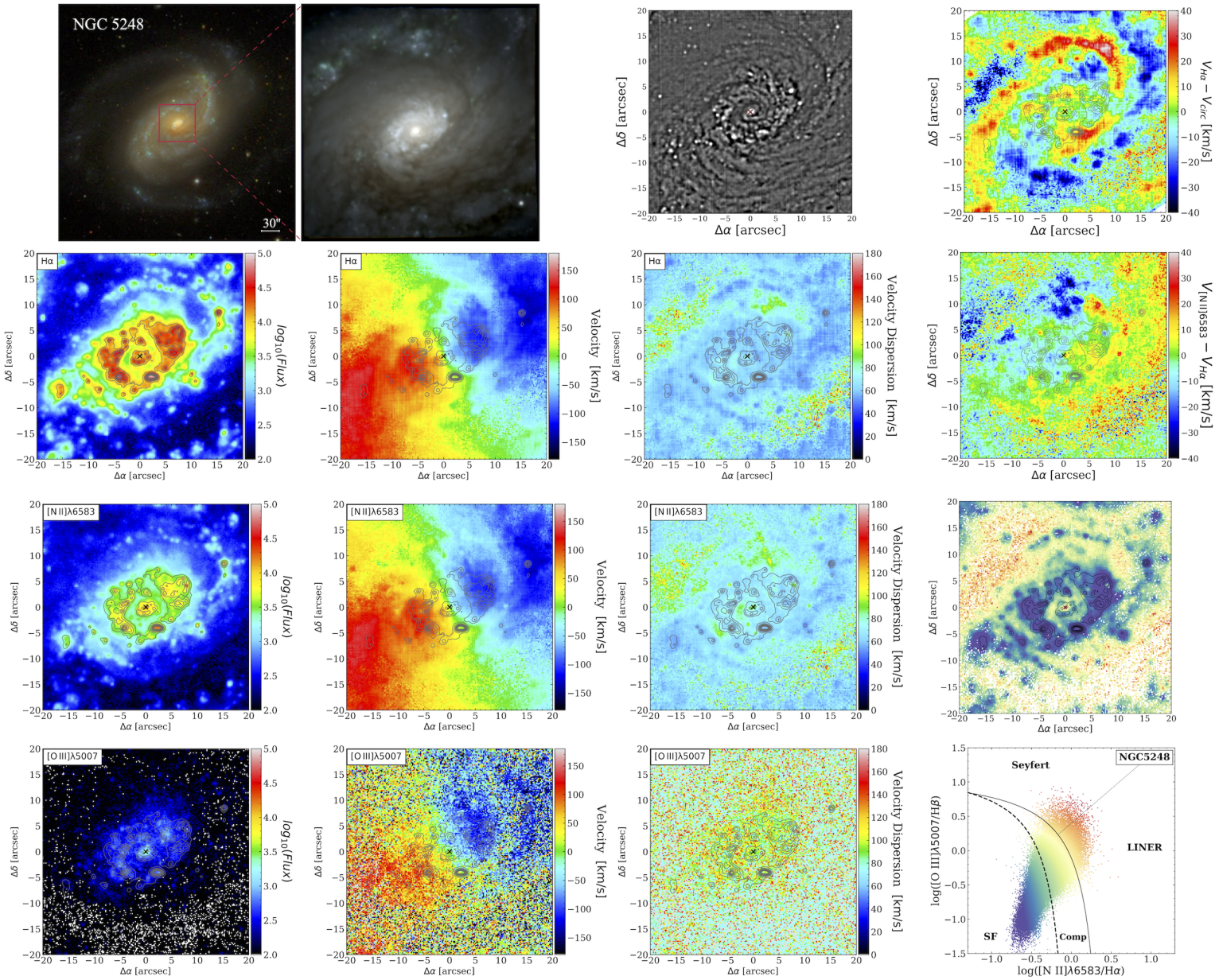


FIGURE 5.18: The diagnostic maps of NGC 5248. Panels are the same as in Fig. 5.1.

## 5.19 NGC 7177

NGC 7177 is a well-studied galaxy in many kinematic and photometric studies (de Jong, 1996; Misselt et al., 1999; Díaz et al., 2000; Simien & Prugniel, 2002; Erwin, 2005; Erwin et al., 2008; Sil'chenko et al., 2010). As shown in the first row (first and second panel) of Fig. 5.19, the galaxy has a bright dusty core, and a bar within ∼10″ radius (Erwin, 2005) surrounded by a ring. The MUSE FOV encompasses the core, the bar and the ring. As shown in the first row (third panel) of Fig. 5.19, several dust lanes are seen within the bar region; more prominent in the East side of the galaxy.

As shown in the second, third and fourth rows (first panels) of Fig. 5.19, the strongest emission across all line groups is confined within the inner ∼3″ radius with two clumps ∼2″ north and south of the nucleus, roughly along the major axis of the bar, seen in H$\alpha$ emission. We also notice extended emission to the east, especially in [O III]$\lambda$5007. There is clumpy H$\alpha$ and [N II]$\lambda$6583 emission indicative of local SF throughout the FOV.

As shown in the second, third and fourth rows (second panels) of Fig. 5.19, the velocity of all line groups shows non-circular motions. Within the ∼3–4″ radius, the zero velocity line has a wiggly shape, with indents at the locations of the two H$\alpha$ clumps. Velocity amplitude at the emission extension to the east is ∼50 kms$^{-1}$ higher than on the other side of the nucleus. The velocity dispersion of H$\alpha$ and [N II]$\lambda$6583, presented in the second and third rows (third panels) of Fig. 5.19, is high in the core and in an extended region ∼3″ towards the northeast and southwest of the centre. Coinciding this region, there appears a dust lane almost perpendicular to the bar. Upon a careful examination of the spectra of spaxels with relatively high velocity dispersions, we confirm that there is no need for a secondary component in the fitting during the kinematic extraction, and the high velocity dispersion values are intrinsic. Where clumpy H$\alpha$ and [N II]$\lambda$6583 emission is seen, throughout the FOV, the velocity dispersion of H$\alpha$ and [N II]$\lambda$6583 is around ∼50–60 kms$^{-1}$. There are velocity dispersion minima in the emission clumps ∼2″ south and north of the nucleus, and another minimum ∼1–2″ south of the east emission extent, spatially coincident with anomalously high LOS velocity. The velocity dispersions within the remaining regions in the bar are relatively high with values around ∼70–120 kms$^{-1}$.

Fitting the velocity field with `Kinemetry`, we determined the optimal disk orientation parameters as PA of the LON=90° and $i$=46°. These values deviate only slightly from the values obtained from large-scale photometric fits (e.g., Erwin et al., 2008: PA of the LON=83° and $i$=48°). However, when using the large-scale parameters in the disk model, the residual maps exhibit slight signatures of $m$=1 harmonic terms, while using

`Kinemetry`-deduced parameters minimises those artefacts. Therefore, we settle on using parameters estimated from `Kinemetry`.

Several peculiar structures are evident in the residual velocity map, shown in the first row (fourth panel) column of Fig. 5.19. Specifically, two structures with positive residual velocities, exceeding $50\,\mathrm{kms}^{-1}$, coincide with the pattern of the dust lanes. One of these structures, forms an arch to the north of the centre with further extension to the north, while the other extends almost as a straight line over $\sim 7''$ southeast of the centre. In between these two structures, a curved structure with negative velocities, of amplitudes exceeding $70\,\mathrm{kms}^{-1}$, reaches the nucleus from the north. Although these structures appear coherent, they do not seem to be consistent with the classical picture of the inflow of offset lines along the bar; they do not have point symmetry. However, the strong positive and negative velocity residuals are separated by high velocity dispersion region, which may be indicating two streams of gas colliding, as in on-axis inflow along the bars. Thus, the low velocity dispersion regions, with local minima at $\sim 1$–$2''$ north and south of the nucleus, appear also to inflow towards the nucleus.

The velocity difference maps, presented in the second row (fourth panel) column of Fig. 5.19, reveal two regions with consistent velocity differences, with amplitudes around $\sim 15$–$30\,\mathrm{kms}^{-1}$; one region with positive differences to the northwest of the centre, and the other region with negative differences to the east–southeast. Particularly, there are three peaks with maximum velocity differences, coinciding with the three minima in velocity dispersion maps.

The BPT map of the galaxy, shown in the third row (fourth panel) of Fig. 5.19, exhibits composite emission with a slight contribution from LINER emission in the core. This confirms that the contribution from the AGN to the overall gas disturbance in the galaxy is weak, indicating that the high velocity dispersions seen in the core, in an extended region $\sim 3''$ towards the northeast and southwest of the centre, is not associated with the AGN and is caused by another physical mechanism; potentially due to collision of gas along on-axis inflow. Throughout the FOV there is composite emission with a contribution from star formation.

There are complex processes ongoing in the central regions of NGC 7177. Despite this complexity, there is not a dominant influence from the AGN outflows within the inner kpc of the galaxy. Moreover, there are also no compelling signatures of extended shocks. However, the observed kinematics may be consistent with on-axis inflow along the bar, which I explained in Chapter 1 (Sect.1.2). Therefore, based on the kinematic categories defined in Sect. 6.1, NGC 7177 falls under the "other perturbations" category.

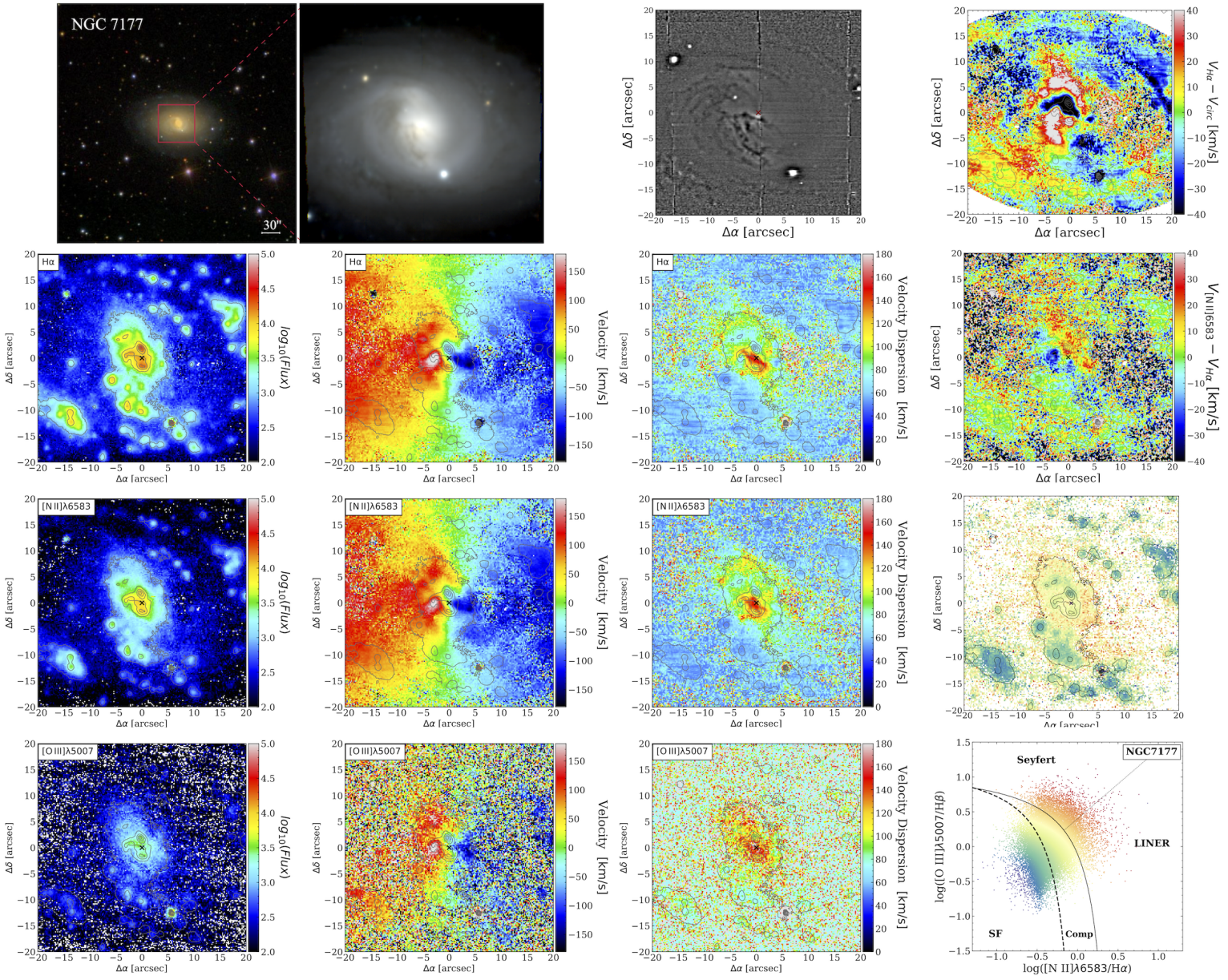


FIGURE 5.19: The diagnostic maps of NGC 7177. Panels are the same as in Fig. 5.1.

## 5.20 NGC 7513

As shown in the first row (first and second panel) of Fig. 5.20, NGC 7513 has a bright core, a strong bar (Buta et al., 2009) within ∼30″ radius, and two dusty star-forming spiral arms connecting to the ends of the bar. The MUSE FOV, covers the core, the entire bar region with some portion of the spiral arms. The structure map of the galaxy, shown in the first row (third panel) of Fig. 5.20, enunciates straight dust lanes within 12″ along the leading side of the bar, they pass the nucleus at ∼2″ distance and continue ∼5″ into the trailing sides.

As shown in the second, third and fourth rows (first panels) of Fig. 5.20, within ∼6″ radius, the emission across all line groups is weak, particularly for [O III]λ5007. Along the bar there is clumpy Hα and [N II]λ6583 emission, weak in the inner 12″ radius, significantly stronger outside of it, indicating local SF along the bar lanes. In velocity maps of Hα and [N II]λ6583, shown in second and third rows (second panels) of Fig. 5.20, the zero velocity line is bent by 90° at ∼10″ radius, roughly at the locations where line emission becomes strong. The velocity dispersion of Hα and [N II]λ6583, shown in the second and third rows (third panels) of Fig. 5.20, is generally low. The values are ∼70 $\mathrm{kms}^{-1}$ in the core and ∼50 $\mathrm{kms}^{-1}$ within the regions with clumpy emission along the bar.

The disk inclination implied by `Kinemetry` converged around 46°. However, the radial distribution of the PA of the LON ranged between 100–130°. Examining different residual velocity maps, after altering the fixed PA of the LON between the accepted range of 100-130°, I settled on using 105° as this value raised the least amount of artefacts. The final fixed parameters in the disk model, $i$ 46° and PA of the LON 105° agree well with the parameters estimated from large-scale fits (Erwin et al., 2024).

The residual velocity map, shown in the first row (fourth panel) of Fig. 5.20, exhibits two straight coherent structures along the bar, on its trailing side, with amplitudes up to 80 $\mathrm{kms}^{-1}$; one exhibiting positive and one exhibiting negative velocities. These structures extend beyond the bend of the zero velocity line, continuing outside the frame, all the way to the emanation of the spiral arms from the bar. This might indicate, that gas overshot the nucleus and streams to the other bar end along the bar. In this scenario, the gas is outflowing instead of inflowing. However, this is likely oversimplified, as the structures in residual velocity maps do not reflect the bend in the zero velocity line, which indicates different gas kinematics in the outer regions of the bar, where strong line emission is present, and the inner regions.

The velocity difference map, shown in the second row (fourth panel) of Fig. 5.20 is noisy and shows no outstanding structures. The BPT map, in the third row (fourth panel) of Fig. 5.20, exhibits a combination of composite LINER type emission in the core and contribution from SF along the bar lanes, where clumpy emission is seen.

The residual velocity maps of NGC 7513 show prominent coherent structures along the bar, with the largest amplitudes compared to the structures seen in the other galaxies I studied in this thesis. These structures appear as straight shocks along the bar, but they are on the trailing side of the bar, rather than the leading side as the typical extended shocks are. Unlike the classical picture of the extended shocks leading to an inflow, these structures are indicative of outflows. However, while we assume a counter-clockwise rotation for NGC 7513, it is challenging to definitively identify the trailing and leading sides due to the galaxy's orientation and the complex appearance of its spiral arms. Therefore, we acknowledge that if the galaxy's rotation were clockwise, the observed structures in the residual velocity map would align with the classical textbook example of straight shocks along the bar. Nevertheless, I classify this galaxy as showing no signatures of extended shocks in gas. Based on the kinematic categories defined in Sect. 6.1, NGC 7513 falls under the "other perturbations" category.

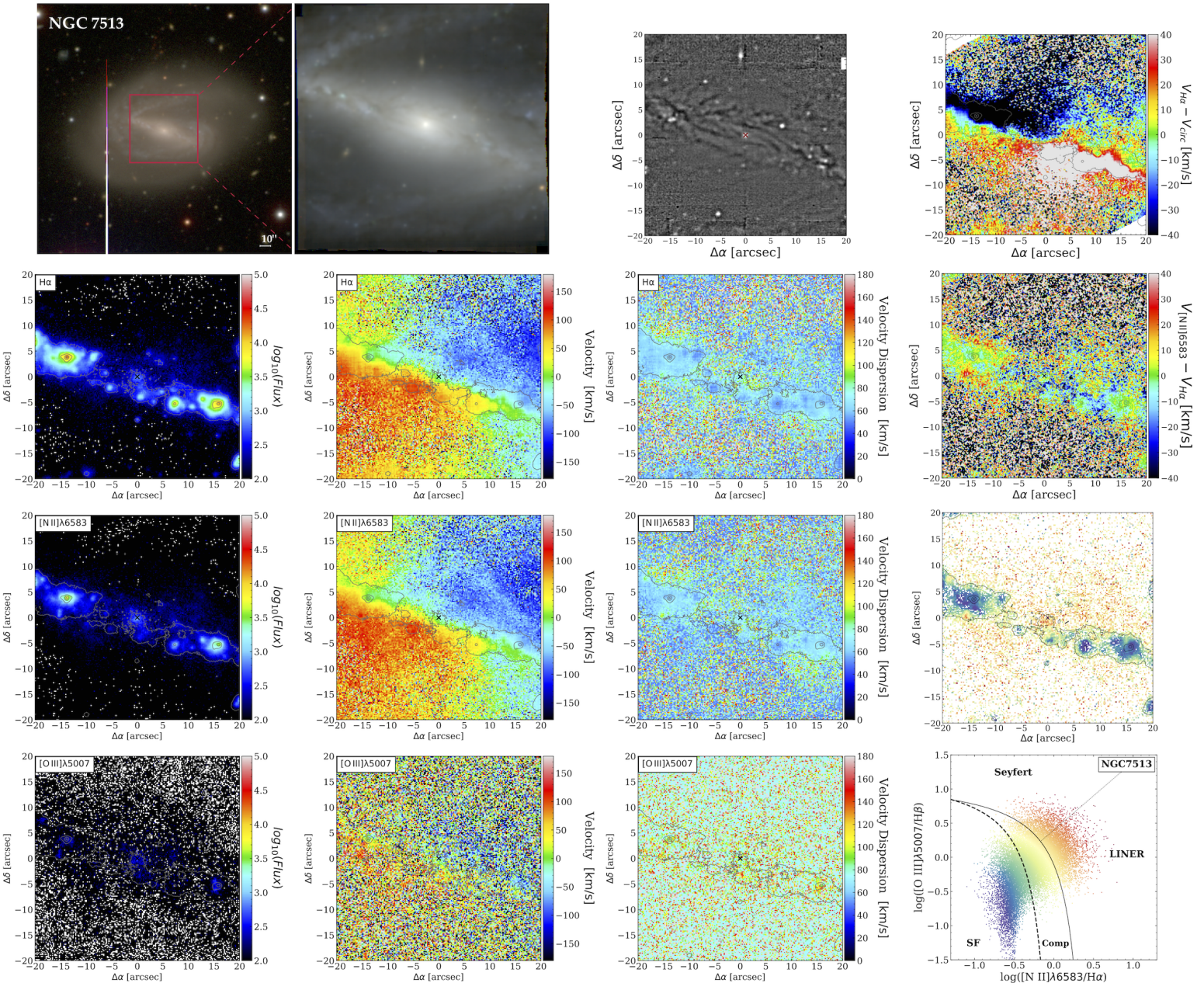


FIGURE 5.20: The diagnostic maps of NGC 7513. Panels are the same as in Fig. 5.1.

# Chapter VI

# Statistical analysis of the galaxy sample

In this chapter, I present preliminary results from my upcoming publication on the analysis of the galaxy sample studied in this thesis. Section 6.1 presents the classification of galaxies based on extended shock signatures obtained from their individual analysis (presented in Sect. 5) and the dominant emission type in their nucleus. Section 6.2 presents determining the characteristics of the extended shocks and the sample galaxies. Section 6.3 focuses on the statistical analysis of the sample, exploring correlations between galaxy classifications and characteristics, and examining the relation with the presence of nuclear bars and rings.

## 6.1 Classification of galaxies based on the signatures of extended shocks and nuclear emission types

The individual examination of each galaxy studied in this thesis, as I presented in Sect. 5, allowed me to classify these galaxies into five distinct categories. This classification is based on the extended shock signatures I identified from the diagnostic maps in my methodology. I further refer to this classification as the "kinematic category".

The first kinematic category is defined as ***"coherent shocks"***. Galaxies in this category exhibit compelling, extended shock signatures that span coherently – either straight or spiralling inward – over large distances into the inner parsec regions, typically characterised by high residual velocities or significant velocity amplitude differences. NGC 5248 can be given as an example, with its residual velocity map exhibiting an almost textbook example of the extended shocks in bars (or ovals) (see Sect. 5.18), similar to those shown in Fig. 1.6, Sect. 1.3.

The second category is defined as ***"broken shocks"***. Galaxies in this category exhibit structures of extended shocks. However, unlike the structures observed in the former kinematic category, these structures appear rather discontinuous, possibly due to strong

local activities disrupting the propagation of the shocks. These structures are characterised by high residual velocity or/and velocity difference amplitudes, also typically following the continuous dust patterns which can be associated with loci of shock compression. NGC 1433 can be shown as an example of galaxies under this category. Its residual velocity map exhibits several extended structures with large velocity amplitudes, that curve along its nuclear disk and align with multiple dust structures (see Sect. 5.5).

The third category is defined as ***"other perturbations"***, which includes galaxies that do not exhibit compelling signatures of extended shocks, associated with inflow. However, the kinematic fields of these galaxies are strongly perturbed. In most of these galaxies, the inner kpc regions are dominated by local shocks from SF and/or AGN activity. One such galaxy, NGC 7513, exhibits shock signatures extending over large radii, but these are associated with outflowing gas rather than inflow (see Sect. 5.20). Therefore, this galaxy falls under the "other perturbations" category.

The fourth category is ***"AGN dominated"***. Although galaxies in this category may exhibit extended shock signatures further out in their bar regions, within the innermost regions the kinematics are dominated by strong outflows from AGNs, preventing the tracing of shock signatures to the nucleus. NGC 613 serves as a good example, as I explained in Sect. 5.3. Unlike the "other perturbations" category, where galaxies may also be influenced by AGN activities but the shock signatures can still be traced to the nucleus, the "AGN dominated" category includes galaxies where outflows prevent such tracing.

The final category is defined as ***"unperturbed"***. Galaxies under this category have relatively unperturbed kinematic fields and show no evidence of extended shocks. The residual velocity maps typically exhibit perturbations coming from lopsidedness with low amplitudes. NGC 4237 can be shown as an example of galaxies under this category (see Sect. 5.11). It is important to note that although both "other perturbations" and "unperturbed" categories include galaxies without shock signatures, galaxies within the former category have significantly perturbed kinematic fields, unlike the galaxies in the latter category. The kinematic category assigned to each galaxy in the sample I studied in this thesis is presented in Table 3.

Furthermore, I also categorised the galaxies studied in this thesis based on the dominant emission type in their nuclear regions, to explore the correlation between the type of nuclear emission and the presence of extended shocks. In Fig. 6.1, I present the ***BPT diagram of the sample*** I studied in this thesis. Each point on the diagram represents a single galaxy, colour-coded according to the kinematic category assigned based on the signatures of extended shocks identified in each. The location of each point on the BPT diagram is determined by the ratio of emission line fluxes measured within

a 150 pc radius. The diagnostic lines based on relations from Kewley et al. (2001) Kauffmann et al. (2003) and Cid Fernandes et al. (2011) separate the regions for SF, Composite, LINER, and Seyfert nuclear emission type categories, same as in Sect. 3.2. This classification is used for identifying the primary source of ionisation emitted from the nucleus of each galaxy.

Consequently, based on the BPT diagram of the sample, I have assigned a nuclear emission type to each galaxy, which are presented in the third column of Table 3. I note that, because of strong broad emission from its AGN, NGC 1566 had unreliable H$\alpha$ and [N II]$\lambda$6583 flux measurements within its inner $\sim$1″ but the flux measurements of [O III]$\lambda$5007 and H$\beta$ were not significantly affected. Therefore, to represent the uncertainty in the x-axis position of this galaxy on the BPT diagram of the sample, I have marked its location with two horizontal arrows, indicating its position could shift either to the left or right. While previous studies have classified this galaxy as Seyfert/LINER type (e.g., Alloin et al., 1985; Woo & Urry, 2002), I have decided not to assign a nuclear emission type obtained from other works to ensure consistency across the galaxies I analysed in this study based on the BPT diagram of the sample.

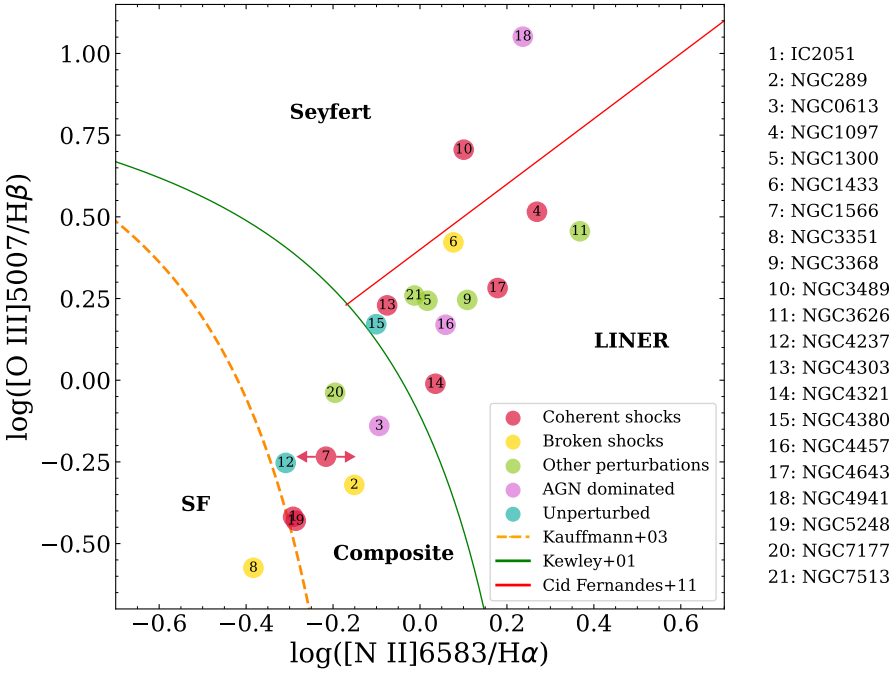


FIGURE 6.1: The BPT diagram of the galaxy sample studied in this thesis. The orange, green, and red lines show Kauffmann et al. (2003), Kewley et al. (2001), and Cid Fernandes et al. (2011) fits respectively. These lines determine the regions associated with different ionisation mechanisms: SF, Composite, LINER, and Seyfert. Each point on the diagram, numbered and specified on the right, corresponds to a specific galaxy. The points are colour-coded by the categories assigned based on the extended shock signatures observed: "coherent shocks" in red, "broken shocks" in yellow, "other perturbations" in green, "AGN dominated" in purple, and "unperturbed" in cyan.

TABLE 3: The individual findings for the sample galaxies studied in this thesis. Columns show: (1) galaxy ID; (2) the kinematic category and (3) nuclear emission type category defined in Sect. 6.1; (4) minimum and (5) maximum positive and negative deprojected velocity amplitudes obtained in Sect. 6.2.1; (6) average H$\alpha$ velocity dispersion of each galaxy obtained in Sect. 6.2.2; (7) the presence of nuclear bars and (8) nuclear rings determined in CBS – the keywords indicate "N": absence, "Y": presence, "Y?": potential presence and "?": uncertainty of nuclear bars or rings.

| **Galaxy ID** (1) | **Kinematic Category** (2) | **Nuclear Emission Type** (3) | **Min Vel. [km/s]** (4) | **Max Vel. [km/s]** (5) | $\overline{\sigma}$ **[km/s]** (6) | **Nuclear Bar** (7) | **Nuclear Ring** (8) |
|---|---|---|---|---|---|---|---|
| IC2051 | Coherent Shocks | Composite | $-15, 20$ | $-40, 65$ | $77.57 \pm 0.38$ | N | Y |
| NGC289 | Broken Shocks | Composite | $-20, 15$ | $-65, 90$ | $72.88 \pm 0.2$ | N | N |
| NGC0613 | AGN dominated | Composite | $-30, 40$ | $-90, 110$ | $103.92 \pm 0.27$ | N | Y |
| NGC1097 | Coherent Shocks | LINER | $-50, 40$ | $-130, 150$ | $83.01 \pm 0.13$ | Y | Y |
| NGC1300 | Other Perturbations | LINER | – | – | $72.36 \pm 0.23$ | N | Y |
| NGC1433 | Broken Shocks | LINER | $-20, 25$ | $-116, 115$ | $76.11 \pm 0.28$ | Y | Y |
| NGC1566 | Coherent Shocks | – | $-20, 20$ | $-80, 70$ | $94.73 \pm 0.71$ | Y? | Y? |
| NGC3351 | Broken Shocks | SF | $-25, 12$ | $-95, 50$ | $85.81 \pm 0.12$ | N | Y |
| NGC3368 | Other Perturbations | LINER | - | - | $104.74 \pm 0.4$ | Y | N |
| NGC3489 | Coherent Shocks | Seyfert | $-12, 8$ | $-40, 30$ | $70.28 \pm 0.24$ | N | ? |
| NGC3626 | Other Perturbations | LINER | – | – | $76.09 \pm 0.49$ | Y | N |
| NGC4237 | Unperturbed | Composite | $-5, 5$ | $-20, 18$ | $54.90 \pm 0.05$ | N | N |
| NGC4303 | Coherent Shocks | LINER | $-15, 10$ | $-50, 20$ | $71.42 \pm 0.2$ | Y | Y |
| NGC4321 | Coherent Shocks | LINER | $-15, 15$ | $-55, 55$ | $67.85 \pm 0.09$ | Y | Y |
| NGC4380 | Unperturbed | LINER | $-4, 9$ | $-13, 20$ | $53.91 \pm 0.09$ | N | Y? |
| NGC4457 | AGN dominated | LINER | $-35, 45$ | $-125, 120$ | $87.05 \pm 0.44$ | Y | N |
| NGC4643 | Coherent Shocks | LINER | $-20, 20$ | $-110, 70$ | $70.92 \pm 0.36$ | N | N |
| NGC4941 | AGN dominated | Seyfert | $-20, 15$ | $-60, 45$ | $89.35 \pm 0.44$ | Y | N |
| NGC5248 | Coherent Shocks | Composite | $-15, 20$ | $-50, 60$ | $63.37 \pm 0.08$ | N | Y |
| NGC7177 | Other Perturbations | Composite | – | – | $81.85 \pm 0.41$ | N | N |
| NGC7513 | Other Perturbations | LINER | – | – | $59.56 \pm 0.4$ | N | N |

## 6.2 Obtaining the characteristics of the sample galaxies studied in this thesis

### 6.2.1 Determining the deprojected velocity residual amplitudes of extended shocks

As I explained in Sect. 1.3, not all extended structures in the residual velocity maps should be associated with extended shocks in gas. To deduce whether a coherent signature has a shock nature, it should have large velocity amplitudes. Therefore, I explore the strength of velocity residual amplitudes of the signatures I associated with the extended shocks.

The velocity we measure from a galaxy includes only a component of the LOS velocity. Working under the assumption that the motion of gas is confined within the disk of a galaxy, we need to adjust for the disk inclination angle relative to our LOS, to obtain deprojected velocities. This adjustment is done using the formula $V_{true} = V_{LOS}/sin(i)$, where $V_{true}$ is the deprojected velocity, $V_{LOS}$ is the observed LOS velocity, and $i$ is the inclination angle of the galaxy. By applying this correction, I produced a residual velocity map for each galaxy that displays the true, or deprojected, residual velocities. Since these residual velocity maps are generally noisy, to reduce the level of noise I applied box filter convolution. The value of each spaxel represents the average of surrounding spaxels within a $3 \times 3$ grid. These maps are presented in Appendix B, Fig. B.3.

Upon examining the deprojected residual velocity maps, for both positive and negative velocities, I recorded the highest and lowest amplitudes along the coherent structures, which I associated as the signatures of extended shocks. For each galaxy, these values are presented in the fourth and fifth columns of Table 3, and shown in Fig. 6.2. For galaxies in the "AGN dominated" category, I cannot trace the kinematic structures down to the nucleus. However, I measured the amplitudes from the extended shock signatures along their bars. Galaxies falling under the "other perturbations" category are excluded from this analysis since their kinematic maps lack clear signatures of extended shocks. While it might be reasonable also to exclude galaxies under the "unperturbed" category, I have included them for comparison. For these galaxies, the recorded values are located in the regions that show kinematic signatures that are associated with perturbations from lopsidedness.

As discussed in Sects. 1.2 and 1.3, coherent structures in the residual velocity field presented in Fig. 1.6 show deprojected velocity amplitudes of about 40 $\mathrm{kms}^{-1}$. These velocity amplitudes correspond to a nuclear spiral shock that causes a velocity jump

of approximately 70 $\mathrm{kms}^{-1}$ in the gas (see Fig. 1.3). Fig. 6.2 reveals that in the majority of galaxies studied in this thesis, the highest deprojected residual velocity amplitudes, recorded along the coherent structures associated with extended shocks, are $\sim$50 $\mathrm{kms}^{-1}$ or higher. These amplitude values are similar to the amplitudes seen in other galaxies (see Sect. 1.3), which are associated with spiral shocks extending to the nucleus (Zurita et al., 2004; Fathi et al., 2008; Blasco-Herrera et al., 2013; Schnorr-Müller et al., 2016, 2017). These values correspond to strong shocks that cause velocity jumps even larger than 70 $\mathrm{kms}^{-1}$, as seen in models. Particularly, for galaxies like NGC 1097 and NGC 1433, the deprojected velocity amplitudes exceed 100 $\mathrm{kms}^{-1}$, indicating much stronger shocks and larger velocity jumps. These findings are consistent with the modelled velocity jumps of $\sim$100 $\mathrm{kms}^{-1}$ by Athanassoula (1992) and of $\sim$70 $\mathrm{kms}^{-1}$ by (Maciejewski, 2004b), observed when extended shocks are present (see Fig. 1.2).

Amongst galaxies with extended shock signatures, categorised under "coherent shocks" and "broken shocks", NGC 4303 stands out as an outlier due to its low positive deprojected velocity amplitude of $\sim$20 $\mathrm{kms}^{-1}$. This amplitude value is at least a factor of 2 smaller than those typically observed in galaxies under the same kinematic categories. However, this difference can be justified given that in the residual map of NGC 4303, the coherent structure with negative velocities associated with extended shocks did not have a clear counterpart with positive velocities. The regions where I recorded the positive velocity amplitudes are those I identified as potentially corresponding to a counterpart. The low deprojected residual velocity amplitudes along this potential counterpart imply the absence of a shock there.

Conversely, Fig. 6.2 also reveals that the highest deprojected residual velocity amplitudes seen in galaxies under the "unperturbed" category do not exceed 20 $\mathrm{kms}^{-1}$, which is a factor of 2 or more smaller than those seen in galaxies under the other kinematic categories. Since the galaxies under the "unperturbed" category are also the only two unbarred galaxies in the sample I studied in this thesis, this further emphasises the importance of bar dynamics in driving extended shocks and gas inflows to the innermost regions. Moreover, in the majority of galaxies, the lowest residual velocity amplitudes recorded along the coherent kinematic structures associated with extended shocks, are around the same values as those observed in unbarred galaxies. These observations mean that the regions I recorded the lowest amplitudes are more indicative of wave propagation phenomena and are not necessarily indicating regions of shock propagation.

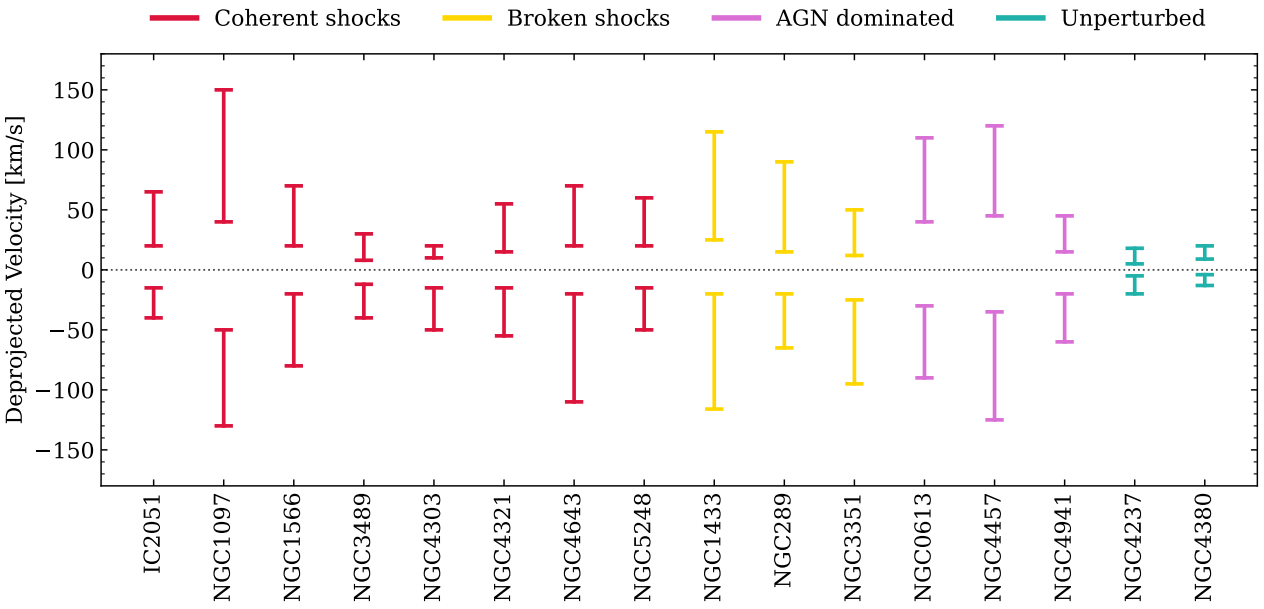


FIGURE 6.2: The distribution of deprojected residual velocity amplitudes of the extended shock signatures, colour-coding represent different kinematic categories. The colours represent the galaxies falling under "coherent shocks" in red, "broken shocks" in yellow, "AGN dominated" in purple and "unperturbed" in cyan.

### 6.2.2 Obtaining the average H$\alpha$ velocity dispersion of galaxies

As shown in Figs. 2.17, 2.18 and 2.19, the velocity dispersion of all emission line groups across the sample show a large variety. While some galaxies, such as the ones with AGN outflows, show extremely high velocity dispersions, less perturbed systems like NGC 5248, have smaller velocity dispersions across the MUSE FOV. Similar to AGN outflows, extended shocks with large amplitudes can potentially cause turbulence in the gas of galaxies, elevating velocity dispersions. In further, I explore the correlation between the presence of extended shocks and the average H$\alpha$ velocity dispersion within the inner regions of the galaxies in the sample I studied in this thesis.

Throughout this analysis, I assume that the velocity dispersion is isotropic. To calculate an average H$\alpha$ velocity dispersion for each galaxy, I first defined an elliptical region with a semi-major axis 1 kpc. The shape of the ellipse is determined based on the galaxy inclination and position angle, ensuring that the major axis is aligned with the observed orientation of the galaxy. I then applied an amplitude-over-noise (AON) threshold of 20 (Sarzi et al., 2006) to exclude noisy spaxels within the defined elliptical region, which might otherwise affect the resulting velocity dispersion. This threshold is determined by examining the distribution of spaxels on the plane defined by the H$\alpha$ velocity dispersion and AON for each galaxy individually, confined within the defined elliptical region, as

presented in Appendix B, Fig. B.4. Spaxels with low AON and high velocity dispersion indicate measurements from noisy spaxels, where the velocity dispersions are artificially high due to inaccurate Gaussian fitting, likely caused by low signal. After excluding the noisy spaxels, I took an average of velocity dispersions recorded in the remaining spaxels across the entire elliptical region. The average H$\alpha$ velocity dispersions of all galaxies within the sample are provided in Table 3.

In Fig. 6.3, I present the distribution of average H$\alpha$ velocity dispersions for galaxies across all kinematic categories, where the average is calculated using the arithmetic mean. It is evident that galaxies in the "unperturbed" category exhibit the lowest average H$\alpha$ velocity dispersions, with values less than 55 kms$^{-1}$. Even though there is a bit of a spread, the majority of galaxies when combining those in "coherent shocks" and "broken shocks" categories have average H$\alpha$ velocity dispersions $\sim$70 kms$^{-1}$ or higher. NGC 1566, exhibit an average H$\alpha$ velocity dispersion of $\sim$ 95 kms$^{-1}$, but I note that the turbulence in the central regions of this galaxy might be dominated by AGN outflows (see Sect. 5.6). The galaxies under the "AGN dominated" category exhibit average H$\alpha$ velocity dispersions larger than 85 kms$^{-1}$, these high values can be attributed to strong AGN outflows dominating their kinematics. Lastly, galaxies in the "other perturbations" category show a wider spread of average H$\alpha$ velocity dispersions, with no obvious trend or clustering.

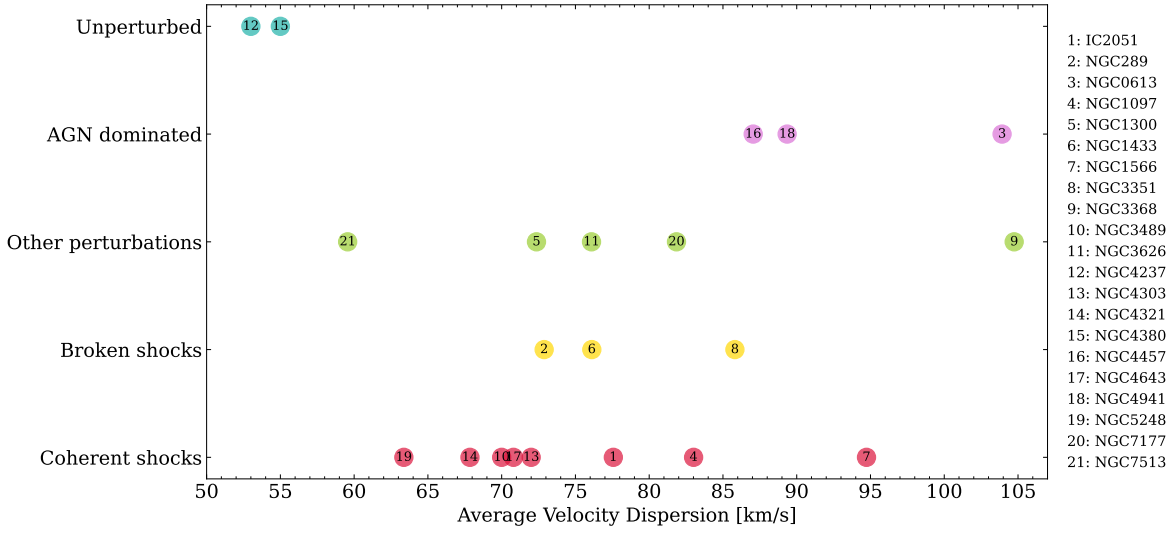


FIGURE 6.3: The distribution of average H$\alpha$ velocity dispersion of galaxies in different kinematic categories marked by different colours. Each point on the diagram marked with a number correspond to a specific galaxy as stated on the right.

## 6.3 Statistical studies of the correlations

### 6.3.1 The dominance of extended shocks within the inner kpc region of galaxies

Figure 6.4 presents the number of galaxies in each kinematic category, colour-coded according to the nuclear emission type category, both categorisations are based on the description in Sect. 6.1. For completeness, NGC 1566 is included in this figure but is marked in grey colour, since I did not assign a nuclear emission type category to it, due to unreliable H$\alpha$ and [N II]$\lambda$6583 flux measurements within its inner 1″. The figure reveals that 11 out of 21 (∼52%) of galaxies show signatures of extended shocks. Among these galaxies, 8 out of 11 are in the "coherent shocks" category, while the remaining 3 are in the "broken shocks" category. Moreover, 7 out of 21 galaxies (∼33%) do not show signatures of extended shocks. Among these galaxies, 2 out of 7 are under the "unperturbed" category and 5 out of 7 are under the "other perturbations" category. The remaining 3 galaxies (∼15%) are in the "AGN dominated" category.

Despite the limited sample size of 21 galaxies in my thesis, a noteworthy finding is that approximately 52% of these galaxies exhibit signatures of extended shocks within their inner kpc. I note that this 52% might represent a lower limit. Extended shock signatures observed along the bars of galaxies under the "AGN dominated" category, which cannot be traced down to the nucleus due to outflows dominating the kinematic fields, might propagate to the nucleus, which would increase the prevalence of extended shock signatures across the sample I studied. Therefore, this significant proportion, with at least 52%, suggests that extended shocks can be the dominant mechanism of gas inflows to the nucleus.

One of the strongest observational findings of my analysis is that the two galaxies, NGC 4237 and NGC 4380, of the "unperturbed" category, are also the only two unbarred galaxies within the sample I studied in this thesis. Unlike the galaxies in other kinematic categories, these two galaxies exhibit very quiescent kinematic fields and they lack extended shock signatures, which may be attributed to their unbarred morphology. This observation confirms the significance of bars, causing perturbation in the disks, driving extended shocks and facilitating gas inflows to the nucleus. According to Erwin (2018), within a sample of galaxies with stellar masses $\sim 10^{10} M_{\odot}$, approximately 60% of galaxies are barred, with the remaining ∼40% being unbarred. Given this distribution, one might expect to find around 8 unbarred galaxies in a sample of 21. However, my study only includes 2 unbarred galaxies, primarily due to the criteria of sample selection. Although studying the kinematic fields of these two galaxies leads to one of the strongest

observational conclusions of my research, this conclusion is statistically not significant due to the small number of unbarred galaxies in my sample.

Furthermore, I found no distinct correlation between the nuclear emission type categories derived from the BPT diagram of the sample and the kinematic categories defined by the presence of extended shock signatures in the galaxies I studied. This lack of correlation is not surprising when considering the differing timescales between the inflowing gas and the AGN's lifetime. The flickering or variability of AGN activity, which occurs over shorter timescales, can potentially erase any correlation that might otherwise be expected. Additionally, the small sample size may also contribute to the observed lack of correlation.

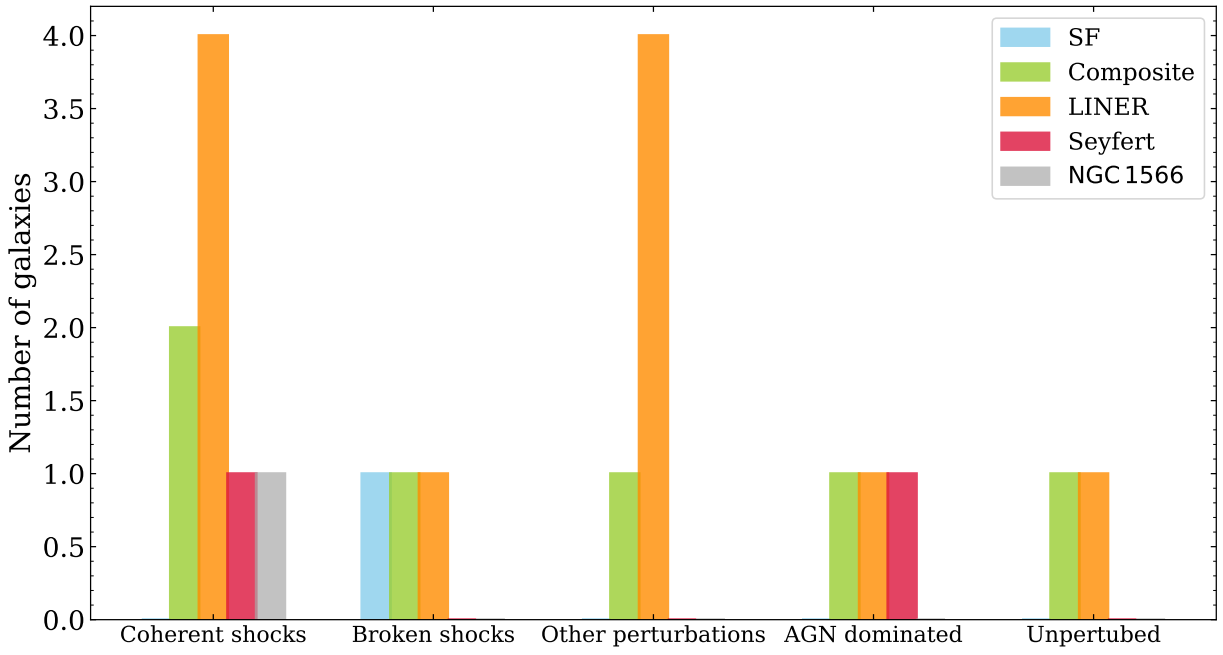


FIGURE 6.4: The distribution of galaxies by kinematic categories colour-coded based on their nuclear emission types, both classifications are defined in Sect. 6.1. Different colours represent SF in blue, composite emission in green, LINER in orange, and Seyfert in red. NGC 1566, which has an uncertain nuclear emission type, is represented in grey.

### 6.3.2 The correlation between extended shocks and average H$\alpha$ velocity dispersion

In Fig. 6.5 I present the distribution of the highest and lowest deprojected residual velocity amplitudes, recorded along the coherent kinematic structures associated with extended shock signatures against the average velocity dispersion of each galaxy.

The figure illustrates that amongst galaxies classified under "coherent shocks" and "broken shocks" categories, the galaxies with the highest deprojected residual velocity amplitudes tend to have larger average velocity dispersions. Although this is a weak correlation, this observation might suggest that the extended shocks with large deprojected residual velocity amplitudes are capable of causing turbulence, thereby elevating the overall disturbance of gas and increasing velocity dispersion within these galaxies. Moreover, galaxies in "coherent shocks" and "broken shocks" categories, exhibiting signatures of extended shocks with relatively lower deprojected residual velocity amplitudes also have lower average velocity dispersions. This indicates that the shocks occurring in these galaxies may not be strong enough to cause additional turbulence to increase the average velocity dispersion.

Galaxies falling under the "AGN dominated" category also exhibit high average velocity dispersions which can be attributed to strong outflows dominating their kinematic fields. However, due to small number of these galaxies, there is not a statistically significant conclusion on the correlation between amplitude level and average H$\alpha$ velocity dispersion of these galaxies.

On the other hand, galaxies with the lowest residual velocity amplitudes, classified under the "unperturbed" category, exhibit the lowest average velocity dispersions across the sample I studied in this thesis. This further confirms the quiescent nature of the kinematic fields in these galaxies, and the absence of shocks or high energy mechanisms ongoing to contribute to the overall velocity dispersion within the inner kpcs.

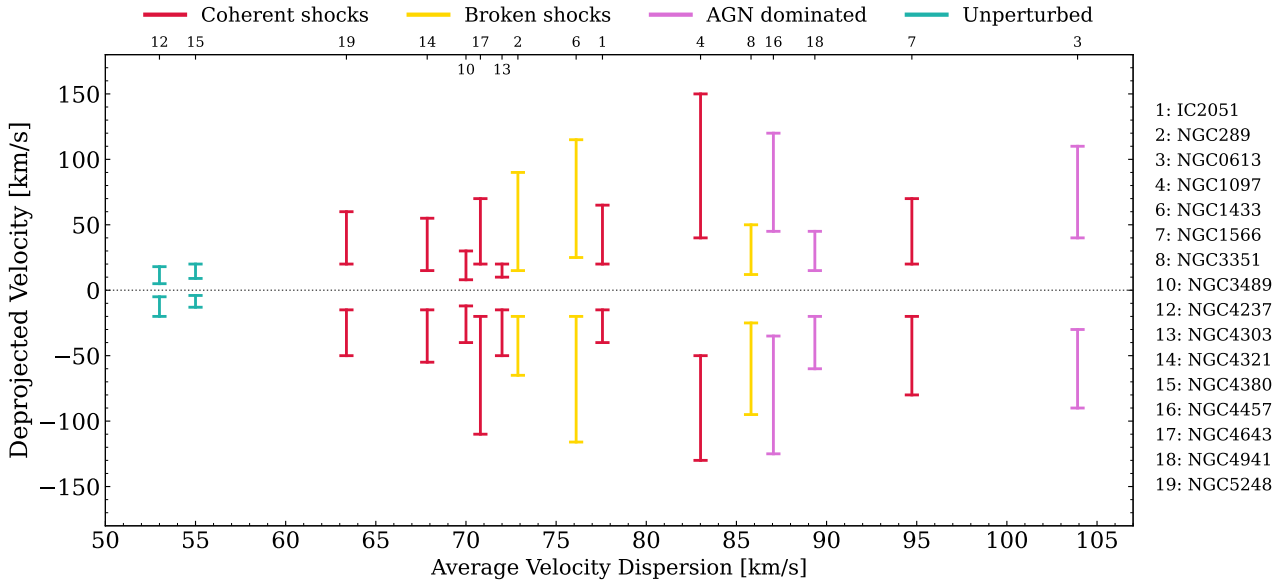


FIGURE 6.5: The deprojected residual velocity amplitudes against the average H$\alpha$ velocity dispersion of the galaxies in different kinematic categories marked by different colours. The colours represent the galaxies in "coherent shocks" in red, "broken shocks" in yellow, "AGN dominated" in purple and "unperturbed" in cyan. The numbers along the top edge of the frame, which represent Galaxy IDs, are consistent with those used in Fig. 6.3.

### 6.3.3 The correlation between extended shocks and stellar mass of galaxies

In Fig. 6.6, I present the distribution of stellar masses for galaxies in each kinematic category. Across the sample studied in this thesis, the majority of galaxies under "coherent shocks" have relatively high stellar masses compared to the majority of those in other kinematic categories. Notably, one galaxy, NGC 3489, which has the lowest stellar mass amongst all galaxies in the sample, appears as an outlier. In Fig. 6.7, I present the distribution of deprojected residual velocity amplitudes for extended shocks alongside the stellar mass of galaxies in each kinematic category. Galaxies under the "other perturbations" category are excluded from this figure. The figure reveals a positive correlation, although a rather weak correlation, where extended shocks with larger amplitudes tend to occur in galaxies whose stellar masses are at least twice as high as those of galaxies with shocks with smaller amplitudes. NGC 1433 and NGC 4457 appear as the two outliers of this trend, exhibiting large amplitudes while having relatively lower stellar masses.

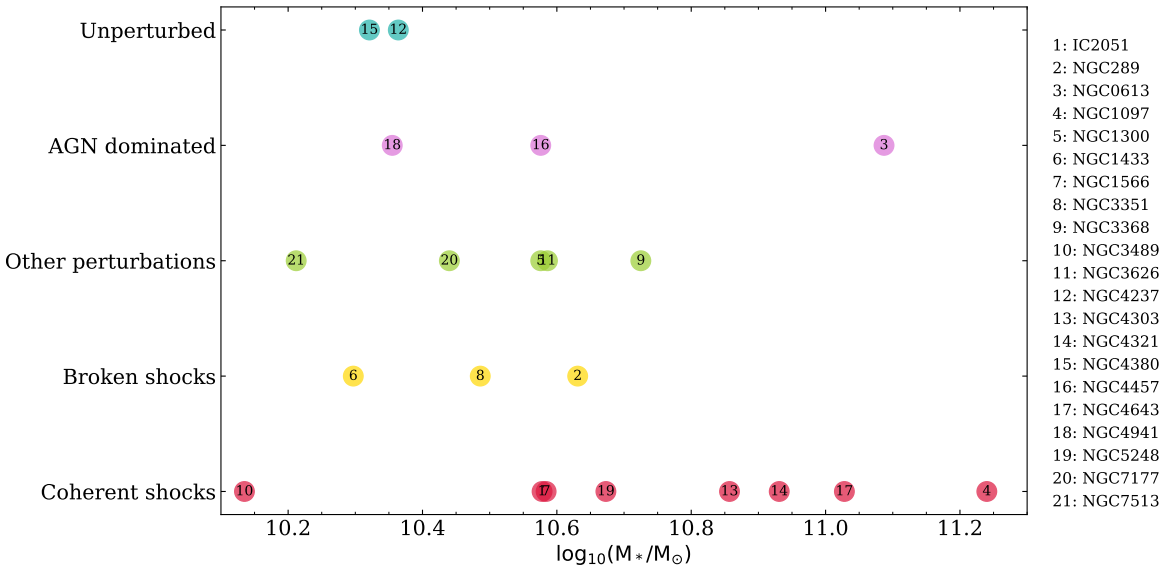


FIGURE 6.6: The distribution stellar mass of galaxies in each kinematic category, marked by different colours. Each point on the diagram marked with a number correspond to a specific galaxy as stated on the right.

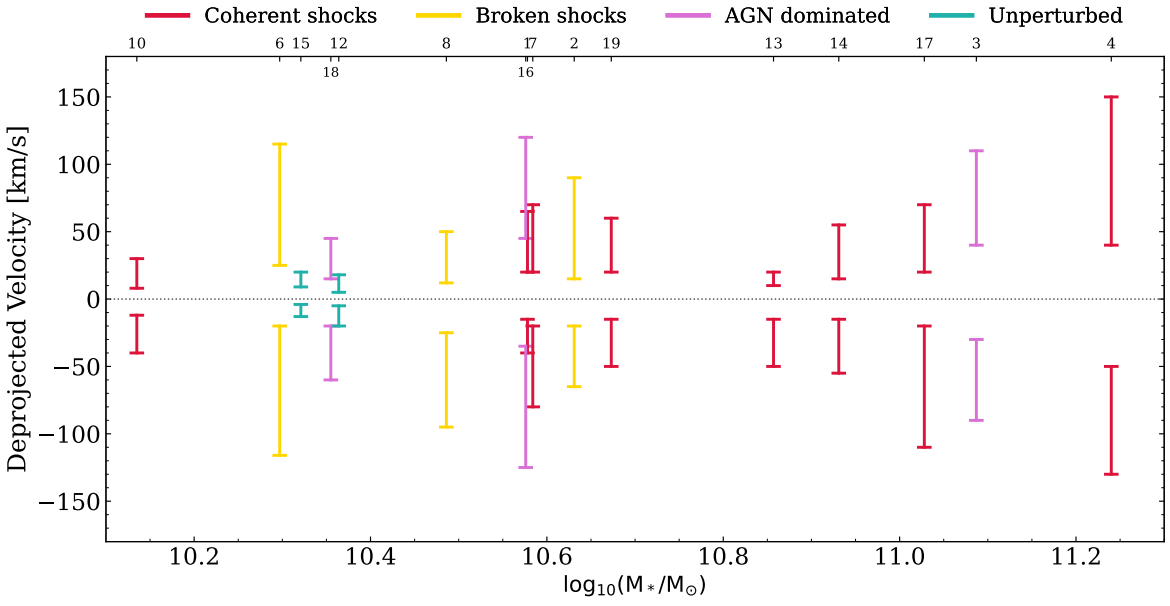


FIGURE 6.7: The deprojected residual velocity amplitudes against stellar mass of the galaxies in different kinematic categories. The colours represent the galaxies in "coherent shocks" in red, "broken shocks" in yellow, "AGN dominated" in purple and "unperturbed" in cyan. The numbers along the top edge of the frame, which represent Galaxy IDs, are consistent with those used in Fig. 6.6.

### 6.3.4 The correlation of extended shocks with the presence of nuclear bars and nuclear rings

As I discussed in Chapter 1 (Sect. 1.1.2), nuclear bars and nuclear rings carry important roles during the transport of gas to the nucleus. While nuclear bars are seen as one of the primary mechanisms of inflow to the nucleus of galaxies (Shlosman et al., 1989; Shlosman, 2001; Martini et al., 2003c; Namekata et al., 2009; Li et al., 2023), nuclear rings are typically seen as barriers of gas transport to the nucleus where inflowing gas accumulates on (Piner et al., 1995; Sheth et al., 2005; Sormani et al., 2015).

In this section, I explore the correlation between the presence of extended shocks and the presence of nuclear bars and nuclear rings obtained from CBS. As described in Chapter 2, the CBS has a diverse sample of galaxies and aims to consistently extract their central stellar structures, such as nuclear star clusters (Ashok et al., 2023), nuclear bars, and rings (Erwin et al., 2024). In the last two columns of Table 3, I provide whether the galaxies in my study host nuclear bars or rings based on the classification within CBS. CBS's publication detailing these findings of central stellar structures is currently in progress (Erwin et al., 2024).

#### 6.3.4.1 Correlations with nuclear bars

Amongst the 21 galaxies, 8 have nuclear bars, while 12 do not. One galaxy, namely NGC 1566, exhibits a potential presence of a nuclear bar. Because of this uncertainty, this galaxy is excluded from further statistical analysis but is kept in Fig. 6.8 for completeness, marked with white hatches. Therefore, the total number of galaxies considered for examining the correlation between the presence of extended shocks and nuclear bars is 20.

Figure 6.8 shows the fraction of galaxies in each kinematic category, grouped by the presence (top panel) and the absence (bottom panel) of nuclear bars. The colours represent different nuclear emission type categories obtained from the BPT diagram of the sample in each kinematic category. In the top panel of the figure, it is evident that all galaxies with nuclear bars have either LINER or Seyfert type emission dominating their inner 150 pc region. Notably, there are no galaxies with star-forming or composite type emission dominating the inner 150 pc regions that host nuclear bars. These observations indicate that the presence of nuclear bars is preventing SF from dominating in the innermost regions. The bottom panel of the figure shows that the fraction of galaxies without nuclear bars does not show a clear correlation with different nuclear emission types. Moreover, neither the top nor the bottom panel reveals a statistically significant fraction standing out in any particular kinematic category.

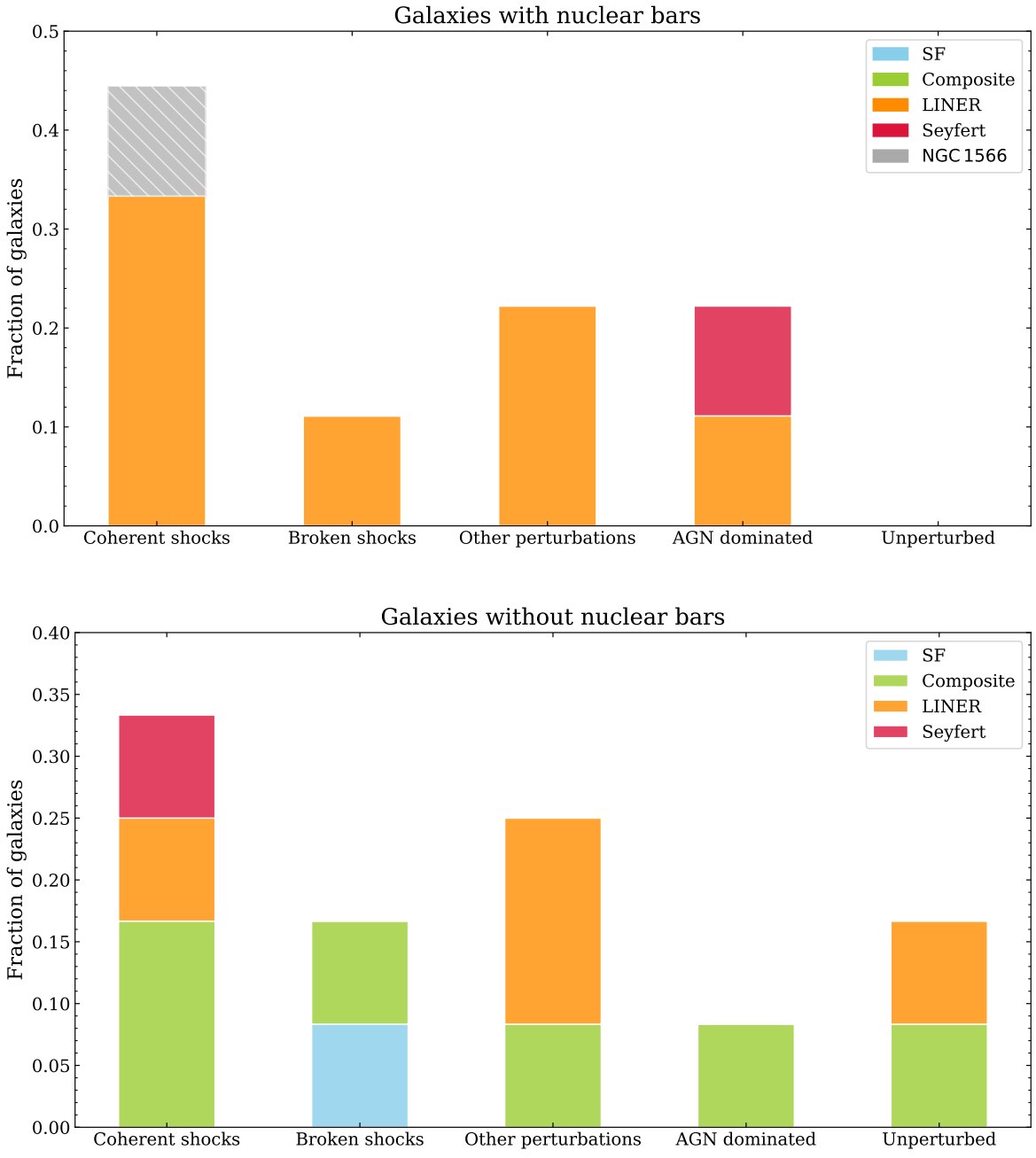


FIGURE 6.8: The fraction of galaxies in each kinematic category is shown, grouped by the presence (top) and absence (bottom) of nuclear bars. The colours represent different nuclear emission type categories based on the BPT diagram of the sample: SF in blue, composite in green, LINER in orange, and Seyfert in red. NGC 1566, which has an uncertain nuclear emission type is represented in grey. Galaxies that exhibit the potential presence of a nuclear bar are marked with white hatches.

#### 6.3.4.2 Correlations with nuclear rings

Furthermore, amongst 21 galaxies in the sample I studied in this thesis, 9 galaxies host nuclear rings, while another 9 galaxies do not. As for the remaining galaxies, two of them are classified as potentially having a nuclear ring, and one of them has an uncertain classification. Since these galaxies do not provide the presence of nuclear rings confidently, I excluded them from my further statistical analysis and description. Therefore, the total number of galaxies I considered when examining the correlation between the presence of extended shocks and nuclear rings is 18. However, in Fig. 6.9, I included the two galaxies that potentially have nuclear rings for completeness.

Figure 6.9 presents the fraction of galaxies in each kinematic category, grouped by the presence (top panel) and the absence (bottom panel) of nuclear rings within their inner kpc. The colours represent different nuclear emission type categories. There appears to be no significant correlation between galaxies with or without nuclear rings and the nuclear emission types, regardless of the kinematic category.

The top panel of the figure reveals that approximately 75% of galaxies (7 out of 9) with nuclear rings exhibit extended shock signatures. Of these, approximately 55% (5 out of 9) fall under the "coherent shocks" category and the remaining ∼25% (2 out of 9) fall under the "broken shocks" category. On the other hand, the bottom panel of the figure reveals that approximately 55% (5 out of 9) of galaxies without nuclear rings do not exhibit signatures of extended shocks; ∼45% (4 out of 9) of galaxies these galaxies are in the "other perturbations" and the remaining ∼10% (1 out of 9) is in the "unperturbed" category. The fraction of galaxies without nuclear rings exhibiting extended shock signatures is low with a total ∼20% (2 out of 9) between the "coherent shocks" and "broken shocks" category. These observations strongly agree with the concept of gas inflow along the bars contributing to the formation of the nuclear rings within the inner kpc of the galaxies. Moreover, strong disturbances caused by other perturbations, such as local SF and AGN activities, within the inner kpc of galaxies, which fall under the "other perturbations" category, might inhibit the formation of nuclear rings in these galaxies.

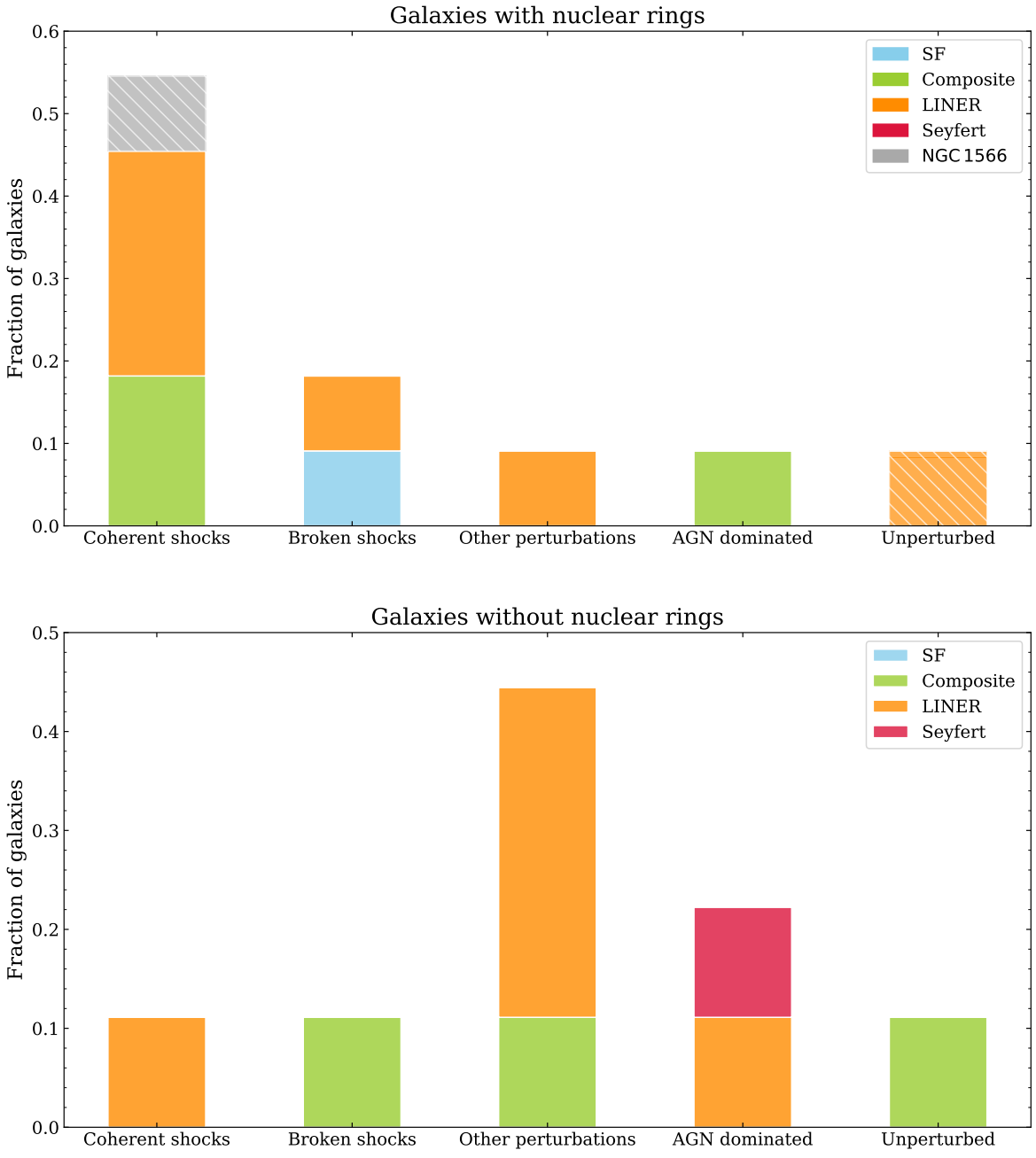


FIGURE 6.9: The fraction of galaxies in each kinematic category is shown, grouped by the presence (top) and absence (bottom) of nuclear rings. The colours represent different nuclear emission type categories based on the BPT diagram: star-forming (SF) in blue, composite in green, LINER in orange, and Seyfert in red. NGC 1566, which has an uncertain nuclear emission type, is represented in grey. Galaxies that exhibit the potential presence of a nuclear ring are marked with white hatches.

# Chapter VII

# Summary & Conclusions of the Thesis

Gas inflows significantly affect the evolution of galaxies by enhancing star formation (Ellison et al., 2011; Prieto et al., 2019), leading to the formation of substructures such as gaseous and stellar rings (Buta & Combes, 1996; Martini et al., 2003b; Fathi et al., 2005; Kim & Stone, 2012; Sormani et al., 2015), and triggering starbursts (Mazzuca et al., 2008). Furthermore, gas reaching the nucleus can feed the AGN (Davies et al., 2014), trigger AGN outflows (Audibert et al., 2019), and consequently cause quenching by suppressing star formation (Donnari et al., 2021). Mechanisms triggering gas inflows, particularly inflow to the nucleus, have been a prominent focus of numerous observational and theoretical studies. For instance, simulations have revealed that non-axisymmetric potentials such as large-scale bars and ovals can trigger prominent morphological substructures in the gaseous medium (Athanassoula, 1992), such as dust lanes, spirals and rings within the inner kpc. These non-axisymmetric potentials efficiently transport gas towards the inner kpc by generating torques that put gas clouds on intersecting trajectories. This leads to extended shocks, in which the gas loses angular momentum and funnels inwards. These extended shocks in observations appear as coherent kinematic structures, which I studied in this thesis.

While the mechanism of bar-driven gas inflows to the inner kpc regions of galaxies is well established, the mechanisms of inflow to the innermost pc regions remain unclear. Understanding the inflow of gas to the nuclei is important to understanding the processes of nuclear feeding, the growth of SMBHs and the consequent influence of the evolution of host galaxies.

In this thesis, using data from MUSE IFU of VLT, I searched for kinematic signatures of extended shocks in ionised gas within the inner kpc regions of 21 nearby galaxies, aiming to determine whether extended shocks are the dominant mechanism of inflow to the nucleus.

Because of its high spatial sampling and large $60''\times60''$ FoV, observations from MUSE maximise my prospect of finding coherent kinematic structures associated with extended

shocks within the inner kpc of galaxies. I derived the LOSVD moments – flux, velocity and velocity dispersion of three distinct emission line groups (H$\alpha$, [N II]$\lambda$6583 and [O III]$\lambda$5007) using a pipeline called DAP, which fits the emission lines with single Gaussians for extraction purposes. In certain regions of a few galaxies, where the spectra were affected by emission from additional sources, I improved the Gaussian fitting by incorporating a secondary component to fit the excess emission. This approach allowed separating the main source of emission from the additional emission source along the LOS, removing the incorrect measurements caused by inappropriate fits and replacing these with accurate values, and improved the robustness of my further analysis.

In my pilot study using galaxy NGC 1097, documented in my publication Kolcu et al. (2023), I developed a methodology of identifying the kinematic signatures of extended shocks, comprising both model dependent and independent methods.

Signatures of extended shocks are best highlighted in residual velocity maps when the underlying circular motion of the disk is removed from the observed velocity field. However, I showed that subtracting the circular velocity of a flat disk may not reveal coherent kinematic structures when they are obscured by the incorrectly fitted disk. This consequently yields artefacts in the residual velocity map coming from the wrong model fit, which obscure real coherent structures present in the data. On the other hand, even when the residual velocity maps do not show coherent kinematic structures, which may be due to difficulty of fitting the disk model, shocks can still be evident as continuous structures in the velocity difference maps between distinct emission line groups, such as in H$\alpha$ and [N II]$\lambda$6583, as the former is more associated with SF and the latter is more associated with shocks. Nevertheless, these differences might be disguised in the presence of strong SF or AGN activity that dominates the velocity fields.

I studied the BPT maps of galaxies, to understand the primary sources of ionisation within their inner kpc. It is important to note that AGN outflows can also strongly dominate the ionisation in central regions, obscuring signatures of extended shocks or SF. To complement my analysis, I also constructed structure maps to examine the spatial alignment between the dust structures and the kinematic signatures of extended shocks. This can provide additional support for the existence of extended shocks, as they are often expected to enhance the dust density. However, if the region has low optical depth, the presence of continuous dust structures may not be apparent since there may be no dust to rely on. It is worth noting that continuous dust structures within galaxies can also arise from differential rotation, which indicate that the origin of such structures is not necessarily extended shocks.

Based on the above, my thesis research proves that relying solely on one method might not be sufficient to dismiss the presence of extended shocks and it is crucial to use multiple approaches while searching for coherent extended shocks in gas.

After applying my methodology to the sample of 21 galaxies, constructed based on the Composite Bulges Survey sample as I described in Chapter. 2, I classified these galaxies into five kinematic categories based on the presence and characteristics of extended shock signatures identified through their diagnostic maps. These categories include: (i) Coherent Shocks, where galaxies exhibit coherent continuous structures, with high amplitudes, extending across large distances that are indicative of extended shocks; (ii) Broken Shocks, characterised by discontinuous structures with large amplitudes, often following a similar pattern to that of the dust lanes that indicate shock compression; (iii) Other Perturbations, where galaxies lack extended shock signatures and their kinematics are dominated by other perturbations, such as local star formation, AGN activities and overshot gas; (iv) AGN Dominated, in which outflows from the AGN dominate the innermost regions of galaxies, preventing tracing the shock structures to the nucleus; (v) Unperturbed; where galaxies have relatively unperturbed kinematic maps with no evidence of shock activity other than structures caused by perturbations from lopsidedness.

Additionally, each galaxy was grouped based on the type of emission dominating its nucleus, which was computed from the ratio of line emission integrated over the central 150 pc radius. The emission type categories include star-forming, composite, LINER, and Seyfert, providing insights into the nuclear activities and processes dominating the inner 150 pc region of the galaxies.

The statistical analysis across the sample based on these groupings reveals that:

1. Despite a limited sample size of 21 galaxies, it can be concluded that approximately 52% of galaxies within the sample exhibited extended shock signatures within their inner kpc regions, suggesting these shocks could be a dominant mechanism for gas inflows to the nucleus. This figure may be a lower limit estimate, as the extended shocks along the bars in galaxies under the "AGN dominated" category, which in total forms 15% of the population, may be extending into the nucleus but they can not be traced due to obscuration from AGN outflows.

2. There is no distinct correlation between the nuclear emission type and extended shock signatures in the galaxies I studied. This may be attributed to the differing timescales of gas inflow and AGN activity, as well as the small sample size.

3. Galaxies under the "coherent shocks" and "broken shocks" categories typically exhibit deprojected residual velocity amplitudes 50 $\mathrm{kms}^{-1}$ or higher across the

structures associated with extended shocks. This implies the presence of strong shocks and large velocity jumps, in alignment with theoretical models. Conversely, the amplitudes within structures observed in galaxies classified under the "unperturbed" category, the only two unbarred galaxies in the sample, were significantly lower, not exceeding $20\,\mathrm{kms}^{-1}$. These subtle changes in velocity suggest the absence of shock mechanisms in these galaxies. Instead, the observed structures point to a wave-like behaviour, but likely originating from other mechanisms, such as spiral density waves or differential rotation. This analysis affirms the critical role of bars in driving extended shocks, thus facilitating gas inflows.

4. Most galaxies exhibiting large deprojected residual velocity amplitudes also show large average velocity dispersions. Conversely, galaxies with lower deprojected residual velocity amplitudes exhibit lower average velocity dispersions. These suggest that stronger extended shocks often lead to more turbulent kinematic fields.

5. Deprojected residual velocity amplitudes have a positive correlation with stellar mass, such that the majority of galaxies with larger velocity amplitudes also tend to have higher stellar masses.

Further, I examined the correlation between extended shock signatures and the central stellar structures recovered in the Composite Bulges Survey. I particularly focused on the presence of nuclear rings and nuclear bars. This analysis reveals that:

1. Galaxies with nuclear bars host either a LINER or Seyfert type core, indicating nuclear bars prevent SF activities to dominate the innermost regions of galaxies. I found no statistical significance between the presence or absence of nuclear bars and any kinematic category.

2. Approximately 75% of galaxies with nuclear rings exhibit signatures of extended shocks, with the majority, 55%, falling under the "coherent shocks" category. Conversely, about 55% of galaxies without nuclear rings are categorised in "other perturbations". These findings support the claim of gas inflows along bars contribute to the formation of nuclear rings, while strong local perturbations may inhibit this formation. I found no significant statistical correlation between the presence or absence of nuclear rings and the nuclear emission types.

The methodology I developed in this thesis provides new means of finding coherent kinematic structures, associated with extended shocks and inflows. Although the sample size is limited, my findings suggest that extended shocks can be the predominant mechanism driving inflows to the nuclei of galaxies. Expanding this study with a larger sample size could not only strengthen the statistical significance of my findings but also

potentially uncover stronger correlations between the presence of extended shocks and the characteristics of the galaxies such as the nuclear emission types, stellar masses, and distinct central stellar structures.

*"I am fine!"*

Ross Geller

*"I'm gonna go get one of those job things"*

Rachel Green

*"If I'm harsh with you, it's only because you're doing it wrong"*

Monica Geller

*"My eyes, my eyes!"*

Phoebe Buffay

*"This is all just a moo point"*

Joey Tribbiani

*"I make jokes when I am uncomfortable"*

Chandler Bing

# Chapter VIII

# Future Outlook

In this section, I briefly explain the additional projects I am involved in. The project described in Sect. 8.1, is within the Physics at High Angular resolution in Nearby GalaxieS (PHANGS) Collaboration, lead by myself under supervision of Dr Mattia Sormani. I present the underlying motivation of the project. However, I emphasise that I am currently working on the analysis and the results are preliminary. I aim to submit the results of this project by September 2024. The second project described in Sect. 8.2 outlines the independent research project I aim to conduct in future, which is inspired by my doctoral research.

## 8.1 Extreme cloud collisions in nearby barred galaxies

The Central Molecular Zone (CMZ), at a radial distance $R \leq 200\,\mathrm{pc}$ ($|l| \leq 1.5°$) from the Galactic Centre, has been a subject of extensive research (Molinari et al., 2011; Henshaw et al., 2016; Gramze et al., 2023a). CMZ exhibits complex dynamical activities due to its interactions with its surroundings. Particularly, gas inflows funnelled to the innermost regions via the bar significantly contribute to the perturbed kinematics observed there (Sormani & Barnes, 2019).

In the vicinity of CMZ, a group of compact clouds is revealed as dominating the kinematics, prominently seen in molecular gas (e.g., CO emission), have very wide velocity spreads ($\Delta v$), exceeding $100\,\mathrm{kms}^{-1}$, and are confined within a narrow longitude (Liszt, 2006, 2008; Sormani et al., 2019; Gramze et al., 2023a). These structures are referred to as extended velocity features (EVFs) (Sormani et al., 2019). To demonsterate example of EVFs, in Fig. 8.1, I present CO(1–0) emission and the corresponding PV diagram of the CMZ. I mark the EVFs reported by former works within the given region.

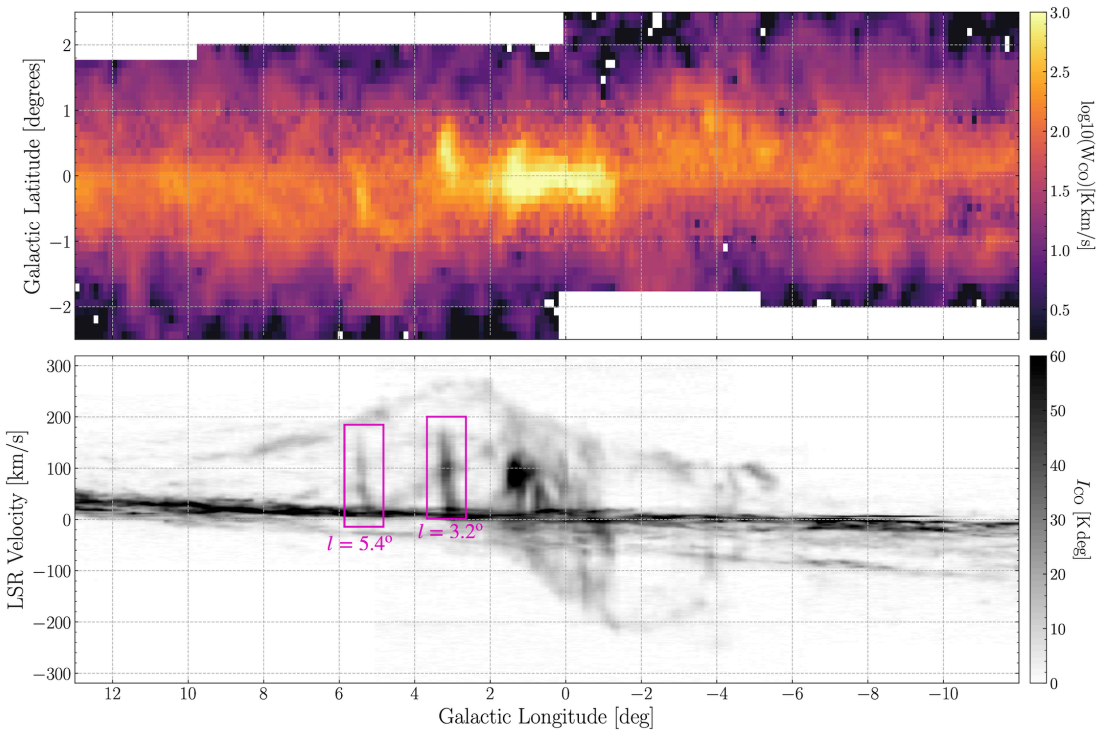


FIGURE 8.1: The CO(1–0) diagnostic maps of the CMZ. Position-position diagram with total CO intensity, constructed using data from Bitran et al., 1997 (top) position-velocity diagram with two prominent EVFs, highlighted based on Liszt (2008) with magenta boxes (bottom).

Several mechanisms and interpretations are put forward for the origin of the EVFs. They are proposed to be (i) elongated gaseous structures that are parallel to our line of sight (Stark & Bania, 1986; Boyce et al., 1989; Lee et al., 1999; Baba et al., 2010); (ii) remnants of giant magnetic loops (Parker, 1966; Fukui et al., 2006; Fujishita et al., 2009; Torii et al., 2010); (iii) suggestive of the presence of intermediate-mass black holes, whose gravitational influences could account for the observed dynamic gas movements (Oka et al., 2016, 2017; Takekawa et al., 2019b,a); (iv) dense lumps of matter crossing the dust lanes of the Galaxy's bar, and the velocity spread is caused due to interactions of matter and the bar (Fux, 1999; Liszt, 2006, 2008).

Recent simulations of Sormani et al. (2019) reveal that EVFs naturally emerge in the gas flow in barred potentials, due to the collision of gas clouds with different line-of-sight velocities along the bar lanes of galaxies. As the gas moves inwards along one of the galaxy's bar lanes, it often overshoots its intended path towards the galactic centre, continuing on a trajectory that leads it directly into the opposing bar lane, where it collides with gas present there. This localised collision gives rise to the characteristic signatures of EVFs, which are *large velocity gradient* over a *compact longitude*. A representation of this mechanism obtained from models is demonstrated in Fig. 8.2. Supporting theory

from these simulations, evidence of cloud-cloud collisions is shown in a recent observational study of molecular gas in CMZ Gramze et al. (2023a). This study focused on the G5 cloud within CMZ, which is presumed to be at a cloud collision site, where they discern an EVF in position-velocity (PV) diagrams, exhibiting a $\Delta v$ of $\sim$100 kms$^{-1}$.

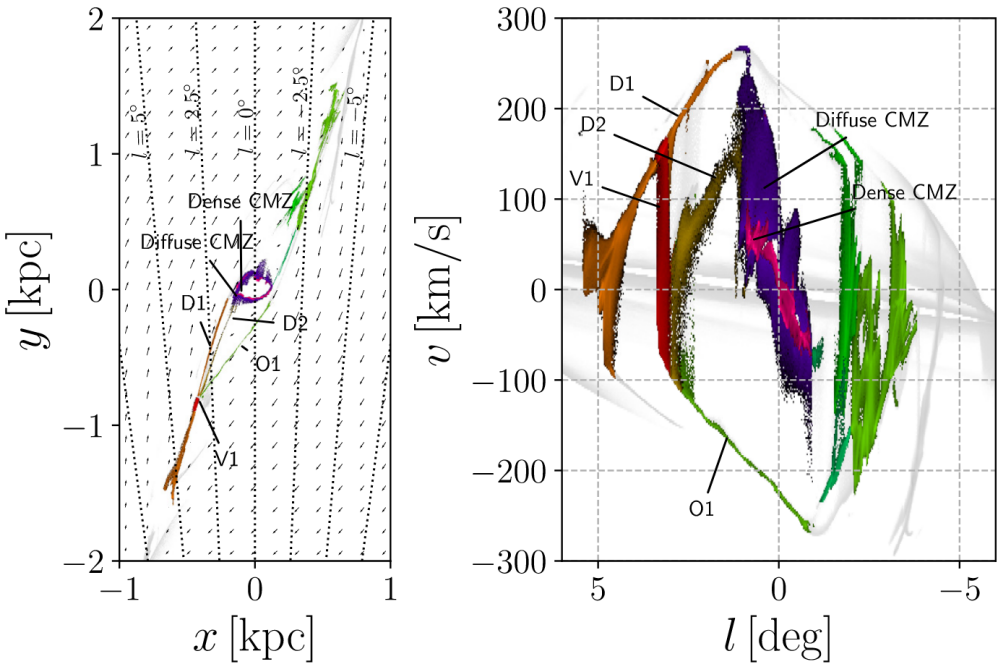


FIGURE 8.2: The mechanism of overshooting gas streams along galactic bar lanes, adopted from Sormani et al. (2019). Features in the (x, y) plane (left) and their projection to the (l, v) plane (right) for the simulation snapshot at $t = 178$ Myr. Arrows in the left-hand panels show the velocity field in the rotating frame of the bar. Some of the interesting features are marked: V1 resembles the EVF observed at l=5.4° in Fig. 8.1, which originates as the material on the 'overshooting' feature O1 collides with the material in the dust lane D1.

To deduce whether the cloud collision scenario proposed by simulations can be the primary mechanism originating EVFs in CMZ, I aim to find EVFs in external galaxies, which can be analogous to those found in the Milky Way. Studying external galaxies offers us a panoramic view to enrich our understanding of the dynamic processes that give rise to EVFs, thus providing us with insights into dominant dynamical mechanisms within the CMZ of our galaxy.

Using CO(2–1) emission data obtained from the Atacama Large Millimeter/submillimeter Array (ALMA), I studied 29 nearby barred galaxies from PHANGS Survey. PHANGS is a multi-wavelength programme spanning from the far-UV to radio wavelengths, aiming to sample all stages of the star formation and feedback cycle. A part of this survey, PHANGS-ALMA, primarily aims mapping and studying the CO(2–1) emission of 90 nearby star-forming galaxies in the southern sky (Leroy et al., 2021b). Providing high angular and physical resolution, $\sim 1''$ and $\sim$100pc respectively, across a

large field, $\sim 2' \times 2'$, observations from ALMA revolutionised the studies of the molecular gas in nearby galaxies. Additionally, in this work, I also used NIR images from the James Webb Space Telescope (JWST), provided by PHANGS-JWST Treasury Survey (Lee et al., 2023), to search for signatures of overshot gas streams to the cloud collision regions.

In this work, I focused on a sample of 29 nearby galaxies classified as barred in the PHANGS sample Stuber et al. (2023b). Using ALMA emission cubes with a resolution of approximately $2''$ (or $\sim$120–150 pc), I constructed and analysed the CO(2–1) intensity maps and PV diagrams for each galaxy. I searched these diagrams for signatures of EVFs. To complement this kinematic search, I also examined composite NIR images constructed using JWST data, searching for overshot streams of gas that extend from one bar end to the other, all the way to the regions where EVFs occur

Within the sample I studied in this work, I identified 9 galaxies with EVFs, exhibiting $\Delta v$ measurements ranging approximately from 40 to 100 $\mathrm{km s^{-1}}$. In regions where EVFs are prominent in the PV diagrams, localised enhancements in CO(2–1) intensity were observed. In all galaxies, EVFs appear along the bar lanes at varying distances from the centres of their host galaxies. Figure 8.3 presents NGC 1512 as an example of a galaxy with identified EVFs.

Further in this project, I will compute the molecular mass contents confined within the regions where EVFs are identified. I will search for correlations between the characteristics of EVFs and the bar and general characteristics of the galaxies. Additionally, using other available data, such as H$\alpha$ emission, from PHANGS, and from potentially external sources, I will investigate whether these collisions could potentially trigger star formation (SF).

Led by Dr Yixian Cao, and in collaboration with myself and Mattia Sormani and several other PHANGS members, we recently proposed to map the CO(2–1) line around EVF regions of three galaxies with $\sim 1''$ ($\sim$100 pc) resolution. This is submitted to ALMA Cycle 11 under the Project ID 2024.1.01030.S. Given this proposal is successful, these deeper observations will enable us to conduct several follow-up studies that examine the kinematics of faint molecular gas streams in greater detail.

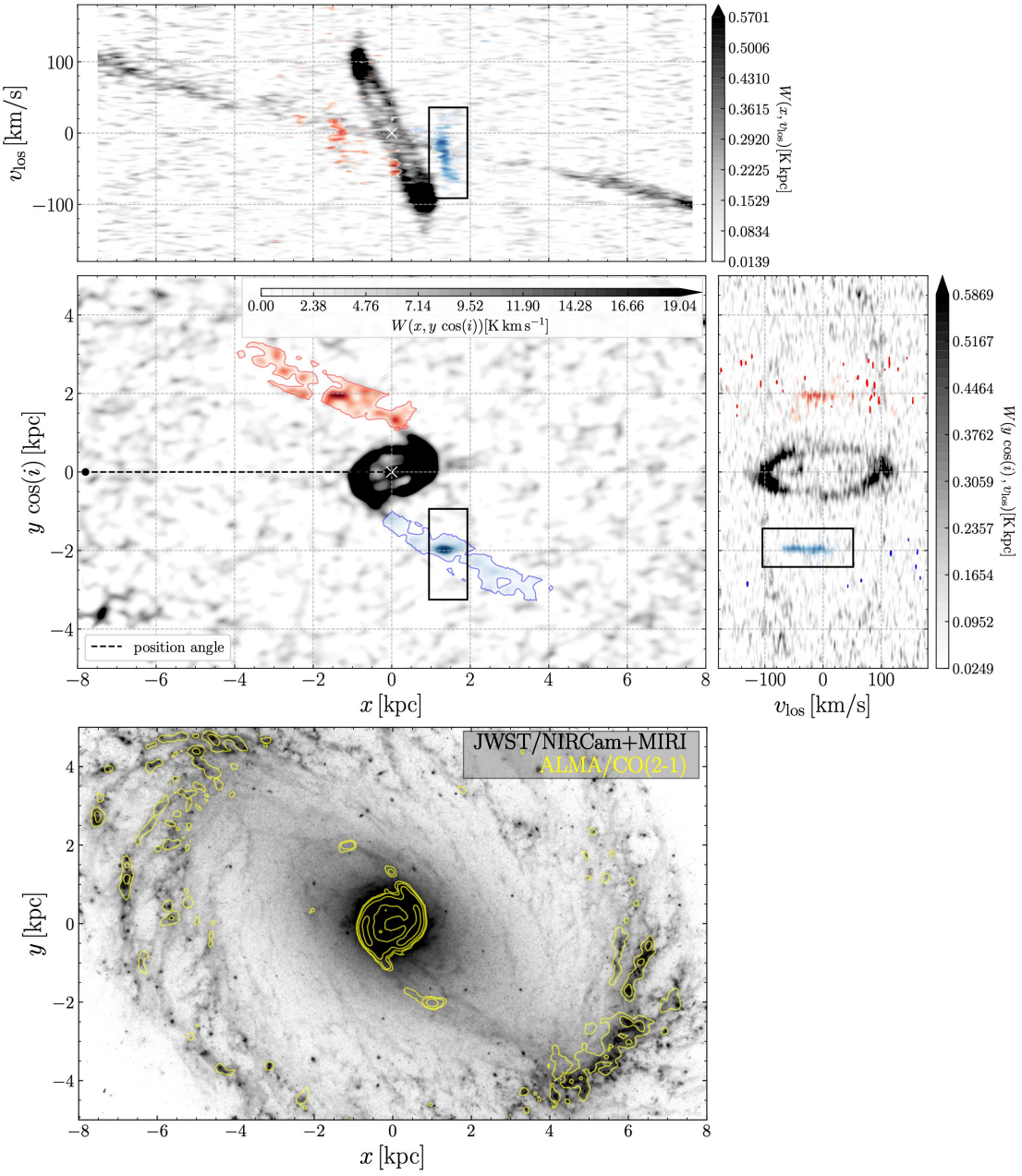


FIGURE 8.3: The diagnostic maps for NGC 1512. *top:* the PV diagram, integrated along the x-axis of the PP diagram shown in the middle left panel. *middle:* the CO(2–1) intensity map, PP diagram (left) and the PV diagram, integrated along the y-axis of the middle left panel (right). *bottom:* JWST composite image overlaid with CO(2–1) intensity contours. The galaxy is rotated in such the kinematic PA of the LON is aligned with x-axis. Red and blue highlighted regions indicate dust lanes on the red- and blue-shifted sides of the galaxy, respectively. The black boxes in the PP and PV diagrams outline the region of EVFs. The centre of the galaxy is marked with an "x".

## 8.2 Multi-wavelength insights into how the synergy between large-scale interactions and internal dynamics shapes galaxy gas kinematics

For field galaxies in isolation, the gas is redistributed due to *internal mechanisms*, such as bars. Due to non-axisymmetric torques generated by the bar, gas clouds along the bar can collide and become shocked, leading to loss of angular momentum and inflow of gas towards the inner regions of the galaxy (e.g., Athanassoula, 1992). On the other hand, for galaxies in dense clusters or groups, along with internal processes, external *large-scale interactions* (e.g., mergers and ram-pressure stripping; RPS) also impact the gas distribution in the central regions (e.g., Boselli & Gavazzi, 2006; Kapferer et al., 2009), leading gas inflows (e.g., (Robertson et al., 2006; Lagos et al., 2018)).

While many studies delve deeply into the internal processes and characteristics of individual galaxies, they frequently overlook the crucial context of their surrounding environments. Conversely, the majority of research dedicated to clusters and groups tends to concentrate solely on the effect of the environment on global properties, such as star formation rates (SFR), without focusing on how the effect propagates in galaxies.

The lack of connection between the two fields of research leaves a significant question in debate: ***what is the dominant physical process causing transformations and quenching in galaxies as a function of environment?*** Given most galaxies are in cluster or group environments, to understand their evolution across cosmic time, my goal is to comprehensively combine the study of both large-scale interactions and internal processes.

Building upon the methodology I developed during my doctoral research to identify and study the signatures of gas inflows, as explained in detail in Chapter 3, I aim to study the gas kinematics of ∼50-100 nearby galaxies ($\sim z < 0.05$) in diverse environments – clusters, groups and field – across the entire galaxy extents, from outskirts to nucleus. I will determine in which environment gas inflow signatures are most prominent, and correlate this with the presence of a bar and the types of large-scale interactions acting on each galaxy. This study will establish whether internal or external processes drive the gas inflow to the nucleus, and therefore determine the mechanism dominating galaxy evolution as a function of environment.

Despite numerous studies on SFR and AGN activity in the literature, there remains a notable gap in the study of the resolved gas kinematics of nearby cluster/group galaxies, mainly due to instrumental limitations in the past. The advent of new generation IFUs, particularly MUSE/VLT, allows us to study the gas kinematics with sub-kpc

level details in nearby galaxies, from their outskirts towards their nucleus, and within their environments. Coupling this kinematic data with high-resolution imaging and/or spectroscopy in different wavelengths from recent facilities like JWST, Euclid, ELT (in future), allows correlating the gas kinematics with morphologies and merger histories of the galaxies. This high-resolution study of gas will also provide an excellent test for hydrodynamical simulations (e.g., EAGLE and IllustrisTNG) in understanding the galaxy evolution across cosmic time.

To conduct this research I have initiated several collaborations granting me access to a rich multi-wavelength data set to carry out my planned research. These include archival and scheduled data from the ESO large program *"MAUVE (MUSE and ALMA Unveiling the Virgo Environment)"* (PIs: L. Cortese & B. Catinella), covering 40 late-type Virgo Cluster galaxies, at different infall stages; MAUVE incorporates data from the "VERTICO" Survey with ALMA, providing molecular gas data for multi-phase comparisons. The first results on MAUVE is presented in Watts et al. (2024).

For group galaxies, I have data from *Complete Local-Volume Groups Sample, CLoGS* (PI: E. O'Sullivan), comprising 53 local groups ($z$ <0.01), providing data across X-ray (Chandra), radio (GMRT, VLA), and sub-mm (IRAM-30m, APEX) wavebands (O'Sullivan et al., 2017). While 18 early-type central galaxies in CLoGS already have MUSE data, I plan to propose new MUSE observations for late-type galaxies to enrich the survey.

For field galaxies, I aim to include MUSE data from *"PHANGS"*, which resolves details down to ∼100 pc for entire galaxy extents; central regions of 6 mutual galaxies with CBS are already characterised in my current work. PHANGS provide publicly available ALMA and JWST data, which can be used for complementary multi-phase studies.

Furthermore, as a part of my new PDRA role at the University of Nottingham I will have access to data from Euclid, which will well complement my planned research with MUSE. The resolution and field-of-view of Euclid will allow studying the entire extent of the nearby galaxies, and their clusters/groups with unprecedented details, both in optical and NIR, while probing the nature of their interactions and environments, and focusing on their multi-phase gas kinematics. By coupling the high-resolution MUSE data I have through various surveys, with imaging from Euclid, I am interested in understanding the nature of the intracluster light in cluster and group centres, with a particular focus on studying the gas flows in those regions.

***What open questions I am interested in exploring?***

**(Q1) Do large-scale interactions shape the central regions of galaxies, together with bars?**

Spectroscopic studies show that the enhanced SF in the galaxy central regions, isolated or in clusters, can be attributed to the presence of bars (e.g., Coelho & Gadotti, 2011; Sánchez-García et al., 2023). However, the impact of large-scale interactions on the central SF enhancement is still being debated (e.g., Chown et al., 2019).

**(Q2) Which mechanism predominantly drives the gas kinematics at different infall stages?**

Galaxies inhabiting different cluster regions will be influenced by their environment differently (e.g., Jaffé et al., 2015). To understand whether large-scale interactions dominate the shock wave propagation to the centres of the galaxies over internal processes, it is important to examine the gas kinematics of galaxies at different infall stages, as a function of the environmental properties.

**(Q3) Do extended shocks dominate central galaxy regions more in groups than clusters?**

Galaxy groups are the most common and diverse environments where galaxies reside (e.g., Tully, 1988), and they are crucial for studying gas turbulence, AGN and stellar feedback processes (e.g.,Vulcani et al., 2018). Due to the low intra-group densities, it is unexpected for group galaxies to face violent stripping processes, and this expectation leaves the study of the large-scale interactions in groups largely unexplored. Groups have shallower gravitational potentials and smaller separations between members compared to clusters, so, mergers and tidal interactions occur more often in groups than in clusters (e.g., McIntosh et al., 2008). Moreover, my previous research Kolcu et al. (2022a), has shown that galaxies can retain their gas reservoir for long times and distances during their infall, giving extended shocks more time to reach the central regions of galaxies in groups than clusters, where it can accumulate and trigger AGN activities.

# Appendices

## A Supplementary maps for the pilot study with NGC 1097

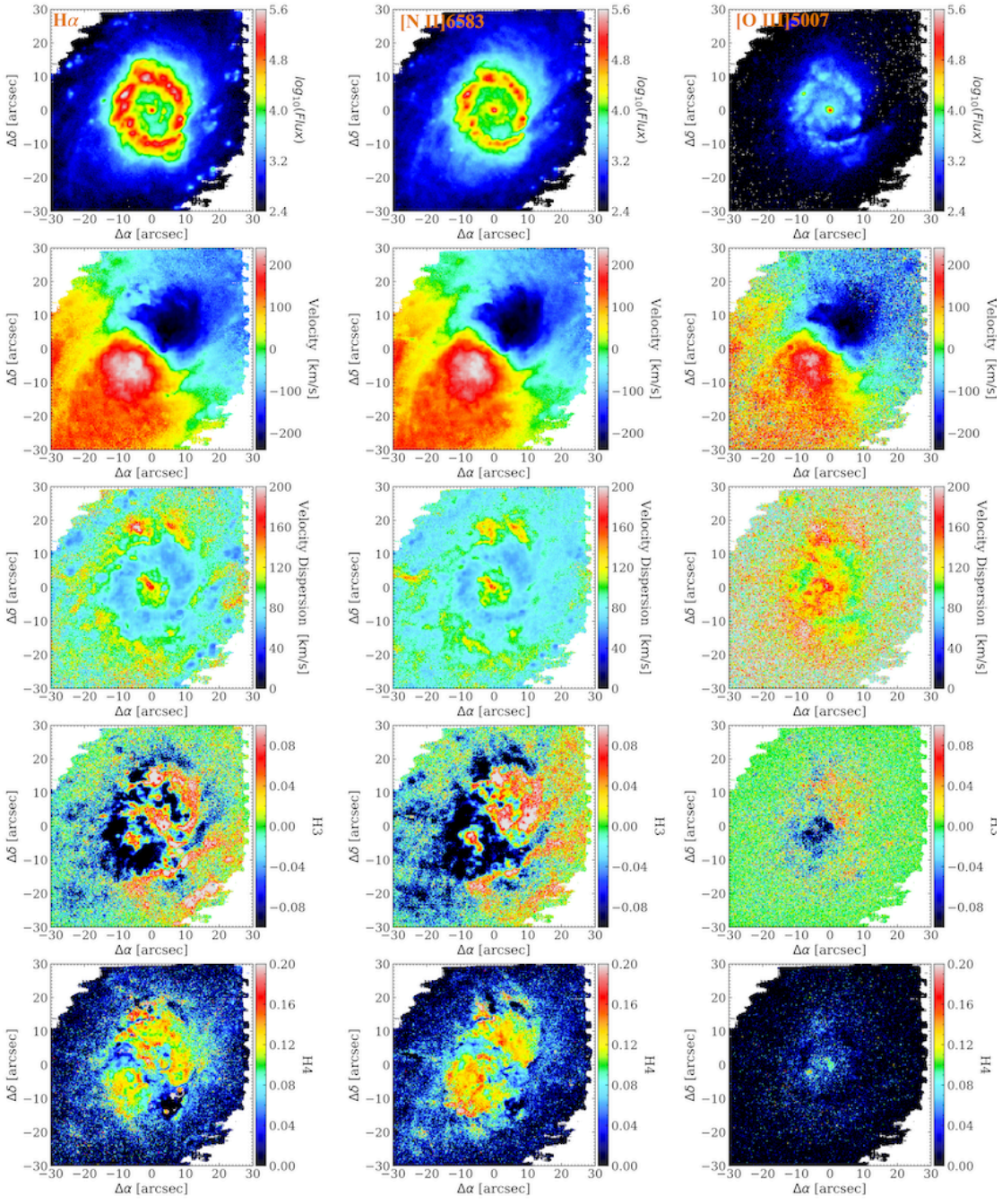


FIGURE A.1: LOSVD moments for fits including higher order moments (h3 and h4). Columns show H$\alpha$ (left), [N II]$\lambda$6583 (middle) and [O III]$\lambda$5007 (right). The units of the flux measurements are $10^{-20}$ergs$^{-1}$cm$^{-2}$spaxel$^{-1}$.

# B Supplementary collective plots for sample galaxies studied in this thesis

Figures B.1 and B.2 are to help the reader to have a collective look to the resultant diagrams of the methodology applied to the sample galaxies.

Figure B.3 presents the averaged deprojected residual velocity fields used to calculate the highest and lowest amplitudes along the structures associated with extended shocks (see Sect. 6.2.1).

Figure B.4 shows the distribution of velocity dispersion and AON, which is used to remove the noisy spaxels while calculating the average velocity dispersion of the galaxies in Sect. 6.3.2.

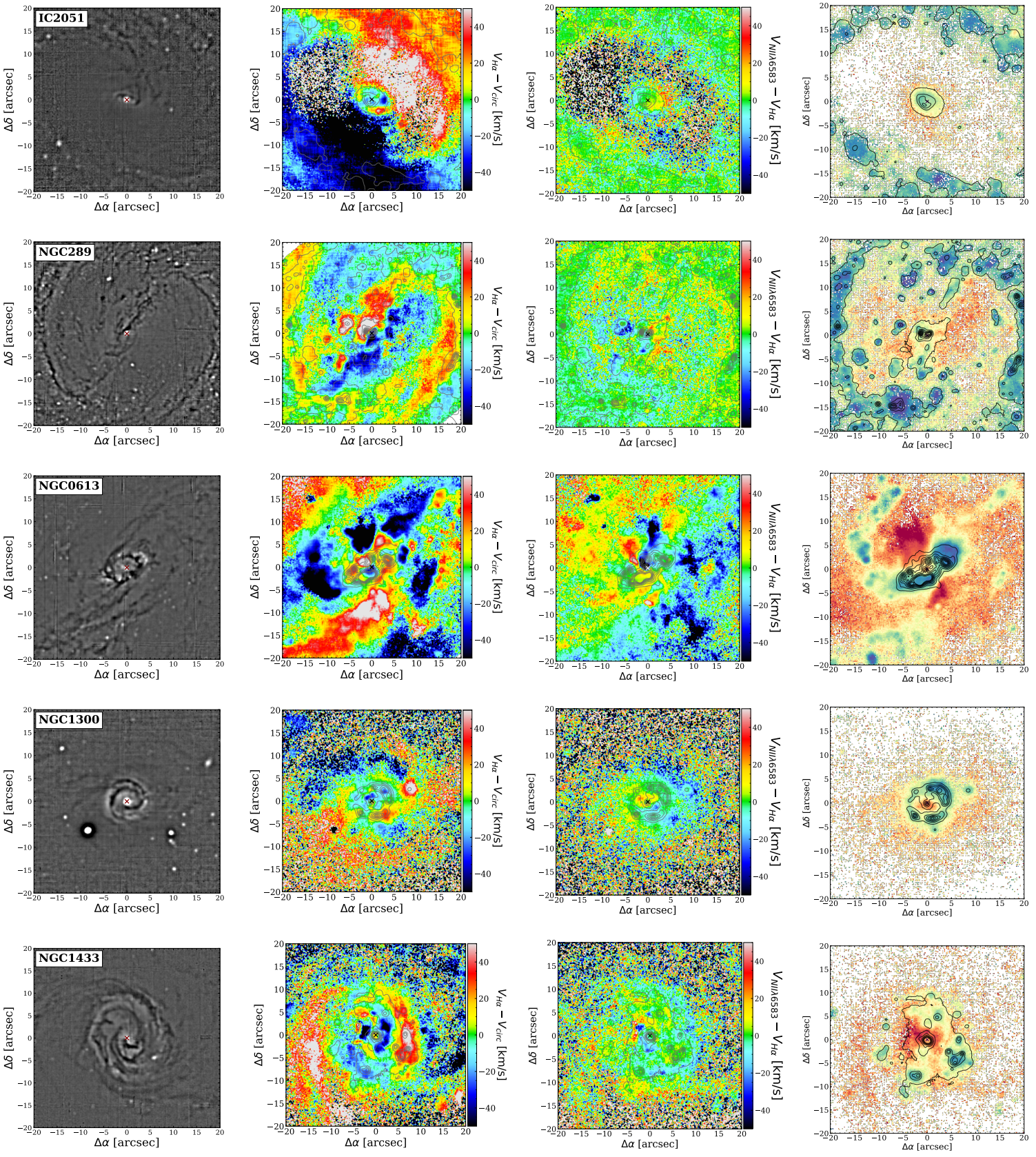


FIGURE B.1: The diagnostic maps of galaxies studied in this thesis. The structure map (first column) the residual velocity maps (second column) the velocity difference maps (third column) the spatial map with each spaxel colour coded based on the points represented in the respective BPT diagram Fig. B.2 (fourth column). Contours on the diagrams in the last three columns represent H$\alpha$ flux. The centre of each galaxy is marked with an "X".

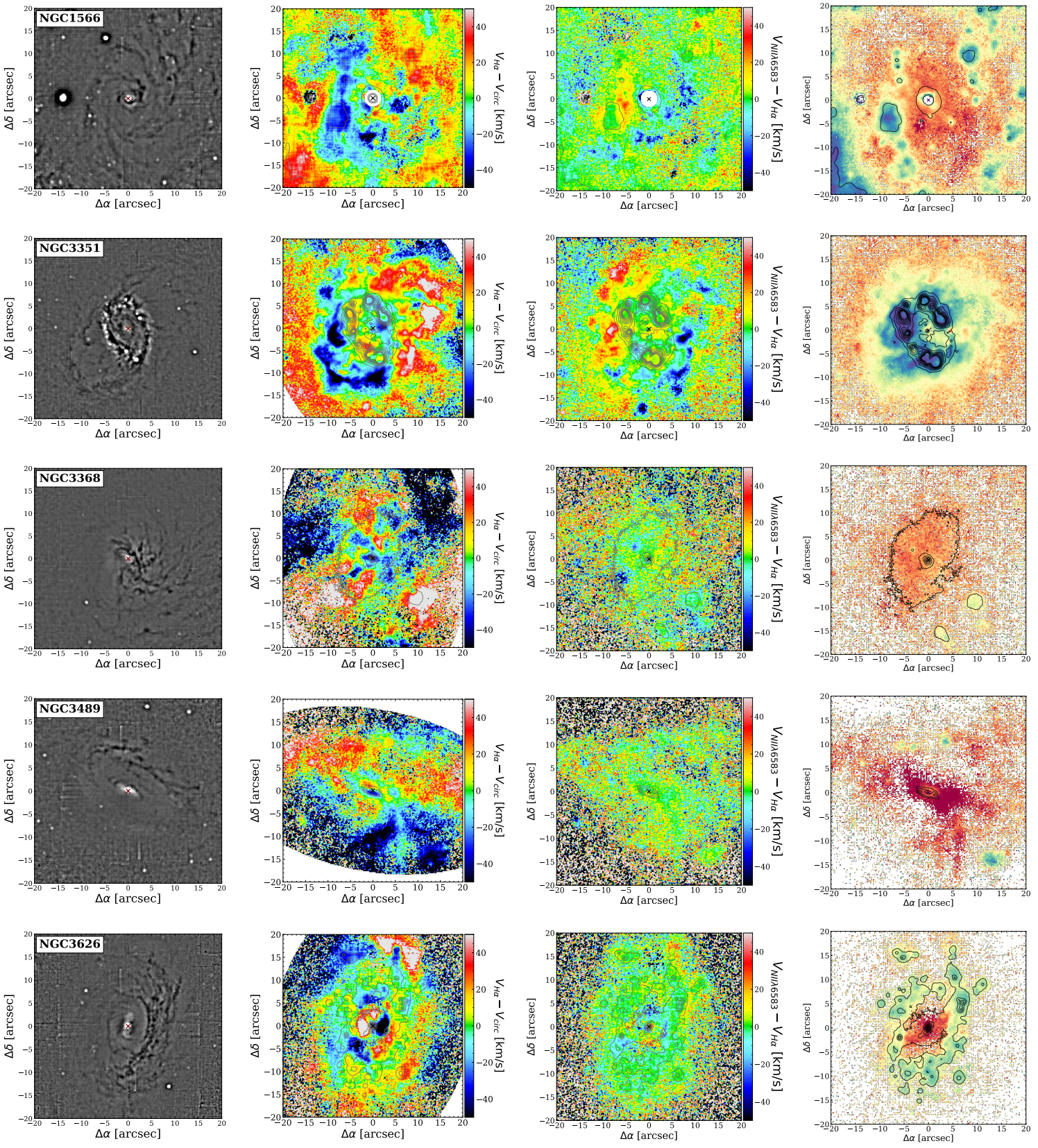


FIGURE B.1: continued.

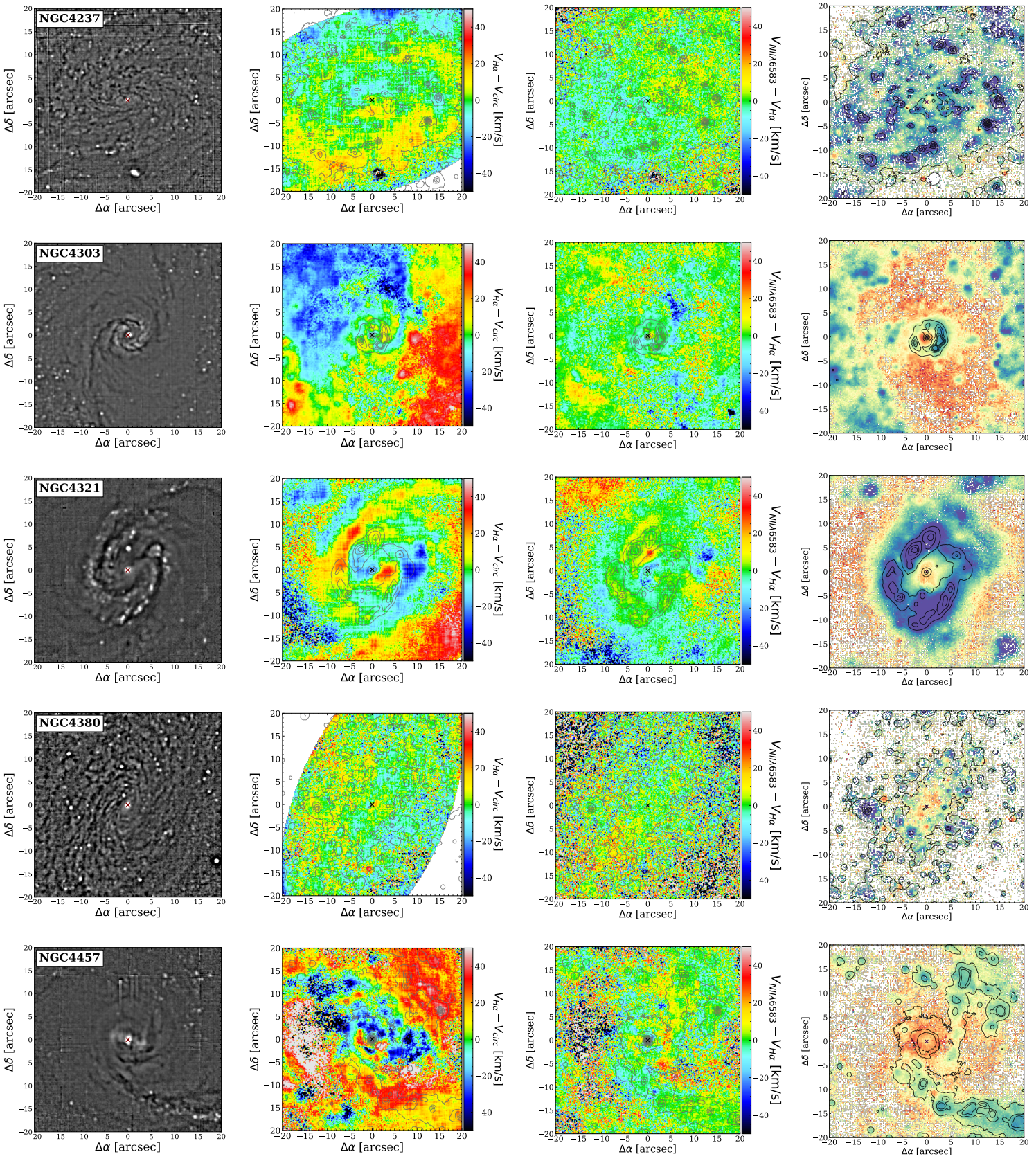


FIGURE B.1: continued.

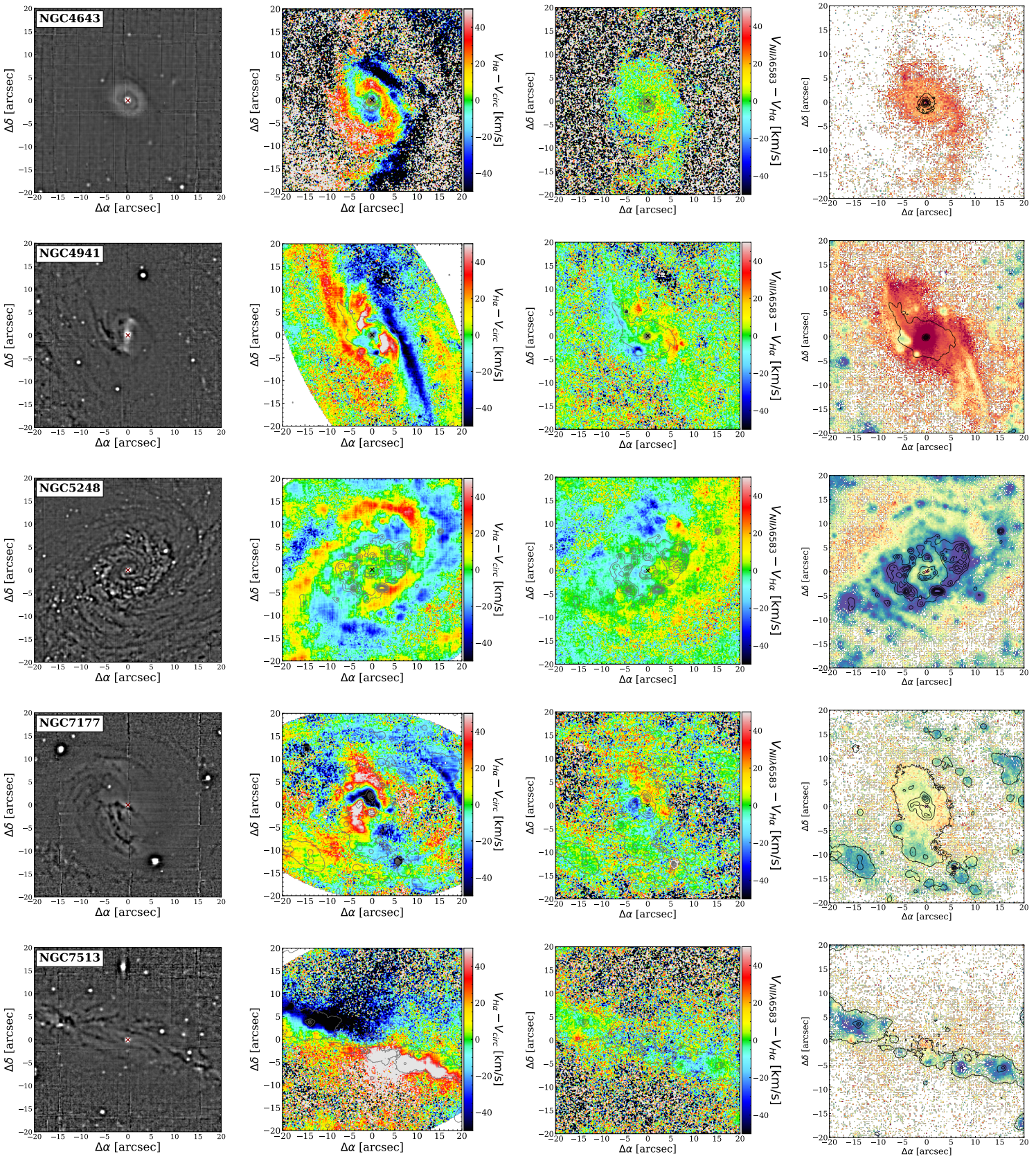


FIGURE B.1: continued.

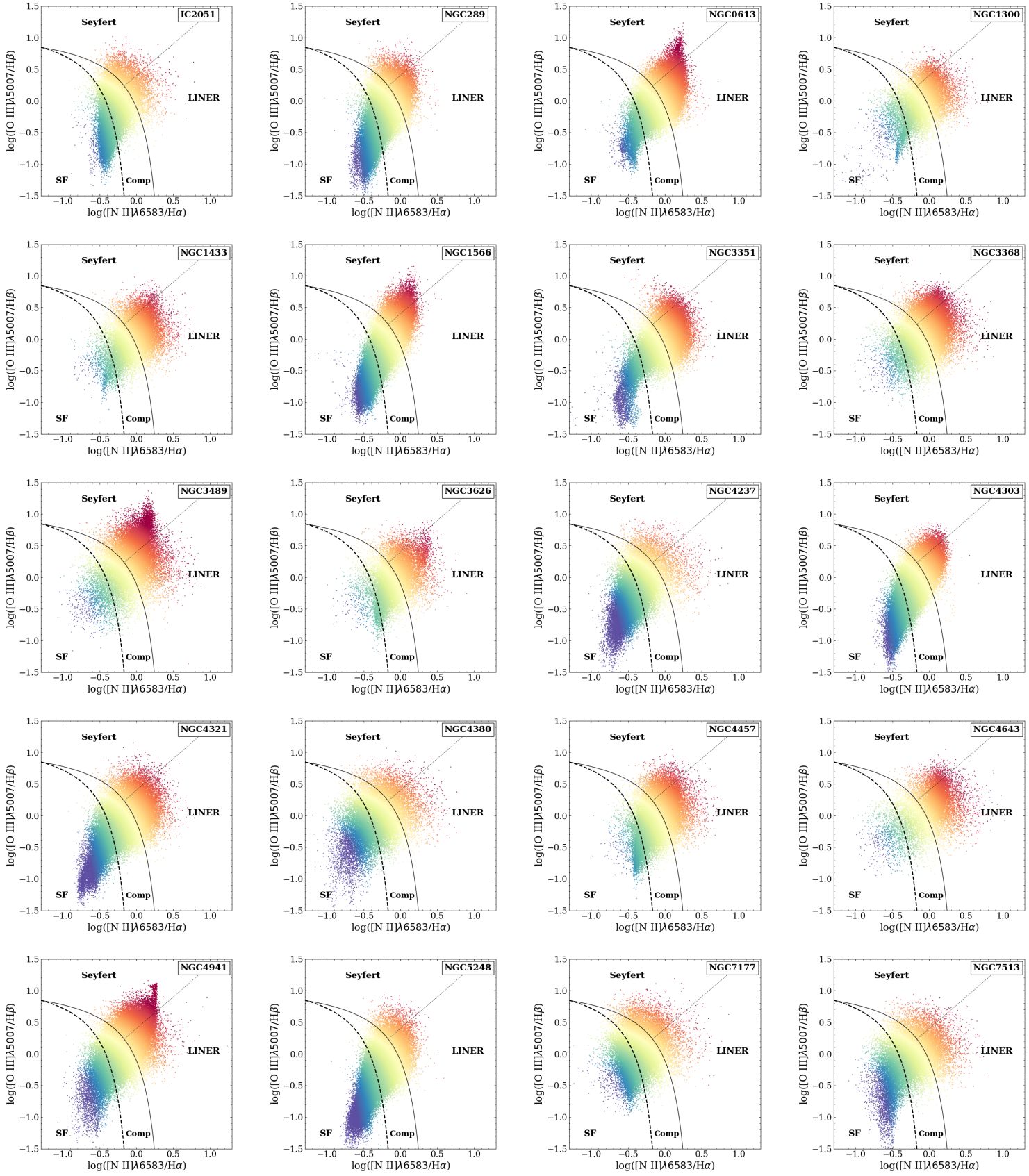


FIGURE B.2: The BPT diagrams of the galaxies within the sample studied in this thesis. Solid, dashed and dotted lines represent the Kewley et al. (2001); Kauffmann et al. (2003); Cid Fernandes et al. (2011) fits respectively which establish the dominating ionisation mechanisms as star-forming (SF), Composite, LINER and Seyfert. The colour coding is based on the distance from the (Kewley et al., 2001) line.

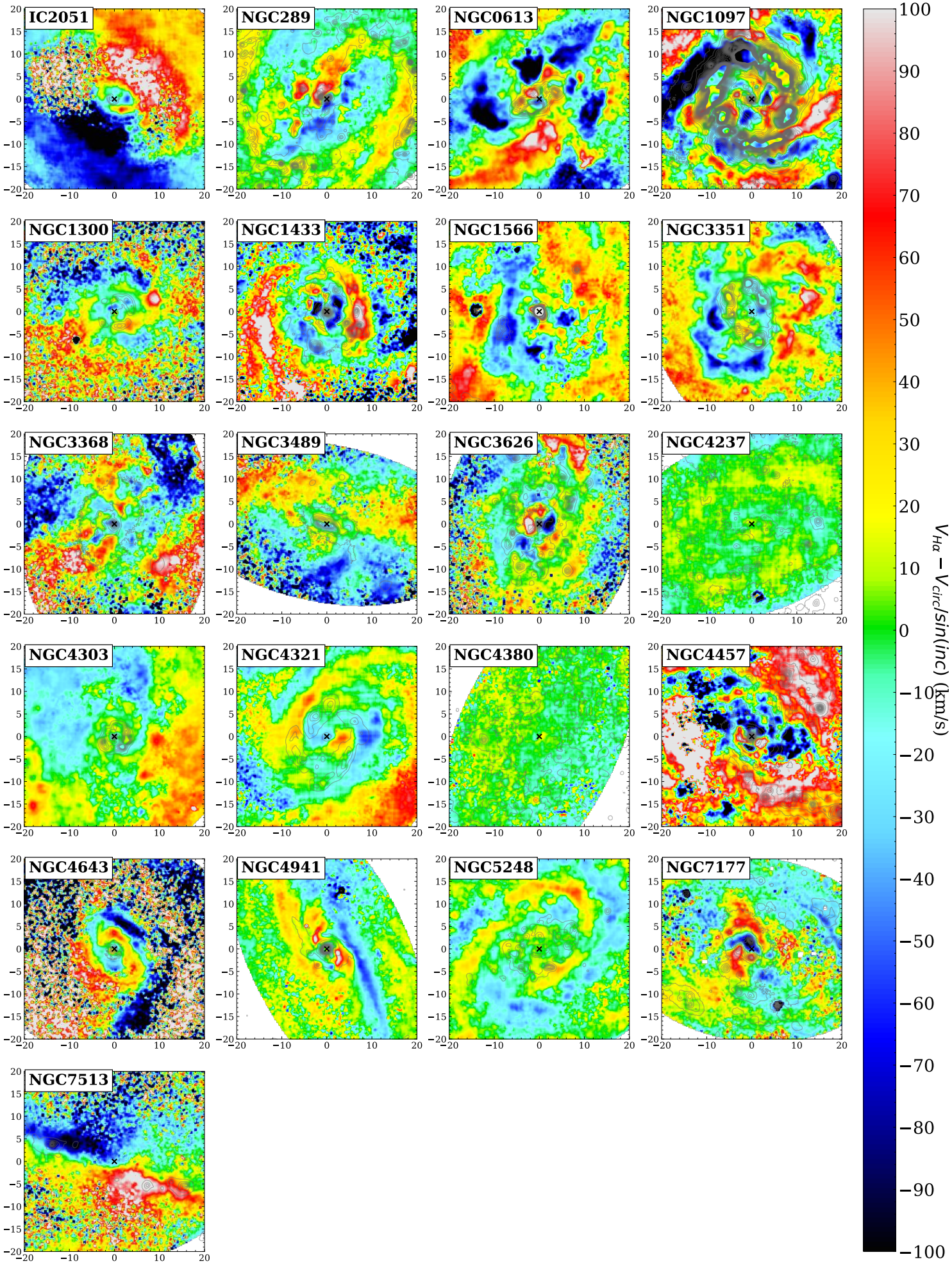


FIGURE B.3: Deprojected residual velocity maps of the galaxy sample studied in this thesis. Value within each spaxel on the map represents the average value of a 3×3 grid of spaxels, totalling 9 spaxels. The grey contours represent the H$\alpha$ emission.

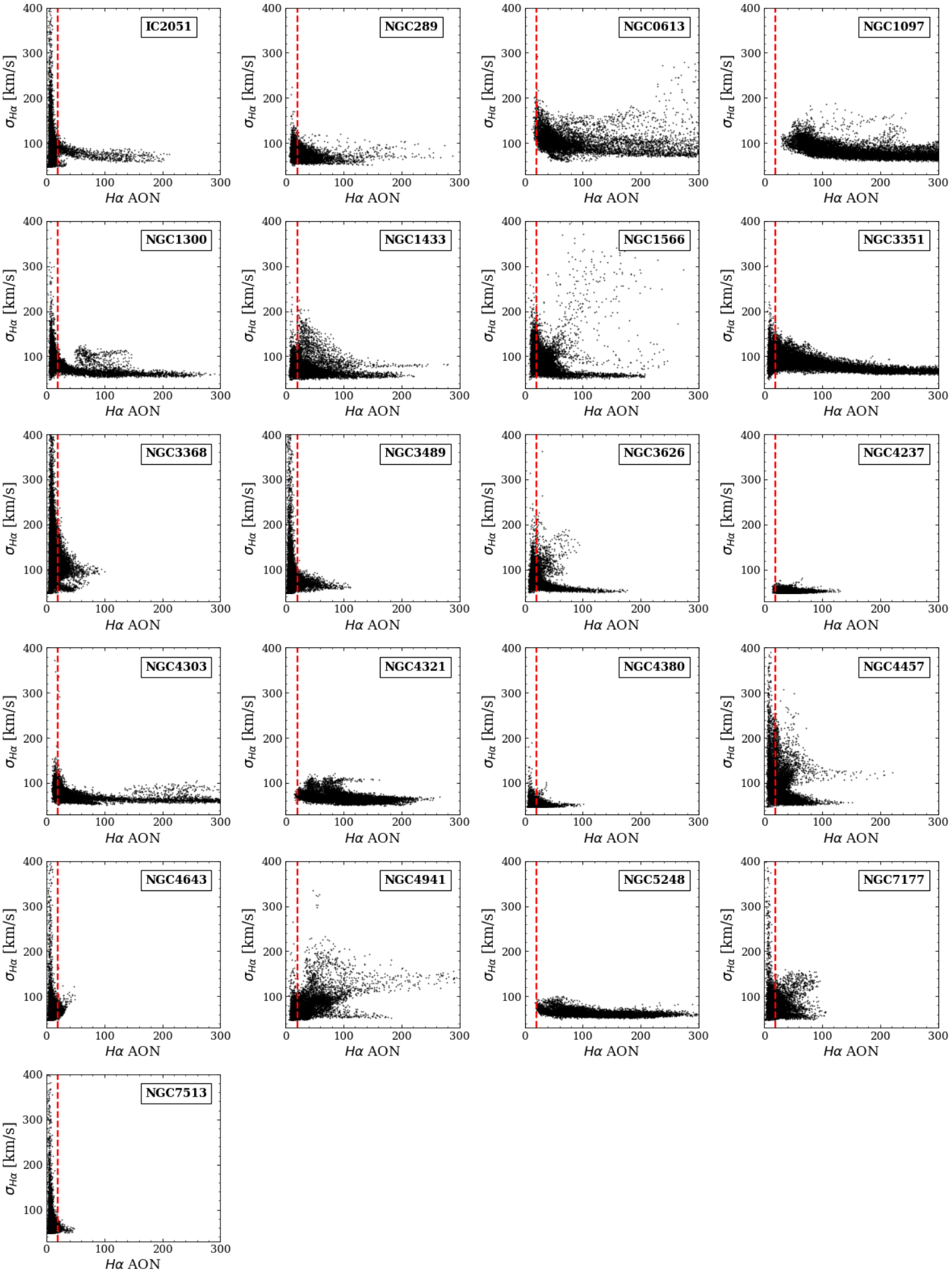


FIGURE B.4: The distribution of spaxels within the inner kpc on the plane defined by the H$\alpha$ velocity dispersion and AON for each galaxy I studied in this thesis. The red dashed line represents the AON=20 threshold.

# C Supplementary Tables

TABLE C.1: Summary of large-scale and Kinemetry inferred disk orientation parameters for the sample galaxies studied in this thesis. Columns show the Galaxy ID, PA of the LON and inclination inferred from `Kinemetry` and large-scale studies. The sources of parameters obtained from large-scale fits are stated in the last column.

| Galaxy ID | PA of the LON `Kinemetry` (deg) | inclination `Kinemetry` (deg) | PA of the LON large-scale (deg) | inclination large-scale (deg) | Source of large-scale parameters |
|---|---|---|---|---|---|
| IC2051 | 60 | 41 | 70 | 56 | Erwin et al. (2024) |
| NGC289 | 125 | 46 | 130 | 46 | Walsh et al. (1997) |
| NGC613 | 110 | 37 | 115 | 37 | Bajaja et al. (1995) |
| NGC1097 | 137 | 35 | 137 | 35 | Fathi et al. (2006) |
| NGC1300 | 107 | 35 | 87 | 35 | Lindblad et al. (1997) |
| NGC1433 | 19.7 | 29 | 19.7 | 29 | Lang et al. (2020) |
| NGC1566 | 40 | 37 | 35 | 31 | Lang et al. (2020) |
| NGC3351 | 23 | 46 | 10 | 46 | Erwin et al. (2008) |
| NGC3368 | 172 | 46 | 172 | 50 | Erwin et al. (2008) |
| NGC3489 | 80 | 60 | 71 | 58 | Erwin et al. (2008) |
| NGC3626 | 163 | 53 | 163 | 49 | Erwin et al. (2024) |
| NGC4237 | 107 | 53 | 106 | 53 | Chemin et al. (2006) |
| NGC4303 | 135 | 42 | 132 | 23.5 | Lang et al. (2020) |
| NGC4321 | 155 | 36 | 152 | 32 | Haan et al. (2008) |
| NGC4380 | 161 | 59 | 157 | 59 | Erwin et al. (2024) |
| NGC4457 | 80 | 20 | 80 | 19 | Erwin et al. (2024) |
| NGC4643 | 58 | 43 | 53 | 38 | Erwin et al. (2008) |
| NGC4941 | 25 | 60 | 21 | 48 | Gutiérrez et al. (2011) |
| NGC5248 | 114 | 44 | 114 | 45 | Haan et al. (2008, 2009a) |
| NGC7177 | 90 | 46 | 83 | 48 | Erwin et al. (2008) |
| NGC7513 | 105 | 46 | 105 | 46 | Erwin et al. (2024) |

TABLE C.2: The PSF FHWM (seeing) values recorded during MUSE observations of galaxies studied in this thesis. The columns show: Galaxy ID, seeing recorded during the observations and the AO corrected seeings computed based on (Fusco et al., 2020).

| Galaxy ID | Seeing | AO corrected seeing |
|---|---|---|
| IC2051 | 0.79 | - |
| NGC289 | 0.70 | - |
| NGC0613 | 1.00 | - |
| NGC1097 | 0.80 | - |
| NGC1300 | 1.00 | - |
| NGC1433 | 0.90 | - |
| NGC1566 | 0.84 | 0.56 |
| NGC3351 | 0.70 | - |
| NGC3368 | 0.84 | 0.49 |
| NGC3489 | 0.96 | 0.52 |
| NGC3626 | 0.842 | 0.48 |
| NGC4237 | 0.726 | 0.44 |
| NGC4303 | 0.80 | - |
| NGC4321 | 1.31 | 0.86 |
| NGC4380 | 0.70 | 0.49 |
| NGC4457 | 0.99 | 0.59 |
| NGC4643 | 0.90 | - |
| NGC4941 | 1.21 | - |
| NGC5248 | 0.70 | - |
| NGC7177 | 1.024 | 0.89 |
| NGC7513 | 1.198 | 0.58 |

# Bibliography


Abbate F., Possenti A., Tiburzi C., Barr E., van Straten W., Ridolfi A., Freire P., 2020, Nature Astronomy, 4, 704

Alexander D. M., Hickox R. C., 2012, , 56, 93

Allard E. L., Peletier R. F., Knapen J. H., 2005, The Astrophysical Journal Letters, 633, L25

Allington-Smith J., et al., 2002, , 114, 892

Allison J. R., Sadler E. M., Meekin A. M., 2014, Monthly Notices of the Royal Astronomical Society, 440, 696

Alloin D., Pelat D., Phillips M., Whittle M., 1985, The Astrophysical Journal, 288, 205

Alonso-Herrero A., et al., 2019, Astronomy & Astrophysics, 628, A65

Anand G. S., et al., 2021, Monthly Notices of the Royal Astronomical Society, 501, 3621

Ann H. B., Thakur P., 2005, The Astrophysical Journal, 620, 197

Annibali F., Bressan A., Rampazzo R., Zeilinger W. W., Danese L., 2007, Astronomy & Astrophysics, 463, 455

Annibali F., Bressan A., Rampazzo R., Zeilinger W. W., Vega O., Panuzzo P., 2010, Astronomy & Astrophysics, 519, A40

Antonucci R., 1993, Annual Review of Astronomy and Astrophysics, 31, 473

Arp H., 1981, The Astrophysical Journal Supplement Series, 46, 75

Ashok A., et al., 2023, The Astrophysical Journal, 958, 100

Asmus D., Hönig S. F., Gandhi P., Smette A., Duschl W. J., 2012, in Journal of Physics Conference Series. p. 012034 (arXiv:1112.1417), doi:10.1088/1742-6596/372/1/012034

Athanassoula E., 1984, , 114, 319

Athanassoula E., 1992, Monthly Notices of the Royal Astronomical Society, 259, 345

Athanassoula E., Machado R. E. G., Rodionov S. A., 2013, Monthly Notices of the Royal Astronomical Society, 429, 1949

Atkinson J. W., et al., 2005, Monthly Notices of the Royal Astronomical Society, 359, 504

Audibert A., et al., 2019, Astronomy & Astrophysics, 632, A33

Audibert A., et al., 2020, arXiv e-prints, p. arXiv:2011.09133

Audibert A., Combes F., García-Burillo S., Dasyra K., 2021, IAU Symposium, 359, 307

Baba J., Saitoh T. R., Wada K., 2010, , 62, 1413

Bacon R., et al., 1995, , 113, 347

Bacon R., Emsellem E., Copin Y., Monnet G., 2000, in van Breugel W., Bland-Hawthorn J., eds, Astronomical Society of the Pacific Conference Series Vol. 195, Imaging the Universe in Three Dimensions. p. 173

Bacon R., et al., 2001, Monthly Notices of the Royal Astronomical Society, 326, 23

Bacon R., et al., 2010, in McLean I. S., Ramsay S. K., Takami H., eds, Society of Photo-Optical Instrumentation Engineers (SPIE) Conference Series Vol. 7735, Ground-based and Airborne Instrumentation for Astronomy III. p. 773508, doi:10.1117/12.856027

Bajaja E., Wielebinski R., Reuter H. P., Harnett J. I., Hummel E., 1995, , 114, 147

Baldwin J. A., Phillips M. M., Terlevich R., 1981, , 93, 5

Barnes J. E., Hernquist L., 1996, The Astrophysical Journal, 471, 115

Beck R., Wielebinski R., 2013, in Oswalt T. D., Gilmore G., eds, , Vol. 5, Planets, Stars and Stellar Systems. Volume 5: Galactic Structure and Stellar Populations. p. 641, doi:10.1007/978-94-007-5612-0˙13

Beck, R. Shoutenkov, V. Ehle, M. Harnett, J. I. Haynes, R. F. Shukurov, A. Sokoloff, D. D. Thierbach, M. 2002, A&A, 391, 83

Beck, R. Fletcher, A. Shukurov, A. Snodin, A. Sokoloff, D. D. Ehle, M. Moss, D. Shoutenkov, V. 2005, A&A, 444, 739

Belfiore F., et al., 2019, The Astronomical Journal, 158, 160

Bendo G. J., Joseph R. D., 2004, The Astronomical Journal, 127, 3338

Bewketu Belete A., et al., 2021, arXiv e-prints, p. arXiv:2105.06867

Bitran M., Alvarez H., Bronfman L., May J., Thaddeus P., 1997, , 125, 99

Bittner A., et al., 2019, Astronomy & Astrophysics, 628, A117

Bittner A., et al., 2020, Astronomy & Astrophysics, 643, A65

Bittner A., et al., 2021, Astronomy & Astrophysics, 646, A42

Bland-Hawthorn J., Freeman K. C., Quinn P. J., 1997, The Astrophysical Journal, 490, 143

Blasco-Herrera J., Fathi K., Östlin G., Font J., Beckman J. E., 2013, Monthly Notices of the Royal Astronomical Society, 435, 1958

Böker T., Falcón-Barroso J., Schinnerer E., Knapen J. H., Ryder S., 2008, The Astronomical Journal, 135, 479

Bolatto A. D., Leroy A. K., Rosolowsky E., Walter F., Blitz L., 2008, The Astrophysical Journal, 686, 948

Bonnarel F., Boulesteix J., Georgelin Y. P., Lecoarer E., Marcelin M., Bacon R., Monnet G., 1988, Astronomy & Astrophysics, 189, 59

Boselli A., Gavazzi G., 2006, , 118, 517

Bosma A., 1978, PhD thesis, University of Groningen, Netherlands

Bowen D. V., Chelouche D., Jenkins E. B., Tripp T. M., Pettini M., York D. G., Frye B. L., 2016, The Astrophysical Journal, 826, 50

Boyce P. J., Cohen R. J., Dent W. R. F., 1989, Monthly Notices of the Royal Astronomical Society, 239, 1013

Bundy K., et al., 2015, The Astrophysical Journal, 798, 7

Buta R., Combes F., 1996, , 17, 95

Buta R., Crocker D. A., 1993, The Astronomical Journal, 106, 939

Buta R. J., Knapen J. H., Elmegreen B. G., Salo H., Laurikainen E., Elmegreen D. M., Puerari I., Block D. L., 2009, The Astronomical Journal, 137, 4487

Buta R. J., et al., 2015, The Astrophysical Journal Supplement Series, 217, 32

Calzetti D., Armus L., Bohlin R. C., Kinney A. L., Koornneef J., Storchi-Bergmann T., 2000, The Astrophysical Journal, 533, 682

Calzetti D., et al., 2021, The Astrophysical Journal, 913, 37

Cantiello M., et al., 2018, The Astrophysical Journal, 856, 126

Canzian B., 1993, The Astrophysical Journal, 414, 487

Cappellari M., 2017, Monthly Notices of the Royal Astronomical Society, 466, 798

Cappellari M., Copin Y., 2003, Monthly Notices of the Royal Astronomical Society, 342, 345

Cappellari M., Emsellem E., 2004, , 116, 138

Chapon D., Mayer L., Teyssier R., 2013, Monthly Notices of the Royal Astronomical Society, 429, 3114

Chemin L., et al., 2006, Monthly Notices of the Royal Astronomical Society, 366, 812

Chown R., et al., 2019, Monthly Notices of the Royal Astronomical Society, 484, 5192

Cid Fernandes R., Gu Q., Melnick J., Terlevich E., Terlevich R., Kunth D., Rodrigues Lacerda R., Joguet B., 2004, Monthly Notices of the Royal Astronomical Society, 355, 273

Cid Fernandes R., Stasińska G., Mateus A., Vale Asari N., 2011, Monthly Notices of the Royal Astronomical Society, 413, 1687

Ciri R., Bettoni D., Galletta G., 1995, Nature, 375, 661

Coelho P., Gadotti D. A., 2011, The Astrophysical Journal Letters, 743, L13

Cole S., Lacey C. G., Baugh C. M., Frenk C. S., 2000, Monthly Notices of the Royal Astronomical Society, 319, 168

Colina L., Wada K., 2000, The Astrophysical Journal, 529, 845

Combes F., 2003, in Collin S., Combes F., Shlosman I., eds, Astronomical Society of the Pacific Conference Series Vol. 290, Active Galactic Nuclei: From Central Engine to Host Galaxy. p. 411 (arXiv:astro-ph/0210232), doi:10.48550/arXiv.astro-ph/0210232

Combes F., Gerin M., 1985, Astronomy & Astrophysics, 150, 327

Comerón S., Knapen J. H., Beckman J. E., Laurikainen E., Salo H., Martínez-Valpuesta I., Buta R. J., 2010, Monthly Notices of the Royal Astronomical Society, 402, 2462

Contopoulos G., Grosbol P., 1989, , 1, 261

Cortés J. R., Kenney J. D. P., Hardy E., 2015, The Astrophysical Journal Supplement Series, 216, 9

Crespo Gómez A., Piqueras López J., Arribas S., Pereira-Santaella M., Colina L., Rodríguez del Pino B., 2021, arXiv e-prints, p. arXiv:2104.06790

Croton D. J., et al., 2006, Monthly Notices of the Royal Astronomical Society, 365, 11

D'Onghia E., Burkert A., Murante G., Khochfar S., 2006, Monthly Notices of the Royal Astronomical Society, 372, 1525

Davies R. I., Maciejewski W., Hicks E. K. S., Tacconi L. J., Genzel R., Engel H., 2009, The Astrophysical Journal, 702, 114

Davies R., et al., 2011, The Astrophysical Journal, 741, 69

Davies R. I., et al., 2014, The Astrophysical Journal, 792, 101

Davies R. I., et al., 2015, The Astrophysical Journal, 806, 127

Decarli R., Gavazzi G., Arosio I., Cortese L., Boselli A., Bonfanti C., Colpi M., 2007, Monthly Notices of the Royal Astronomical Society, 381, 136

Di Matteo T., Springel V., Hernquist L., 2005, Nature, 433, 604

Di Teodoro E. M., Fraternali F., 2015, Monthly Notices of the Royal Astronomical Society, 451, 3021

Díaz A. I., Álvarez M. Á., Terlevich E., Terlevich R., Sánchez Portal M., Aretxaga I., 2000, Monthly Notices of the Royal Astronomical Society, 311, 120

Diehl S., Statler T. S., 2006, Monthly Notices of the Royal Astronomical Society, 368, 497

Donnari M., et al., 2021, Monthly Notices of the Royal Astronomical Society, 500, 4004

Dumas G., Mundell C. G., Emsellem E., Nagar N. M., 2007, Monthly Notices of the Royal Astronomical Society, 379, 1249

Dutton A. A., van den Bosch F. C., 2012, Monthly Notices of the Royal Astronomical Society, 421, 608

Duval M. F., Athanassoula E., 1983, Astronomy & Astrophysics, 121, 297

ESA/Hubble & NASA 2022, Eye of the galaxy, `https://esahubble.org/images/potw2211a/`

ESA/Hubble & NASA Erwin P., 2019, Discs and Bulges, https://esahubble.org/images/potw1950a/

ESO Press Release 2004, The President and the Galaxy, ESO Press Release, 12/2004

Eisenhauer F., et al., 2003, in Iye M., Moorwood A. F. M., eds, Society of Photo-Optical Instrumentation Engineers (SPIE) Conference Series Vol. 4841, Instrument Design and Performance for Optical/Infrared Ground-based Telescopes. pp 1548–1561 (arXiv:astro-ph/0306191), doi:10.1117/12.459468

Ellison S. L., Nair P., Patton D. R., Scudder J. M., Mendel J. T., Simard L., 2011, Monthly Notices of the Royal Astronomical Society, 416, 2182

Elmegreen D. M., Elmegreen B. G., Chromey F. R., Hasselbacher D. A., 1996, The Astrophysical Journal, 469, 131

Elmegreen D. M., Chromey F. R., Bissell B. A., Corrado K., 1999, The Astronomical Journal, 118, 2618

Elmegreen B. G., Elmegreen D. M., Vollbach D. R., Foster E. R., Ferguson T. E., 2005, The Astrophysical Journal, 634, 101

Elmegreen B. G., Elmegreen D. M., Sánchez Almeida J., Muñoz-Tuñón C., Dewberry J., Putko J., Teich Y., Popinchalk M., 2013, The Astrophysical Journal, 774, 86

Emsellem E., Greusard D., Combes F., Friedli D., Leon S., Pécontal E., Wozniak H., 2001, Astronomy & Astrophysics, 368, 52

Emsellem E., Goudfrooij P., Ferruit P., 2003, Monthly Notices of the Royal Astronomical Society, 345, 1297

Emsellem E., Renaud F., Bournaud F., Elmegreen B., Combes F., Gabor J. M., 2015, Monthly Notices of the Royal Astronomical Society, 446, 2468

Emsellem E., et al., 2021, arXiv e-prints, p. arXiv:2110.03708

Emsellem E., et al., 2022, Astronomy & Astrophysics, 659, A191

Englmaier P., Gerhard O., 1997, Monthly Notices of the Royal Astronomical Society, 287, 57

Englmaier P., Shlosman I., 2000, The Astrophysical Journal, 528, 677

Erroz-Ferrer S., et al., 2019, Monthly Notices of the Royal Astronomical Society, 484, 5009

Erwin P., 2004, Astronomy & Astrophysics, 415, 941

Erwin P., 2005, Monthly Notices of the Royal Astronomical Society, 364, 283

Erwin P., 2011, Memorie della Societa Astronomica Italiana Supplementi, 18, 145

Erwin P., 2018, Monthly Notices of the Royal Astronomical Society, 474, 5372

Erwin P., Sparke L. S., 2003, The Astrophysical Journal Supplement Series, 146, 299

Erwin P., Pohlen M., Beckman J. E., 2008, The Astronomical Journal, 135, 20

Erwin P., et al., 2015, Monthly Notices of the Royal Astronomical Society, 446, 4039

Erwin P., et al., 2021a, Monthly Notices of the Royal Astronomical Society, 502, 2446

Erwin P., et al., 2021b, Monthly Notices of the Royal Astronomical Society, 502, 2446

Erwin P., et al., 2024, in prep

Eskridge P. B., et al., 2000, The Astronomical Journal, 119, 536

Eskridge P. B., et al., 2002, The Astrophysical Journal Supplement Series, 143, 73

Fabian A. C., 2012, Annual Review of Astronomy and Astrophysics, 50, 455

Falcón-Barroso J., et al., 2006, Monthly Notices of the Royal Astronomical Society, 369, 529

Falcón-Barroso J., Böker T., Schinnerer E., Knapen J. H., Ryder S., 2008, in Bureau M., Athanassoula E., Barbuy B., eds, Vol. 245, Formation and Evolution of Galaxy Bulges. pp 177–180 (arXiv:0709.0353), doi:10.1017/S1743921308017584

Fall S. M., Efstathiou G., 1980, Monthly Notices of the Royal Astronomical Society, 193, 189

Fanali R., Dotti M., Fiacconi D., Haardt F., 2015, Monthly Notices of the Royal Astronomical Society, 454, 3641

Fathi K., 2004, PhD thesis, University of Groningen

Fathi K., van de Ven G., Peletier R. F., Emsellem E., Falcón-Barroso J., Cappellari M., de Zeeuw T., 2005, Monthly Notices of the Royal Astronomical Society, 364, 773

Fathi K., Storchi-Bergmann T., Riffel R. A., Winge C., Axon D. J., Robinson A., Capetti A., Marconi A., 2006, The Astrophysical Journal Letters, 641, L25

Fathi K., et al., 2008, The Astrophysical Journal Letters, 675, L17

Fathi K., et al., 2013, The Astrophysical Journal Letters, 770, L27

Fischer T. C., Crenshaw D. M., Kraemer S. B., Schmitt H. R., 2013, The Astrophysical Journal Supplement Series, 209, 1

Fragkoudi F., Athanassoula E., Bosma A., 2016, Monthly Notices of the Royal Astronomical Society, 462, L41

Franx M., van Gorkom J. H., de Zeeuw T., 1994, The Astrophysical Journal, 436, 642

Freedman W. L., et al., 2001a, The Astrophysical Journal, 553, 47

Freedman W. L., et al., 2001b, The Astrophysical Journal, 553, 47

Freeman K. C., 1970, The Astrophysical Journal, 160, 811

Freeman P., Rosolowsky E., Kruijssen J. M. D., Bastian N., Adamo A., 2017, Monthly Notices of the Royal Astronomical Society, 468, 1769

Friedli D., Benz W., 1993, Astronomy & Astrophysics, 268, 65

Fujishita M., et al., 2009, , 61, 1039

Fukui Y., et al., 2006, Science, 314, 106

Fusco T., et al., 2020, Astronomy & Astrophysics, 635, A208

Fux R., 1999, Astronomy & Astrophysics, 345, 787

Gadotti D. A., 2009, Monthly Notices of the Royal Astronomical Society, 393, 1531

Gadotti D. A., et al., 2019, Monthly Notices of the Royal Astronomical Society, 482, 506

Gadotti D. A., et al., 2020, Astronomy & Astrophysics, 643, A14

Galletta G., 1996, in Buta R., Crocker D. A., Elmegreen B. G., eds, Astronomical Society of the Pacific Conference Series Vol. 91, IAU Colloq. 157: Barred Galaxies. p. 429

Ganda K., Falcón-Barroso J., Peletier R. F., Cappellari M., Emsellem E., McDermid R. M., de Zeeuw P. T., Carollo C. M., 2006, Monthly Notices of the Royal Astronomical Society, 367, 46

Gao Y., Egusa F., Liu G., Kohno K., Bao M., Morokuma-matsui K., Kong X., Chen X., 2021, arXiv e-prints, p. arXiv:2104.04928

García-Burillo S., Sempere M. J., Bettoni D., 1998, The Astrophysical Journal, 502, 235

García-Burillo S., Combes F., Schinnerer E., Boone F., Hunt L. K., 2005, Astronomy & Astrophysics, 441, 1011

García-Burillo S., et al., 2014, Astronomy & Astrophysics, 567, A125

Goodman J., 2003, Monthly Notices of the Royal Astronomical Society, 339, 937

Goubert P. H., Bluck A. F. L., Piotrowska J. M., Maiolino R., 2024, Monthly Notices of the Royal Astronomical Society, 528, 4891

Gramze S. R., Ginsburg A., Meier D. S., Ott J., Shirley Y., Sormani M. C., Svoboda B. E., 2023a, The Astrophysical Journal, 959, 93

Gramze S. R., Ginsburg A., Meier D. S., Ott J., Shirley Y., Sormani M. C., Svoboda B. E., 2023b, The Astrophysical Journal, 959, 93

Greusard D., Friedli D., Wozniak H., Martinet L., Martin P., 2000, , 145, 425

Grosbøl P., Patsis P. A., Pompei E., 2004, Astronomy & Astrophysics, 423, 849

Gutiérrez L., Erwin P., Aladro R., Beckman J. E., 2011, The Astronomical Journal, 142, 145

Haan S., Schinnerer E., Mundell C. G., García-Burillo S., Combes F., 2008, The Astronomical Journal, 135, 232

Haan S., Schinnerer E., Emsellem E., García-Burillo S., Combes F., Mundell C. G., Rix H.-W., 2009a, The Astrophysical Journal, 692, 1623

Haan S., Schinnerer E., Emsellem E., García-Burillo S., Combes F., Mundell C. G., Rix H.-W., 2009b, The Astrophysical Journal, 692, 1623

Haffner L. M., Reynolds R. J., Tufte S. L., 1999, The Astrophysical Journal, 523, 223

Haynes M. P., Jore K. P., Barrett E. A., Broeils A. H., Murray B. M., 2000, The Astronomical Journal, 120, 703

Heald G. H., Rand R. J., Benjamin R. A., Collins J. A., Bland-Hawthorn J., 2006, The Astrophysical Journal, 636, 181

Heller C. H., Shlosman I., 1994, The Astrophysical Journal, 424, 84

Heller C. H., Shlosman I., 1996, The Astrophysical Journal, 471, 143

Heller C. H., Shlosman I., Athanassoula E., 2007, The Astrophysical Journal Letters, 657, L65

Henshaw J. D., et al., 2016, Monthly Notices of the Royal Astronomical Society, 457, 2675

Hermosa Muñoz L., Márquez I., Cazzoli S., Masegosa J., Agís-González B., 2022a, Astronomy & Astrophysics, 660, A133

Hermosa Muñoz L., Márquez I., Cazzoli S., Masegosa J., Agís-González B., 2022b, Astronomy & Astrophysics, 660, A133

Hicks E. K. S., Davies R. I., Malkan M. A., Genzel R., Tacconi L. J., Müller Sánchez F., Sternberg A., 2009, The Astrophysical Journal, 696, 448

Hill A. S., Benjamin R. A., Haffner L. M., Gostisha M. C., Barger K. A., 2014, The Astrophysical Journal, 787, 106

Ho L. C., 2008, Annual Review of Astronomy and Astrophysics, 46, 475

Ho L. C., Filippenko A. V., Sargent W. L. W., 1997, The Astrophysical Journal Supplement Series, 112, 315

Ho L. C., Li Z.-Y., Barth A. J., Seigar M. S., Peng C. Y., 2011, The Astrophysical Journal Supplement Series, 197, 21

Hopkins P. F., Hernquist L., 2006, The Astrophysical Journal Supplement Series, 166, 1

Hopkins P. F., Quataert E., 2010, Monthly Notices of the Royal Astronomical Society, 407, 1529

Hopkins P. F., et al., 2009, Monthly Notices of the Royal Astronomical Society, 397, 802

Hu Y., Lazarian A., Beck R., Xu S., 2022, arXiv e-prints, p. arXiv:2206.05423

Hughes M. A., et al., 2005, The Astronomical Journal, 130, 73

Husemann B., Bennert V. N., Scharwächter J., Woo J. H., Choudhury O. S., 2016, Monthly Notices of the Royal Astronomical Society, 455, 1905

Ishibashi W., Fabian A. C., 2014, Monthly Notices of the Royal Astronomical Society, 441, 1474

Izumi T., et al., 2013, , 65, 100

Izumi T., et al., 2017, The Astrophysical Journal Letters, 845, L5

Jaffé Y. L., Smith R., Candlish G. N., Poggianti B. M., Sheen Y.-K., Verheijen M. A. W., 2015, Monthly Notices of the Royal Astronomical Society, 448, 1715

Jana A., Naik S., Kumari N., 2022, Journal of Astrophysics and Astronomy, 43, 4

Jogee S., 2006, in Alloin D., ed., , Vol. 693, Physics of Active Galactic Nuclei at all Scales. p. 143, doi:10.1007/3-540-34621-X˙6

Jungwiert B., Combes F., Axon D. J., 1997, , 125, 479

Kalinova V., Colombo D., Sánchez S. F., Kodaira K., García-Benito R., González Delgado R., Rosolowsky E., Lacerda E. A. D., 2021, Astronomy & Astrophysics, 648, A64

Kapferer W., Sluka C., Schindler S., Ferrari C., Ziegler B., 2009, Astronomy & Astrophysics, 499, 87

Kauffmann G., et al., 2003, Monthly Notices of the Royal Astronomical Society, 346, 1055

Kendall S., Kennicutt R. C., Clarke C., Thornley M. D., 2008, Monthly Notices of the Royal Astronomical Society, 387, 1007

Kennicutt Robert C. J., 1998, Annual Review of Astronomy and Astrophysics, 36, 189

Kennicutt R. C., Evans N. J., 2012, Annual Review of Astronomy and Astrophysics, 50, 531

Kewley L. J., Dopita M. A., Sutherland R. S., Heisler C. A., Trevena J., 2001, The Astrophysical Journal, 556, 121

Kewley L. J., Groves B., Kauffmann G., Heckman T., 2006, Monthly Notices of the Royal Astronomical Society, 372, 961

Kim W.-T., Stone J. M., 2012, The Astrophysical Journal, 751, 124

Kim W.-T., Seo W.-Y., Stone J. M., Yoon D., Teuben P. J., 2012, The Astrophysical Journal, 747, 60

Kim T., et al., 2024, arXiv e-prints, p. arXiv:2405.00107

Knapen J. H., 2005, Astronomy & Astrophysics, 429, 141

Knapen J. H., Beckman J. E., Shlosman I., Peletier R. F., Heller C. H., de Jong R. S., 1995a, The Astrophysical Journal Letters, 443, L73

Knapen J. H., Beckman J. E., Heller C. H., Shlosman I., de Jong R. S., 1995b, The Astrophysical Journal, 454, 623

Knapen J. H., Shlosman I., Heller C. H., Rand R. J., Beckman J. E., Rozas M., 2000, The Astrophysical Journal, 528, 219

Kocevski D. D., et al., 2012, The Astrophysical Journal, 744, 148

Kolcu T., 2023, A MUSE view on gas inflows to the nuclei of barred galaxies, doi:10.5281/zenodo.8124480, https://doi.org/10.5281/zenodo.8124480

Kolcu T., Crossett J. P., Bellhouse C., McGee S., 2022a, Monthly Notices of the Royal Astronomical Society, 515, 5877

Kolcu T., Crossett J. P., Bellhouse C., McGee S., 2022b, Monthly Notices of the Royal Astronomical Society, 515, 5877

Kolcu T., et al., 2023, Monthly Notices of the Royal Astronomical Society, 524, 207

Komugi S., Sofue Y., Kohno K., Nakanishi H., Onodera S., Egusa F., Muraoka K., 2008, The Astrophysical Journal Supplement Series, 178, 225

Koribalski B., Dettmar R. J., Mebold U., Wielebinski R., 1996, Astronomy & Astrophysics, 315, 71

Krajnović D., Cappellari M., de Zeeuw P. T., Copin Y., 2006, Monthly Notices of the Royal Astronomical Society, 366, 787

Krause M., Hummel E., Beck R., 1989, Astronomy & Astrophysics, 217, 4

Kriss G. A., Hartig G. F., Armus L., Blair W. P., Caganoff S., Dressel L., 1991, The Astrophysical Journal Letters, 377, L13

Lacerda E. A. D., Sánchez S. F., Mejía-Narváez A., Camps-Fariña A., Espinosa-Ponce C., Barrera-Ballesteros J. K., Ibarra-Medel H., Lugo-Aranda A. Z., 2022, , 97, 101895

Lagos C. d. P., et al., 2018, Monthly Notices of the Royal Astronomical Society, 473, 4956

Laine S., Shlosman I., Knapen J. H., Peletier R. F., 2002, The Astrophysical Journal, 567, 97

Lang P., et al., 2020, The Astrophysical Journal, 897, 122

Langan I., et al., 2023, arXiv e-prints, p. arXiv:2301.10779

Larson R. B., Tinsley B. M., Caldwell C. N., 1980, The Astrophysical Journal, 237, 692

Laurikainen E., Salo H., Buta R., Knapen J. H., 2011, Monthly Notices of the Royal Astronomical Society, 418, 1452

Leaman R., et al., 2019, Monthly Notices of the Royal Astronomical Society, 488, 3904

Lee C. W., Lee H. M., Ann H. B., Kwon K. H., 1999, The Astrophysical Journal, 513, 242

Lee J. C., et al., 2023, The Astrophysical Journal Letters, 944, L17

Legodi L. S., Taylor A. R., Stil J. M., 2021, Monthly Notices of the Royal Astronomical Society, 500, 576

Leroy A. K., et al., 2009, The Astronomical Journal, 137, 4670

Leroy A. K., et al., 2021a, The Astrophysical Journal Supplement Series, 255, 19

Leroy A. K., et al., 2021b, The Astrophysical Journal Supplement Series, 257, 43

Li Z., Sellwood J. A., Shen J., 2017, The Astrophysical Journal, 850, 67

Li Z., et al., 2023, The Astrophysical Journal, 958, 77

Lin L.-H., Wang H.-H., Hsieh P.-Y., Taam R. E., Yang C.-C., Yen D. C. C., 2013, The Astrophysical Journal, 771, 8

Lin L., Li C., He Y., Xiao T., Wang E., 2017, The Astrophysical Journal, 838, 105

Lin L., et al., 2020, Monthly Notices of the Royal Astronomical Society, 499, 1406

Lindblad P. O., 1999, , 9, 221

Lindblad P. A. B., Kristen H., 1996, Astronomy & Astrophysics, 313, 733

Lindblad P. A. B., Kristen H., Joersaeter S., Hoegbom J., 1997, Astronomy & Astrophysics, 317, 36

Liszt H. S., 2006, Astronomy & Astrophysics, 447, 533

Liszt H. S., 2008, Astronomy & Astrophysics, 486, 467

Liu D., et al., 2023, Astronomy & Astrophysics, 672, A36

Lopez-Rodriguez E., et al., 2021, The Astrophysical Journal, 923, 150

Machida M., et al., 2009, , 61, 411

Maciejewski W., 2004a, Monthly Notices of the Royal Astronomical Society, 354, 883

Maciejewski W., 2004b, Monthly Notices of the Royal Astronomical Society, 354, 892

Maciejewski W., Athanassoula E., 2007, Monthly Notices of the Royal Astronomical Society, 380, 999

Maciejewski W., Teuben P. J., Sparke L. S., Stone J. M., 2002, Monthly Notices of the Royal Astronomical Society, 329, 502

Madau P., Dickinson M., 2014, Annual Review of Astronomy and Astrophysics, 52, 415

Man Z.-y., Peng Y.-j., Kong X., Guo K.-x., Zhang C.-p., Dou J., 2019, Monthly Notices of the Royal Astronomical Society, 488, 89

Mannucci F., Cresci G., Maiolino R., Marconi A., Gnerucci A., 2010, Monthly Notices of the Royal Astronomical Society, 408, 2115

Marconi A., et al., 2003, The Astrophysical Journal, 586, 868

Marino A., et al., 2011, Monthly Notices of the Royal Astronomical Society, 411, 311

Márquez I., Masegosa J., González-Martin O., Hernández-Garcia L., Pović M., Netzer H., Cazzoli S., del Olmo A., 2017, Frontiers in Astronomy and Space Sciences, 4, 34

Martín S., et al., 2015, Astronomy & Astrophysics, 573, A116

Martini P., Pogge R. W., 1999, The Astronomical Journal, 118, 2646

Martini P., Regan M. W., Mulchaey J. S., Pogge R. W., 2003a, The Astrophysical Journal Supplement Series, 146, 353

Martini P., Regan M. W., Mulchaey J. S., Pogge R. W., 2003b, The Astrophysical Journal, 589, 774

Martini P., Regan M. W., Mulchaey J. S., Pogge R. W., 2003c, The Astrophysical Journal, 589, 774

Martini P., Dicken D., Storchi-Bergmann T., 2013, The Astrophysical Journal, 766, 121

Mayer L., Kazantzidis S., Escala A., 2008, , 79, 1284

Mazzalay X., et al., 2014, Monthly Notices of the Royal Astronomical Society, 438, 2036

Mazzuca L. M., Knapen J. H., Veilleux S., Regan M. W., 2008, The Astrophysical Journal Supplement Series, 174, 337

McIntosh D. H., Guo Y., Hertzberg J., Katz N., Mo H. J., van den Bosch F. C., Yang X., 2008, Monthly Notices of the Royal Astronomical Society, 388, 1537

McKee C. F., Ostriker E. C., 2007, Annual Review of Astronomy and Astrophysics, 45, 565

Mei S., et al., 2005, arXiv e-prints, pp astro–ph/0506314

Menacho V., Bik G. Ö. A., Adamo A., Bergvall N., Della Bruna L., Hayes M., Melinder J., Rivera-Thorsen E. T., 2021, arXiv e-prints, p. arXiv:2105.11017

Menéndez-Delmestre K., Sheth K., Schinnerer E., Jarrett T. H., Scoville N. Z., 2007, The Astrophysical Journal, 657, 790

Mihos J. C., Hernquist L., 1996, The Astrophysical Journal, 464, 641

Miller R. H., 1978a, The Astrophysical Journal, 224, 32

Miller R. H., 1978b, The Astrophysical Journal, 226, 81

Misselt K. A., Clayton G. C., Gordon K. D., 1999, , 111, 1398

Moiseev A. V., 2001, Bulletin of the Special Astrophysics Observatory, 51, 140

Moiseev A. V., Valdés J. R., Chavushyan V. H., 2004, Astronomy & Astrophysics, 421, 433

Molinari S., et al., 2011, The Astrophysical Journal Letters, 735, L33

Möllenhoff C., Heidt J., 2001, Astronomy & Astrophysics, 368, 16

Muñoz-Mateos J. C., et al., 2013, The Astrophysical Journal, 771, 59

Muñoz-Mateos J. C., et al., 2015, The Astrophysical Journal Supplement Series, 219, 3

Müller Sánchez F., Davies R. I., Genzel R., Tacconi L. J., Eisenhauer F., Hicks E. K. S., Friedrich S., Sternberg A., 2009, The Astrophysical Journal, 691, 749

Namekata D., Habe A., Matsui H., Saitoh T. R., 2009, The Astrophysical Journal, 691, 1525

Navarro J. F., Frenk C. S., White S. D. M., 1995, Monthly Notices of the Royal Astronomical Society, 275, 56

Navarro J. F., Frenk C. S., White S. D. M., 1997, The Astrophysical Journal, 490, 493

Nemmen R. S., Storchi-Bergmann T., Yuan F., Eracleous M., Terashima Y., Wilson A. S., 2006, The Astrophysical Journal, 643, 652

Nemmen R. S., Storchi-Bergmann T., Eracleous M., 2014, Monthly Notices of the Royal Astronomical Society, 438, 2804

Neumann J., et al., 2020, Astronomy & Astrophysics, 637, A56

Nowak N., Thomas J., Erwin P., Saglia R. P., Bender R., Davies R. I., 2010, Monthly Notices of the Royal Astronomical Society, 403, 646

O'Sullivan E., et al., 2017, Monthly Notices of the Royal Astronomical Society, 472, 1482

Oka T., Mizuno R., Miura K., Takekawa S., 2016, The Astrophysical Journal Letters, 816, L7

Oka T., Tsujimoto S., Iwata Y., Nomura M., Takekawa S., 2017, Nature Astronomy, 1, 709

Osterbrock D. E., Ferland G. J., 2006, Astrophysics of gaseous nebulae and active galactic nuclei. University Science Books

Otte B., Reynolds R. J., Gallagher J. S. I., Ferguson A. M. N., 2001, The Astrophysical Journal, 560, 207

Otte B., Gallagher J. S. I., Reynolds R. J., 2002, The Astrophysical Journal, 572, 823

Pan H.-A., et al., 2022, The Astrophysical Journal, 927, 9

Park K., Bogdanović T., 2017, The Astrophysical Journal, 838, 103

Parker E. N., 1966, The Astrophysical Journal, 145, 811

Patsis P. A., Athanassoula E., 2000, Astronomy & Astrophysics, 358, 45

Pérez-Ramírez D., Knapen J. H., Peletier R. F., Laine S., Doyon R., Nadeau D., 2000, Monthly Notices of the Royal Astronomical Society, 317, 234

Piner B. G., Stone J. M., Teuben P. J., 1995, The Astrophysical Journal, 449, 508

Pogge R. W., Martini P., 2002, The Astrophysical Journal, 569, 624

Pohlen M., et al., 2010, Astronomy & Astrophysics, 518, L72

Prieto M. A., Maciejewski W., Reunanen J., 2005, The Astronomical Journal, 130, 1472

Prieto M. A., Fernandez-Ontiveros J. A., Bruzual G., Burkert A., Schartmann M., Charlot S., 2019, Monthly Notices of the Royal Astronomical Society, 485, 3264

Querejeta M., et al., 2015, The Astrophysical Journal Supplement Series, 219, 5

Querejeta M., et al., 2021, Astronomy & Astrophysics, 656, A133

Quillen A. C., Frogel J. A., Kuchinski L. E., Terndrup D. M., 1995, The Astronomical Journal, 110, 156

Regan M. W., Mulchaey J. S., 1999, The Astronomical Journal, 117, 2676

Regan M. W., Vogel S. N., Teuben P. J., 1997, The Astrophysical Journal Letters, 482, L143

Roberts W. W. J., Roberts M. S., Shu F. H., 1975, The Astrophysical Journal, 196, 381

Roberts I. D., et al., 2023, arXiv e-prints, p. arXiv:2305.14823

Robertson B., Bullock J. S., Cox T. J., Di Matteo T., Hernquist L., Springel V., Yoshida N., 2006, The Astrophysical Journal, 645, 986

Rogstad D. H., Lockhart I. A., Wright M. C. H., 1974, The Astrophysical Journal, 193, 309

Rosario D. J., et al., 2012, Astronomy & Astrophysics, 545, A45

Rosolowsky E., et al., 2021, Monthly Notices of the Royal Astronomical Society, 502, 1218

Rubin V. C., Kenney J. D. P., Young J. S., 1997, The Astronomical Journal, 113, 1250

Ryder S. D., Knapen J. H., Takamiya M., 2001, Monthly Notices of the Royal Astronomical Society, 323, 663

Salo H., et al., 2015, The Astrophysical Journal Supplement Series, 219, 4

Sánchez-García O., et al., 2023, The Astrophysical Journal, 945, 99

Sánchez S. F., et al., 2012, Astronomy & Astrophysics, 538, A8

Sánchez S. F., et al., 2016a, Revista Mexicana de Astronomía y Astrofísica, 52, 21

Sánchez S. F., et al., 2016b, Revista Mexicana de Astronomía y Astrofísica, 52, 171

Sánchez S. F., et al., 2022, The Astrophysical Journal Supplement Series, 262, 36

Sanders R. H., Huntley J. M., 1976, The Astrophysical Journal, 209, 53

Sandstrom K., et al., 2010, Astronomy & Astrophysics, 518, L59

Santoro F., Tadhunter C., Baron D., Morganti R., Holt J., 2020, Astronomy & Astrophysics, 644, A54

Sarzi M., et al., 2006, Monthly Notices of the Royal Astronomical Society, 366, 1151

Schawinski K., Simmons B. D., Urry C. M., Treister E., Glikman E., 2012, Monthly Notices of the Royal Astronomical Society, 425, L61

Schinnerer E., Maciejewski W., Scoville N., Moustakas L. A., 2002, The Astrophysical Journal, 575, 826

Schinnerer E., et al., 2019, The Messenger, 177, 36

Schnorr-Müller A., Storchi-Bergmann T., Robinson A., Lena D., Nagar N. M., 2016, Monthly Notices of the Royal Astronomical Society, 457, 972

Schnorr-Müller A., Storchi-Bergmann T., Nagar N. M., Robinson A., Lena D., 2017, Monthly Notices of the Royal Astronomical Society, 471, 3888

Schoenmakers R. H. M., Franx M., de Zeeuw P. T., 1997, Monthly Notices of the Royal Astronomical Society, 292, 349

Schöier F. L., van der Tak F. F. S., van Dishoeck E. F., Black J. H., 2005, Astronomy & Astrophysics, 432, 369

Schwarz M. P., 1981, The Astrophysical Journal, 247, 77

Seidel M. K., Falcón-Barroso J., Martínez-Valpuesta I., Sánchez-Blázquez P., Pérez I., Peletier R., Vazdekis A., 2016, Monthly Notices of the Royal Astronomical Society, 460, 3784

Sellwood J. A., 1980, Astronomy & Astrophysics, 89, 296

Shaw M. A., Combes F., Axon D. J., Wright G. S., 1993, Astronomy & Astrophysics, 273, 31

Sheth K., Vogel S. N., Regan M. W., Thornley M. D., Teuben P. J., 2005, The Astrophysical Journal, 632, 217

Sheth K., et al., 2010, , 122, 1397

Sheth K., Melbourne J., Elmegreen D. M., Elmegreen B. G., Athanassoula E., Abraham R. G., Weiner B. J., 2012, The Astrophysical Journal, 758, 136

Shimizu T. T., et al., 2019, Monthly Notices of the Royal Astronomical Society, 490, 5860

Shlosman I., 2001, in Knapen J. H., Beckman J. E., Shlosman I., Mahoney T. J., eds, Astronomical Society of the Pacific Conference Series Vol. 249, The Central Kiloparsec of Starbursts and AGN: The La Palma Connection. p. 55

Shlosman I., Noguchi M., 1993, The Astrophysical Journal, 414, 474

Shlosman I., Frank J., Begelman M. C., 1989, Nature, 338, 45

Sil'Chenko O. K., Smirnova A. A., 2010, Astronomy Letters, 36, 319

Sil'chenko O. K., Moiseev A. V., Shulga A. P., 2010, The Astronomical Journal, 140, 1462

Silk J., 2013, The Astrophysical Journal, 772, 112

Simien F., Prugniel P., 2002, Astronomy & Astrophysics, 384, 371

Smajić S., Moser L., Eckart A., Busch G., Combes F., García-Burillo S., Valencia-S. M., Horrobin M., 2015, Astronomy & Astrophysics, 583, A104

Smirnova K. I., Wiebe D. S., 2019, Astronomy Reports, 63, 445

Somerville R. S., Davé R., 2015, Annual Review of Astronomy and Astrophysics, 53, 51

Sormani M. C., Barnes A. T., 2019, Monthly Notices of the Royal Astronomical Society, 484, 1213

Sormani M. C., Binney J., Magorrian J., 2015, Monthly Notices of the Royal Astronomical Society, 449, 2421

Sormani M. C., Sobacchi E., Fragkoudi F., Ridley M., Treß R. G., Glover S. C. O., Klessen R. S., 2018, Monthly Notices of the Royal Astronomical Society, 481, 2

Sormani M. C., et al., 2019, Monthly Notices of the Royal Astronomical Society, 488, 4663

Sormani M. C., et al., 2023a, Monthly Notices of the Royal Astronomical Society, 523, 2918

Sormani M. C., et al., 2023b, Monthly Notices of the Royal Astronomical Society, 523, 2918

Sosa-Brito R. M., Tacconi-Garman L. E., Lehnert M. D., Gallimore J. F., 2001, The Astrophysical Journal Supplement Series, 136, 61

Spekkens K., Sellwood J. A., 2007, The Astrophysical Journal, 664, 204

Stark A. A., Bania T. M., 1986, The Astrophysical Journal Letters, 306, L17

Stoklasová I., Ferruit P., Emsellem E., Jungwiert B., Pécontal E., Sánchez S. F., 2009, Astronomy & Astrophysics, 500, 1287

Storchi-Bergmann T., Schnorr-Müller A., 2019, Nature Astronomy, 3, 48

Storchi-Bergmann T., Rodriguez-Ardila A., Schmitt H. R., Wilson A. S., Baldwin J. A., 1996, The Astrophysical Journal, 472, 83

Storchi-Bergmann T., et al., 2003, The Astrophysical Journal, 598, 956

Storchi-Bergmann T., Dors Oli L. J., Riffel R. A., Fathi K., Axon D. J., Robinson A., Marconi A., Östlin G., 2007, The Astrophysical Journal, 670, 959

Strong A. W., et al., 1988, Astronomy & Astrophysics, 207, 1

Stuber S. K., et al., 2021, Astronomy & Astrophysics, 653, A172

Stuber S. K., et al., 2023a, Astronomy & Astrophysics, 676, A113

Stuber S. K., et al., 2023b, Astronomy & Astrophysics, 676, A113

Swartz D. A., Yukita M., Tennant A. F., Soria R., Ghosh K. K., 2006, The Astrophysical Journal, 647, 1030

Takekawa S., Oka T., Tokuyama S., Tanabe K., Iwata Y., Tsujimoto S., Nomura M., Shibuya Y., 2019a, , 71, S21

Takekawa S., Oka T., Iwata Y., Tsujimoto S., Nomura M., 2019b, The Astrophysical Journal Letters, 871, L1

Teng Y.-H., et al., 2022, The Astrophysical Journal, 925, 72

Terashima Y., Ho L. C., Ptak A. F., Mushotzky R. F., Serlemitsos P. J., Yaqoob T., Kunieda H., 2000, The Astrophysical Journal, 533, 729

Thakur P., Ann H. B., Jiang I.-G., 2009, The Astrophysical Journal, 693, 586

Thater S., 2019, in ALMA2019: Science Results and Cross-Facility Synergies. p. 129 (arXiv:1911.11491), doi:10.5281/zenodo.3585459

Tody D., 2000, in Murdin P., ed., , Encyclopedia of Astronomy and Astrophysics. p. 2923, doi:10.1888/0333750888/2923

Tonry J. L., Dressler A., Blakeslee J. P., Ajhar E. A., Fletcher A. B., Luppino G. A., Metzger M. R., Moore C. B., 2001, The Astrophysical Journal, 546, 681

Torii K., et al., 2010, , 62, 1307

Tress R. G., Sormani M. C., Glover S. C. O., Klessen R. S., Battersby C. D., Clark P. C., Hatchfield H. P., Smith R. J., 2020, Monthly Notices of the Royal Astronomical Society, 499, 4455

Tully R. B., 1987, The Astrophysical Journal, 321, 280

Tully R. B., 1988, Nearby galaxies catalog

Vazdekis A., et al., 2015, Monthly Notices of the Royal Astronomical Society, 449, 1177

Veron-Cetty M. P., Veron P., 1986, , 66, 335

Véron-Cetty M. P., Véron P., 2006, Astronomy & Astrophysics, 455, 773

Villforth C., et al., 2014, Monthly Notices of the Royal Astronomical Society, 439, 3342

Vollmer B., Soida M., Beck R., Chung A., Urbanik M., Chyży K. T., Otmianowska-Mazur K., Kenney J. D. P., 2013, Astronomy & Astrophysics, 553, A116

Vulcani B., et al., 2018, Monthly Notices of the Royal Astronomical Society, 480, 3152

Vynatheya P., Saha K., Ghosh S., 2021, arXiv e-prints, p. arXiv:2105.03183

Walcher C. J., Coelho P. R. T., Gallazzi A., Bruzual G., Charlot S., Chiappini C., 2015, Astronomy & Astrophysics, 582, A46

Walsh W., Staveley-Smith L., Oosterloo T., 1997, The Astronomical Journal, 113, 1591

Watts A. B., Catinella B., Cortese L., Power C., Ellison S. L., 2021, Monthly Notices of the Royal Astronomical Society, 504, 1989

Watts A. B., et al., 2024, Monthly Notices of the Royal Astronomical Society, 530, 1968

Westfall K. B., et al., 2019, The Astronomical Journal, 158, 231

Westoby P. B., Mundell C. G., Nagar N. M., Maciejewski W., Emsellem E., Roth M. M., Gerssen J., Baldry I. K., 2012, The Astrophysical Journal Supplement Series, 199, 1

Williams T. G., et al., 2021, The Astronomical Journal, 161, 185

Wilson A. S., Baldwin J. A., Ulvestad J. S., 1985, The Astrophysical Journal, 291, 627

Wong T., Blitz L., Bosma A., 2004a, The Astrophysical Journal, 605, 183

Wong T., Blitz L., Bosma A., 2004b, The Astrophysical Journal, 605, 183

Woo J.-H., Urry C. M., 2002, The Astrophysical Journal, 579, 530

Woo J.-H., Son D., Bae H.-J., 2017, The Astrophysical Journal, 839, 120

Wood K., Mathis J. S., 2004, Monthly Notices of the Royal Astronomical Society, 353, 1126

Wood K., Haffner L. M., Reynolds R. J., Mathis J. S., Madsen G., 2005, The Astrophysical Journal, 633, 295

Zurita A., Relaño M., Beckman J. E., Knapen J. H., 2004, Astronomy & Astrophysics, 413, 73

de Jong R. S., 1996, Journal of Astronomical Data, 2, 1

de Lorenzo-Cáceres A., Falcón-Barroso J., Vazdekis A., Martínez-Valpuesta I., 2008, The Astrophysical Journal Letters, 684, L83

de Lorenzo-Cáceres A., et al., 2019, Monthly Notices of the Royal Astronomical Society, 484, 5296

de Sá-Freitas C., et al., 2023a, Astronomy & Astrophysics, 671, A8

de Sá-Freitas C., et al., 2023b, Astronomy & Astrophysics, 678, A202

de Vaucouleurs G., de Vaucouleurs A., Corwin Herold G. J., Buta R. J., Paturel G., Fouque P., 1991, Third Reference Catalogue of Bright Galaxies

de Zeeuw P. T., et al., 2000, The Newsletter of the Isaac Newton Group of Telescopes, 2, 11

de Zeeuw P. T., et al., 2002, Monthly Notices of the Royal Astronomical Society, 329, 513

van de Ven G., Fathi K., 2010, The Astrophysical Journal, 723, 767

van der Kruit P. C., Allen R. J., 1978, Annual Review of Astronomy and Astrophysics, 16, 103

van der Laan T. P. R., et al., 2013, Astronomy & Astrophysics, 556, A98

van der Marel R. P., Franx M., 1993a, The Astrophysical Journal, 407, 525

van der Marel R. P., Franx M., 1993b, The Astrophysical Journal, 407, 525